Silicon photonic materials obtained by ion implantation and rapid thermal processing

A thesis submitted to the University of Manchester for the degree of Doctor of Philosophy (PhD) in the Faculty of Engineering and Physical Sciences

2010

Iain Forbes Crowe

School of Electrical and Electronic Engineering

'To get to the essence of things, one has to work long and hard'

- Vincent van Gogh

List of contents

Word count:	61461

List of figures

Chapter 6

List of tables

Name: Iain Forbes Crowe
University: The University of Manchester
Research degree and year: PhD, 2010
Thesis title: Silicon photonic materials obtained by ion implantation and rapid thermal processing

Abstract

The original work presented in this thesis describes research into Si-based luminescent materials, prepared specifically by ion implantation and rapid thermal processing of thermal oxide films. An in-depth optical characterisation, employing photoluminescence (PL) and Raman spectroscopy was complimented with electron microscopy, revealing the source of efficient room temperature PL as nano-scale silicon inclusions (Si-NCs). The evolution of the Si-NC size and density with isothermal and isochronal annealing may be described using classical thermodynamics according to a diffusion limited, Ostwald ripening process. Values for the coarsening rate and activation energy, extracted from the evolution of the Si-NC size with annealing indicate that the transport of Si atoms and precipitate formation are enhanced in ion implanted films, attributable to the presence of vacancy and interstitial defects generated during ion irradiation.

The PL and Raman spectra are well correlated with the evolving Si-NC size and density according to the quantum confinement (QC) model in which samples containing larger clusters emit at longer wavelengths. However, the formation of bound exciton states within the band gap of small clusters (< 2nm), as a result of specific surface chemistries, suppresses higher energy emissions. The increase in PL intensity with annealing was exactly correlated with the increase in PL lifetime, characteristic of the removal of non-radiative defects. A dependence of the PL dynamics on emission energy, with higher energies exhibiting shorter lifetimes, further evidences the QC effect. Blue shifted emission at high excitation flux and/or low temperature is correspondent with the slower PL dynamics and preferential saturation at longer wavelengths. Raman spectra were fit using a phonon confinement model, from which Si-NC size distributions were extracted and found to compare favourably with those obtained from TEM images. Stresses in the films, determined from the Raman peak position, were used as an independent method for calculating the Si surface energy, which is very close to the literature values.

A single, high temperature anneal of Si and erbium (Er) co-doped films revealed a preferential aggregation of Er at the Si-NC formation site, which is of particular importance for the photo-sensitization of Er PL around $1.5\mu m$. The Er PL was enhanced in the presence of Si-NCs by several orders of magnitude compared with a reference SiO_2:Er. Whilst broadband pumping of the Er via Si-NCs evidences a non-resonant energy transfer mechanism with an efficiency which depends on the Si-NC size, the process is limited at high excitation flux by a combination of low sensitizer (Si-NC) density and non-radiative losses.

Finally the Si-NC PL intensity in phosphorus (P) co-doped films was studied and found to depend strongly on the annealing conditions and P concentration. For lower temperature treatments, a factor 2 PL enhancement, relative to an un-doped reference was obtained, attributed to the passivation of Si-NC surface defects. Higher temperature treatments resulted in the monotonic quenching of the PL with increasing P concentration, attributed to the introduction of an efficient Auger recombination channel as a result of the ionization of P-donors inside large Si-NCs. A simple statistical model predicts this behaviour and provides an incidental estimate of the Si-NC size.

Declaration

No portion of the work referred to in this thesis has been submitted in support of an application for another degree or qualification of this or any other university or other institute of learning

Copyright statement

The author of this thesis (including any appendices and/or schedules to this thesis) owns certain copyright or related rights in it (the "Copyright") and he has given The University of Manchester certain rights to use such Copyright, including for administrative purposes.

Copies of this thesis, either in full or in extracts and whether in hard or electronic copy, may be made **only** in accordance with the Copyright, Designs and Patents Act 1988 (as amended) and regulations issued under it or, where appropriate, in accordance with licensing agreements which the University has from time to time. This page must form part of any such copies made.

The ownership of certain Copyright, patents, designs, trade marks and other intellectual property (the "Intellectual Property") and any reproductions of copyright works in the thesis, for example graphs and tables ("Reproductions"), which may be described in this thesis, may not be owned by the author and may be owned by third parties. Such Intellectual Property and Reproductions cannot and must not be made available for use without the prior written permission of the owner(s) of the relevant Intellectual Property and/or Reproductions.

Further information on the conditions under which disclosure, publication and commercialisation of this thesis, the Copyright and any Intellectual Property and/or Reproductions described in it may take place is available in the University IP Policy (see http://www.campus.manchester.ac.uk/medialibrary/policies/intellectual-property.pdf), in any relevant Thesis restriction declarations deposited in the University Library, The University Library's regulations (see http://www.manchester.ac.uk/library/aboutus/regulations) and in The University's policy on presentation of Theses.

Acknowledgements

I would like to express my sincerest gratitude to the following for their professional, and in some cases personal support throughout this project, without whom it would certainly not have reached conclusion:

Noémie, my long suffering, but fortunately patient girlfriend for her love and support throughout, not to mention her *Gratin Dauphinois* – Qu'est-ce que je ferais sans toi?

My family, whose love, support and guidance got me here in the first place.

Dr. Matthew Halsall, my supervisor, for his encouragement, expert advice and sense of humour.

Prof. Andy Knights (McMaster University) and Prof. Russ Gwilliam (University of Surrey) for the never ending supply of samples and expert advice on ion implantation and annealing techniques.

Dr. Uschi Bangert, Reza Jalili-Kashtiban and James Eccles (Manchester Materials Science Centre) and Dr. Mahri Gass (Daresbury SuperSTEM) for providing advice and valuable assistance in obtaining superb microscopy images and EELS maps. I am also extremely grateful to Dr. Bangert for reading my end of year reports (typically at short notice!).

Dr. Oksana Hulko (McMaster University) for X-TEM microscopy images and associated statistical data on nano-clusters, whose patience in the provision of which is gratefully acknowledged.

Dr. Tyler Roschuk (Imperial College London) for useful discussions surrounding rare-earth luminescence in silicon rich oxides and nitrides

Dr. Tony Kenyon and Dr. Maciej Wojdak (University College London) for assistance with PL transient measurements and continuing fruitful discussions surrounding the luminescence from silicon nano-clusters.

Eric Whittaker for technical support throughout my project and Malcolm McGowan for the countless gallons of liquid nitrogen that he kindly lent (!) to me over the past few years.

All of the support staff in electrical and electronic engineering at the University of Manchester and finally, the Engineering and Physical Sciences Research Council (EPSRC) UK for financing my doctoral training award.

Publications

Spatially correlated erbium and Si nanocrystals in coimplanted SiO$_2$ after a single high temperature anneal

I. F. Crowe, R. Jalili-Kashtiban, B. Sherliker, U. Bangert, M. P. Halsall, A. P. Knights, and R. M. Gwilliam, Journal of Applied Physics **107** (2010)

Structural and compositional study of Erbium-doped silicon nanocrystals by HAADF, EELS and HRTEM techniques in an aberration corrected STEM

R. J. Kashtiban, U. Bangert, I. F. Crowe, M. P. Halsall, B. Sherliker, A. J. Harvey, J. Eccles, A. P. Knights, R. M. Gwilliam, and M. Gass, Journal of Physics: Conference Series; Vol. **209** (IoP, Oxford, UK, 2010)

Formation of Si-nanocrystals in SiO$_2$ via Ion Implantation and Rapid Thermal Processing

I. F. Crowe, O. Hulko, A. P. Knights, N. P. Hylton, M. P. Halsall, S. Ruffell, and R. M. Gwilliam, SPIE - Photonics West; Vol. **7606** (SPIE, San Francisco, USA, 2010)

Optical spectroscopy of Er doped Si-nanocrystals on sapphire substrates fabricated by ion implantation into SiO$_2$

N. P. Hylton, I. F. Crowe, A. P. Knights, M. P. Halsall, S. Ruffell, and R. M. Gwilliam, SPIE - Photonics West; Vol. **7606** (SPIE, San Francisco, USA, 2010)

Observation of non-radiative de-excitation processes in silicon nanocrystals

A. P. Knights, J. N. Milgram, J. Wojcik, P. Mascher, I. F. Crowe, B. Sherliker, M. P. Halsall, and R. M. Gwilliam, Physica status solidi (a) **206,** 969-972 (2009)

Structure and Luminescence of Rare Earth-doped Silicon Oxides Studied Through XANES and XEOL

T. Roschuk, P. Wilson, J. Li, K. Dunn, J. Wojcik, I. F. Crowe, R. Gwilliam, M. Halsall, A. Knights, and P. Mascher, ECS Transactions **25,** 213-222 (2009)

Combined Super-STEM imaging, EEL and PL spectroscopy of un-doped and Er doped SRSO on Si

I. F. Crowe, T. R. Roschuk, U. Bangert, B. Sherliker, M. P. Halsall, A. P. Knights, and P. Mascher, Conference on Optoelectronic and Microelectronic Materials and Devices, 2008. COMMAD 2008 (IEEE, Australian National University (ANU), Canberra, 2008), p. 163-165

1   Introduction

1.1   Background

The trend in developing ever smaller, faster electronic architectures that are increasingly affordable and importantly accessible, has to date continued to validate the prediction in 1965[1] by *Intel* co-founder, Gordon Moore that *"…the complexity for minimum component costs has increased at a rate of roughly a factor of two per year…Certainly, over the short term this rate can be expected to continue, if not to increase…"*. Evidence for the validity of this prediction can currently be found in almost every area of electronics, ranging from the number of transistors on a single chip (currently running at ~2 billion[2]), ultra-fast processing speeds (3.8GHz for *Intel Core i7 965*) and more recently in digital camera pixel densities (3rd generation mobile phone technology includes an integrated camera with 12 million pixels).

Despite this impressive capacity for processing information, transporting it to the wider network is becoming increasingly demanding as a result of the bandwidth limitations imposed by the continued use of high density metallic interconnects. Miniaturisation of these interconnects has led to a number of additional issues, for example smaller cross-sections yield higher parasitic RC coupling delays whilst 'cross talk' between these densely packed transmission lines can lead to corruption in the transmitted data[3]. Such issues, un-checked, have the capacity to forestall the apparent usefulness of high speed processing and the rate of technological advance could begin to deviate from *Moore's law* within the current decade. If the electronics sector is to meet the voracious global demand for ever increasing computing capacity and speed it therefore requires somewhat of a step change in technology.

The most natural technological progression for the longer term would be a transition to an optoelectronic platform in which chip-to-chip, board-to-board and all network communication is carried by light via integrated waveguides and fibre-optic links[4]. This would significantly enhance the information capacity with anticipated bandwidths in the region of Tb/s, improve transmission accuracy and completely remove electronic coupling delays. So that the development time and cost of such technologies does not impact heavily on the consumer, it is highly likely that the optoelectronic components for such a platform will, to some degree

have to meet the fundamental requirement for compatibility with silicon processing. The current and historical investment in the industry (~$500 billion in 2005)[5] then dictates that the most cost effective way to achieve this is through the use of technology that is either completely CMOS compatible or by a cost effective post-process hybridization of III-V materials with silicon[6].

Indeed silicon photonics is already a very active field in which a variety of optical components have already been demonstrated[5]. Whilst a fully integrated silicon optoelectronics platform may still be some years away, it is likely that we will begin to see technologies such as 'fiber-to-the-home' maturing rather earlier as a result of the increasing demand for ultra-fast internet. Further improvements should follow if the fiber can be directly coupled to the microprocessor so that received light signals can be converted to electronic signals at the chip level.

However, it is the inverse problem of efficient photon generation from silicon that represents the largest technical challenge. Despite its established position as the leading electronic material, there are a number of fundamental reasons why bulk silicon is almost perfectly *unsuited* to optoelectronics, which is why it has not previously been considered as a material for photonic applications.

First of all bulk silicon belongs to a class of semiconductor materials that exhibit an *indirect* band-gap, which means that the difference in the momentum of electrons at the bottom of the conduction band (CB) and that of the corresponding holes at the top of the valence band (VB) is non-zero. This arises in particular because of the lattice symmetry of silicon and means that radiative transitions between electronic conduction and valence states are electric-dipole 'forbidden'[7]. That is, they cannot occur without the assistance of some perturbation that is capable of temporarily altering this symmetry, most commonly this is via electron interaction with lattice vibrations (phonons) of specific energy and momentum. The processes of absorption, emission and electron-phonon interaction in bulk silicon are illustrated schematically by **Figure 1-1**.
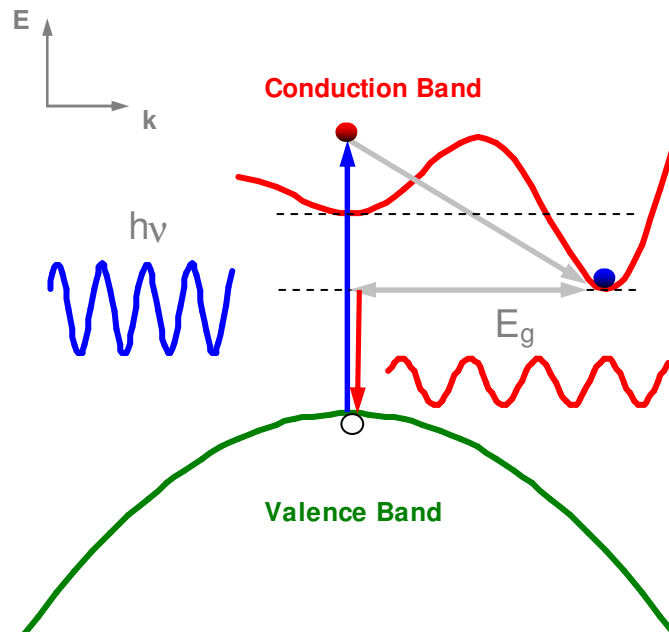
Figure 1-1 Schematic energy-wavevector (E-k) representation of the bulk Si electronic energy structure close to the band edges. Absorption (blue) and emission (red) processes are represented by vertical arrows, i.e. k ~ 0 due to the negligible photon momentum. Indirect absorption and relaxation of electrons to the conduction band edge are both lattice vibration (phonon) assisted processes (grey arrows in ⁺ve k direction). Band edge radiative recombination then necessarily requires further electron-phonon interactions to recover the difference in momentum (grey arrow in ⁻ve k direction)

The electron-phonon interaction occurs with a low probability and so the excited electronic state persists for some time (on the order of milliseconds) during which carriers diffuse and may be captured at trapping centres or recombine non-radiatively via processes such as *free carrier absorption* (FCA) or *Auger recombination*[8]. FCA describes an electron-photon interaction in which the energy from incoming photons is absorbed by carriers already in the conduction band (free carriers) resulting in energy draining intra-band transitions. *Auger* recombination describes electron-electron interactions in which an excited electronic state is relaxed by transferring energy to another electron. Both of these processes occur on rapid (~ns) timescales and therefore compete favourably with radiative recombination in bulk Si.

The indirect band structure is *less* critical where Si is employed in photo-detector applications (testament to which are the hugely successful Si photo-diode and photo-voltaic cell) because phonons generated during the excitation process are simply absorbed as 'tolerable' material heating. For applications in which silicon is required to generate photons however, the requirement for phonon assistance in the radiative relaxation process (in order to conserve momentum) yields an extremely low value ($\eta \sim 10^{-6}$)[9] for the internal quantum efficiency.

The actual photon energy, characteristic of transitions across the bulk Si band gap (~1.12eV at 300K) corresponds to an emission wavelength of ~1.1µm, which is not especially desirable for optoelectronic applications in any case. For example this band is not coincident with the principal transmission windows of silica fiber, nor is it applicable to visible light sources for display and lighting technologies.

Finally, pure crystalline silicon does not lend itself particularly well to wave-guided optical modulation either because its' crystal symmetry (and hence weak dipole moment) exhibit extremely weak 2nd order nonlinear effects such as the *Pockel's* effect[10].

In spite of these physical constraints, the research community has rallied in recent years and a number of intelligent designs has so far led to the demonstration of almost all of the necessary components for a fully integrated CMOS compatible photonics platform[9], with one major exception; an efficient, electrically pumped Si laser. Whilst a *Raman* based Si laser[11] was reported, its lasing wavelength ~1690nm and reliance on photo- rather than electrical injection of carriers means it has limited application. A hybrid III-V quantum well laser bonded to a silicon waveguide in silicon-on-insulator emitting around 1568nm was also demonstrated[6], although the fabrication of this device is relatively complex (and therefore costly) and does not strictly satisfy the current CMOS compatibility standard. Electroluminescent light sources based on band engineered alloys of silicon with germanium in $Si_{1-x}Ge_x$ quantum well type structures and Si/Ge super-lattices were also demonstrated although the emission for these also tends to be limited to the infra-red[9, 12]. Impurity mediated luminescence has also been shown to enhance the light yield from silicon by localising electron-hole pairs at iso-electronic centres created by the presence of electrically neutral dopant species[12]. Yet another approach was reported by Green *et al*[13] in which a highly pure, moderately doped bulk Si LED was demonstrated. By combining material purity, to reduce non-radiative recombination, with improved light extraction, through the

use of a highly reflective back surface and a textured top surface, the authors of [13] were able to demonstrate an efficiency of ~1% at room temperature.

Perhaps the most promising luminescent materials though are those based on the quantum confinement of electron and hole states in for example silicon nano-clusters. The discovery of bright red (room temperature) luminescence from porous silicon (p-Si) in 1990 by Canham *et al*[14] was attributed to an increase in the radiative transition as a result of carriers confined to nano-meter scale silicon wires. This work sparked an intensive global research frenzy, which has led to a plethora of works describing the preparation and characterisation of luminescent silicon based nano-structures. Of particular note are the numerous demonstrations of photo-excited optical gain[15-17], which opens up the possibility of developing amplifiers, LEDs and perhaps lasers. The development of electroluminescent devices has however lagged somewhat due to limitations associated with device lifetime. The excitation mechanism in this case, i.e. hot electron impact ionization, proceeds via tunnelling of electrons through the thin oxide in a MOS type device. This gradually degrades the dielectric layers surrounding the nano-clusters resulting in electrical breakdown and device failure. However, Walters *et al*[18] recently described a field effect electroluminescent device based on a bi-polar excitation scheme, whereby carriers of opposite sign are injected into the nano-clusters *sequentially* from the same semiconductor channel, rather than *simultaneously* as in a conventional p-n junction type device. The different tunnelling mechanisms involved in this case essentially place a much lower stress on the dielectric layers and the authors reported a respectable lifetime of ~5×10^9 cycles.

When one considers the stakes involved in combining the vast amount of time and money invested in the silicon microelectronics industry with the potential gains to be made by extending this to include silicon photonics, it is not surprising that there has been an ever-growing interest from research groups the world over. This is evidenced by the increasing publication rate in the field and the wide range of potential applications already described, as illustrated by **Figure 1-2**.
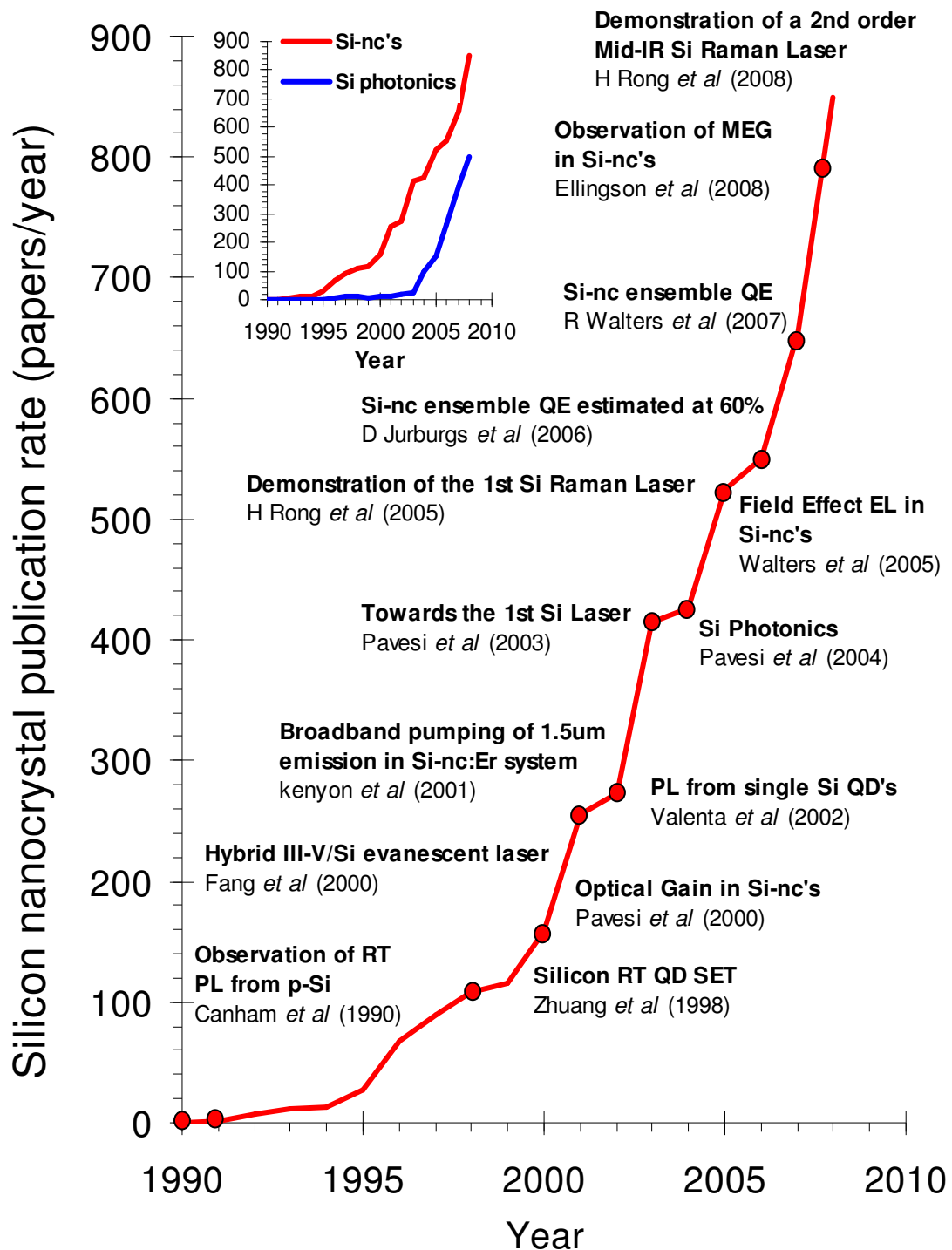
Figure 1-2 Exponentially rising silicon nanocrystal publication rate in the twenty year period since the first observation of room temperature luminescence from p-Si by Canham *et al*[14]**. Data obtained from a Google Scholar search for "silicon nanocrystals". The inset reveals that the result of a similar search for "silicon photonics" lags that of "silicon nanocrystals" by several years but follows a similar trend**

1.2   What is a silicon nano-cluster?

In the context of this thesis a silicon nano-cluster is a nano-scale silicon inclusion typically formed from less than 5000 atoms[19, 20] embedded within a relatively thick amorphous SiO_2 host matrix, an example of which is shown in **Figure 1-3**.
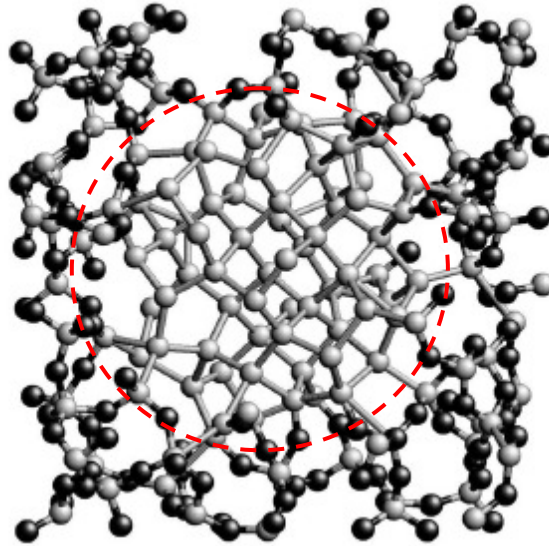
Figure 1-3 Molecular dynamics atomistic simulation of a 1.3nm silicon nano-cluster (circled red) embedded in amorphous SiO_2. Silicon and oxygen atoms are shown as grey and black spheres respectively, adapted after [21]

The formation of clusters of like atoms proceeds, from an excess of those atoms in the host matrix by a diffusion process, which is governed by classical thermodynamics and which acts to reduce the *Gibbs* or volume free energy[8, 19]. Very small clusters are essentially molecules with chemical bonds that differ from those of the bulk material but as the cluster size increases (a process that is accelerated for increasing atomic excesses and particularly during high temperature thermal treatment), it naturally adopts the unit cell and bonding configuration of the bulk material[22]. For silicon clusters, this means crystallizing in the diamond structure as verified by high resolution electron microscopy[23].

A number of molecular dynamics atomistic simulations have been developed to describe the structural formation of such nano-clusters in amorphous silica[19-21]. Whilst the exact shape naturally depends on the preparation, there is general agreement that the minimum energy configuration, at least for nano-clusters smaller than ~5nm, is pseudo-spherical, which has also been evidenced by

electron microscopy studies[24]. **Figure 1-4** shows an example of such an image from a sample prepared via PECVD by collaborators at McMaster University.
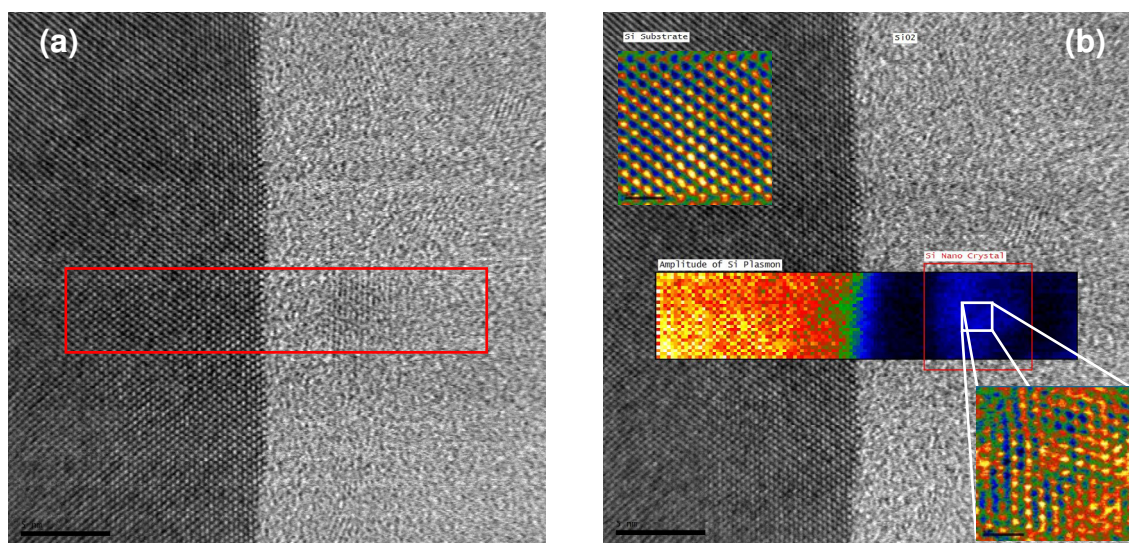
Figure 1-4 (a) Bright field STEM image (scale bar = 5nm) of silicon nano-crystals embedded in amorphous SiO$_2$ (the red box is the electron energy loss (EEL) scan area). (b) The same image with superimposed EELS map derived from the relative intensity of the Si energy loss peak ~17eV. A strong (red) signal appears in the substrate and a weak (blue) signal reveals the silicon nano-crystal in the centre of the image. The insets are high resolution images (scale bar = 1nm) of the lattice structure of the silicon substrate (top) and silicon nano-crystal (bottom). Figures adapted from [25]

In terms of the optical properties of silicon nano-clusters, it is highly likely that subtle changes in shape will complicate their electronic band structure which in turn should affect their absorption and emission characteristics[26]. In addition to the shape there is strong evidence that the electronic structure is influenced by the effects of strain[27] as well as the chemical nature and geometry of interface bonds[28-30]. The latter in particular has been implicated in the luminescence process by several groups[31-33] with the suggestion that specific interfacial bonding configurations and surface terminating species can lead to the formation of defect-like levels within the forbidden gap of the nano-cluster or insulating host matrix. For silicon nano-clusters embedded in an oxide host the most likely candidates appear to be the Si-O-Si type bonds or the covalent Si=O (silanone) complex[31, 32, 34]. Indeed there were a number of notable works suggesting that the latter in

particular might be a critical component for the formation of a third or fourth population inversion level for realising optical gain in such materials[15, 35, 36].

Whilst the strain, structure and chemical nature of the interface likely complicates the electronic energy structure of the silicon nano-cluster, it is now widely accepted that their size and therefore quantum confinement plays a critical role in enhancing the radiative transition probability relative to bulk Si[37-40].

1.3   Quantum confinement in silicon nano-clusters

The implications of physical and electronic confinement of charge carriers on the nano-meter scale were predicted in the first half of the last century. However, it has been the ability to engineer semiconductor structures on the nano-meter scale using more modern growth techniques, over which we have increasingly accurate control that has more recently given us the ability to demonstrate devices based on such phenomena[41]. A plethora of texts are available[42] in which more detailed quantum mechanical treatments can be found but it is pertinent to summarise here some of the important features of quantum confinement that are particularly relevant in understanding the luminescence from Si-nanocrystals.

In general, quantum confinement effects refer to those manifestations in the electronic (and vibrational) properties of a material that arise specifically as a result of spatial confinement of the electronic wave-function (or phonon mode) in at least one dimension. Experimental observation of these manifestations, for example via optical spectroscopy is possible when the confining length scale becomes comparable to the period of the wave-function of the confined particle[43]. The wave-functions of particles in the bulk media are responsible for many of the inherent material properties and altering them by the imposition of boundaries effects changes in these properties. For example changes in the electronic transition energies will manifestly change the absorbing and emitting characteristics whereas changes in phonon dispersion will affect properties such as the specific heat capacity. Further reductions in size result in a continuously increasing departure of the material specific properties from the bulk, which yields enormous device potential from an engineering standpoint.

As we have seen, radiative transitions in *indirect* band gap semiconductors such as silicon require the assistance of momentum conserving phonons. The imposition of boundary conditions on the electron and hole wave-functions in

silicon, for example by their spatial confinement in silicon nano-clusters embedded in wide gap insulating hosts, therefore has an especially profound effect. As carriers are confined in real space, their associated wave-functions spread out in momentum space, which is a direct consequence of the non-commutitivity of position and momentum according to *Heisenberg's* uncertainty principle, expressed mathematically as:

$$\Delta p_x \Delta x \geq \hbar \tag{1}$$

Spatial localisation of an electron to the region $\Delta x \sim d$ then yields an uncertainty in the x-component of the electron momentum, p_x of an amount of order $\hbar/d$.

This strong symmetry breaking in confined systems relaxes the k-conservation rule, reduces the excited state lifetime and significantly increases the probability that an excited electronic state will relax to another, generating a photon in the process. As the degree of spatial confinement increases, fewer wave-functions are able to satisfy the boundary conditions and as such the bulk k-states become increasingly focussed around specific energies, which reduces the density of states (DOS) for a given energy range. This is apparent from the *Schrodinger* equation for a particle confined to an infinite square potential well, for which standing wave-like solutions are obtained within the confined region. In contrast to the continuum of allowed k-states in bulk semiconductors, it can be shown that the allowed k-states for the confined particle reduces to[42]:

$$k_n = \frac{n\pi}{d}; n = 1, 2, 3... \tag{2}$$

And the corresponding allowed electronic energy states then yield the familiar result:

$$E_n = \frac{\hbar^2 k_n^2}{2m_e^*} = \left(\frac{\hbar^2}{2m_e^*} \right) \left(\frac{n^2 \pi^2}{d^2} \right) \tag{3}$$

For the $n = 1$ state we obtain a 'zero-point' or confinement energy, ΔE which for electrons effectively increases the energy of the conduction band edge relative to the bulk material according to equation (4):

$$E_{confined}^{CB} = E_{bulk}^{CB} + \Delta E = E_{bulk}^{CB} + \left(\frac{\hbar^2}{2m_e^*} \right) \left(\frac{\pi^2}{d^2} \right) \tag{4}$$

If this is extended to include the confinement of an electron-hole pair inside a nano-cluster, then the confinement energy encompasses the individual kinetic energies of both the electron and hole and an electron-hole interaction term[44]:

$$E^g_{confined} = E^g_{bulk} + \Delta E = E^g_{bulk} + \frac{\hbar^2}{2}\frac{\pi^2}{d^2}\left(\frac{1}{m^*_e}+\frac{1}{m^*_h}\right) - \frac{1.786e^2}{\varepsilon d} + ... \qquad (5)$$

The first term on the right describes the bulk band gap, the second the energy dependence of the electron-hole confinement, which raises the band gap as $1/d^2$ and the last term accounts for a correlation effect arising from a shielded *Coulomb* potential between electron and hole, which acts to lower the confined band gap as $1/d$. This is an extremely important result for silicon because it means that the confined band gap is shifted to the visible part of the electromagnetic spectrum relative to bulk silicon simply by reducing the nano-cluster size. This is summarized schematically in **Figure 1-5** for glass bound silicon nano-clusters of different sizes.
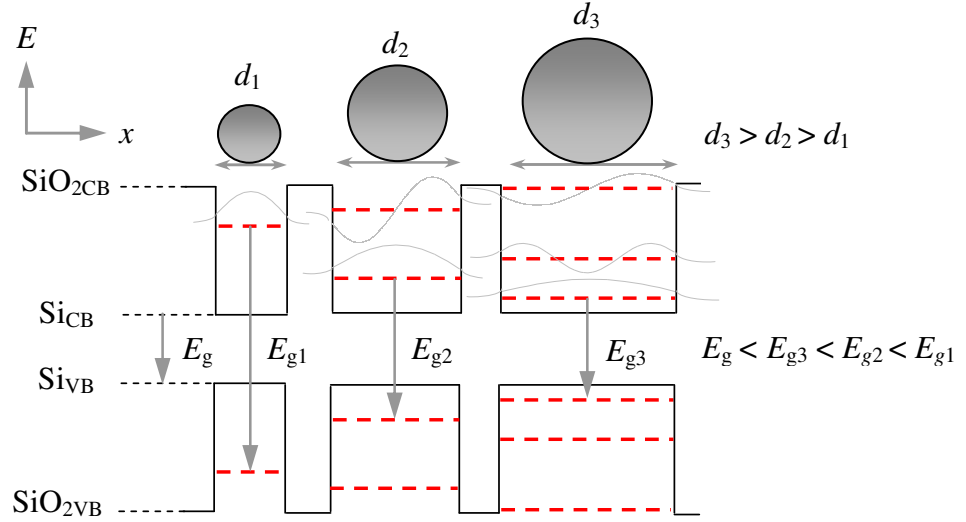
Figure 1-5 Schematic representation of the effect of spatial confinement (1D) on the energy levels of different size silicon nano-clusters. Increasing the confinement effectively increases the band gap energy (grey arrows), represented by the *n* = 1 transition for all three nano-cluster sizes. In real systems containing a large density of different size nano-clusters, transitions may be further complicated by the mixing of states between neighbouring nano-clusters

This increase in the band gap energy and the spatial confinement of electrons and holes to the nano-meter scale favours the formation of an exciton bound state over dissociation, which dominates in bulk semiconductors at room temperature. This provides a convenient definitive criterion for the onset of quantum confinement effects, being the point at which the confining length scale is smaller than the excitonic *Bohr* radius[43]:

$$a_b = \frac{4\pi h^2 \varepsilon_0 \varepsilon_r}{e^2}\left(\frac{1}{m_e^*} + \frac{1}{m_h^*}\right) \tag{6}$$

which for silicon is ~4.3nm. Confinement on this scale greatly reduces the carrier diffusion length relative to bulk Si, which suppresses the probability of encountering defects, particularly if the nano-cluster interface with the SiO_2 is free of electron trapping centres such as the dangling bond (P_b – type) defect[47]. Thermally enhanced non-radiative relaxation processes such as FCA or *Auger* recombination should also be suppressed relative to the bulk case because the larger band gap reduces the intrinsic carrier population for a given temperature, all of which enhances the radiative transition probability.

It is clear from the preceding discussion that despite maintaining the same internal bonding geometries as bulk Si (ignoring the effects of stress[*]), silicon nano-clusters should exhibit extremely different optical characteristics. Indeed there is strong evidence that the *indirect* nature of the band gap is preserved in silicon nano-crystals[46], which means that radiative transitions should necessarily be phonon mediated, whilst proceeding with greater probability relative to the bulk case. Kovalev *et al*[40] showed that the phonon assisted transition probability increases in direct proportion to the confinement energy. However, this work also critically revealed a non-zero probability for *quasi-direct* optical transitions, i.e. radiative transitions without the assistance of momentum conserving phonons. In fact, the probability of these *quasi-direct* transitions was also found to increase with the inverse nano-cluster size (increasing confinement energy) so that for very small clusters, this may represent the most probable transition.

---

[*] Huge stresses can result from the lattice mismatch at the nano-cluster/oxide interface, which can affect the bonding geometry and therefore band structure[45].   H. Hofmeister, F. Huisken and B. Kohn, The European Physical Journal D - Atomic, Molecular, Optical and Plasma Physics **9** (1), 137-140 (1999).

1.4   Applications of silicon nano-clusters

It is pertinent to summarise here some of the specific technology areas in which silicon nano-cluster based materials might expect to find application in the near to medium term. The bulk of the research falls into four main categories.

1.4.1   Display and lighting technologies

Clearly the consequences of quantum confinement that give rise to a blue-shifted emission spectrum, which is tuneable depending upon the silicon nano-cluster size[48, 49] make them very attractive materials to the field of display and lighting technologies. For example, Lee *et al*[50] demonstrated white light emission from colloidal silicon nano-crystals under UV photo-excitation whilst Tan *et al*[51] reported a dual colour (450nm and 650-700nm) electroluminescent device. Silicon nano-clusters embedded in silicon nitrides are also being intensively studied as the active medium for LEDs[52, 53].

1.4.2   Photo-voltaics

As well as their blue shifted emission spectra, the absorbing states of silicon nano-clusters are also blue shifted relative to bulk Si[54, 55]. The absorption edge can be tuned further by doping with shallow impurities such as phosphorus and boron[56] and this, in particular, has led to silicon nano-cluster based materials being identified as potential candidates for improved efficiency, multi-junction solar cells[57-61]. Furthermore, Timmerman *et al*[62] recently showed that silicon nano-cluster based materials exhibit a phenomenon commonly referred to as *multiple exciton generation* (although in this article it is referred to as space separated quantum cutting (SSQC)) in which two low energy photons are generated after absorbing a single high energy photon. In this particular work, the authors of [62] demonstrated the effect in a sample in which silicon nano-clusters were coupled to multiple luminescent erbium (Er^{3+}) ions as illustrated by **Figure 1-6**.
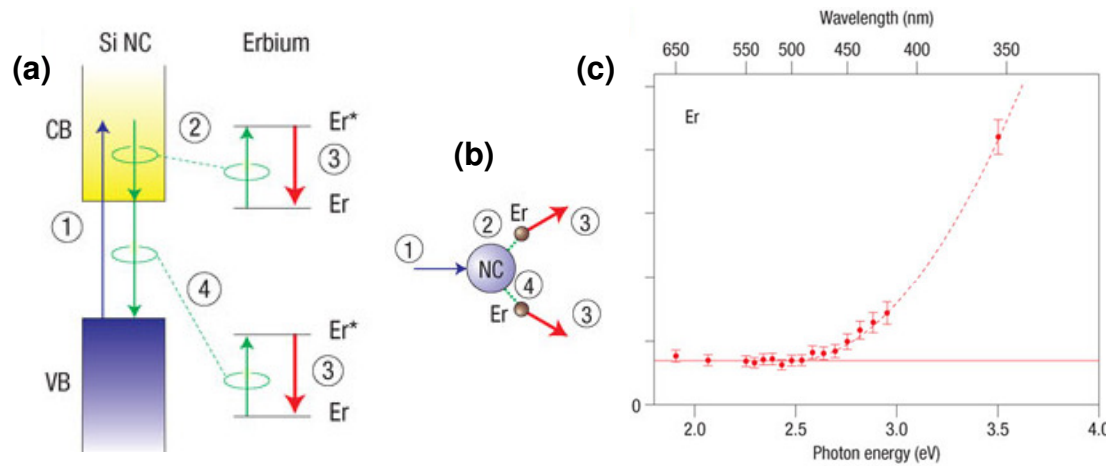
Figure 1-6 (a) Schematic of the SSQC process: 1) Excitation of the silicon nano-cluster with a high-energy photon creating a hot electron–hole pair with excess energy; 2) intra-band *Auger* process exciting an Er^{3+} ion and removing the excess energy; 3) erbium-related PL; and 4) excitation of a second Er^{3+} ion by the conventional inter-band *Auger* process. (b) Schematic illustrating the SSQC process with excitation of two nearby Er^{3+} ions. (c) Relative quantum efficiency of erbium-related PL (1535 nm) as a function of excitation energy with the SSQC process evident above 2.5eV. Figures taken from reference [62]

At low excitation energies the sensitizing silicon nano-cluster excites at most one erbium ion through an inter-band *Auger* type exciton recombination process and the quantum efficiency[†] remains constant indicating a single photon process (one photon in, one photon out). As the excitation energy was increased above ~2.5eV, photons were divided by the silicon nano-cluster between two erbium ions through a combination of hot carrier phonon assisted intra-band and inter-band *Auger* relaxation processes. This was evidenced by the sudden increase in the measured photon generation efficiency and is therefore particularly relevant to photovoltaic technology because it has the potential to enhance their efficiency beyond the *Schockley-Queisser* limit[‡] through the generation of multiple carriers from single photons.

[†] Quantum efficiency is defined here as the ratio of the effective excitation cross section of the erbium photoluminescence to the absorbed fraction of incident photons at a particular wavelength
[‡] http://en.wikipedia.org/wiki/Shockley%E2%80%93Queisser_limit

1.4.3   Photo-sensitizers

Isolated glass bound erbium luminescent centres (Er^{3+}) conveniently exhibit an optical transition around 1.5μm which corresponds to the low-loss transmission window in silica based optical fiber. The erbium doped fiber amplifier (EDFA) was developed from this material to provide the telecommunications industry with a means to achieving long haul communications. However, the excitation cross section of the erbium is small ($\sim 10^{-21} cm^2$), which translates to an equivalent cavity length of tens of meters of fiber required for the gain medium. The spectrally narrow gain cross section of the erbium also requires expensive wavelength stabilized pump lasers. Whilst these issues are not critical to the telecommunications industry, they render the EDFA technology useless as an integrated optoelectronic component.

The presence of silicon nano-clusters in such materials is known to exhibit a photo-sensitizing effect on the erbium luminescent centres[63-66] and enhances the erbium cross section by as much as four orders of magnitude[67]. The overlap of nano-cluster absorbing states with erbium excited states means that this photo-sensitization is effective over a broadband of exciting wavelengths, which removes the requirement for expensive pump sources. Furthermore the erbium emission in this material system is virtually insensitive to temperature, which is not the case for erbium doped bulk silicon. This is because the silicon nano-cluster band-gap is increased relative to that of bulk silicon, which effectively removes the non-radiative back transfer channel for thermalized electrons between erbium and silicon nano-clusters. This material therefore holds much promise as an integrated waveguide amplifier for inter-chip communication at 1.5μm. Operation of integrated opto-electronic components at this wavelength would simplify the coupling of signals to the wider network via fiber.

1.4.4   Single electron tunnelling (SET) devices

Another important application area identified for silicon nano-clusters is that of the single electron tunnelling (SET) transistor[68]. The ability to control the flow of the fundamental unit of charge has enormous implications for increasing capacity whilst reducing device power consumption. A schematic of a SET device is shown in **Figure 1-7**.
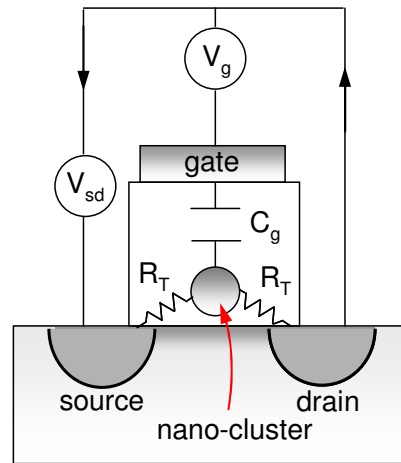
Figure 1-7 Schematic representation of a silicon nano-cluster single electron transistor (SET) showing the equivalent circuit components

The operation of a SET is similar to a conventional transistor except that the conducting channel is replaced by a nano-cluster or quantum dot embedded in a dielectric material. The nano-cluster acts as an island electrode separated from the source and drain terminals by thin (~few nm) dielectric barriers, which represent a high resistive impedance, R_T to current flow. The nano-cluster is also capacitively coupled through a much thicker dielectric barrier to a gate electrode. With the bias and gate voltages set to zero, i.e. $V_{sd} = V_g = 0$ no current can flow between source and drain terminals. However, for a sufficiently small bias voltage (few mV) the current through the device is controlled by the availability of unoccupied discrete energy states within the nano-cluster. The energy level separation, ΔE of these states is fixed by the nano-cluster size due to the quantum confinement effect and, for very small nano-clusters ($\leq$ 10nm), can be much larger than the thermal energy of electrons, k_BT, even at room temperature[69]. This limits the charging of the nano-cluster to one electron at a time according to the availability of unoccupied energy levels, which is controlled by the gate voltage. When a single electron is added to the nano-cluster, the charge on the gate-nano-

cluster capacitor increases by $e = C_g V_g$, which creates an electrostatic potential in the nano-cluster, U that blocks a second electron from entering under the same bias voltage. The addition of a second electron then requires an increase in energy, which is equal to the electrostatic potential energy, U plus the energy separating two quantized energy states in the nano-cluster, ΔE. For a fixed bias voltage, this energy can only be provided by increasing the gate voltage by ΔV_g. The sequential nature of tunnelling and the filling of the discrete nano-cluster electronic energy states manifests in measurable conductance oscillations, with period ΔV_g. The characteristic electrostatic potential energy for a charged spherical nano-cluster with diameter, d and surface area, πd^2 embedded in a medium with a dielectric constant, ε is given by:

$$U = \frac{2e^2}{\varepsilon d} \approx \frac{e^2}{C_g} \tag{7}$$

Then from the experimental determination of the gate voltage period, ΔV_g it is possible to calculate the energy level separation from:

$$\Delta E = \Delta V_g - \frac{2e^2}{\varepsilon d} \tag{8}$$

The sharp conductance peaks mean that very small increments in the gate voltage around the value corresponding to the position of a peak will produce extremely large changes in the output current. In this mode the SET can be configured as a sensitive amplifier.

Zhuang *et al*[70] demonstrated such a device in which the island electrode was a 12nm silicon nano-cluster with $\Delta E \sim$ 110meV through which drain current oscillations could be observed all the way up to room temperature.

The discrete nature of the nano-cluster SET means that they are also being proposed as high density, rapid read/write storage media for low voltage non-volatile memory devices[71-74]. Configured this way, the SET requires a very long charge retention time, $\Delta t = R_T C_g$, for which a very stable *Coulomb* blockade effect is required. According to the *Heisenberg* uncertainty principle, charging of the nano-cluster should provide an increase in the electrostatic potential, $\Delta U \geq \hbar/\Delta t = \hbar/R_T C_g$, which in turn sets a minimum limit for the tunnelling resistance, $R_T \sim \hbar/e^2 \sim$ 26kΩ.

1.5   Thesis outline

The original work presented in this thesis focuses on the mechanisms giving rise to luminescence in annealed silicon-rich silica thin films obtained in particular using CMOS compatible processes, specifically ion implantation and rapid thermal processing (RTP). Much of the reported work in this area describes films prepared using chemical vapour deposition followed by lengthy furnace anneals[67, 75, 76]. These works have tended to focus on processing variables such as the relative concentrations of excess silicon and co-doped species to enhance the light yield around 1.5µm whereas we have chosen to explore in greater detail the early formation dynamics of the silicon nano-clusters themselves, specifically by varying the annealing conditions. For this reason we have maintained a similar concentration of excess silicon throughout this study with a view to isolating any measurable nano-cluster size effects, either on the nano-cluster emission or the emission from co-doped species, specifically erbium. Characterisation of samples has been achieved through optical spectroscopy using analytical techniques such as photoluminescence and *Raman* combined with structural and compositional analyses via electron microscopy and electron energy loss spectroscopy (EELs).

Chapter 2 describes the general experimental techniques employed throughout this study. This includes sample fabrication, with particular emphasis on CMOS compatible processes; thermal oxidation of silicon, ion implantation and rapid thermal processing as well as the analytical techniques described above.

Chapter 3 provides a detailed description of the evolution of silicon-rich silica films during thermal treatment. The early stage formation dynamics of silicon nano-clusters within the films is presented from a classical thermodynamics perspective, evidence for which is taken from an in-depth statistical analysis of the nano-crystal size and density distribution in the films obtained from dark field electron microscopy images.

Chapter 4 deals specifically with the optical characterisation of the silica films containing silicon nano-clusters. The evolution of the optical properties with annealing is correlated with structural changes in nano-cluster size and density, as determined from the electron microscopy images. The effect of molecular hydrogen incorporation on the luminescence using a relatively low temperature, post process anneal in forming gas is presented along with an in-depth

photoluminescence study, including lifetime, temperature and power dependence of the silicon nano-cluster related emission. Finally, we examined the evolution of *Raman* spectra associated with the silicon optical phonon modes as a function of the annealing conditions. A modified phonon confinement model (PCM) is presented to describe the measured data from which we obtained information on the size distribution, which appears to be well correlated with the structural evolution. The *Raman* peak shift relative to bulk Si turns out to have a complex dependence on both size distribution and relative stress in the film, from which we were able to establish accurate values for the silicon nano-cluster surface tension using the *Young-Laplace* relation.

Chapter 5 examines the effect of silicon nanocrystals on erbium co-doped silica thin films. In particular we demonstrate broadband excitation of the erbium at room temperature using filtered light from a commercial flash-lamp. This evidences the presence of an extremely efficient, non-resonant energy transfer mechanism that has previously been implicated in the efficient sensitization of the erbium luminescent centres in such films. We also used a combined electron microscopy and electron energy loss spectroscopy technique to establish the relative formation site of the silicon nano-clusters with respect to erbium ions. Co-implanting silicon and erbium before applying a single, high temperature anneal step appears to limit the diffusion dynamics, size and chemical nature of erbium clusters and places them very close to the silicon nano-cluster surface, which is thought to be important in obtaining efficient sensitization efficiencies. Furthermore we reveal that the sensitizing efficiency and radiaitve rate of the erbium are both functions of the mean silicon nano-cluster size, which can be controlled using rapid thermal processing to produce intense erbium luminescence after extremely short thermal treatments.

Finally, in chapter 6 we present a detailed study of the effect of phosphorus co-doping on the silicon nano-cluster luminescence. Observations of an enhancement or quenching of the silicon nano-cluster luminescence with phosphorus doping depends on the annealing conditions, from which we infer a dependence on the silicon nano-cluster size. Samples annealed for shorter times and/or at lower temperatures contain a larger fraction of small (< 2nm) silicon nano-clusters, which exhibit an enhanced luminescence over a specific phosphorus concentration range compared with un-doped films. For samples annealed for longer times and/or at higher temperatures, the luminescence is always monotonically

quenched with increasing phosphorus concentration regardless of the preparation. This indicates that the ionization of the phosphorus ions inside silicon nano-clusters is only effective in samples containing larger nano-clusters. The additional electron provided by the phosphorus donor creates an efficient non-radiative channel due to *Auger* recombination. A simple statistical model describes our measured data and provides an incidental estimate of the silicon nano-cluster size distribution.

1.6   References

1.   G. E. Moore, in *Electronics* (1965), Vol. 38.
2.   J. Robertson, in *USA Today* (New York, 2008).
3.   A. K. Palit, W. Anheier and J. Schloeffel, Proceedings of the 15th GI/GMM/ITG Workshop on Testmethoden und Zuverlassigkeit von Schaltungen und Systemen, 42-47 (2003).
4.   S. Comeau, McGill Reporter **34** (12) (2002).
5.   G. T. Reed, *Silicon photonics*. (John Wiley & Sons Ltd, Chichester, 2008).
6.   H. Park, A. Fang, S. Kodama and J. Bowers, Opt. Express **13** (23), 9460-9464 (2005).
7.   L. Brus, The Journal of Physical Chemistry **98** (14), 3575-3581 (1994).
8.   D. J. Lockwood, *Device Applications of Silicon Nanocrystals and Nanostructures*. (Springer US, 2009).
9.   L. Pavesi, L. Dal Negro, N. Daldosso, Z. Gaburro, M. Cazzaneli, F. Iacona, G. Franzò, D. Pacifici, F. Priolo, S. Ossicini, M. Luppi, E. Degoli and R. Magri, 26th International Conference on the Physics of Semiconductors **171**, 261-268 (2002).
10.   N. K. Hon, K. K. Tsia, D. R. Solli and B. Jalali, Applied Physics Letters **94** (9), 091116-091113 (2009).
11.   O. Boyraz and B. Jalali, Opt. Express **12** (21), 5269-5273 (2004).
12.   D. Lockwood, Journal of Materials Science: Materials in Electronics **20** (0), 235-244 (2009).
13.   M. A. Green, J. Zhao, A. Wang, P. J. Reece and M. Gal, Nature **412** (6849), 805-808 (2001).
14.   L. T. Canham, Applied Physics Letters **57** (10), 1046-1048 (1990).
15.   L. Pavesi, L. Dal Negro, C. Mazzoleni, G. Franzo and F. Priolo, Nature **408** (6811), 440-444 (2000).
16.   P. M. Fauchet, J. Ruan, H. Chen, L. Pavesi, L. Dal Negro, M. Cazzaneli, R. G. Elliman, N. Smith, M. Samoc and B. Luther-Davies, Optical Materials **27** (5), 745-749 (2005).
17.   J. Lee, Journal of lightwave technology **23** (1), 19 (2005).
18.   R. J. Walters, G. I. Bourianoff and H. A. Atwater, Nat Mater **4** (2), 143-146 (2005).
19.   J. K. Bording and J. Tafto, Physical Review B **62** (12) (2000).
20.   R. Soulairol and F. Cleri, Solid State Sciences **12** (2), 163-171 (2010).
21.   F. Djurabekova and K. Nordlund, Physical Review B **77** (11), 115325 (2008).
22.   L. Brus, Journal of Physics and Chemistry of Solids **59** (4), 459-465 (1998).
23.   R. A. Bley and S. M. Kauzlarich, Journal of the American Chemical Society **118** (49), 12461-12462 (1996).
24.   K. C. Scheer, R. A. Rao, R. Muralidhar, S. Bagchi, J. Conner, L. Lozano, C. Perez, M. Sadd and J. B. E. White, Journal of Applied Physics **93** (9), 5637-5642 (2003).
25.   I. F. Crowe, T. R. Roschuk, U. Bangert, B. Sherliker, M. P. Halsall, A. P. Knights and P. Mascher, in *Conference on Optoelectronic and Microelectronic Materials and Devices, 2008. COMMAD 2008* (IEEE, Australian National University (ANU), Canberra, 2008), pp. 163-165.

26.   F. Trani, G. Cantele, D. Ninno and G. Iadonisi, physica status solidi (c) **2** (9), 3435-3439 (2005).
27.   P. S. Yadav, R. K. Yadav, S. Agrawal and B. K. Agrawal, Progress in Crystal Growth and Characterization of Materials **52**, 10-14 (2006).
28.   D. König, J. Rudd, M. A. Green and G. Conibeer, Solar Energy Materials and Solar Cells **93** (6-7), 753-758 (2009).
29.   M. Luppi and S. Ossicini, Materials Science and Engineering B **101** (1-3), 34-38 (2003).
30.   N. Daldosso, M. Luppi, S. Ossicini, E. Degoli, R. Magri, G. Dalba, P. Fornasini, R. Grisenti, F. Rocca, L. Pavesi, S. Boninelli, F. Priolo, C. Spinella and F. Iacona, Physical Review B **68** (085327) (2003).
31.   M. V. Wolkin, J. Jorne, P. M. Fauchet, G. Allan and C. Delerue, Physical Review Letters **82** (1), 197 (1999).
32.   J. S. Biteen, N. S. Lewis, H. A. Atwater and A. Polman, Applied Physics Letters **84** (26), 5389-5391 (2004).
33.   A. Y. Kobitski, K. S. Zhuravlev, H. P. Wagner and D. R. T. Zahn, Physical Review B **63** (11), 115423 (2001).
34.   N. B. Nguyen, C. Dufour and S. Petit, Journal of Physics: Condensed Matter **20** (45), 455209 (2008).
35.   L. Dal Negro, M. Cazzanelli, N. Daldosso, Z. Gaburro, L. Pavesi, F. Priolo, D. Pacifici, G. Franzò and F. Iacona, Physica E: Low-dimensional Systems and Nanostructures **16** (3-4), 297-308 (2003).
36.   L. Dal Negro, L. Pavesi, G. Pucker, G. Franzò and F. Priolo, Optical Materials **17** (1-2), 41-44.
37.   J. Derr, K. Dunn, D. Riabinina, F. Martin, M. Chaker and F. Rosei, Physica E: Low-dimensional Systems and Nanostructures **41** (4), 668-670 (2009).
38.   A. Hryciw, A. Meldrum, K. S. Buchanan and C. W. White, Nuclear Instruments and Methods in Physics Research Section B: Beam Interactions with Materials and Atoms **222** (3-4), 469-476 (2004).
39.   D. Kovalev, H. Heckler, G. Polisski and F. Koch, physica status solidi (b) **215** (2), 871-932 (1999).
40.   D. Kovalev, H. Heckler, M. Ben-Chorin, G. Polisski, M. Schwartzkopff and F. Koch, Physical Review Letters **81** (13), 2803 (1998).
41.   Y. Masumoto and T. Takagahara, *Semiconductor quantum dots.* (Springer-Verlag, Berlin, 2002).
42.   B. H. Bransden and C. J. Joachain, *Introduction to Quantum Mechanics.* (Longman Group, London, 1989).
43.   P. F. Trwoga, A. J. Kenyon and C. W. Pitt, Journal of Applied Physics **83** (7), 3789-3794 (1998).
44.   C. Q. Sun, T. P. Chen, B. K. Tay, S. Li, H. Huang, Y. B. Zhang, L. K. Pan, S. P. Lau and X. W. Sun, Journal of Physics D: Applied Physics **34**, 3470-3479 (2001).
45.   H. Hofmeister, F. Huisken and B. Kohn, The European Physical Journal D - Atomic, Molecular, Optical and Plasma Physics **9** (1), 137-140 (1999).
46.   J. P. Wilcoxon and G. A. Samara, Applied Physics Letters **74** (21), 3164-3166 (1999).
47.   A. Stesmans and V. V. Afanas'ev, Applied Physics Letters **80** (11), 1957-1959 (2002).
48.   R. K. Soni, L. F. Fonseca, O. Resto, M. Buzaianu and S. Z. Weisz, Journal of Luminescence **83-84**, 187-191 (1999).
49.   J. Heitmann, F. Müller, M. Zacharias and U. Gösele, Advanced Materials **17** (7), 795-803 (2005).

50.   L. Soojin, C. Woon Jo, H. Il Ki, C. Won Jun and L. Jung Il, physica status solidi (b) **241** (12), 2767-2770 (2004).

51.   W. K. Tan, Q. Chen, J. D. Ye, M. B. Yu, G.-Q. Lo and D. L. Kwong, IEEE Electron Device Letters **29** (4), 344-346 (2008).

52.   K. S. Cho, N.-M. Park, T.-Y. Kim, K.-H. Kim, G. Y. Sung and J. H. Shin, Applied Physics Letters **86** (7), 071909-071903 (2005).

53.   L.-Y. Chen, W.-H. Chen and F. C.-N. Hong, Applied Physics Letters **86** (19), 193506-193503 (2005).

54.   P. Mishra and K. P. Jain, Materials Science and Engineering B **95** (3), 202-213 (2002).

55.   Z. Ma, X. Liao, G. Kong and J. Chu, Applied Physics Letters **75** (13), 1857-1859 (1999).

56.   F. Iori, E. Degoli, R. Magri, I. Marri, G. Cantele, D. Ninno, F. Trani, O. Pulci and S. Ossicini, Physical Review B **76** (8), 085302 (2007).

57.   E. C. Cho, M. A. Green, G. Conibeer, A. Song, Y. H. Cho, G. Scardera, S. Huang, S. Park, X. J. Hao, Y. Huang and L. V. Dao, Advances In Optoelectronics 2007 (2007).

58.   G. Conibeer, M. Green, R. Corkish, Y. Cho, E.-C. Cho, C.-W. Jiang, T. Fangsuwannarak, E. Pink, Y. Huang, T. Puzzer, T. Trupke, B. Richards, A. Shalav and K.-l. Lin, Thin Solid Films **511-512**, 654-662 (2006).

59.   V. Svrcek, A. Slaoui, J. C. Muller, J. L. Rehspringer, B. Hönerlage, R. Tomasiunas and I. Pelant, Physica E: Low-dimensional Systems and Nanostructures **16** (3-4), 420-423 (2003).

60.   V. Svrcek, A. Slaoui and J. C. Muller, Thin Solid Films **451-452**, 384-388 (2004).

61.   X. J. Hao, E. C. Cho, G. Scardera, Y. S. Shen, E. Bellet-Amalric, D. Bellet, G. Conibeer and M. A. Green, Solar Energy Materials and Solar Cells **93** (9), 1524-1530 (2009).

62.   D. Timmerman, I. Izeddin, P. Stallinga, I. N. Yassievich and T. Gregorkiewicz, Nature Photonics **2** (2), 105-109 (2008).

63.   B. Garrido, C. Garcia, P. Pellegrino, D. Navarro-Urrios, N. Daldosso, L. Pavesi, F. Gourbilleau and R. Rizk, Applied Physics Letters **89** (16), 163103-163103 (2006).

64.   C. J. Oton, W. H. Loh and A. J. Kenyon, Applied Physics Letters **89** (3), 031116 (2006).

65.   M. F. Cerqueira, M. Losurdo, M. Stepikhova, P. Alpuim, G. Andres, A. Kozanecki, M. J. Soares and M. Peres, Thin Solid Films **517** (20), 5808-5812 (2009).

66.   G. Franzò, V. Vinciguerra and F. Priolo, Applied Physics A: Materials Science & Processing **69** (1), 3-12 (1999).

67.   A. J. Kenyon, C. E. Chryssou, C. W. Pitt, T. Shimizu-Iwayama, D. E. Hole, N. Sharma and C. J. Humphreys, Journal of Applied Physics **91** (1), 367-374 (2002).

68.   N. Takahashi, H. Ishikuro and T. Hiramoto, Applied Physics Letters **76** (2), 209-211 (2000).

69.   K. Likharev, IEEE Proceedings **87**, 606-632 (1999).

70.   L. Zhuang, L. Guo and S. Y. Chou, Applied Physics Letters **72** (10), 1205-1207 (1998).

71.   P. Normand, P. Dimitrakis, E. Kapetanakis, D. Skarlatos, K. Beltsios, D. Tsoukalas, C. Bonafos, H. Coffin, G. Benassayag, A. Claverie, V. Soncini, A. Agarwal, C. Sohl and M. Ameen, Microelectronic Engineering **73-74**, 730-735 (2004).

72.   H. Coffin, C. Bonafos, S. Schamm, M. Carrada, N. Cherkashin, G. Ben Assayag, P. Dimitrakis, P. Normand, M. Respaud and A. Claverie, Materials Science and Engineering: B **124-125**, 499-503 (2005).

73.   R. A. Rao, H. P. Gasquet, R. F. Steimle, G. Rinkenberger, S. Straub, R. Muralidhar, S. G. H. Anderson, J. A. Yater, J. C. Ledezma, J. Hamilton, B. Acred, C. T. Swift, B. Hradsky, J. Peschke, M. Sadd, E. J. Prinz, K. M. Chang and J. B. E. White, Solid-State Electronics **49** (11), 1722-1727 (2005).

74.   D. N. Kouvatsos, V. Ioannou-Sougleridis and A. G. Nassiopoulou, Applied Physics Letters **82** (3), 397-399 (2003).

75.   F. Priolo, G. Franzo, D. Pacifici, V. Vinciguerra, F. Iacona and A. Irrera, Journal of Applied Physics **89** (1), 264-272 (2001).

76.   G. Franzò, F. Iacona, V. Vinciguerra and F. Priolo, Materials Science and Engineering B **69-70**, 335-339 (2000).

2 General experimental techniques

2.1 Sample Preparation

2.1.1 SiO$_2$ film growth

We used a standard micro-fabrication technique, specifically 'wet' thermal oxidation to obtain films of high temperature oxide (HTO) on either (100) silicon substrates or grown from a layer of sputtered Si on Al$_2$O$_3$ substrates. The oxidizing agent, in our case water vapour (H$_2$O) was introduced into a standard cylindrical cavity quartz tube furnace (QTF) heated to 1000°C at 1 atmosphere to react with pre-installed Si wafers according to the reaction described by equation (9):

$$Si(solid) + 2H_2O(gas) \rightarrow SiO_2(solid) + 2H_2 \qquad (9)$$
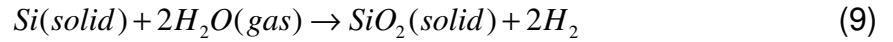
The oxidizing agent diffuses into the bare silicon substrate with which it forms an atomically flat interface[77]. A layer-by-layer oxide growth then proceeds by the partial consumption of the uppermost layers of the silicon substrate, the ratio of film growth to substrate consumption being a function of their relative densities according to $x_0/x_{Si} = N_{Si}/N_0$. With $N_{Si} = 5 \times 10^{22}$ atoms/cm^3 and $N_0 \sim 2.3 \times 10^{22}$ molecules/cm^3, $x_0/x_{Si} \sim 2.17$ as illustrated by **Figure 2-1**.
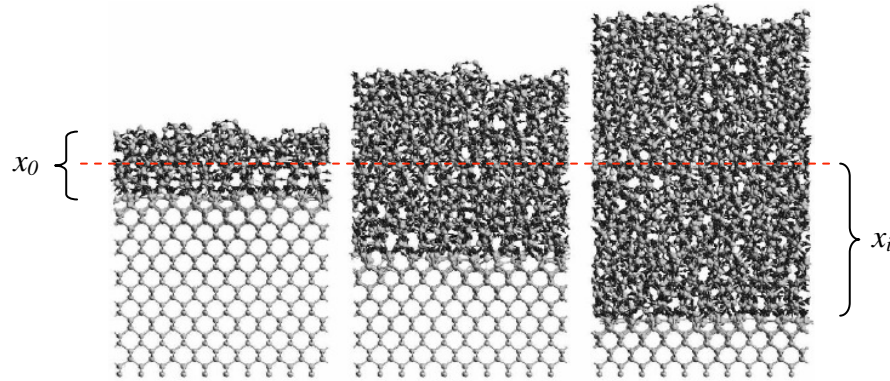
Figure 2-1 Molecular dynamics atomistic simulation of (a) x_0 **= 1nm, (b)** x_0 **= 3nm and (c)** x_0 **= 5nm oxide growth on Si (001). The red dashed line indicates the approximate level of the original substrate. Image adapted after [77]**

A generalised model for the resulting film growth was first described in 1965 by Deal and Grove[78]. Although more recent variants have been proposed[79], the former is fairly well established and predicts reaction rates and corresponding film growth with reasonable accuracy.

The rate of growth of an oxide layer depends on the flux of the oxidizing species (O_2 or H_2O), the reaction rate at the gas-oxide and oxide-silicon interfaces, the diffusion of the oxidizing species through the existing oxide layer and the equilibrium concentration (solubility) of the oxidant in the oxide.

In their model, Deal and Grove assumed the presence of an initial (native) oxide layer, thickness x_i at time $t = 0$ on the silicon surface and derived a general quadratic expression for the rate of growth of an oxide layer of thickness, x_0:

$$x_0^2 + Ax_0 = Bt + x_i^2 + Ax_i \tag{10}$$

which can be rewritten:

$$x_0^2 + Ax_0 = B(t + \tau) \tag{11}$$

with:

$$\tau = (x_i^2 + Ax_i)/B \tag{12}$$

Where τ represents a shift in the oxidation time interval that takes into account the presence of the initial oxide layer, x_i prior to the start of the growth reaction. Solution of the quadratic equation (11) then yields the oxide thickness as a function of time:

$$x_0(t) = \frac{A}{2}\sqrt{1 + \frac{t + \tau}{A^2/4B}} - 1 \tag{13}$$

The discriminant of equation (13) reveals two modes of operation; i) for relatively short oxidation times, i.e. $t << A^2/4B$, where a linear oxidation law is obtained:

$$x_0 = \frac{B}{A}(t + \tau) \tag{14}$$

Where B/A is known as the *linear rate constant* and ii) for relatively long oxidation times, i.e. $t >> A^2/4B$, a parabolic oxidation law is obtained:

$$x_0^2 \cong B(t + \tau) \tag{15}$$

Where B is known as the *parabolic rate constant*. These rate constants for the different temporal regimes of oxidation depend on the oxidation temperature, T according to the *Arrhenius* relations:

$$B/A = (B/A)_0 \exp\left(-\frac{E_{A_1}}{kT}\right) \tag{16}$$

$$B = B_0 \exp\left(-\frac{E_{A_2}}{kT}\right) \qquad (17)$$

Where k is the *Boltzmann* constant and E_{A_1} and E_{A_2} are two different activation energies to oxidation. Values for $(B/A)_0$, B_0, E_{A_1} and E_{A_2} are well documented for both 'wet' (H_2O) and 'dry' (O_2) oxidation[80] and so one can easily calculate the required oxide thickness as a function of time for a given oxidation temperature. Representative curves for the 'long time' regimes (parabolic rate) for 'wet' and 'dry' thermal oxidation are shown for comparison in **Figure 2-2**.
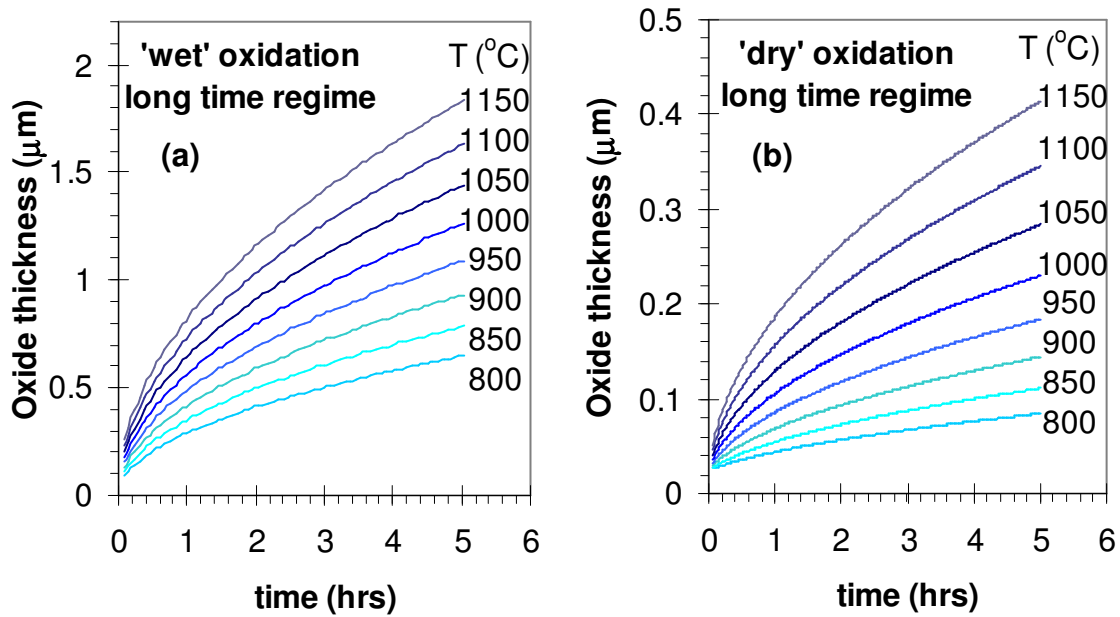
Figure 2-2 Calculated oxide thickness as a function of oxidation time for a range of temperatures (indicated) for (a) 'wet' (H_2O) and (b) 'dry' (O_2) oxidation. The calculation assumes the *parabolic oxidation law*, equation (15) with values for E_{A2} and B_0 taken from http://en.wikipedia.org/wiki/Deal-Grove_model

A clear benefit of the 'wet' technique for producing HTO films is the rate of oxidation. This is because the equilibrium concentration (or solid solubility) is orders of magnitude larger for H_2O than for O_2 and therefore the *parabolic rate constant*, B for the 'wet' technique is much larger than that for the 'dry' technique[78]. This fact enabled us to produce 500nm HTO films at $1000^{\circ}C$ in around 1 hour compared with ~24 hours using the 'dry' technique.

Whilst 'dry' oxidation may be preferred for specific device requirements on account of the superior quality oxide, which generally exhibits a lower density of surface electron traps and higher dielectric strength[81], for our purposes, the 'wet' oxidation

was preferred for obtaining relatively thick oxide (500nm) films in relatively short times. The density of surface electron trapping defects is known to be reduced in any case by post oxidation annealing in a nitrogen rich ambient[82].

2.1.2   Ion implantation

For all of the samples described in this study, the excess Si and co-doped species were incorporated into the SiO_2 films via ion implantation by collaborators in the group of Professor Russell Gwilliam at the Surrey Ion Beam Centre. The technique of ion implantation involves the modification of a target material (in our case SiO_2) using a highly energetic beam of ions. Ion beam formation and control of the ion trajectory is executed using a particle accelerator, an example schematic of which is shown in **Figure 2-3**.
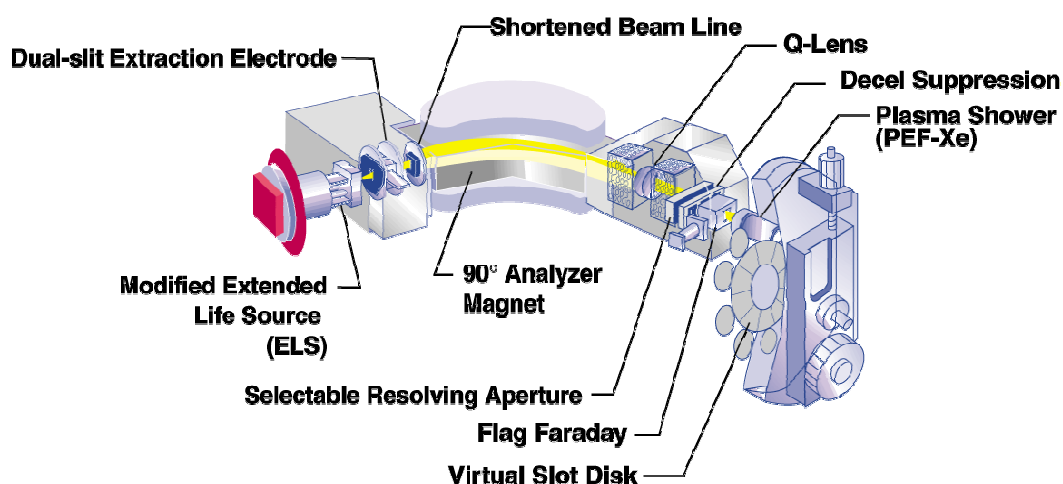
Figure 2-3 Component schematic of a modern low energy (< 10keV), high current (mA) beam-line ion implanter, image courtesy of [[83]]

The ions (positively charged atoms) are generated by 'stripping' electrons from the source material (e.g. tetrafluorosilane, SiF_4) in a plasma discharge from where they are extracted under vacuum via high voltage pre-acceleration towards a mass analyzing magnet. The magnet facilitates the selection of a desired chemical species, isotope and charge state to achieve a highly pure beam of ions. For example, an ion beam containing all known isotopes of Si with kinetic energy, $E = \frac{1}{2}mv^2$ entering a magnetic field, B will diverge according to the respective charge to mass ratio of all of the isotopes following $R = mv/qB$. Since the radius of curvature of the ion trajectory, R is proportional to the ion mass, heavier ions will traverse

larger radii of curvature than lighter ions of the same charge. By controlling the magnetic field precisely one can effectively tune the beam of ions that exits the magnet through a narrow aperture. This way for example, one can select a pure beam of ^{28}Si and reject all other isotopes. The pure ion beam is then accelerated towards and focussed at the target using a series of electromagnetic 'lenses' that also facilitate rastering of the beam over the specific target area of the sample to be implanted. Accurate control over the depth and concentration of implanted ions is achieved, simply by controlling the accelerating voltage (energy of the ions) and beam current respectively during the irradiation period. For this reason ion implantation has replaced chemical diffusion doping of electronic materials as the preferred technique for silicon complimentary metal oxide semiconductor (CMOS) processing[83].

As the ions enter the target they gradually lose energy and slow down through a combination of inelastic (electronic) and elastic (nuclear) scattering processes according to the theory originally proposed by Lindhard, Scharff and Schiott[84] in 1963, now commonly referred to as *LSS theory*.

Electronic scattering occurs through the excitation or ionisation of the target atoms, which accumulates as the ion travels through the target material. This generates a retarding electric field between the positively charged ion moving through a 'sea' of electrons, analogous to a 'drag' force on the implanted ions[85]. Such processes are characterised by a relatively small energy loss per collision and results in only fractional displacement of the target atoms, which may relax back to their original sites by emitting phonons. These losses dominate at higher implant energies or for lighter ions, the trajectory for which through the first few atomic layers of the target material is virtually unaltered from the angle of incidence.

Nuclear collision processes on the other hand refer to the transfer of a much larger fraction of energy from the implanted ion to the target nuclei, which can result in the displacement of atoms from their original lattice sites. In the most extreme case this leads to vacancy and/or interstitial type point defects (damage) extending from the surface to the implanted range within the target material. Both the recoiled ion and displaced target atom can go on to distribute the remainder of their energy and momentum to other target atoms in a collision cascade process. These losses provide a larger contribution to the total energy loss at lower implant

energies or as the ion gradually slows down towards the end of its trajectory in the target material. The various scattering processes are represented schematically by **Figure 2-4**.
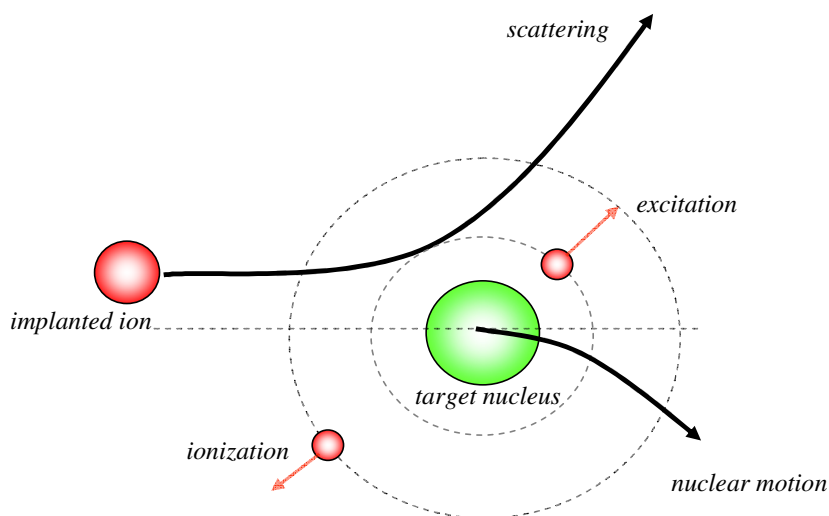
Figure 2-4 Schematic representation of the nuclear and electronic scattering processes that occur during ion implantation. Electronic scattering processes include excitation and ionization of the target atoms whereas the nuclear collision dynamics are determined by screened *Coulomb* interactions governed by *Lennard-Jones* like inter-atomic potentials

The stopping of an ion in a target material is a stochastic process and hence implantation results in a statistical distribution of the implanted ion range. Most modern computational approaches employ *Monte Carlo* simulations[86-88] to predict the ion range distributions, which they are now able to do to within an accuracy of ~5% for ions implanted into amorphous elemental target materials[86]. Predicting the range distribution for ions implanted into crystal targets can be complicated by the effect of channelling[89]. For example, if the ion beam is aligned with a particular crystallographic plane the stopping force or energy loss per unit path length may be significantly lower (and the ion range significantly longer) than that predicted. This is particularly problematic for the creation of shallow junctions in electronic devices but can be circumvented in practice by tilting the target crystal a few degrees off-axis during implantation.

During the course of this work, we used the freeware simulation *Stopping and Range of Ions in Matter* (SRIM 2003) developed by Ziegler *et al*[86] to predict ion range and concentration profiles for Si and co-doped species implanted into silica targets. This particular software is based on the binary collision approximation[90] in which

the scattering angle and energy loss associated with nuclear collisions is determined from a set of sequential isolated collision events between the implanted ion and individual target atoms. Between these binary collisions, the ion is assumed to follow a straight line trajectory during which it loses energy only via electronic scattering. Once the ion energy falls below some threshold value it stops and the spatial coordinates of the end point of the trajectory are used to generate the range profile. To achieve statistically relevant results during this study we simulated a large number of trajectories (on the order of 10000) for each implant profile. This minimizes errors in the calculated range as illustrated by **Figure 2-5**.
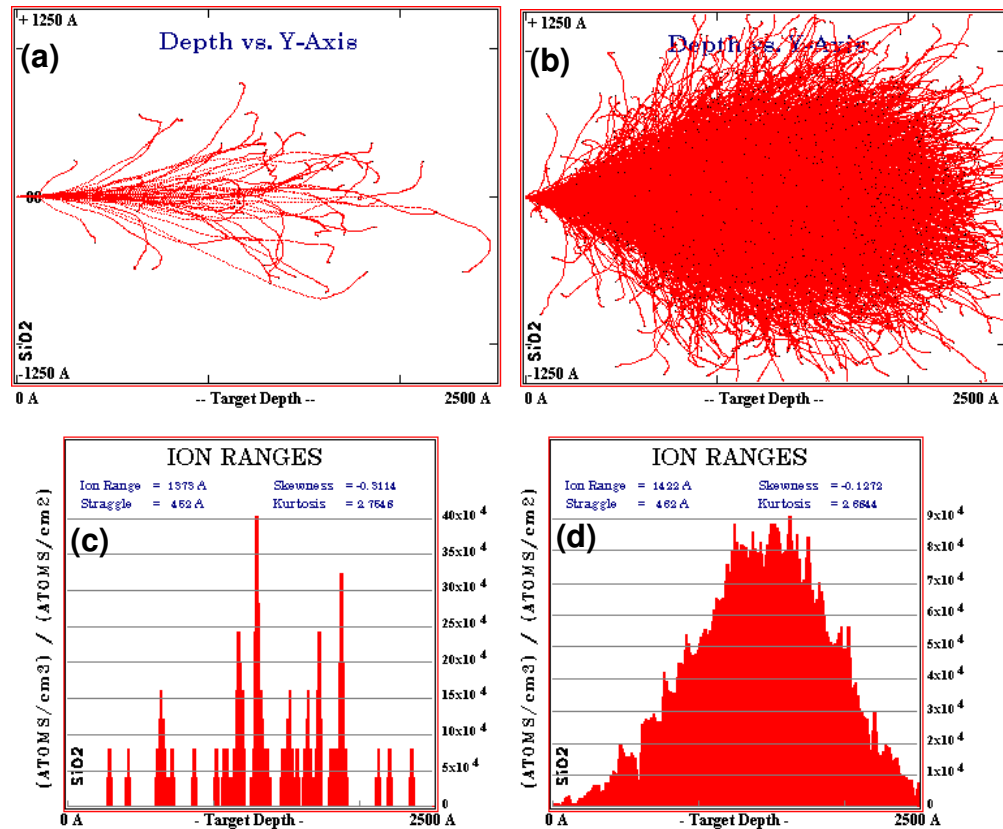
Figure 2-5 Simulated 1D ion trajectories for (a) 50 and (b) 5000 Si$^+$ ions implanted at 100keV, 0° into SiO$_2$ (2.2gcm^{-3}) simulated using SRIM 2003. (c) and (d) show the corresponding ion range profiles which yield projected ranges, R$_P$ = 137.3 and 142.2nm respectively. Note that after just 20 ions, the simulation yields a value for the projected range, R$_P$ = 126.5nm and after 10000 ions, R$_p$ = 142.2nm (which is identical to that obtained after 5000 ions)

The final implantation profile is therefore a strong function of both the beam energy, E typically quoted in (keV) and the dose, Φ typically quoted in atoms/cm^2. The latter is obtained from the time integrated beam current, I according to equation (18)[91]:

$$\int_0^{\Phi} d\Phi = \int_0^t \frac{Idt}{q_iA} \Rightarrow \Phi = \frac{It}{q_iA} \tag{18}$$

Where t is the irradiation time, A the beam area or spot size and q_i is the charge per ion. With typical beam currents in the μA to mA range, dopant concentrations of ~10^{11} to 10^{16} atoms/cm^2 can be obtained in just a few seconds and whole wafers can be implanted in just a few minutes.

Due to the statistical nature of the collisions and according to *LSS theory*[84], the implant profile, $n(x)$ in an amorphous material can be approximated by a *Gaussian* distribution according to[91]:

$$n(x) = \frac{\Phi}{\sqrt{2\pi}\Delta R_p} \exp\left(-\frac{\left(x-R_p\right)^2}{2\Delta R_p^{\,2}}\right) \tag{19}$$

Where x is the depth, R_P is the 'projected range' or the range at which most ions will stop and ΔR_P is known as the 'straggle', which is effectively the standard deviation from R_P. We used SRIM to calculate implantation profiles for Si and co-implanted species such as phosphorus and erbium into SiO$_2$. Typical Si$^+$ profiles in SiO$_2$ are shown for a range of energies in **Figure 2-6**.
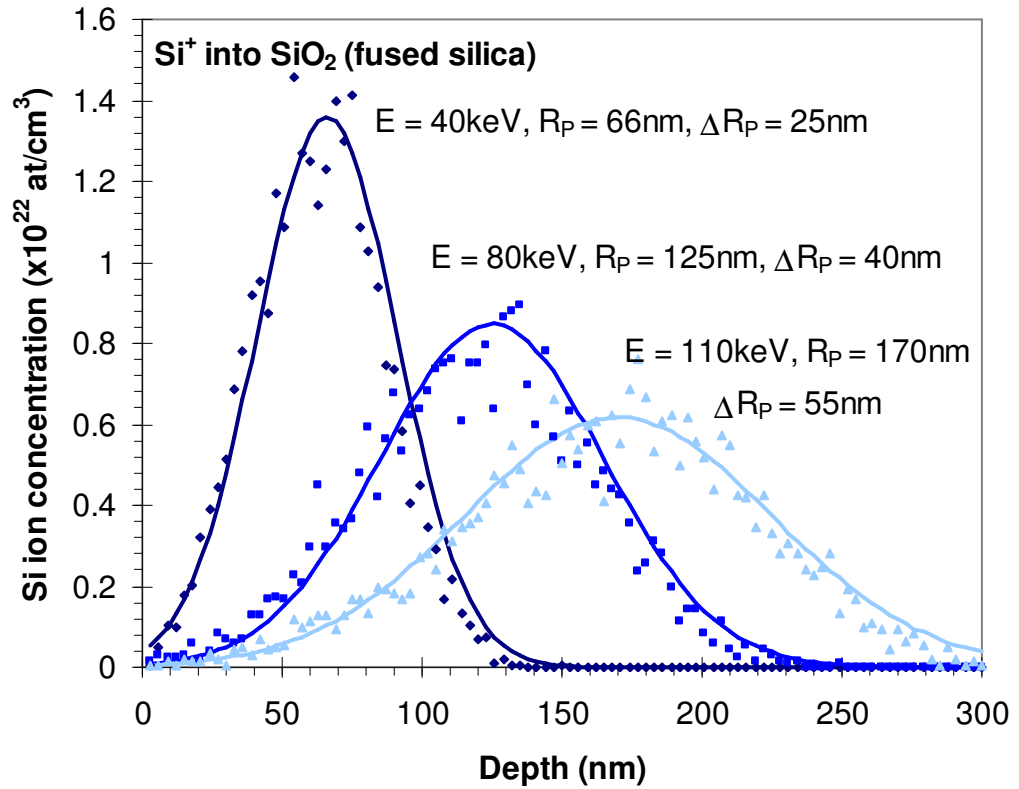
Figure 2-6 Calculated Si$^+$ implantation profiles for a range of energies all implanted to the same dose (8×10^{16}cm^{-2}) using SRIM 2003. Although the area under the curves are identical, the ordinate, in atoms per cm^3 shows how the concentration of the Si$^+$ in the silica matrix varies for a given dose, simply by changing the implant energy. The lines are Gaussian fits to the data using equation (19) from which values for R$_P$ and ΔR$_P$ were determined

The ion beam centre at the University of Surrey is equipped with a suite of *in-situ* depth profiling measurement techniques such as Rutherford Backscattering Spectrometry (RBS), which is capable of verifying the implant profiles predicted by the SRIM algorithm. RBS data was collected for a selection of the samples described in this study using a 2MeV He$^+$ beam using a *Tandetron* accelerator and the ion beam analysis executed using *DataFurnace* software[92] by Scientists in the group of Dr. Chris Jeynes at the University of Surrey. An example RBS profile, taken from the reported results[93] is shown along with that predicted by SRIM scaled to a TEM image in **Figure 2-7** for a Si$^+$ implanted (80keV) 500nm oxide film.
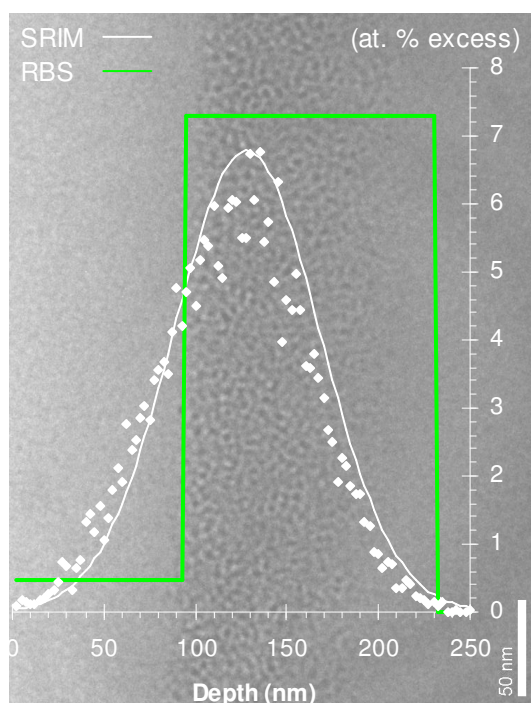
Figure 2-7 Low magnification TEM dark field image of the implanted (80keV) silicon layer in thermally grown SiO$_2$. The overlay (scaled to the image) shows the implant profiles predicted by SRIM 2003 (white) compared to that measured at the University of Surrey using RBS (green)

The RBS profile is in very good agreement with the position of the Si$^+$ layer observed in the TEM image. Whilst the peak concentration predicted by SRIM also agrees quantitatively with the RBS data, we see that the profile is shifted slightly towards the surface. Errors in the predicted implant distribution are likely explained

by the choice of oxide density (~2.2gcm^{-3}) in the SRIM calculation, which can vary in reality, dependent on the exact preparation.

2.1.3   Rapid Thermal Annealing (RTA)

Thermal processing of ion implanted semiconductor and insulating targets is common practice for removing the damage created within the target material as described above. In order to attain thermodynamic equilibrium the molecular system of any material will spontaneously reorganise, for example via diffusion to reduce the volume or *Gibbs* free energy[94]. For binary solutions (or alloys of a material containing type A and B atoms) the free energy will be minimised naturally by the formation of like atomic bonds, i.e. by clustering into A-rich and B-rich groups. The rate that this process precedes is a strong function of the temperature and it can therefore be accelerated by heating, particularly to temperatures above the crystallization temperature[95]. In this study, thermal annealing served two purposes; i) removal of ion irradiation damage and ii) separation of the Si and SiO_2 phases to form silicon nano-clusters from the excess of implanted ions. We used a process known as *Rapid Thermal Annealing* (RTA) in which samples are heated rapidly to high temperature (in our case $\geq 1050^{o}C$) where they are held for very short time periods using a commercial *Jipelec jetfirst* 100 rapid ramp rate lamp annealing system at McMaster University. The development of rapid thermal processing theory and technology has been refined in recent years as a result of its high throughput and process control applicability to the Si microelectronics industry[96]. We used the technique specifically to study the early stages of silicon nano-cluster evolution and in order to control their size and density distribution in erbium co-doped oxides.

The *jetfirst* 100 RTA system houses a set of high power Tungsten filament lamps with extremely fast switching response times in a so-called 'cold-wall' (water-cooled) stainless steel chamber. The chamber is sealed to allow vacuum pressures of ~10^{-2}mbar and gas (in our case N_2) processing. The heat generated by the lamps is mainly in the form of electromagnetic (IR) radiation, which is emitted isotropically. A polished aluminium reflector positioned above the lamps provides a directional source of heating through an air cooled quartz window onto the surface of the sample, which is seated below the lamps on a set of bevelled quartz pins. Beneath the sample is an integrated optical pyrometer and dual

thermocouple set-up for closed loop control of the sample temperature during processing. A microcontroller with built-in calibration for thermal feedback control is used to minimize the difference between the *programmed* temperature and the *actual* temperature as recorded by the thermocouple (and/or pyrometer). A schematic of the system is shown in **Figure 2-8**.
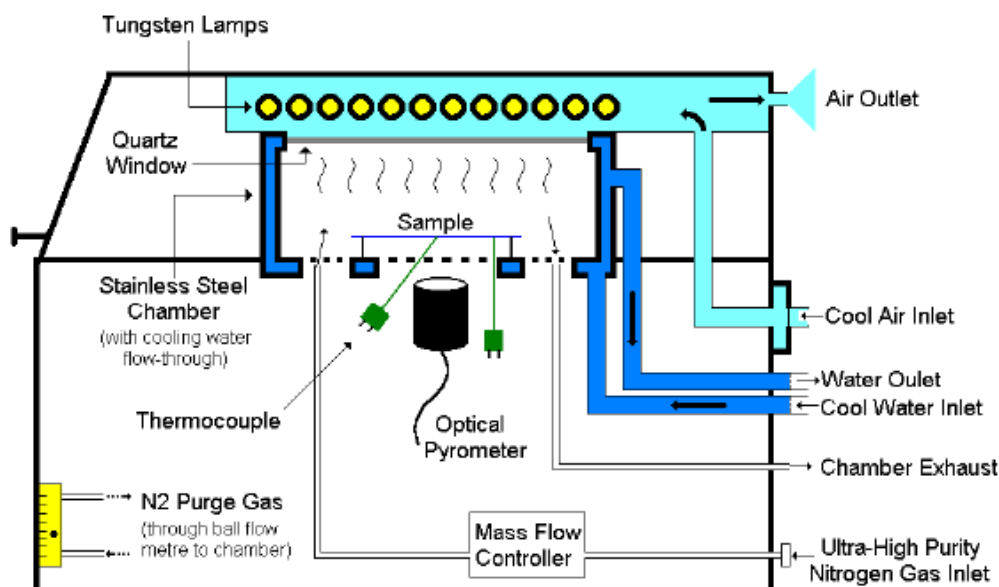
Figure 2-8 Schematic of the *Jipelec JetFirst* 100 Rapid Thermal Processor, courtesy of [97]

Programming is provided via dedicated PC running commercial *Jipelec* software with a graphical user interface for defining time-temperature processes known as 'recipes'. A typical recipe includes an initial 'soak' period (typically 60 to 120s) at 600°C followed by a rapid ramp to a maximum of 1300°C at a rate of up to 150°C/s. Upon reaching the desired temperature, the system holds at that temperature until a pre-programmed time has elapsed after which the lamps are switched off and the chamber temperature and sample are allowed to cool naturally to ambient before the sample can be removed from the system.

For the samples described in this work, we used temperatures in the range 1050 to 1200°C for *programmed* times in the range 1 to 100s using a moderate ramp rate of 22.5^{o}C/s. It is worth noting that the *programmed* anneal time, t_A is an indication only for the time period over which the chamber temperature is held at the desired annealing temperature. The onset of nano-cluster formation and the Si crystallization temperature actually depends on the relative silicon, oxygen and hydrogen concentrations and rate of heating. For example Roura *et al*[98] showed

that relatively large nano-clusters could be formed from *a*-Si films at temperatures as low as 780°C at a heating rate of ~10°C/min. The onset temperature (T_c) for silicon nano-cluster formation during the course of this work could not therefore be determined precisely, rather the *actual* annealing time should be considered to be the time period for which the sample temperature was above ~800°C. Since the heating and cooling rates are fixed for a given volume of material then the relative increases in the *actual* anneal time still reflect a linear increase in the *programmed* anneal time but with an offset that is dependent on the anneal temperature. A typical annealing cycle ('recipe') and *estimated* anneal time as a function of the *programmed* anneal time are shown in **Figure 2-9** for $T_A = 1050$°C.

$$T(t) = T_a + (T_A - T_a)e^{-kt}$$
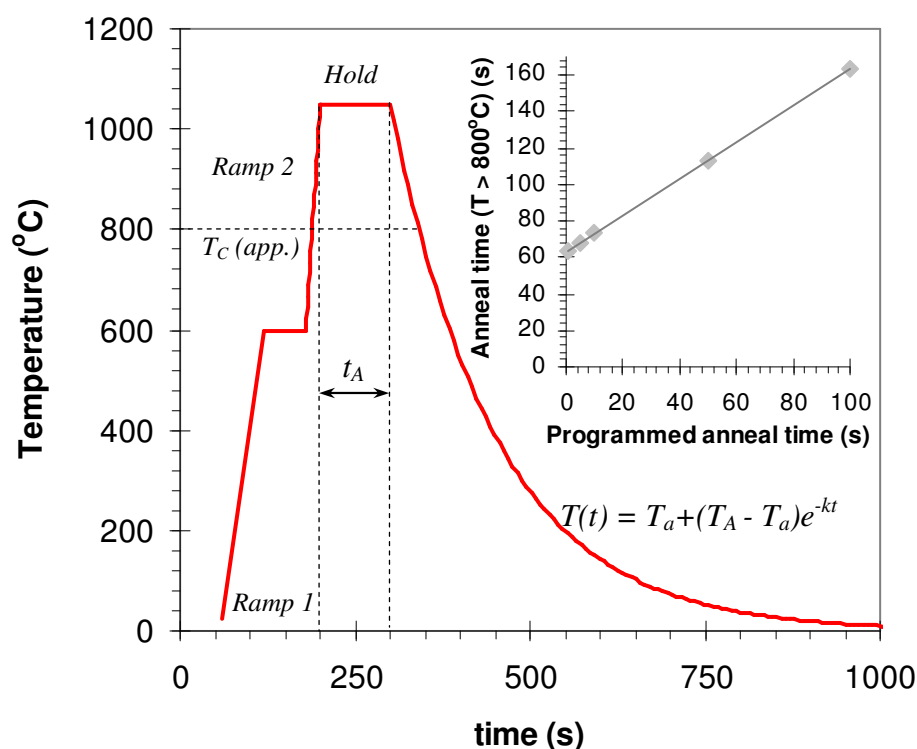
Figure 2-9 *Jipelec JetFirst* **annealing cycle for 1050°C, 100s. Inset: estimated anneal time (T > 800°C) as a function of the programmed anneal time, t_A at T_A = 1050°C. After switching off the lamps the sample temperature is assumed to follow Newton's law of cooling (indicated) with a fixed cooling rate constant,** k

No active cooling was introduced during the course of this work although there is evidence to suggest that the density of charge trapping centres at the Si/SiO$_2$ interface is affected by both the rate of cooling[99] and the atmosphere in which cooling is effected[100], which could be the subject of further investigation.

2.2   Electron Microscopy

2.2.1   Transmission Electron Microscopy (TEM)

The fundamental maximum resolution of any optical imaging system, that is, the minimum distance, d between two structural entities that can still be resolved as two entities rather than merging into an apparently single entity depends on the wavelength of light, λ being used to produce the image according to equation (20):

$$d = \frac{\lambda}{2NA} = \frac{\lambda}{2n\sin\theta} \tag{20}$$

Where $NA = n\sin\theta$ is the lens numerical aperture, θ the lens collecting semi-angle and n the refractive index of the medium in which the lens is immersed. If light is focused using an optical system with circular apertures, the resulting diffraction pattern leads to the empirical maximum resolution known as the *Rayleigh* criterion, equation (21)[101]:

$$d = \frac{1.22\lambda}{2NA} = \frac{1.22\lambda}{2n\sin\theta} = \frac{0.61\lambda}{n\sin\theta} \tag{21}$$

For conventional light microscopes employing the shortest visible wavelength, λ ~400nm and an oil immersed objective lens ($n = 1.56$) with a wide collection angle ~70°, the maximum resolution is limited to ~0.2μm.

The desire to resolve structures on the atomic (nanometer) scale therefore necessitated a more novel approach to imaging microscopy. Around the turn of the 20th century the revolutionary theoretical work of de Broglie had revealed the quantum mechanical wave nature of electrons, which was later verified by measurement of electron diffraction from Nickel by Davisson and Germer[102]. Along with the practical developments of cathode ray tubes, in which the ability to focus an electron beam using magnetic fields had been demonstrated, this ultimately led to the development of the electron microscope in the 1930's.

The 'wave-like' nature of electrons means that an electron beam exhibits similar properties to a beam of electromagnetic radiation but with a wavelength, λ_e, which is orders of magnitude smaller than light. The de Broglie relation provides the wavelength of electrons, λ_e in terms of their momentum, P according to:

$$\lambda_e = \frac{h}{P} = \frac{h}{m_0 v} \tag{22}$$

Where h is Planck's constant and m_0 and v are respectively the rest mass and velocity of the electron. In the TEM the electrons gather momentum as they are accelerated by a high potential, V and so they develop a kinetic energy:

$$eV = \frac{1}{2}m_0 v^2 \tag{23}$$

By substitution we therefore obtain the non-relativistic electron wavelength in terms of the accelerating potential[103]:

$$\lambda_e = \frac{h}{\sqrt{2m_0 eV}} = \frac{1226.39}{\sqrt{V}} \tag{24}$$

This is an extremely important result indicating that the electron wavelength and therefore microscope spatial resolution can be reduced to the pico-meter scale simply by increasing the accelerating potential. For example, at V = 100kV, λ_e ~4pm and the resolution should then be on the order of 2pm, which is 100,000 times more powerful than the best light microscope and critically, smaller than the atomic radius. In reality, this limit has not yet been reached as a result of imperfections in the electron lenses, which leads to optical like aberrations. The highest resolution reported for an electron microscope at the time of writing is ~50pm, which was achieved in a TEM with aberration corrector lenses[104].

In the TEM, electrons are generated either by thermionic or field emission and accelerated to relativistic velocities in an ultra-high vacuum (~10^{-4} to 10^{-9}Pa) using high voltage potentials typically ~100 to 300kV[*]. Control and manipulation of the electron beam is then provided by several stages of electromagnets, the field from which exhibits a 'lensing' effect on the electron trajectory with an adjustable focus according to the current through the magnet coils. A schematic of the electron microscope is shown in **Figure 2-10**.

---

[*] It is important to note here that for accelerating potentials of this magnitude a relativistic correction should be made to the electron wavelength on account of their extremely high velocity, which can be as much as 0.75c in a conventional TEM operating at 300kV
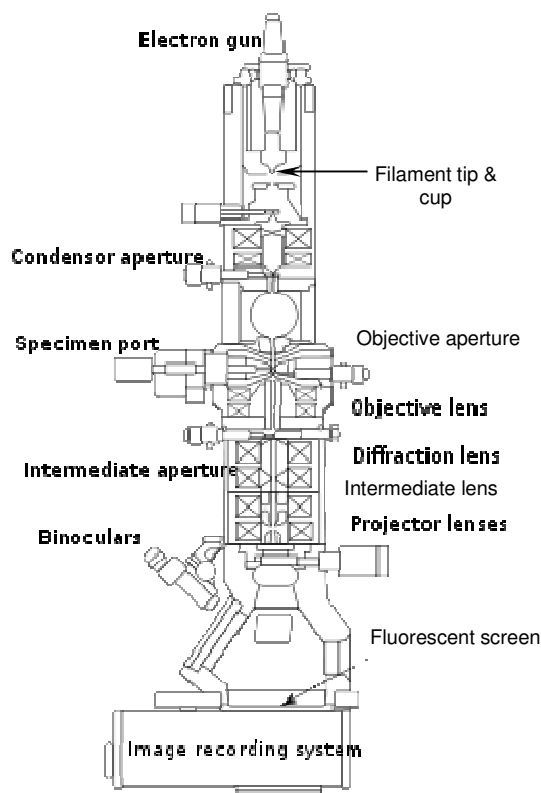
Figure 2-10 Schematic representation showing the principal components of the transmission electron microscope (TEM), adapted after

http://en.wikipedia.org/wiki/Transmission_electron_microscopy

The electron gun consists of a tungsten filament tip, through which a current is passed generating the thermionic electrons. These electrons are accelerated towards the anode through the cup aperture, which is held at a slight negative voltage so that a constricted beam is formed. The beam is then further condensed using a pair of electromagnets and a condenser aperture, which facilitates the focusing and spatial control of the beam at the sample position. The sample is inserted into the microscope normal to the optical axis through a series of interlocks so that the system vacuum may be maintained. The sample holder facilitates *in-situ* translation and rotation of the sample allowing for specific regions of interest to be probed by the beam and diffraction images obtained. Below the sample stage is the second set of electromagnets with a variable aperture positioned in the back focal plane, which together act as an objective lens. The size of the objective aperture limits the scattering angle of electrons reaching the screen/detector enabling image formation in bright or dark field diffraction contrast mode. In bright field mode the image contrast arises as a result of the relative

absorption of electrons in specific parts of the sample, being lower (and thus giving a brighter appearance) in regions where the sample is relatively thin or where the atomic number Z of atoms in the sample is relatively low. Dark field (or diffraction contrast) imaging refers to image formation based on the diffraction of electrons specifically from crystal planes. Specific reflection angles can then be imaged by varying the objective aperture and the relative tilt of the sample so that the resulting contrast depends only on the scattering angle with scattered electrons forming bright regions on the image. The final set of electromagnets provides both magnification in a wide range, typically 50 to 1 million times and projection of the image onto a detector.

In preparing samples for electron microscopy, we followed a fairly standard and well documented procedure[105] that involves building a sample/support stack, which was glued using a commercial (*M-bond*) adhesive and cured at 200°C. A disc, $\phi \sim 2.5$mm is then cut from the stack using an ultrasonic drill and the cross section thinned to ~100μm using graded silicon carbide (SiC) paper. The central region of the disc is further thinned to ~50μm using a dimple grinder before being mounted on a standard 3mm copper support grid using a *cyano-acrylate* adhesive. The central region of the disc is thinned further still using an argon ion beam milling machine, which provides a small hole in the centre of the sample around which there is an electron transparent region, ~100nm thick (or less). A typical sample/support disk and standard TEM support grid are shown schematically in **Figure 2-11**.
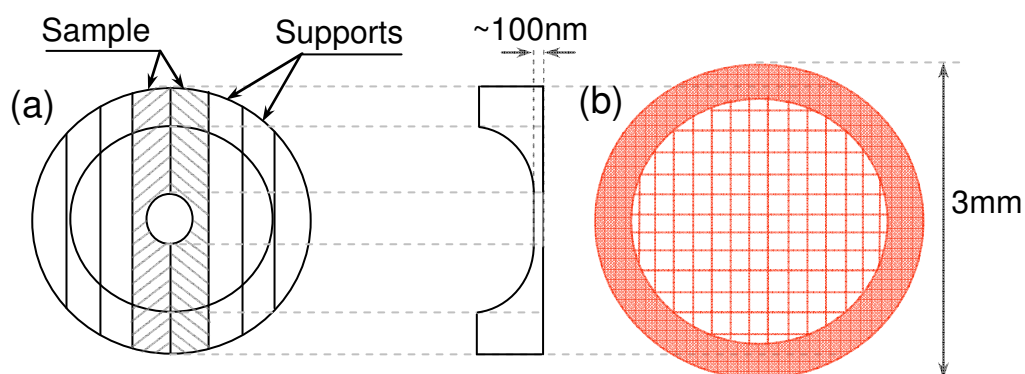
Figure 2-11 (a) Standard sample preparation and (b) support grid for TEM samples

2.2.2   Scanning Transmission Electron Microscopy (STEM)

A variant of the TEM that employs a beam rastering technique adopted from scanning electron microscopy is the scanning transmission electron microscope (STEM). This instrument was developed primarily to augment the imaging capability of the TEM with *in-situ* structural and compositional analyses using the information contained in secondary emissions that arise due to the ionizing nature of the interaction between the electron beam and the sample being studied. In the STEM electrons are generated at a higher flux using a field emission gun (FEG), which yields a narrower beam footprint compared with the TEM. As in the TEM, the beam is formed using an initial set of condenser lenses that reduce the beam area and focus it at the sample plane. An additional set of magnets called scan coils are installed between the condenser and objective lenses, which facilitates the beam rastering across the sample. A third set of magnets on the opposite side of the sample act as a second objective lens, which discriminates the bright field electron signal from that generated by electrons scattered at high angles. A bright field and high angle, annular dark field detector then collect the signals, which are synchronized to the beam position. Bright field image formation in the STEM arises from the relative transmission of un-deflected electrons at each scanning position whereas the dark field image is due to the diffracted or scattered component of the transmitted beam, which provides the compositional information[†]. During the course of this work we used the *SuperSTEM* at the Daresbury research facility, which is a *VG* HB501 field emission STEM fitted with a *Nion* MkII quadrupole-octupole 3rd order aberration corrector to improve resolution. The microscope is capable of providing bright field and high angle annular dark field images to a spatial resolution of ~0.1nm and electron energy loss spectroscopy is concurrently executed using an ultra high vacuum *ENFINA* spectrometer with a spectral resolution of ~0.3eV.

2.2.3   Electron Energy Loss Spectroscopy (EELS)

The reflected and/or transmitted components of an incident mono-energetic electron beam from a specimen contain widely dispersed energy spectra. These

---

[†] The intensity of the scattered signal is proportional to the square of the atomic number, Z of the material from which the beam was scattered

energy spectra are characteristic of the energy imparted (lost) from the incident beam during inelastic collisions resulting in electronic excitations in the material under study[106]. These excitations may arise from the perturbation of loosely bound electrons, which results in low energy plasmon oscillations or the inelastic scattering of core electrons giving rise to sharp, high energy peaks, both of which arise from the probe beam passing through the sample. Measurement of the energy dispersion in the transmitted electron beam combined with high resolution imaging microscopy provides a powerful structural and *in-situ* compositional analytical technique[107].

Intensity and/or chemical 'maps' shown in this study were derived from EELS data acquired during STEM imaging sessions with the assistance of Dr. Mahri Gass at the Daresbury research facility. We used a technique known as spectrum imaging in which an EELS spectrum is collected for each pixel along a defined line or within a defined region of the digital image as the electron beam is scanned over a section of the sample containing features of interest, as illustrated schematically by **Figure 2-12**.
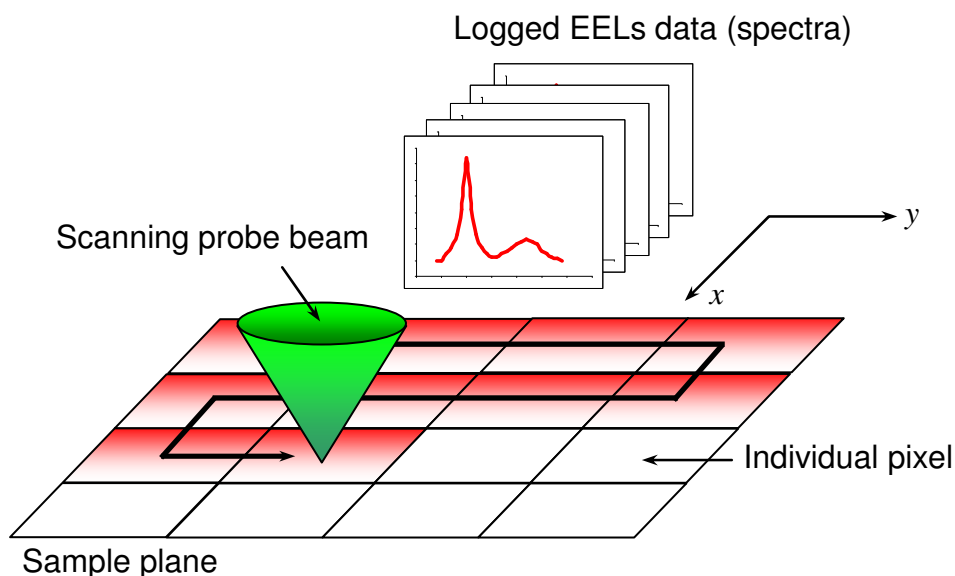
Figure 2-12 Schematic representation of spectrum imaging in the STEM. As the electron beam is scanned across the sample it generates an image in the *x-y* plane and for each pixel in the digital image an EELS spectrum is generated. The EELS data, which indicates the presence of specific elements can then be used to generate compositional or intensity maps during post-processing

Elemental analysis of the EELS data was conducted with the assistance of collaborators in the group of Dr. Ursel Bangert in the Manchester Materials Science centre using *Gatan* Digital Micrograph (DGM)[108]. The DGM software provides a wide range of spectral analysis tools and standard curve fitting algorithms, for example, the Non-Linear Least Squares (NLLS) routine. The NLLS provides a convenient method for fitting single or multiple Gaussian models to an EELS spectral feature to determine its peak position, intensity or FWHM. Since the presence of a particular spectral feature corresponds to the presence of a particular element, pixel by pixel mapping of the Gaussian fitting parameters of the spectral feature associated with that element over an entire spectrum image dataset provides a direct measure of the relative elemental concentration in two dimensions. We used this technique to generate colour maps like the one in **Figure 2-13**, which reveals the spatial distribution and relative concentration of erbium in SiO_2:Si-NC, Er[109].
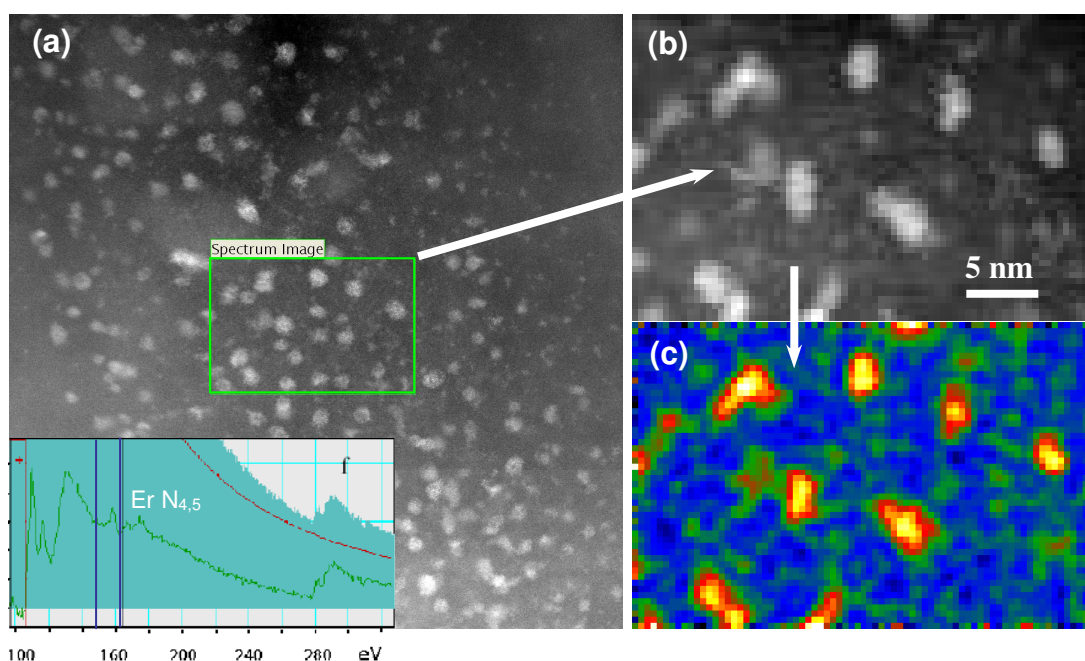
Figure 2-13 (a) High angle annular dark field STEM image of a band of silicon nano-clusters co-doped with erbium ions embedded in SiO_2. The inset is an EELS spectrum showing the Er $N_{4,5}$ electron energy loss edge around 168eV and the green square is the spectrum image, which is enlarged in (b). Filtering of the spectrum image, in this case using the window (167 – 177eV) indicated by the blue lines in the inset produces the intensity map shown in (d). Images courtesy of [109]

Another example is the multi-linear least squares (MLLS) routine, which provides a means for determining the relative contribution of different chemical phases in a mixed phase material by reference to the unique spectral signatures of the unmixed phases. For example in silicon rich silica, the only phases present should be those of SiO_2 and Si, which can be defined as reference spectra. Then, for a particular region of interest in the spectrum image dataset where a contribution of each to the EELS spectrum is expected, for example at the location of a silicon nano-cluster, the MLLS routine will return a fit based on the optimal linear combination of each of the specified reference spectra and return coefficients that are directly proportional to the amount of each phase present. This technique was previously employed to confirm that silicon nano-clusters are made almost entirely of pure Si[110].

This technique can also be extended to an entire spectrum image dataset revealing the relative spatial distribution of each of the reference elements, a technique known as 'chemical phase mapping' or 'chemical fingerprinting'.

2.3   Optical Spectroscopy

2.3.1   Photoluminescence Spectroscopy

Photoluminescence spectroscopy generally refers to the measurement of *spontaneous* radiative transitions between an excited atomic or molecular electronic orbital or energy state, E_n and the ground state, E_0 specifically via the *stimulated absorption* of a photon of energy $E = h\upsilon \geq E_n$. The transition energies or the difference between electronic states are material specific and so the luminescence emission spectra, particularly in conjunction with absorption spectra can yield valuable information directly related to the electronic energy structure of the material being studied.

Solid state luminescence processes generally arise either from isolated atomic or defect sites (luminescent centres) such as those formed by glass bound rare-earth dopants or specific electronic defects *or* they may be a more general property of a material such as those associated with band-edge recombination in bulk semiconductors. For isolated luminescent centres, such transitions are typically schematized by Jablonski diagrams, an example of which is illustrated by **Figure 2-14**.
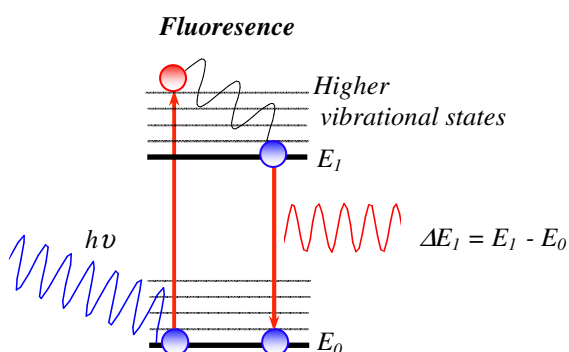
Figure 2-14 *Jablonski* **schematic representation of photon absorption followed by vibrational relaxation and spontaneous emission resulting in** *fluorescence*, **adapted from** http://micro.magnet.fsu.edu/primer/java/jablonski/lightandcolor/

Figure 2-14 shows one possible radiative transition for an isolated luminescent centre following absorption of a photon; namely *fluorescence*. The exact process, corresponding transition energy and transition probability are determined by the quantum state of the system according to a set of selection rules, which are

themselves governed by the statistical distribution of the atomic or molecular electronic states.

In bulk semiconductors, the luminescence typically arises from electron-hole recombination across the band gap between conduction and valence electronic states. At room temperature, this generally gives rise to band-edge emission but at lower temperatures the emission may be red-shifted by an amount that is characteristic of the *Coulomb* interaction between the electron and hole, which binds the two particles together in a quasi-particle *excitonic* state[111]. Whilst the *exciton* itself can diffuse throughout the semiconductor material in a 'free' state, it cannot contribute to current because it has neutral charge. If one or both of the constituent carriers of the *exciton* becomes trapped at a defect or impurity centre in a so-called 'bound' state, the energy of the quasi-particle and therefore electron-hole recombination energy may be lowered further still. Doping of semiconductors can therefore give rise to additional energy levels within the forbidden gap between which electrons and holes can recombine radiatively to give additional, generally red shifted spectral emission features. The different types of transition giving rise to emission from a bulk semiconductor are shown in the Jablonski schematic of **Figure 2-15**.
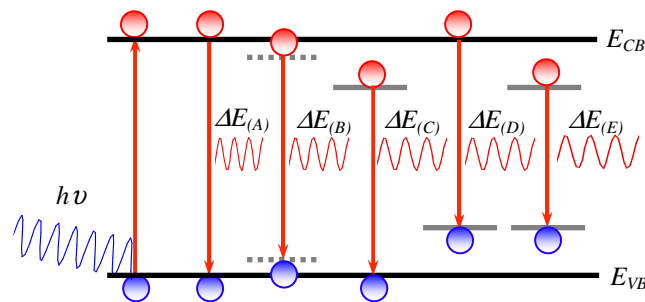
Figure 2-15 Possible radiative transitions observed with photoluminescence in bulk semiconductors, ΔE for (A) band-edge emission (B) free exciton emission (C) free hole – trapped electron type bound exciton state (D) free electron – trapped hole type bound exciton state and (E) trapped electron – trapped hole donor-acceptor pair (DAP), adapted from [111]

For bulk *indirect* band gap semiconductors such as silicon, the quantum mechanical selection rules provide only a weakly allowed band edge transition probability through the electron-phonon interaction, giving a maximum photon energy (for a sufficiently pure material) of[112]:

$$\Delta E_A = \left(E_{CB} - E_{VB} \right) - E_P \qquad (25)$$

Where E_P is the phonon energy.

As we have seen, the effect of quantum confinement of electron and hole wave-functions generally leads to an increase in the band gap and for indirect band gap materials such as silicon, removes the strict requirement for the involvement of phonons in the radiative transition process. Whilst a blue shifted absorption and emission energy should be expected, the actual transition energy in such systems is complicated by a strong *Coulomb* interaction between the electron and hole and is likely to be extremely sensitivity to the nano-cluster surface bonding geometry and chemistry[113]. The increase in the energy of the band edges and the presence of defect-like levels formed within the band gap, for example as a result of strained chemical bonds, which can act as electron 'trapping' centres, increases the probability of bound *exciton* like states, even at room temperature. Emission energies are therefore strongly dependent on the size and surface chemistry in such materials systems, even where the electronic band structure is dominated by quantum confinement effects.

The exact line-shape from an ensemble of emitting centres can be expected to result from a complex combination of homogeneous and inhomogeneous broadening mechanisms. The classic example giving rise to a homogeneously broadened line-shape around a central emission feature is that of *natural* (or *lifetime*) broadening, which is a direct consequence of the non-commutitivity of energy and time according to the Heisenberg uncertainty principal, expressed mathematically as:

$$\Delta E \Delta t \geq \hbar \qquad (26)$$

The persistence of an excited electronic state for some time, $\tau = \Delta t$ means that the exact energy of that state cannot be determined exactly nor can the transition energy between that state and the ground state. Rather, the energy of the

transition is spread by an amount on the order of $\Delta E \sim \hbar/\tau$, which gives rise to spectral features with a *natural* line-width.

The spectral shape can also reveal the extent of the coupling between the electronic charge distribution of the luminescent centre and the surrounding ion cores of the host material. For example, the electronic state(s) of an erbium luminescent centre are particularly sensitive to the local electric (or crystal) field arising from the charge density of their surrounding (host) atoms. In this case, the transition energies may be split according to the neighbourhood symmetry, which can manifest in a broadened emission spectrum for glass bound erbium related centres relative to those embedded in a crystalline host[114].

When studying the luminescence from an ensemble of semiconductor nano-structures, the collective spectrum is likely broadened by the combined effects of size (and therefore band-gap) variation, the persistence of phonon replicas associated with the indirect band structure as well as local field fluctuations.

During the course of this work we employed a variety of techniques to study the photoluminescence including excitation power (flux), temperature and time dependent photoluminescence spectroscopy to characterize the visible, NIR and IR emission from silicon nanocrystal and Er-doped silicon oxide thin films.

Excitation power dependent photoluminescence

For excitation power (flux) dependent measurements in the visible/NIR wavelength range, 500 to 1000nm we used a 50mW 405nm *Coherent* cube laser diode in continuous wave (CW) mode. The laser beam was passed through a 405nm band pass filter and steered towards the sample using a mirror and 90:10 beam-splitter. The laser was focused onto the sample position using a 40x microscope objective lens to a spot size determined, using a *Graticules Ltd* calibrated micro-scale (0.1in/100 lines) and *Panasonic* Super Dynamic charge coupled device (CCD) imaging camera to be ~120μm in diameter. The laser power was varied over a wide range (in excess of two orders of magnitude) by combining the software controlled 50mW range of the laser with neutral density filters. The power density was measured at the sample position with a *Sensor-und Lasertechnik* LP20 pyrometer calibrated at 4.93V/W and the voltage read using a *Tektronix* TDS 220 100MHz 1Gs/s digital storage oscilloscope (DSO). The PL was collected con-focally and passed through either a 500nm (for visible) or 850nm (for IR) long pass

filter to further suppress laser reflections and in the case of IR measurements, any visible PL emissions. The PL signals were dispersed by a single 150 lines/mm grating in a 0.5m spectrometer and detected using an N$_2$-cooled Indium Gallium Arsenide (InGaAs) array detector. A schematic of the experimental set-up is shown in **Figure 2-16**.
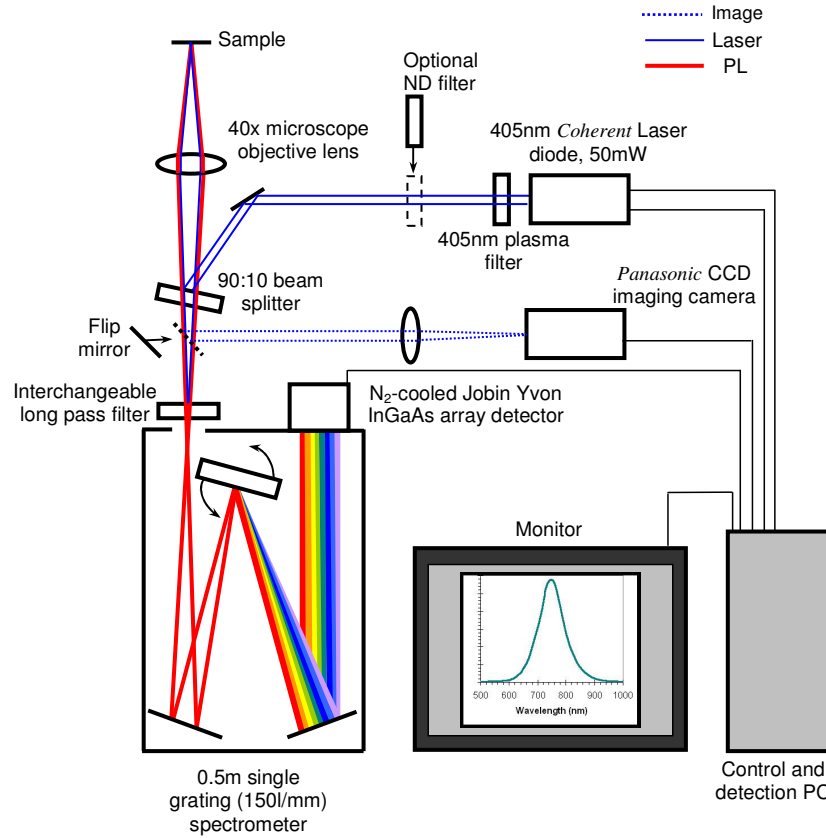
Figure 2-16 Schematic of the experimental set-up for room temperature visible/NIR and IR excitation power dependent photoluminescence measurements

The excitation flux was calculated assuming a spherical laser spot[‡]. Then the power density is the power per unit area, $4P/\pi d^2$ with $d \sim 120\mu m$. The flux is the number of photons of energy, $E = hc/\lambda$ with λ = 405nm arriving at the sample per unit area per unit time, which is calculated from $4x10^{-4}P/E\pi d^2$ (photons/cm^2/s). Errors in calculating the flux can arise from reflections at interfaces across which the refractive index changes. The *Fresnel* equations reveal that the fraction of reflected light at normal incidence (θ_i = 0, $\cos(\theta_i)$ = 1) is only a function of the

---

[‡] In fact the laser footprint is elliptical with a ratio of radii of ~3. However, our assumption of a spherical spot is justified because the laser footprint completely covered the microscope objective entrance aperture providing a circular footprint at the focus. This was verified by the image observed with the camera.

refractive indices, n_1 and n_2 either side of the interface according to equation (27)[115]:

$$R = \left(\frac{n_2 - n_1}{n_2 + n_1} \right)^2 \qquad (27)$$

At the air/oxide interface, $n_1 = 1$ and $n_2 = 1.46$ and R turns out to be ~ 3.5%. Although this is a relatively small fraction of the incident light such that T_1 ~ 96.5% is transmitted through the top oxide layer, in reality one should consider that the transmitted light encounters multiple interfaces as it passes through the entire sample structure as shown schematically in **Figure 2-17**.
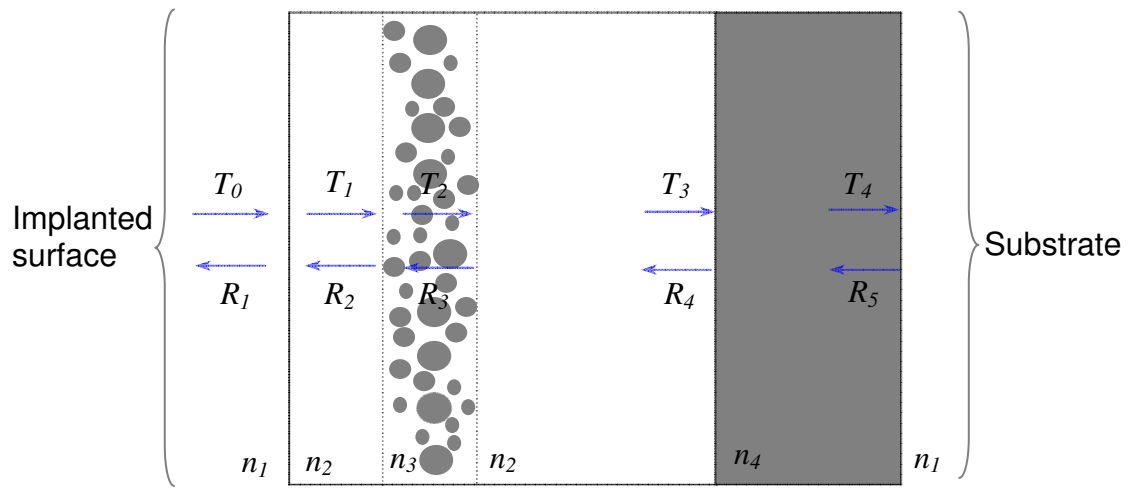
Figure 2-17 Schematic representation of the fractions of transmitted and reflected light at normal incidence as it passes through a SiO$_2$/Si-NC sample on Si

A similar fraction of light could be reflected from the 'effective interface' created by the presence of the Si-NCs, which represents a silicon rich oxide layer. The increase in Si-Si bond formation during high temperature annealing of silicon rich silica should result in a refractive index, $n_3 > n_2$. Indeed Spiga *et al*[116] showed that the refractive index increases in direct proportion with the excess Si content and for SiO$_x$ films in which x was decreased from ~1.91 to 0.85 and annealed at 900$^\text{o}$C, n_3 was shown to increase from ~1.49 to ~2 at 400nm, which puts an upper limit on R_2 of ~2.4% and T_2 should then be of the order of $0.94T_0$.

Excitation power dependent photoluminescence transients

In order to measure the dependence of the excitation power on the PL transients the 405nm laser was operated in pulsed mode. The laser was triggered using a *TTi* TG4001 40MHz DDS arbitrary function generator producing 300μs pulses at 5V with a 50% duty cycle. The PL was detected by a *Thor-labs* PDA36A-EC Si amplified detector positioned in the collection path of the optical axis and the time signals displayed and recorded on a *Tektronix* TDS 220 100MHz 1GS/s dual channel digital real-time oscilloscope. The temporal resolution was limited by the Si detector, which is a function of its gain setting. A gain setting of 0dB gives a temporal resolution of ~60ns decreasing to ~10μs for a gain setting of 50dB. All of the measured luminescence transients exhibited characteristic 1/e times in excess of 10μs over the entire experimental flux range. A schematic of the experimental set-up is shown in **Figure 2-18**.
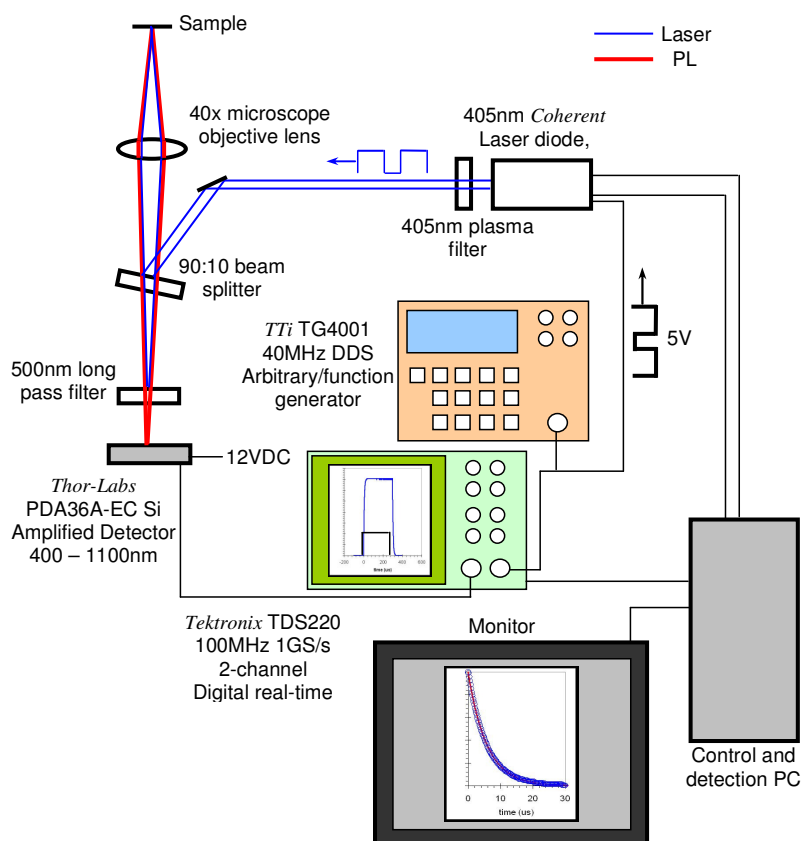
Figure 2-18 Schematic of the experimental set-up for room temperature visible/NIR excitation power dependent photoluminescence transient measurements

A characteristic drive pulse is shown along with measured transients for the laser line and integrated PL emission in **Figure 2-19**.
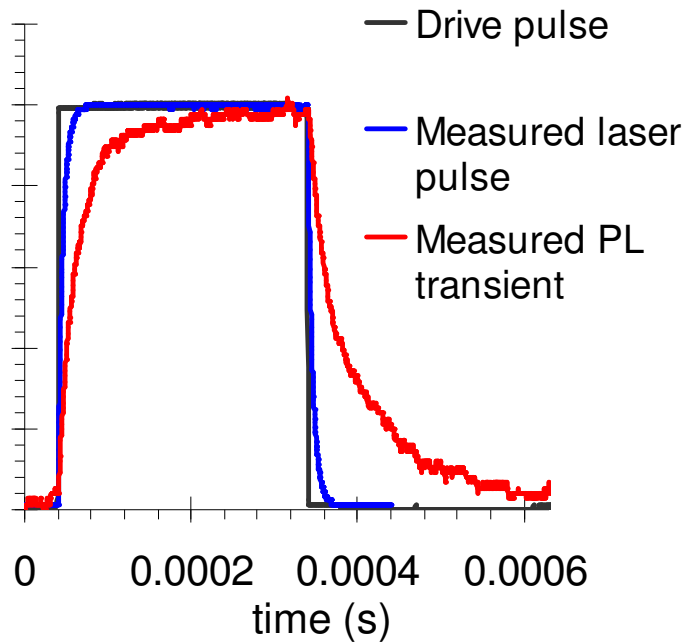
Figure 2-19 Characteristic drive pulse (black) and transient response of the laser (blue) and integrated PL (red) measured using a *Thorlabs* PDA36A-EC Si amplified photo-detector. With the photo-detector amplifier setting at 40dB the laser transient reveals a system response time (1/e) of τ = 5µs. The actual laser response is on the order of a few nano-seconds

Temperature dependent photoluminescence

For low temperature PL measurements in the visible through to IR, the samples were mounted on the cold finger of a recycling Helium (He) cryostat. Photo-excitation was provided by a 10mW 375nm *Coherent cube* laser diode, with an unfocussed spot size of ~4mm. To improve the signal to noise ratio an optical chopper was used to modulate the excitation, which results in a modulated PL signal at the same frequency. The PL was collected using a collimating lens and focused onto the slit of a single 600 lines/mm grating spectrometer and detected using an N_2-cooled *Edinburgh Instruments* EI-L single channel Germanium (Ge) photo-detector. A customised *labview* program drives a stepper motor, which rotates the grating through the desired wavelength range and the intensity at each wavelength is converted to an electrical signal by the photo-detector. This signal is passed to a 'lock-in' amplifier where it is compared against a reference signal at the frequency of the optical chopper. The 'lock-in' amplifier only amplifies input signals from the photo-detector with frequency components and phase that are matched within a narrow band of the reference. Signals with frequency components outside this range or lacking phase coherence within the frequency range, including noise signals are suppressed. An analogue to digital (A/D) converter then passes the amplified signals to the computer via RS232 where they are read in and displayed using the same *labview* program. The sample temperature was monitored via thermocouple and controlled via integrated heater element using an *Oxford Instruments* ITC 503 temperature controller. A schematic of the experimental set-up is shown in **Figure 2-20**.
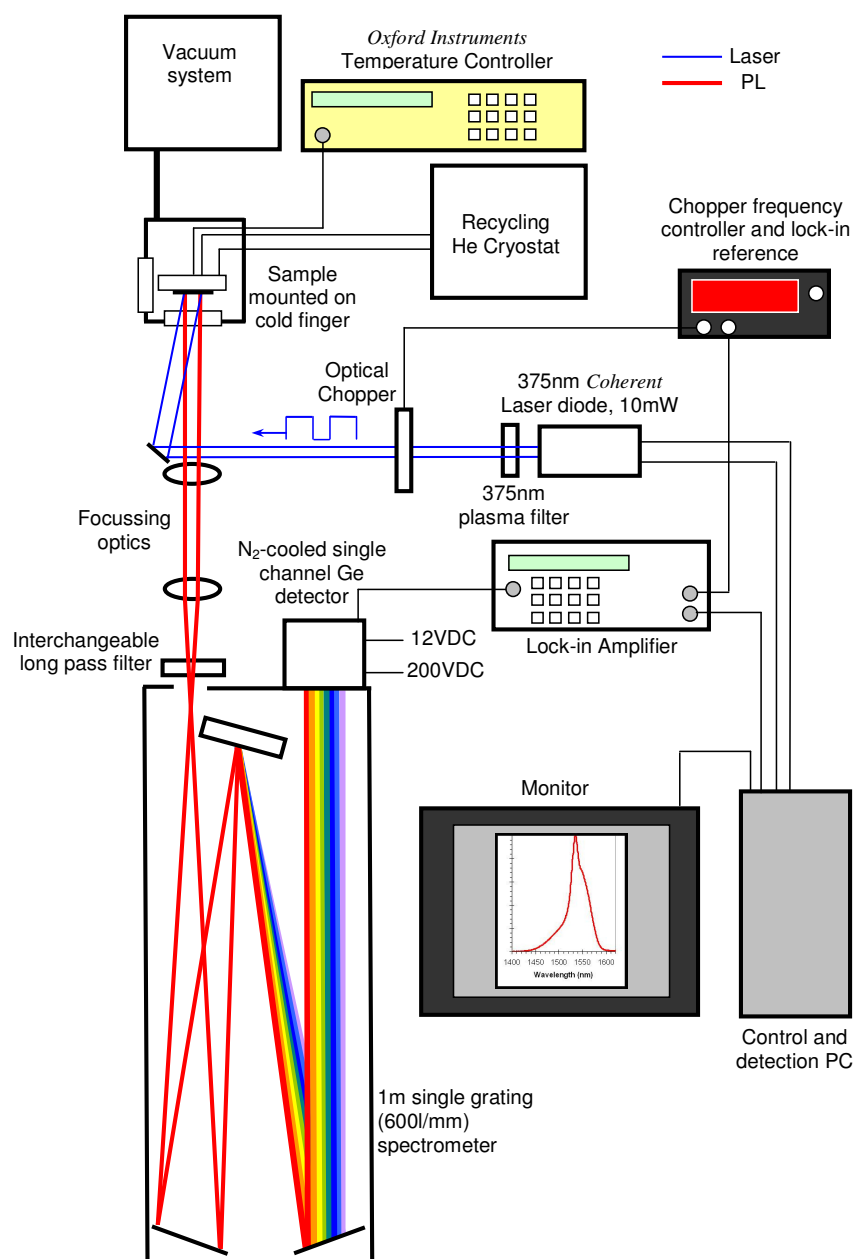
Figure 2-20 Schematic of the experimental set-up for visible/NIR/IR temperature dependent photoluminescence measurements

System response correction

All of the photoluminescence spectra were corrected for the 'system' response, which removes any spectral artifacts associated with the detection system. For example the non-linear response of the detector and grating and filter artifacts can result in apparent shifts or spurious emissions in uncorrected spectra, which give misleading results. We used a broad band tungsten lamp to calibrate the system response, the spectrum from which is calibrated at 3000K. The theoretical spectral intensity profile from such a broad band source is a function of both wavelength and temperature according to Planck's equation for a blackbody radiator[117]:

$$F(\lambda, T) = \frac{2\pi hc^2}{\lambda^5 \exp(hc/\lambda kT) - 1} \tag{28}$$

Where λ is the wavelength of light and c is its speed in a vacuum, h and k are the constants of Planck and Boltzmann respectively and T is the temperature in degrees Kelvin.

The procedure for 'system' correction is as follows; measure the spectrum of the broadband source across the wavelength range of interest to the highest resolution possible to obtain a spectral intensity profile as a function of wavelength, $S(\lambda)$. Then a 'system' correction function exists, $N(\lambda)$ such that the product $S(\lambda)N(\lambda) = F(\lambda)$. The 'system' correction function is then determined from the ratio of the theoretical to the measured blackbody curves, i.e. $N(\lambda) = F(\lambda)/S(\lambda)$, with $N(\lambda)$ a valid correction function for all measured spectra on the same system providing there are no physical changes to the system. **Figure 2-21 (a)** shows the theoretical and measured tungsten lamp spectra along with the ratio of the two, which was used to correct all spectra measured under the same experimental conditions, an example of which is shown in **Figure 2-21 (b)**.
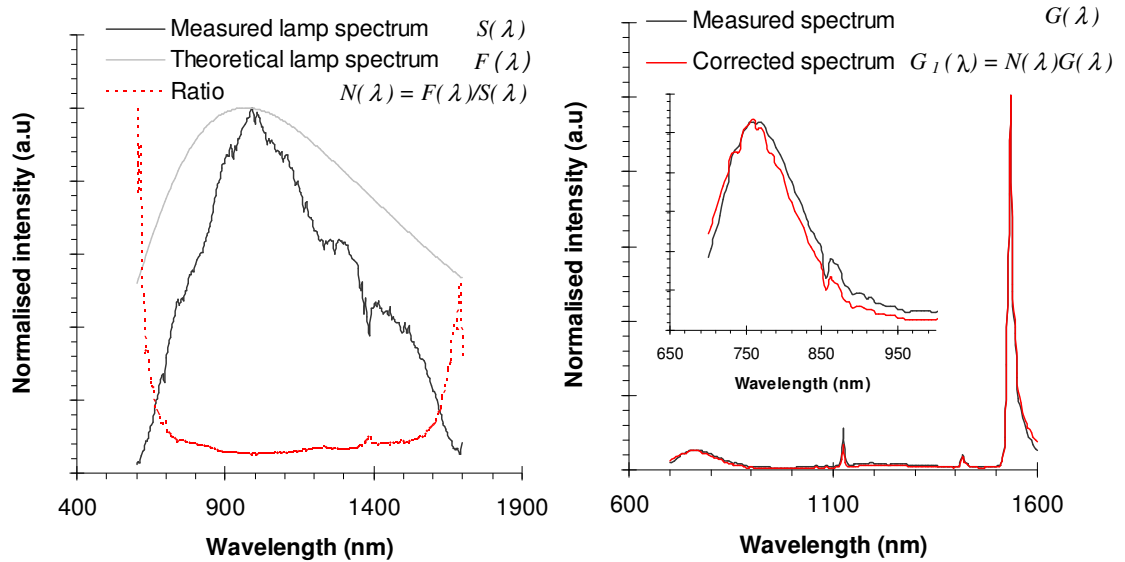
Figure 2-21 (a) Measured (black line, $S(\lambda)$) and theoretical (grey line, $F(\lambda, T)$ from equation (28)) tungsten lamp spectra (T = 3000K) and the ratio, $N(\lambda) = F(\lambda)/S(\lambda)$. (b) Example measured, $G(\lambda)$ and corrected spectra, $G_1(\lambda) = N(\lambda)G(\lambda)$ from a Si$^+$ and Er$^+$ co-implanted silica film on Si. The inset shows the silicon nano-cluster related emission blown-up

2.3.2   Raman Spectroscopy

The *Raman* effect describes the coupling of an incident high frequency time varying electromagnetic field (i.e. monochromatic light) to atomic or molecular *vibrations* of a material, which results specifically in a change in the spectral content of the *scattered* radiation. The shift in the frequency indicates the transfer of energy in the scattering (inelastic collision) process, the magnitude of which is directly related to the vibrations (phonons) of specific atoms or molecules. Under the correct experimental conditions, i.e. adequate suppression of the scattered radiation that shares the same frequency component as the incident radiation, a rich spectral fingerprint is obtained that provides an analytical technique for the chemical characterization of materials through *Raman* spectroscopy.

The classical description of the Raman effect takes into account the polarizability of an atom or molecule, α which is a measure of the ability of an electric field, E to induce a dipole moment, P in that atom or molecule according to equation (29)[118]:

$$\alpha = \frac{P}{E} \tag{29}$$

The instantaneous polarization of a molecule is a sum of its static equilibrium polarizability, α_0 and a time varying term describing the spatial change in polarization from the equilibrium geometry, Δr according to:

$$\alpha = \alpha_0 + \dot{\alpha}\Delta r \tag{30}$$

Where $\dot{\alpha} = \delta\alpha/\delta r$ represents the change in polarizability with respect to the position, r. If we assume that the vibration of the molecule can be represented by a sinusoidal function of the form:

$$\Delta r = r_0 \sin(\omega t) \tag{31}$$

Where r_0 is the maximum vibrational amplitude, ω is the angular frequency of vibration and t is the time. Then the instantaneous polarization may be written:

$$\alpha = \alpha_0 + \dot{\alpha}r_0 \sin(\omega t) \tag{32}$$

Expanding the electric field component of the exciting electromagnetic radiation yields a similar expression for the instantaneous electric field:

$$E = E_0 \sin(\omega_1 t) \tag{33}$$

Where E_0 is the maximum of the electric field, ω_1 is the angular frequency of the field and t is the time. Substituting equations (32) and (33) into equation (29) allows us to write the dipole moment as:

$$P = \alpha_0 E_0 \sin(\omega_1 t) + E_0 r_0 \dot{\alpha} \sin(\omega_1 t) \sin(\omega t) \tag{34}$$

And using the product to sum trigonometric identity, $sin(\theta)sin(\varphi) = \frac{1}{2}cos(\theta - \varphi) - \frac{1}{2}cos(\theta + \varphi)$ allows us to expand equation (34) to show that the oscillating dipole moment is a superposition of oscillations with three distinct frequency components:

$$P = \alpha_0 E_0 \sin(\omega_1 t) + \frac{1}{2} E_0 r_0 \dot{\alpha} \cos([\omega_1 - \omega]t) - \frac{1}{2} E_0 r_0 \dot{\alpha} \cos([\omega_1 + \omega]t) \tag{35}$$

The first term, which is by far the dominant contributor to the total scattering spectrum has the same frequency component, ω_1 as the incident or exciting radiation and constitutes *Rayleigh* scattering. The second and third terms have frequency components $\omega_1 \pm \omega$ and describe *Stokes* and anti-*Stokes* scattering with a combined contribution[§] to the total scattering spectrum on the order of 10^{-5}% and are therefore much weaker than the *Rayleigh* scattering spectrum. *Stokes* and anti-*Stokes* scattering respectively describe the processes by which an atomic or molecular vibration (phonon) is generated or destroyed through interaction with the exciting radiation as illustrated by **Figure 2-22**.

[§] The relative population of atoms or molecules distributed between the ground and 1st vibrational states prior to interaction with the incident electromagnetic radiation is determined by *Boltzmann* statistics and so at room temperature the contribution from *Stokes* scattering to the *Raman* spectrum is typically larger than that from anti-*Stokes* scattering. At sufficiently low temperatures the Anti-*Stokes* scattering component disappears completely

(a) *Rayleigh scattering*   **(b)** *Stokes scattering*   **(c)** *Anti-Stokes scattering*

Virtual energy states

$h\upsilon_1$ $-h\upsilon_1$ $h\upsilon_1$ $-h(\upsilon_1-\upsilon)$ $h\upsilon_1$ $-h(\upsilon_1+\upsilon)$

Vibrational state

Ground state

$h\upsilon$
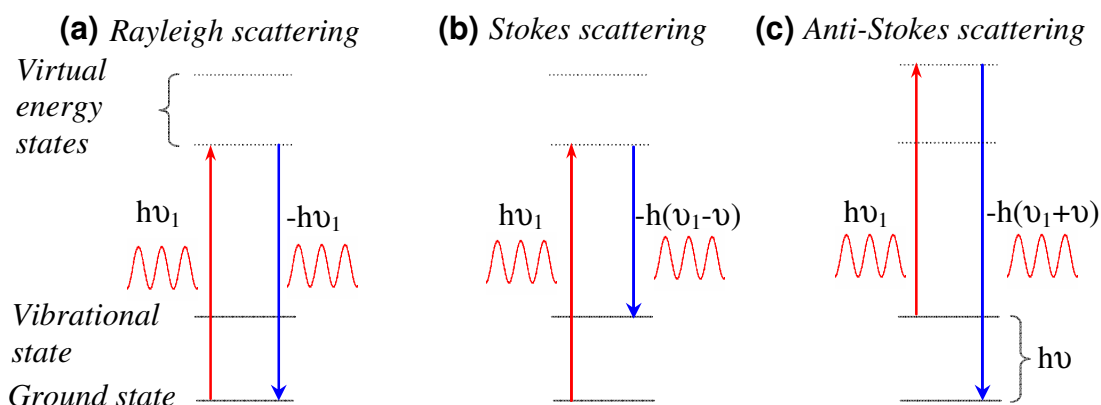
Figure 2-22 (a) *Rayleigh* **scattering in which there is no net change in frequency (energy) between incident and scattered fields (b)** *Stokes* **scattering in which an atomic or molecular vibration of angular frequency, $\omega = 2\pi\upsilon$ is induced by the exciting field (c) anti-*Stokes* scattering in which an atomic or molecular vibration of frequency, $\omega = 2\pi\upsilon$ is destroyed by the exciting field**

The work presented in this thesis was conducted using a commercial *Renishaw* 1000 micro-*Raman* system using a 514nm Ar^+ laser to excite the samples. A schematic of the system is shown in **Figure 2-23**.
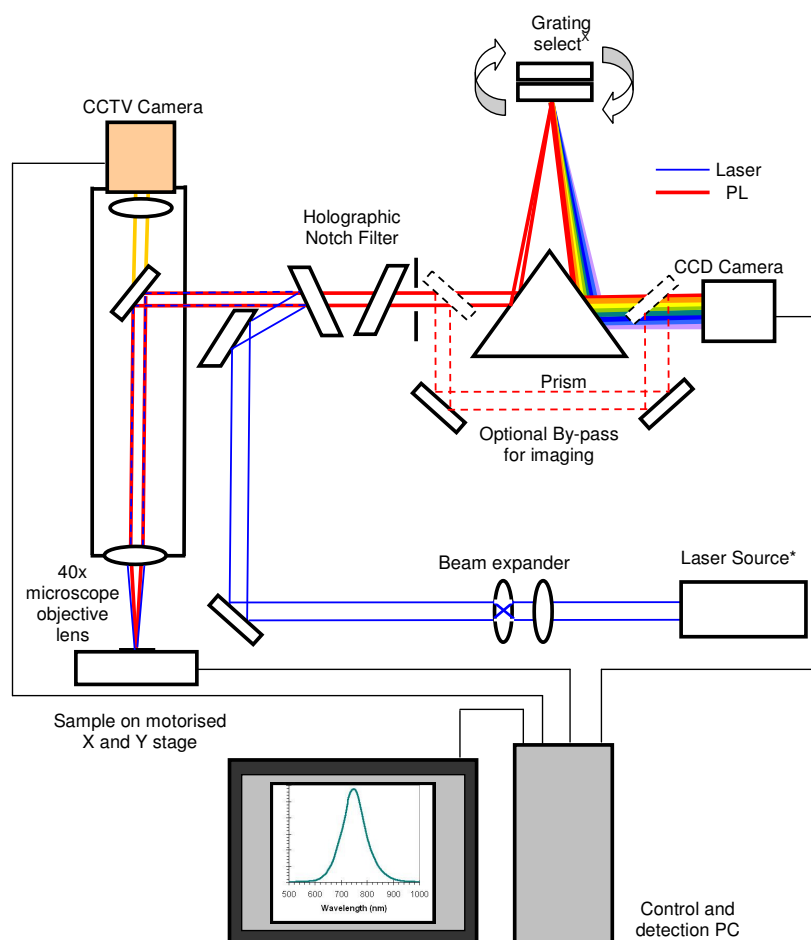
Figure 2-23 Schematic representation of the *Renishaw* 1000 micro-*Raman* spectrometer

The *Renishaw* 1000 system is an integrated spectrometer and optical microscope system with changeable lenses, filters and grating so that it can be used with a variety of laser sources. The laser beam enters the system from the rear where an appropriate plasma filter is installed to remove unwanted cavity modes emanating from the laser. The laser is steered through a fixed separation beam expander and a set of mirrors into the integrated optical microscope where it can be focused using a variety of microscope objective lenses. The sample can be imaged using the same lens either through the microscope binoculars or via CCTV camera mounted at the top of the microscope and the image viewed on the computer monitor. The sample is seated on a computer controlled motorized *X-Y* stage enabling full control over the sample position from which the *Raman* spectra are to be collected. We used a long working distance 40x objective lens to focus the laser and collect *Raman* signals in a backscattering geometry from an area on the sample of ~1 μm^2, hence the term micro-*Raman*. Narrow bandwidth holographic

notch filters are used to suppress reflected laser and *Rayleigh* scattered light from the sample whilst allowing the *Stokes* and anti-*Stokes Raman* scattered signals to pass through. The transmitted light is focused onto an optical slit using an intermediate lens and dispersed using a conventional grating monochromator. The dispersed light is reflected using a prism onto an integrated charge coupled device (CCD) camera. The CCD converts the light into an electrical signal, which is proportional to the light intensity and this is read-in by a computer at each spectral increment to generate the final *Raman* spectra using dedicated *GRAMS*® software. The signal to noise ratio may be improved by 'trimming' the CCD pixel array, increasing the exposure time and accumulating averaged spectra over multiple exposures.

2.4   References

77.   T. Watanabe, K. Tatsumura and I. Ohdomari, Applied Surface Science **237** (1-4), 125-133 (2004).

78.   B. E. Deal and A. S. Grove, Journal of Applied Physics **36** (12), 3770-3778 (1965).

79.   E. Nicollian and A. Reisman, Journal of Electronic Materials **17** (4), 263-272 (1988).

80.   Y. Nishi and R. Doering, *Handbook of Semiconductor Technology*. (Marcel Dekker Inc., New York, 2000).

81.   S. Bruyère, F. Guyader, W. De Coster, E. Vincent, M. Saadeddine, N. Revil and G. Ghibaudo, Microelectronics Reliability **40** (4-5), 691-695 (2000).

82.   S. K. Lai, D. R. Young, J. A. Calise and F. J. Feigl, Journal of Applied Physics **52** (9), 5691-5695 (1981).

83.   L. Rubin and J. Poate, The Industrial Physicist **Feature Article** (June/July), 12-15 (2003).

84.   J. Lindhard, M. Scharff and H. E. Schioett, Journal Name: Kgl. Danske Videnskab. Selskab. Mat. Fys. Medd.; Journal Volume: Vol: 33: No. 14; Other Information: Orig. Receipt Date: 31-DEC-64, Medium: X; Size: Pages: 1-42 (1963).

85.   R. Chennamsetty and I. Escobar, Separation Science and Technology **43** (16), 4009 - 4029 (2008).

86.   J. F. Ziegler, *The Stopping and Range of Ions in Solids (Stopping and Range of Ions in Matter)*. (Pergamon Pr, 1985).

87.   T. Ishitani, R. Shimizu and K. Murata, Japanese Journal of Applied Physics **11** (2), 125-133 (1972).

88.   G. Wang, S. Tian, M. F. Morris, S. J. Morris, B. J. Obradovic, G. Balamurugan and J. A. F. Tasch, presented at the Microelectronic Device Technology, Austin, TX, USA, 1997 (unpublished).

89.   T. M. Liu and W. G. Oldham, IEEE Electron Device Letters **EDL-4** (3), 59-62 (1983).

90.   M. T. Robinson, Radiation Effects and Defects in Solids: Incorporating Plasma Science and Plasma Technology **130** (1), 3 - 20 (1994).

91.   G. Spitzlsperger, (http://www.plasmaetch-gs68.de/tutorials/implant.pdf, 2003).

92.   C. Jeynes, N. P. Barradas, P. K. Marriott, G. Boudreault, M. Jenkin, E. Wendler and R. P. Webb, Journal of Physics D: Applied Physics **36**, R97-R126 (2003).

93.   M. Webb, Internal communication report on RBS results, G390:7, Job No. 1657, 2007.

94.   J. K. Bording and J. Tafto, Physical Review B **62** (12) (2000).

95.   D. A. Porter and K. E. Easterling, *Phase Transformations in Metals and Alloys*, 2 ed. (Chapman and Hall, London, 1992).

96.   E. Dassau, B. Grosman and D. R. Lewin, Computers & Chemical Engineering **30** (4), 686-697 (2006).

97.   D. E. Blakie, MSc Thesis, McMaster University, 2006.

98.   P. Roura, J. Farjas, A. Pinyol and E. Bertran, Nanotechnology **18** (175707) (2007).

99.   D. R. Lamb and F. R. Badcock, International Journal of Electronics **24** (1), 11 - 16 (1968).

100. S. Kaschieva, Solid-State Electronics **41** (3), 413-415 (1997).
101. J. W. Goodman, *Introduction to Fourier Optics*, 3rd Edition ed. (Roberts and Company, 2005).
102. D. B. Williams and C. B. Carter, *Transmission Electron Microscopy - A Textbook for Materials Science*. (Plenum Press, New York, 1996).
103. M. De Graef, *Introduction to Conventional Transmission Electron Microscopy*. (Cambridge University Press, Cambridge, 2003).
104. C. O. Girit, J. C. Meyer, R. Erni, M. D. Rossell, C. Kisielowski, L. Yang, C.-H. Park, M. F. Crommie, M. L. Cohen, S. G. Louie and A. Zettl, Science **323** (5922), 1705-1708 (2009).
105. S. Mitra, *Sample Preparation Techniques in Analytical Chemistry*. (John Wiley & Sons Inc., New York, 2003).
106. R. F. Egerton, *Electron Energy-Loss Spectroscopy in the Electron Microscope*, 2nd ed. (Plenum, New York, 1996).
107. D. A. Muller, L. F. Kourkoutis, M. Murfitt, J. H. Song, H. Y. Hwang, J. Silcox, N. Dellby and O. L. Krivanek, Science **319** (5866), 1073-1076 (2008).
108. Gatan., *EELS Analysis User's Guide Rev. 1.2.1*. (2003).
109. R. J. Kashtiban, U. Bangert, I. F. Crowe, M. P. Halsall, B. Sherliker, A. J. Harvey, J. Eccles, A. P. Knights, R. M. Gwilliam and M. Gass, in *Journal of Physics: Conference Series* (IoP, Oxford, UK, 2010), Vol. 209.
110. I. F. Crowe, T. R. Roschuk, U. Bangert, B. Sherliker, M. P. Halsall, A. P. Knights and P. Mascher, in *Conference on Optoelectronic and Microelectronic Materials and Devices, 2008. COMMAD 2008* (IEEE, Australian National University (ANU), Canberra, 2008), pp. 163-165.
111. D. K. Schroeder, *Semiconductor material and device characterization*, 2nd ed. (John Wiley and Sons, Inc., New York, 1998).
112. J. I. Pankove, *Optical Processes in Semiconductors*. (Dover Publications, New York, 1975).
113. N. Daldosso, M. Luppi, S. Ossicini, E. Degoli, R. Magri, G. Dalba, P. Fornasini, R. Grisenti, F. Rocca, L. Pavesi, S. Boninelli, F. Priolo, C. Spinella and F. Iacona, Physical Review B **68** (085327) (2003).
114. A. V. Kholodkov, K. M. Golant and L. D. Iskhakova, Journal of Non-Crystalline Solids **352**, 3808-3814 (2006).
115. M. Bass, *Handbook of optics*, 3rd Ed. ed. (McGraw Hill, 2010).
116. S. Spiga, G. Tallarida, A. Borghesi, A. Sassella and G. De Santi, Thin Solid Films **325** (1-2), 36-41 (1998).
117. D. J. Amit and Y. Verbin, *Statistical Physics: An Introductory Course*. (World Scientific Publishing Co., 1999).
118. J. R. Ferraro, K. Nakamoto and C. W. Brown, *Introductory Raman Spectroscopy*, 2nd ed. (Elsevier, San Diego, 2003).

3   Formation dynamics of silicon nano-clusters in SiO$_2$

3.1   Introduction

Since the first demonstration of room temperature luminescence from porous silicon (*p*-Si) by Canham *et al* in 1990[119], a wide variety of methods for the preparation of silicon nano-clusters (Si-NCs) has been described. Most of these involve the thermal annealing of silicon supersaturated (Si-rich) silicon oxide (SRSO) or nitride (SRSN) after deposition[120], laser ablation[121], sputtering[122] or thermal evaporation[123] from vapour or solid Si sources. Solution synthesis of colloidal Si-nanocrystals[124] and electro-chemical etching of silicon on insulator (SOI) substrates followed by oxidation were also reported recently and the latter, in particular has led to the observation of narrow spectral emission lines from single Si-NCs[125].

The work described in this chapter describes an extensive collaborative effort with fellow researchers at the Universities of Surrey in the UK and McMaster in Canada to develop samples prepared by Si$^+$ implantation of SiO$_2$ grown by 'wet' thermal oxidation of single crystal (100) silicon substrates to obtain SRSO, followed by high temperature rapid thermal annealing (RTA) to form Si-NCs in the oxide layer. The early stages of nucleation and growth of the Si-NCs were studied and experimental data is presented, which shows the evolution of the Si-NCs as a function of the annealing environment, i.e. isothermal anneal time, t_A and isochronal anneal temperature, T_A. A statistical evaluation of the Si-NC size, density and distribution in the oxide layer, obtained from dark field (DF) cross-sectional transmission electron microscopy (X-TEM) images reveals that the Si-NC formation process in the first 100s of thermal annealing may be adequately described using classical thermodynamics of binary solutions[126]. From the time evolution of the Si-NC mean diameter within a specific annealing temperature range, we obtained values for the cluster coarsening rate constant in the thermally grown SiO$_2$ and the activation energy to precipitate formation. These values indicate that the formation of Si-NCs in implanted oxides proceeds rapidly in the first few seconds of high temperature annealing apparently assisted by the presence of both vacancy and interstitial point defects, presumably generated by

the ion irradiation. Microscopy images reveal the ensemble nano-cluster population to be most accurately represented by a lognormal distribution function from which we obtained characteristic values for the mean particle diameter, $\overline{d}$ and standard deviation, σ as a function of the annealing conditions for a fixed Si excess concentration.

3.2   Background

A general description of the phase segregation process for binary solutions (alloys) was provided, according to classical thermodynamics by Porter and Easterling[126] and more recently a specific treatment of the formation of Si-NCs in SiO$_2$ was summarized by Lockwood[127].

Essentially, the precipitation of Si by annealing SRSO may be treated in a similar way to the homogeneous nucleation and formation of solid clusters in a liquid, i.e. the formation of Si-NCs is driven by a reduction in the volume (or *Gibbs*) free energy at a rate which depends on both the initial Si excess concentration and the annealing temperature. At the same time, this volume free energy reduction is opposed by the energy required to create a precipitate (Si/SiO$_2$) interface and so the total change in the free energy may be written[126]:

$$\Delta G = -V\Delta G_v + A\gamma \tag{36}$$

Where V is the volume of the Si precipitate, A is the SiO$_2$/Si-NC interfacial area and γ is the interfacial energy (surface tension). If the excess free energy is minimized by the formation of spherical nucleii of radius, r then the total change in free energy as a function of r will be[126]:

$$\Delta G(r) = -\frac{4}{3}\pi r^3 \Delta G_v + 4\pi r^2 \gamma \tag{37}$$

Figure 3-1 shows the variation in free energy associated with homogeneous nucleation of a sphere of radius, r for a specific Si excess and annealing environment.
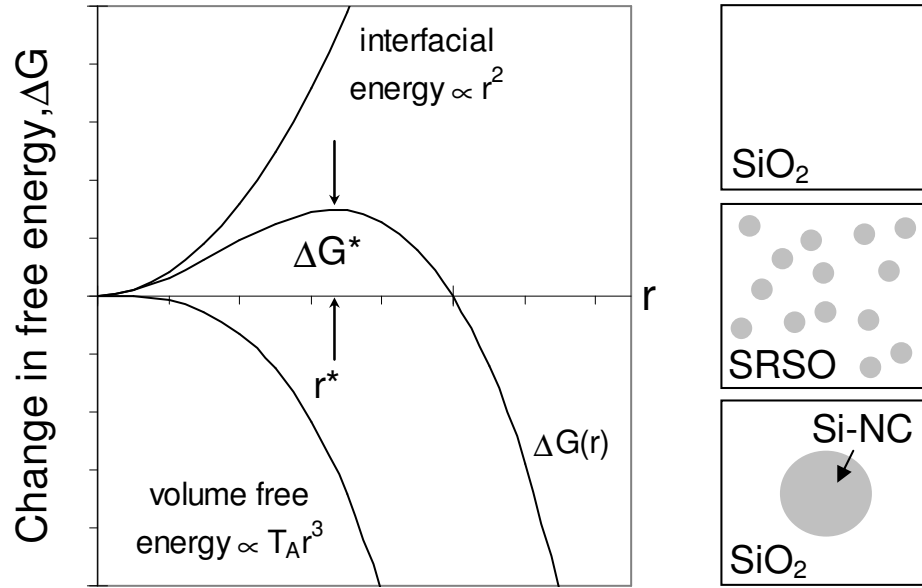
Figure 3-1 (a) The free energy change associated with homogeneous nucleation of a sphere of radius, r and (b) diagrammatic representation of homogeneous nucleation of Si in the SRSO system. Adapted from [126]

The difference in the rate of increase of the areal (interfacial) and volumetric energy terms with precipitate radius, r means that the cluster formation initially results in an increase in the free energy by an amount, ΔG^*. This local maximum represents the activation energy for the nucleation of precipitates with a critical radius, r^*. For a given excess Si concentration and annealing temperature, T_A the excess free energy can therefore be reduced either by further increasing the size of precipitates with $r > r^*$ or by further dissolution of precipitates with $r < r^*$. Since ΔG^* is a turning point, then r^* can be obtained by equating the differential of $\Delta G(r)$ to 0, which yields:

$$r^* = \frac{2\gamma}{\Delta G_v} \tag{38}$$

And ΔG^* may be obtained by substitution of (38) into (37) to give:

$$\Delta G^* = \frac{16\pi\gamma^3}{3\Delta G_v^2} \tag{39}$$

As ΔG_v is proportional to the concentration of excess Si and the annealing temperature[127], the probability of forming clusters (i.e. overcoming the activation energy barrier, ΔG^*) therefore increases with increasing Si excess concentration and/or annealing temperature. In real systems the excess free energy is further

reduced (and the probability of Si-NC formation enhanced) by heterogeneous formation for example at pre-existing defect sites, such as those resulting from ion irradiation. In the presence of vacancy defects for example, the energy required to form an interface (activation energy) should be lowered by the energy required to remove such defects and in this sense, implanted oxides or nitrides may be ideal pre-cursor materials for the thermal preparation of Si-NCs. Evidence of the preferential Si-NC nucleation at pre-existing defect sites was reported by Mokry *et al*[128] in which the Si-NC formation site was shifted with respect to the predicted Si$^+$ implantation depth profile from *Monte Carlo* simulations using the SRIM-2003 algorithm. The ion implanted depth range of Si$^+$ in SiO$_2$ was predicted to be much longer than the actual Si-NC formation site, as determined from TEM images. In fact the formation site was almost perfectly coincident with the site of vacancies generated by the Si$^+$ irradiation, also predicted by SRIM, as illustrated by **Figure 3-2**. The excess Si therefore exhibits a tendency to form clusters in the irradiated region of the matrix during thermal annealing according to an energetically favourable migration (enhanced diffusion) and nucleation process.
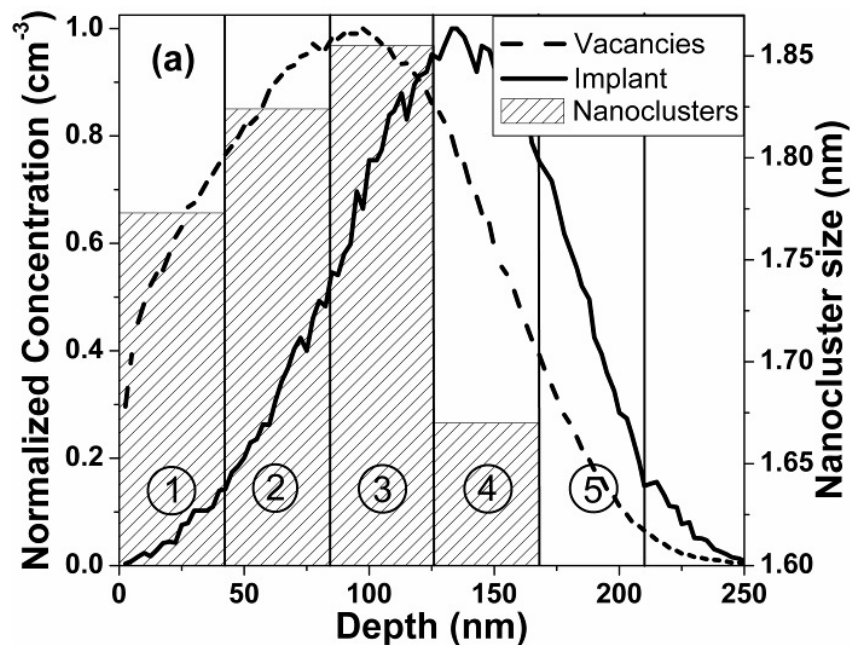
Figure 3-2 The depth distribution of vacancies (dashed line) and implanted Si$^+$ predicted (solid line) by SRIM (left axis) compared with the Si-nanocrystal size distribution obtained from TEM images (right axis), courtesy of [128]

For fixed annealing conditions (t_A, T_A) and fixed Si excess concentration, this result implies that the density and to some extent the size of Si-NCs may be controlled by prior ion irradiation of the host matrix.

After nucleation, the growth of Si-NCs proceeds by a mechanism of coarsening in which the total surface energy is further reduced according to the *Ostwald* ripening process. This is the process by which those clusters with $r > r^*$ grow at the expense of those with $r < r^*$ because precipitate surface atoms are relatively unstable compared to those that form the nucleus. According to the Gibbs-Thomson effect[129], smaller Si-NCs are less stable because the solute concentration at their interface is higher than that for larger nano-crystals. The presence of concentration gradients between different size nano-clusters then results in a net flux of atoms diffusing from small to large nano-clusters under heating so that small clusters shrink and disappear whilst larger clusters grow. Eventually the total surface to volume ratio is reduced until the size and density of the Si-NCs approaches an asymptotic value. In reality a stable asymptotic value for the clusters is never reached, even after many hours of high temperature annealing although for most materials studied, it is reasonably approached within the first 5 minutes of high temperature (> 1000°C) treatments. It is worth noting that this exchange of atoms and therefore the Si-NC growth continues even in the absence of further excess Si.

The wide band-gap of the SiO$_2$ means that it represents a potential as well as a physical barrier between the Si-NCs, which confines photo- or electrically excited carriers within the Si-NCs. Since the quantum mechanical tunnelling probability of excited carriers increases as the barrier thickness is reduced[130], then the spacing between Si-NCs, or their density, which is determined by the initial Si-excess concentration and the annealing conditions (t_A, T_A) can be expected to influence the optical and electronic properties of this material system. For example, if the SiO$_2$ barrier thickness between two different size Si-NCs is sufficiently thin, i.e. if the nano-cluster density is high, an electron in the first excited state of a smaller Si-NC may relax by tunnelling into the first excited state of the conduction band of a larger neighbour. For sufficiently thin barriers, this process may actually proceed in preference to band edge recombination with the respective hole in the same cluster because the latter process is suppressed due to the indirect nature of the Si band structure[131]. Understanding and having the ability to control such

processes is therefore critical if future optoelectronic devices based on silicon nano-technology are to be realised.

3.3   Experimental details

3.3.1   Sample preparation

A large sample set was prepared in collaboration with the groups of Prof. Russell Gwilliam at the Surrey ion beam centre and Prof. Andy Knights at McMaster University. A nominal 500nm SiO$_2$ layer was grown by 'wet' thermal oxidation of (100) Si in a quartz tube furnace (QTF), followed by 80keV Si$^+$ implantation to an areal density of 8×10^{16}cm^{-2}. The wafer was divided up and annealed in a *Jipelec Jetfirst* rapid thermal processing (RTP) unit in an N$_2$ ambient according to the *programmed* anneal times and temperatures in **Table 3-1**.

Sample set ID	Anneal Temperature, T_A ($^{\circ}$C)	Anneal time, t_A (s)
A$_1$	1050	3
A$_2$	1050	10
A$_3$	1050	50
A$_4$	1050	100
B$_1$	1100	1
B$_2$	1100	3
B$_3$	1100	5
B$_4$	1100	10
B$_5$	1100	50
B$_6$	1100	100
C$_1$	1150	3
C$_2$	1150	10
C$_3$	1150	50
C$_4$	1150	100
D$_1$	1200	5
D$_2$	1200	10
D$_3$	1200	50
D$_4$	1200	100

Table 3-1 RTP annealing conditions for sample sets A – D

All of the samples were subsequently annealed in an N$_2$:H$_2$ (5%) forming gas at 500°C for a further 10 minutes to reduce the 'dangling bond' Si-NC/SiO$_2$ interface defect density.

3.3.2 Cross-sectional Transmission Electron Microscopy (X-TEM)

In general, microscopy imaging of Si-NCs in SiO$_2$ is technically challenging on account of the similar atomic number and density of the two materials, which gives rise to a low phase contrast[132]. Whilst high resolution electron microscopy (HREM) images provide the detail required for studying individual nano-clusters, they are not as effective where statistical data on the Si-NC size and density distribution is required. For this study a more accurate and repeatable method, previously reported by Iacona *et al*[133] was implemented. Using a cross-sectional dark field (DF) imaging technique at relatively low magnification, it was possible to obtain a large number of Si-NCs in a single image. The resulting contrast arises due to the diffraction of the TEM beam only from nano-crystal planes that are aligned both with the TEM beam and the detection aperture. The random orientation of the nano-clusters means that this technique always yields an under-estimate of the *absolute* density. However, for *relative* measurements of the nano-cluster size and density distribution as a function of annealing time and temperature, this method provides adequate contrast at low magnification and enables accurate determination of the spatial distribution in the implanted layer. Moreover, the probability of detecting a nano-cluster using this technique is independent of the size, which is not the case for the equivalent conventional HREM imaging technique. In particular with HREM, variations in the sample thickness can lead to an inaccurate determination of the size distribution because thicker parts of the sample only reveal the largest nano-clusters due to the relatively poor signal to noise ratio. On the contrary, thinner areas favour the detection of smaller nano-clusters due to the potential opening up effect[134], where the fringe formation probability is proportional to the inverse nano-cluster size for a randomly chosen reflection angle.

In this study, cross-sectional DF images were obtained using a *Phillips* CM-12 TEM operating at 120kV, with the beam aligned with the <220> zone axis.

3.4   Results and discussion

3.4.1   Cross-sectional Transmission Electron Microscopy (X-TEM)

A selection of the X-TEM DF diffraction contrast images for annealing times in the range 1 to 100s at 1100°C and anneal temperatures in the range 1050 to 1200°C at 10s are shown in **Figure 3-3**.

(a)
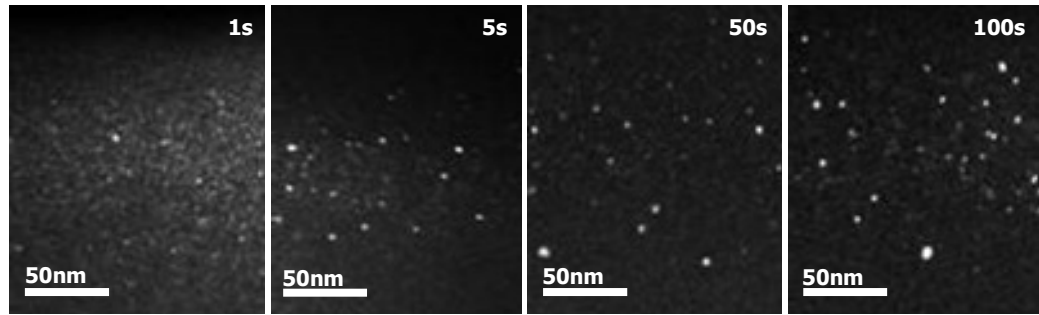
(b)
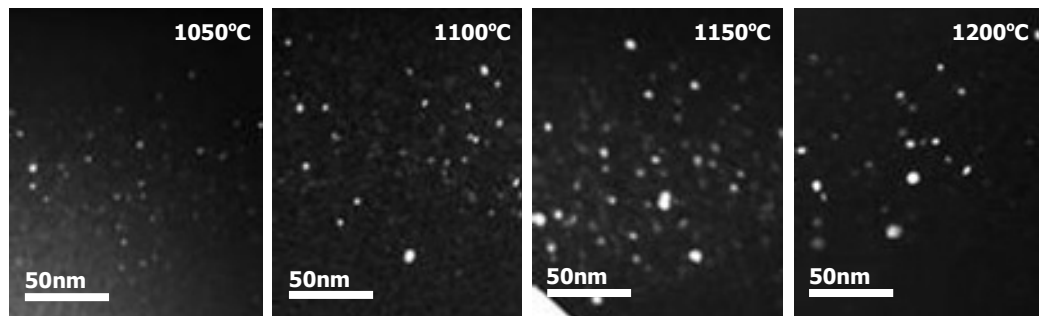
Figure 3-3 'Atlas' of X-TEM DF diffraction contrast images of RTP SRSO samples on (100) Si. Bright spots are Si-NCs aligned with the <220> zone axis. Annealing time and temperature ranges are (a) 1 to 100s at 1100°C and (b) 1050 to 1200°C for 10s respectively and the individual fields of view are 150nm across x 250nm high

It is immediately obvious from the TEM image 'atlas' of **Figure 3-3** that the Si-NC size, density and distribution in the matrix are affected by both annealing time and temperature. Images towards the right of the 'atlas' (long t_A or high T_A) reveal large, sparsely populated Si-NCs whereas those towards the left (short t_A or low T_A) appear to be smaller and more populous. In order to obtain a thorough statistical dataset, around 200 nano-clusters were examined in each image from which the size, density and depth (from the oxide surface) were determined. The uncertainty in estimating the nano-cluster diameter using this de-focussed imaging technique was previously estimated to be ~5% and the minimum detectable nano-

cluster diameter, which is limited by the resolution of the microscope is ~0.7nm[133]. Since the imaging conditions are orientation dependent, it is impossible to establish absolutely what fraction of the total population of Si-NCs is being viewed and so the absolute density could not be determined. However, we have been able to determine a relative Si-NC density based on the assumption that there is no orientation dependence on anneal time or temperature within our experimental range. This seems fair considering that diffraction rings (which are characteristic of polycrystalline material) rather than spots are typically reported, for example via reflection high energy electron diffraction (RHEED) measurements[135]. **Figure 3-4** and **Figure 3-5** show representative stack histograms obtained from the TEM image 'atlas' for the Si-NC size distributions as a function of the isothermal (1100°C) annealing time and isochronal (10s) annealing temperature respectively.
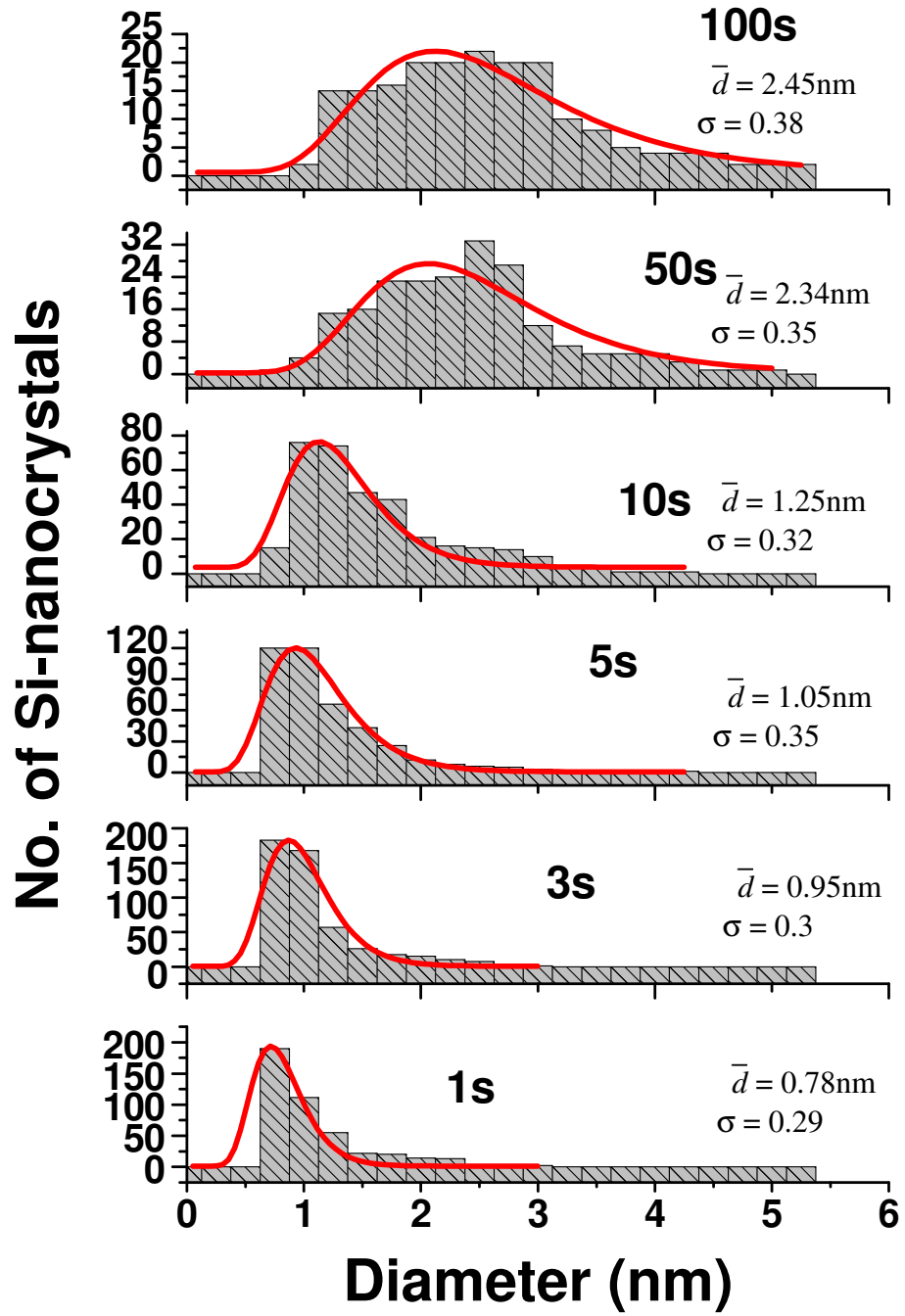
Figure 3-4 Si-NC size distribution as a function of anneal time in the range 1 to 100s at 1100°C (sample set B). The red lines are lognormal fits to the data
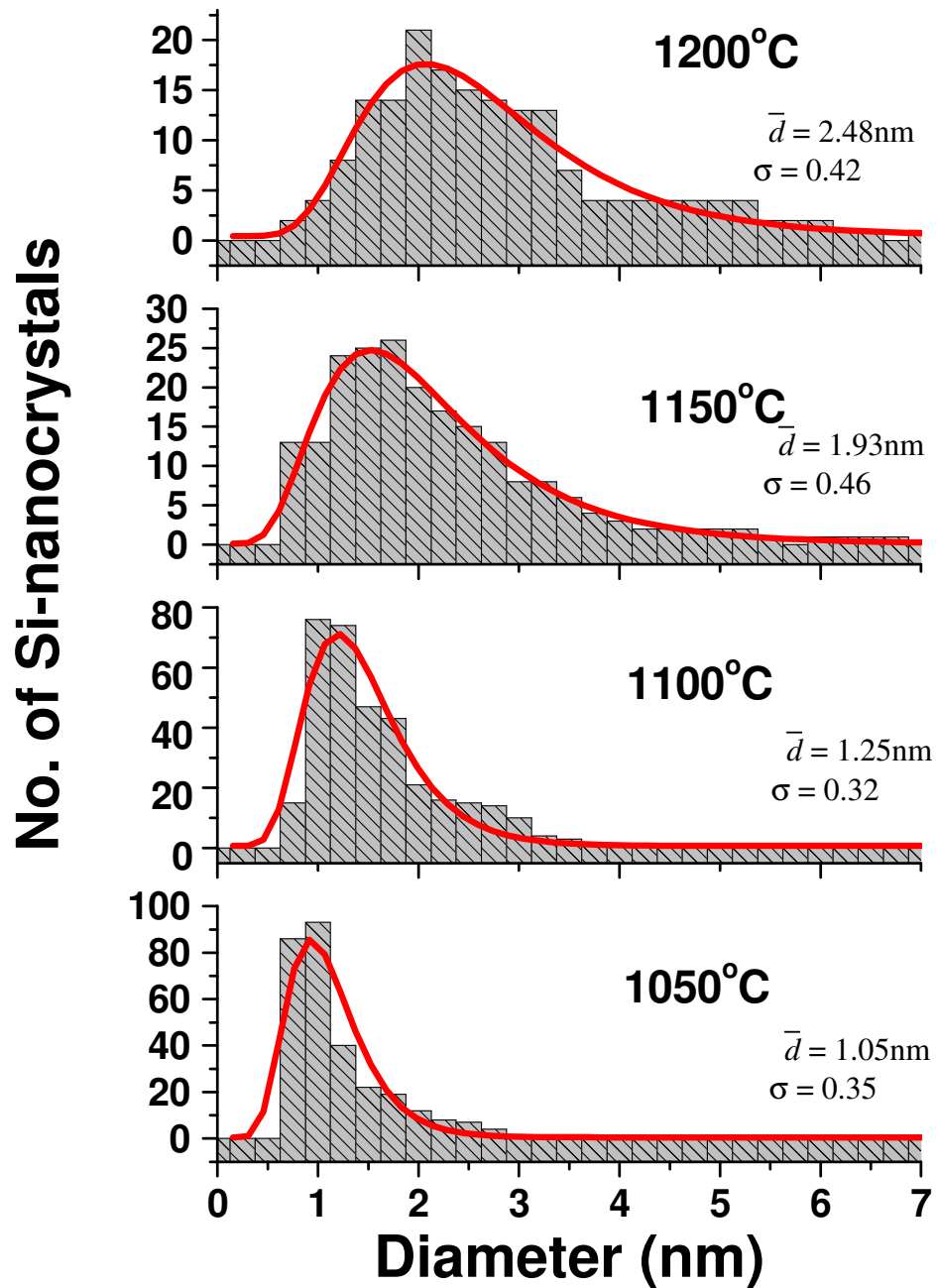
Figure 3-5 Si-NC size distribution as a function of anneal temperature in the range 1050 to 1200°C at 10s (samples A$_2$, B$_4$, C$_2$ and D$_2$). The red lines are lognormal fits to the data

The Si-NC mean diameter and relative precipitate density as a function of anneal time and temperature were extracted from the lognormal fits (red lines) in **Figure 3-4** and **Figure 3-5** and these values are shown in **Figure 3-6**.
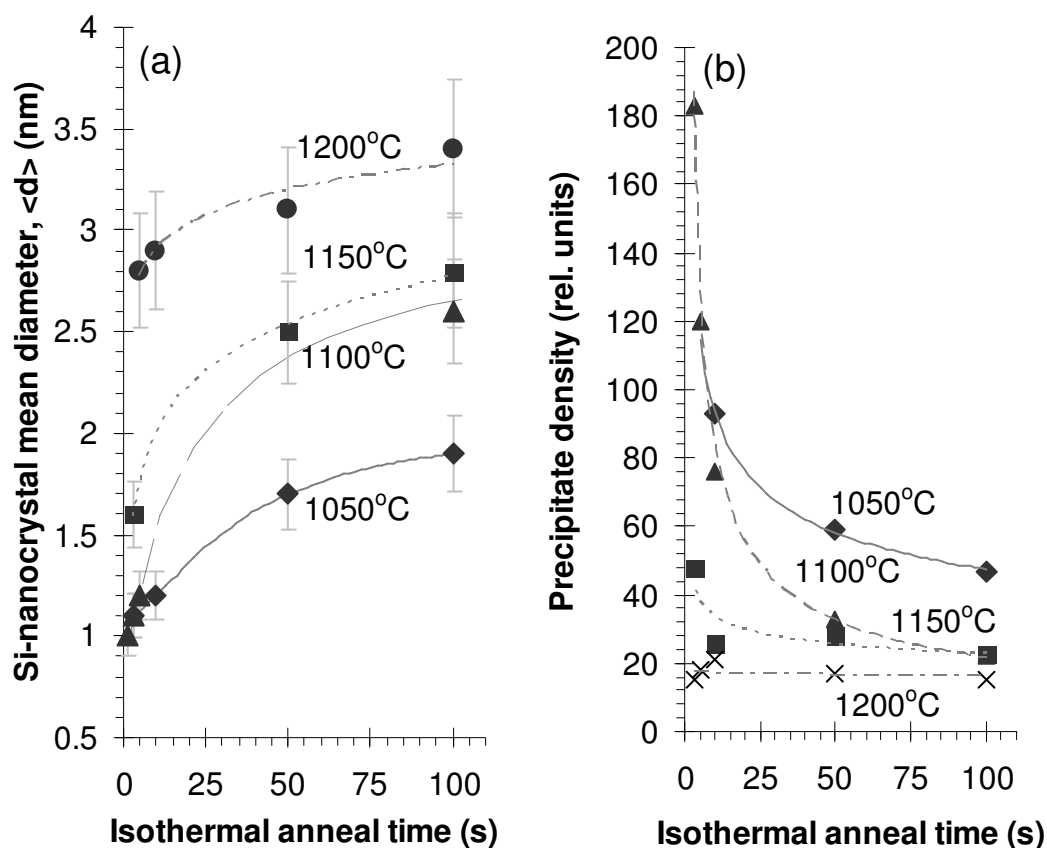
Figure 3-6 Evolution with annealing time of (a) the Si-NC mean diameter and (b) the relative precipitate density for different annealing temperatures. Lines are guides to the eye.

A sharp increase in the Si-NC mean diameter is observed in the first 10s of annealing, which is exactly correlated with a sharp fall in the precipitate density. For longer anneal times, the Si-NC growth and density tend towards asymptotic values within the first few minutes of annealing. Critically, these dynamics are a function of the annealing temperature with the rate of Si-NC growth increasing for higher temperatures. The observed change in precipitate density appears to be inversely proportional to the anneal temperature with much smaller changes detected for the highest anneal temperature. This counter-intuitive observation is likely explained by the fact that for the highest anneal temperature the precipitate density is already approaching an asymptotic limit within the experimental anneal time.

These observations are in precise accordance with the behaviour predicted according to a particle coarsening (or *Ostwald* ripening) model for a binary solution[126] with the end result being that the total number of nano-clusters decreases whilst the mean diameter increases with time. This occurs at a rate,

which is governed both by the initial excess Si concentration and the anneal temperature. Similar results were previously reported for the formation of germanium (Ge) precipitates in implanted SiO$_2$[136] as well as arsenic (As) precipitates in MBE grown LT-GaAs layers[137], indicating that these growth dynamics are generic to cluster precipitation.

If the growth of spherical precipitates is limited by the volume diffusion of Si atoms then the growth dynamics may be described by the Lifshitz–Slyozov-Wagner (LSW) theory[138]. Then, for a specific annealing temperature, the cube of the mean nano-cluster radius should evolve linearly with anneal time according to:

$$<r>^3 - <r_0>^3 = kt_A \tag{40}$$

Where $<r>$ is the mean cluster radius at time $t = t_A$, $<r_0>$ is the mean cluster radius at time $t = 0$ and k is the coarsening rate constant for a given temperature, which is proportional to the diffusion coefficient, D_{Si} and the Si surface energy, γ[126].

Figure 3-7 shows $<r>^3$ as a function of t_A for the different anneal temperatures employed during this study.
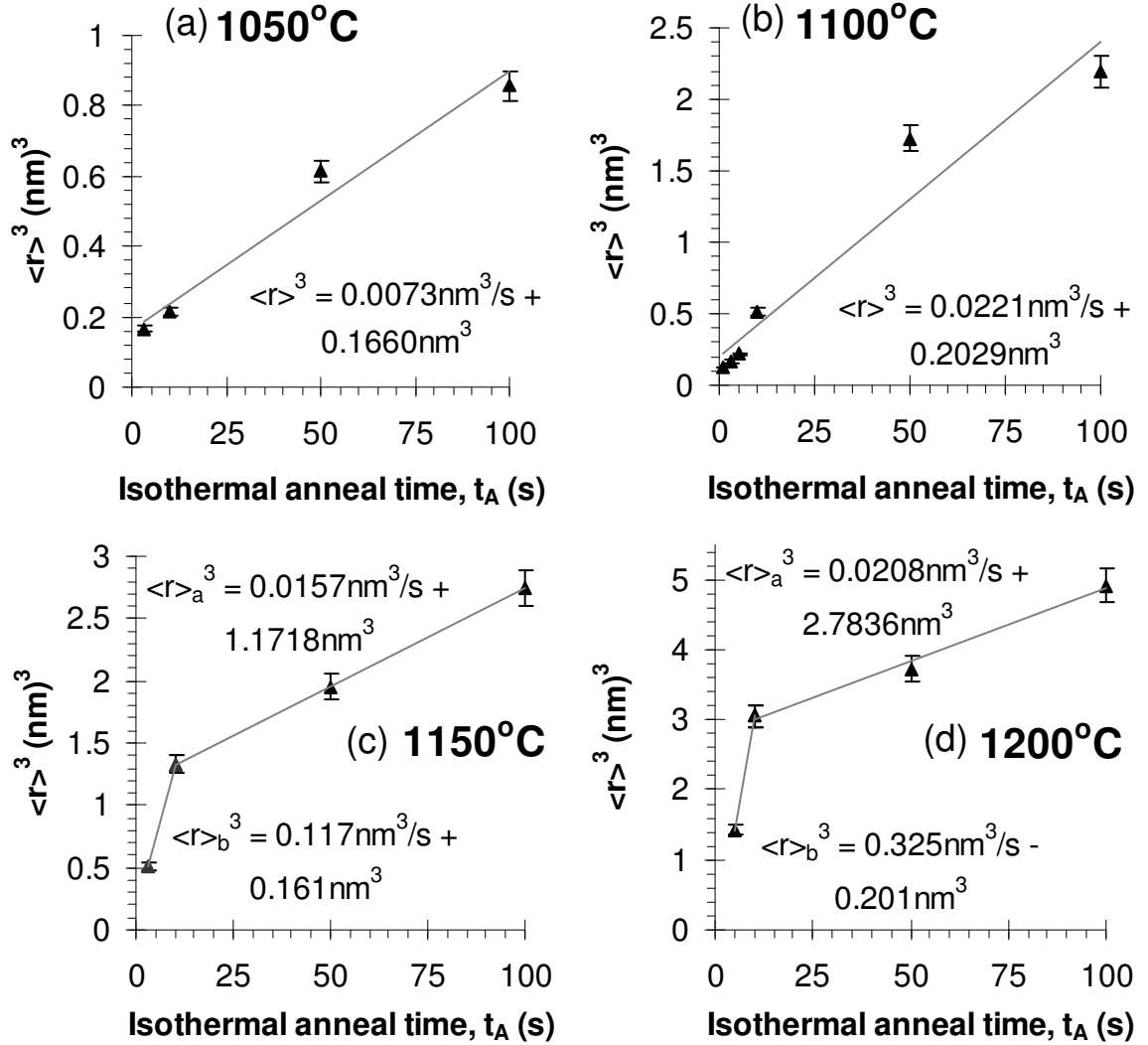
Figure 3-7 Evolution of the cube of the mean Si-NC radius with isothermal anneal time, t_A for T_A = (a) 1050°C (b) 1100°C (c) 1150°C and (d) 1200°C. The gradient of the fitted curves corresponds to the coarsening rate constant, k in equation (40)

For anneal temperatures ≤ 1100°C the data follows a straight line with a single coarsening rate constant, k in equation (40) obtained from the gradient of the straight line fits. We note however that for T_A > 1100°C the data can be described by two regimes, i) for t_A < 10s in which the cluster sizes grow rapidly and ii) for t_A > 10s where a much slower coarsening rate constant is obtained. The fact that the coarsening rate constant is reduced for t_A > 10s for high T_A therefore confirms that the nucleation and growth dynamics rapidly (< 10s) stabilize at higher annealing

temperatures, probably on account of the much larger diffusion coefficient, which increases exponentially with temperature[126].

Equation (40) may be written explicitly in terms of the anneal temperature[136], T_A giving:

$$<r>^3 - <r_0>^3 = \frac{1}{T_A}\exp\left(\frac{-E_A}{k_B T_A}\right)$$
(41)

Where E_A is the activation energy for precipitate formation and k_B is the Boltzmann constant. Hence $T_A(<r>^3 - <r_0>^3)$ follows an Arrhenius law and by plotting $Ln[T_A(<r>^3 - <r_0>^3)]$ as a function of the inverse anneal temperature as in **Figure 3-8**, we can extract the activation energy from the gradient.
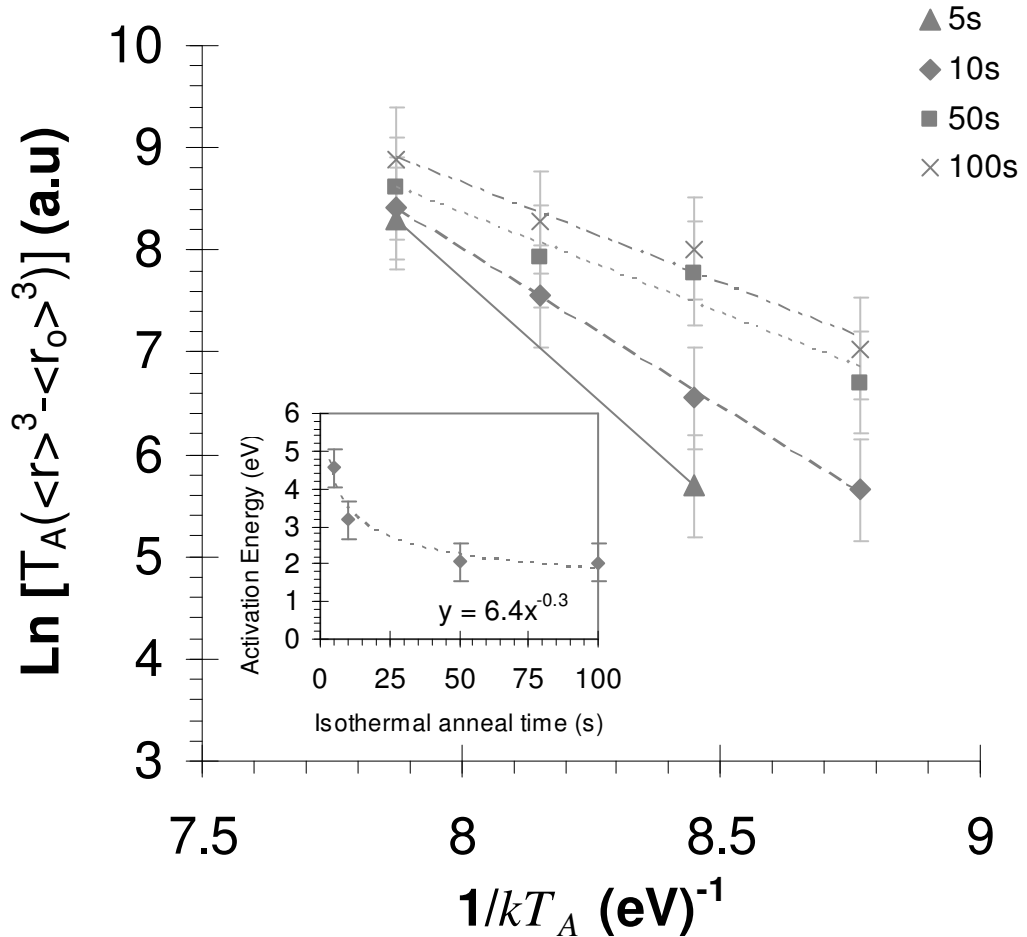
Figure 3-8 Arrhenius plot of Ln[$T_A(<r>^3 - <r_0>^3)$)] as a function of anneal temperature for a range of anneal times. Best fits to the data are straight lines, the gradient of which reveals the activation energy, E_A for Si-precipitate formation. Inset: Activation energy as a function of anneal time

We note that the value we obtained for the activation energy is always lower than the literature value of 4.8eV for Si self-diffusion in SiO$_2$[139]. In fact, the values we obtained are much closer in agreement with that reported by Bonafos *et al*[140], also for Si$^+$ implanted oxide but at a much later stage in the annealing cycle (2.87 ± 0.5eV at t_A = 16h). The inset of **Figure 3-8** suggests that the value for the activation energy may be a function of the annealing time, being monotonously reduced in the annealing time range up to 100s where it approaches an asymptotic value ~2eV. This is exactly the inverse behaviour of that reported for the activation energy of end-of-range (EOR) loop defects in ion implanted bulk Si[139]. In this case, values of 1 – 2eV were obtained at the beginning of the annealing cycle (t = 10s) and increased to 4.4eV for longer annealing times (> 100s). Values of ~2eV were also reported for the activation energy of oxygen interstitial defects[141] or Si self-interstitials[139, 142] in *c*-Si. Dzelme *et al*[141] reported activation energies for oxygen interstitial defects in the range 2.78 to 1.96eV depending upon the relative compression of the Si lattice parameter. This latter observation perhaps suggests that variations in the activation energy are attributable to lattice contraction during formation and crystallization of the nano-clusters.

In general, these results suggest that precipitate formation proceeds rapidly in the first few seconds of high temperature annealing, possibly assisted by the transport and/or removal of vacancy and interstitial defects left over by the ion irradiation. For longer annealing times the cluster growth slows, apparently entering a ripening stage during which the growth of larger clusters should coincide with the decomposition of smaller clusters. Evidence of the preferential Si-nanocluster nucleation at pre-existing defect sites in implanted oxides was already reported by Mokry *et al*[128] as we have shown in **Figure 3-2**. The authors of [128] presented TEM images and SRIM data that showed the Si-nanocrystal formation site to be perfectly coincident with the site of vacancies generated by the Si$^+$ irradiation. Statistical analysis of our X-TEM images also revealed a tendency for the Si-NC formation to migrate towards the surface of the oxide, i.e. in the irradiated region of the matrix with increasing anneal time, as illustrated by **Figure 3-9**.
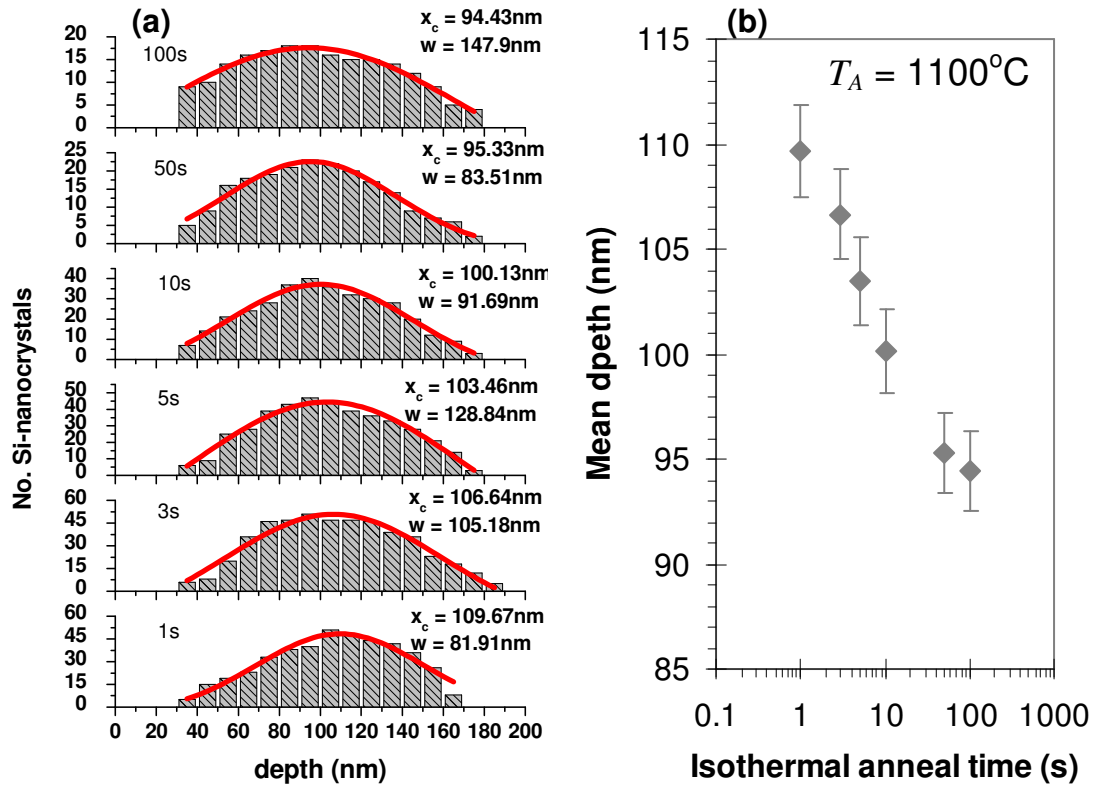
Figure 3-9 (a) Stacked histograms and Gaussian fits (red lines) representing the depth distribution and (b) mean depth of the Si-nanocrystals in the oxide films (determined from the Gaussian fits) as a function of annealing time at 1100°C as determined from the X-TEM images

The excess Si therefore exhibits a tendency to form clusters in the irradiated region of the matrix during thermal annealing according to an energetically favourable migration (enhanced diffusion) and nucleation process. The similar values we have obtained here for E_A compared to that reported in [140] suggests that the Si-nanocrystals are in the advanced stages of ripening even after just 10s of high temperature annealing. For fixed annealing conditions (t_A, T_A) and fixed Si excess concentration, these findings imply that the density and to some extent the size of Si-nanocrystals may be controlled by prior ion irradiation of the host matrix.

3.5   Conclusions

In summary we have shown using a TEM DF imaging technique, that the evolution of Si-nanocrystal size and distribution in ion implanted SiO$_2$ matrices may be described according to classical thermodynamics for binary solutions and fits with the LSW model, even in the early stages (first 100s) of high temperature annealing. We examined the evolution of the Si-nanocrystal size distribution with annealing and found this to be most accurately described by a lognormal distribution function, from which we obtained the mean diameter and approximate size distribution as a function of the annealing conditions.

From the evolution of the nano-cluster size with annealing we were able to determine values for the coarsening rate constant, which increased exponentially from 7.3x10^{-3}nm^{3}s^{-1} at 1050°C to 0.325nm^{3}s^{-1} at 1200°C for annealing times, t_A < 10s. However, for the highest annealing temperatures, > 1100°C we found that the coarsening rate is reduced for t_A > 10s, indicating that the nano-cluster growth rapidly stabilizes, particularly at high T_A. Calculation of the activation energy to precipitate formation revealed a temporal dependence in which the value fell from ~4.5 to ~2eV within the first 100s of annealing. Our observations lead us to conclude that the excess Si exhibits a tendency to form clusters in the irradiated region of the matrix during thermal annealing according to an energetically favourable migration (enhanced diffusion) and nucleation process. This process is likely assisted by the presence of vacancy and/or interstitial type point defects left over by the ion irradiation of the matrix. Further evidence for this preferential migration to pre-existing defect sites was found by examination of the depth distribution as a function of isothermal (1100°C) anneal time. We found that the mean depth of the clusters is proportional to the inverse anneal time, with a shift in position from ~110 to ~95nm (~14% change) below the oxide surface in the first 100s of annealing.

3.6   References

119. L. T. Canham, Applied Physics Letters **57** (10), 1046-1048 (1990).
120. T. R. Roschuk, J. Wojcik, E. A. Irving, M. Flynn and P. Mascher, presented at the Photonics North 2004: Optical Components and Devices, Ottawa, Canada, 2004 (unpublished).
121. V. Švrček, T. Sasaki, R. Katoh, Y. Shimizu and N. Koshizaki, Applied Physics B: Lasers and Optics **94** (1), 133-139 (2009).
122. N. Daldosso, M. Melchiorri, L. Pavesi, G. Pucker, F. Gourbilleau, S. Chausserie, A. Belarouci, X. Portier and C. Dufour, Journal of Luminescence **121** (2), 344-348 (2006).
123. M. Grün, P. Miska, E. Neu, D. Steinmetz, F. Montaigne, H. Rinnert, C. Becher and M. Vergnat, Physica E: Low-dimensional Systems and Nanostructures **41** (6), 998-1001 (2009).
124. J. H. Warner, H. Rubinsztein-Dunlop and R. D. Tilley, The Journal of Physical Chemistry B **109** (41), 19064-19067 (2005).
125. V. Jan, F. Anna, V. Frantiscaronek, A. Frantiscaronek, H. Jana, ccaron, ková, H. Martin, P. Ivan, Kate, rcaron, K. ina, uring, sová, D. ina and L. Jan, Advanced Functional Materials **18** (18), 2666-2672 (2008).
126. D. A. Porter and K. E. Easterling, *Phase Transformations in Metals and Alloys*, 2 ed. (Chapman and Hall, London, 1992).
127. D. J. Lockwood, *Device Applications of Silicon Nanocrystals and Nanostructures*. (Springer US, 2009).
128. C. R. Mokry, P. J. Simpson and A. P. Knights, Group IV Photonics, 2008 5th IEEE International Conference on, 268-269 (2008).
129. http://en.wikipedia.org/wiki/Gibbs%E2%80%93Thomson_effect.
130. B. H. Bransden and C. J. Joachain, *Introduction to Quantum Mechanics*. (Longman Group, London, 1989).
131. V. A. Belyakov, V. A. Burdov, R. Lockwood and A. Meldrum, Advances in Optical Technologies **2008**, 279502 (2008).
132. B. G. Fernandez, M. Lopez, C. Garcia, A. Perez-Rodriguez, J. R. Morante, C. Bonafos, M. Carrada and A. Claverie, Journal of Applied Physics **91** (2), 798-807 (2002).
133. F. Iacona, G. Franzo and C. Spinella, Journal of Applied Physics **87** (3), 1295-1303 (2000).
134. J. O. Malm and M. A. O Keefe, Ultramicroscopy **68** (1) (1997).
135. T. Feng, Y. Hongbing, M. Dicken, J. R. Heath and H. A. Atwater, Applied Physics Letters **86** (033103), 1 - 3 (2005).
136. C. Bonafos, B. Garrido, M. Lopez, A. Perez-Rodriguez, J. R. Morante, Y. Kihn, G. Ben Assayag and A. Claverie, Materials Science and Engineering B **69-70**, 380-385 (2000).
137. Z. Liliental-Weber, X. W. Lin, J. Washburn and W. Schaff, Applied Physics Letters **66** (16), 2086-2088 (1995).
138. I. M. Lifshitz and V. V. Slyozov, Journal of Physics and Chemistry of Solids **19** (1-2), 35-50 (1961).
139. C. Bonafos, D. Mathiot and A. Claverie, Journal of Applied Physics **83** (6), 3008-3017 (1998).
140. C. Bonafos, B. Colombeau, A. Altibelli, M. Carrada, G. Ben Assayag, B. Garrido, M. López, A. Pérez-Rodríguez, J. R. Morante and A. Claverie,

Nuclear Instruments and Methods in Physics Research Section B: Beam Interactions with Materials and Atoms **178** (1-4), 17-24 (2001).
141. J. Dzelme, I. Ertsinsh, B. Zapol and A. Misiuk, physica status solidi (a) **171** (1), 197-201 (1999).
142. K. Kato, Journal of Physics: Condensed Matter **5** (35), 6387-6406 (1993).

4   Optical characterisation of silicon nano-clusters in SiO$_2$

4.1   Introduction

In this chapter we present the results of a detailed optical characterisation of Si-NC samples on silicon prepared via ion implantation and rapid thermal annealing described in the previous chapter, an identical sample annealed for 1 hour and four samples prepared in a similar manner but on Al$_2$O$_3$ (sapphire) substrates. We find that the evolution of the ensemble PL and Raman spectra with annealing are extremely well correlated with the Si-NC size and distribution. Both the mean Si-NC size and distribution of sizes is a function of the annealing time and/or temperature and as a result, we find that for shorter anneal times and/or lower anneal temperatures, the PL spectra is both narrower and blue-shifted with respect to longer and/or higher temperature annealing. This observation is attributed to the fact that smaller Si-NCs exhibit a larger spatial confinement of the electron and hole wave-functions and a corresponding increase in the free exciton band gap. In general these results support a quantum confinement model in which the observed luminescence results in part from the annihilation of excitons at the Si-NC band-edge. However, in agreement with previously reported works[143-146], we note that the effect of the Si-NC size on the emission energy is much smaller than that predicted purely by the quantum confinement model, i.e. $E_{PL} \propto 1/d^2$ with d the nano-crystal diameter. This was previously attributed to lower confinement potentials arising from barrier finiteness[143], which can lead to an increase in the tunnelling probability between nano-crystals, particularly for samples containing a large density of Si-NCs. In addition, we found that the blue-shift with decreasing nano-crystal size is only observed for samples with a mean Si-NC diameter above ~2nm, i.e. further reducing the Si-NC mean diameter appears to have little or no effect on the peak emission energy. This suggests that, for the smallest Si-NCs, the luminescence may be dominated by an alternative recombination mechanism. For example, it is possible that surface related defect states formed within the band gap of small Si-NCs, i.e. the silicon-oxygen double bond (Si=O)[144, 145] act as efficient 'trapping' centres, between which electrons and holes can recombine radiatively but whose intra-gap energies exhibit much smaller dependence on the

Si-NC size. Indeed, similar observations were already reported for porous silicon (p-Si)[144] and oxidized Si-NCs[145].

The effect of SiO$_2$/Si-NC surface passivation on the luminescence using molecular hydrogen was assessed by post preparation forming gas (FG) annealing. We measured the Si-NC exciton related PL spectra for implanted samples pre-annealed for just 1s at 1100°C and post annealed in an N$_2$:H$_2$ (5%) mixture at ambient pressure at 500°C for a range of annealing times. We found good agreement between our measured data and that reported for Si-NC samples prepared via PECVD[147], notably that the PL intensity is improved by around an order of magnitude after the FG treatment and that there appears to be a selective passivation of centres emitting at longer wavelengths. We varied the FG annealing time from 0 to 3600s at 500°C and found that much of the observed PL enhancement was obtained in the first 100s, above which the luminescence intensity tends to an asymptotic limit. This is consistent with the rapid and efficient removal of non-radiative decay channels, the most likely candidate being the so-called 'dangling bond' type defect (P_b centre) at the Si-NC/SiO$_2$ interface where disorder and strain is likely to be most prevalent.

We also present the results of spectrally resolved photoluminescence transients, carried out in collaboration with the group of Dr. Tony Kenyon at the University College London, from which we calculated the Si-NC cross section and relative number of emitting Si-NCs as a function of emission energy. The cross section increases monotonically with energy across the emission spectrum whilst the relative density of emitting Si-NCs follows the spectral emission shape. This supports the hypothesis for exciton migration from small to large Si-NCs, i.e. excitation of small Si-NCs is more effective but emission tends to be dominated by the larger Si-NCs. The effect of excitation power on the steady state and transient luminescence from Si-NCs reveals a blue-shift in the emission spectrum and a monotonic decrease in the cross section with increasing excitation power. These observations are associated with a diminishing number of available states due to a saturation effect, specifically for centres emitting at longer wavelengths, i.e. large Si-NCs on account of their relatively slower decay dynamics compared to smaller Si-NCs emitting at shorter wavelengths.

The temperature dependence of the steady state nano-crystal luminescence is also presented and the data reasonably well described according to a simple

model proposed by Duong *et al*[148], which takes into account the effects of exchange splitting of the exciton levels into spin-singlet and spin-triplet states as well as two non-radiative carrier escape processes; via tunnelling at low temperature and thermal activation at higher temperatures.

Finally we examined the Raman spectra from Si-NC samples prepared on sapphire substrates as a function of the annealing conditions after Si$^+$ implantation and rapid thermal processing. The Raman spectra exhibit peak shifts and an asymmetric broadening to low frequencies similar to previously reported observations[149-153]. We used a modified phonon confinement model (PCM) to describe the observed Raman line-shape. By selecting an appropriate phonon confinement function, which describes a lognormal distribution of allowed optical modes due to the fact that we observe a lognormal distribution of Si-NC sizes, we could accurately replicate the measured spectra and extract values for the mean Si-NC size and distribution as a function of the annealing conditions. Excellent correlation was found for the size distributions obtained via Raman and those obtained from the size histograms associated with the X-TEM images in the previous chapter only for samples annealed for very short times or lower anneal temperatures, i.e. those containing the smallest Si-NCs. Samples annealed for longer times or at higher temperature, which yield both a larger Si-NC mean diameter and broader size distribution appear to exhibit a bi-modal distribution suggesting that solute continues to be extracted from the matrix to form Si-NCs for annealing times at least as long as 300s at 1100°C.

4.2   Experimental Details

4.2.1   Sample preparation

In addition to the samples described in the previous chapter, the optical characterisation of a further three sample sets is described in this chapter, all of which were prepared in collaboration with the groups of Prof. Russell Gwilliam at the Surrey ion beam centre and Prof. Andy Knights at McMaster University. The samples were prepared by 'wet' thermal oxidation of either single crystal (100) silicon or sputter deposited silicon (200nm) on Al$_2$O$_3$ (sapphire) substrates following the procedure described in Chapter 2. In all cases, the oxidation process was carried out at 1000°C for around 60 minutes, which yields SiO$_2$ films with a nominal thickness of ~500nm. This was followed by Si$^+$ implantation for a range of ion beam energies and areal densities as described by **Table 4-1**. Subsequently all of the samples were annealed in a *Jipelec jetfirst* rapid thermal processing unit in an N$_2$ ambient for a range of annealing times and temperatures also given in **Table 4-1**.

Sample set ID	Implant energy (keV)	Si areal density (cm^{-2})	Anneal Temp, T_A (^{o}C)	Anneal time, t_A (s)	FG anneal time, t_{FG} (s) at 500°C
E	80	8x10^{16}	1100	3600	600
F$_1$	40	1x10^{17}	1100	1	0
F$_2$	40	1x10^{17}	1100	1	100
F$_3$	40	1x10^{17}	1100	1	1000
F$_4$	40	1x10^{17}	1100	1	3600
*G$_1$	110	8x10^{16}	1100	10	600
G$_2$	110	8x10^{16}	1100	60	600
G$_3$	110	8x10^{16}	1050	120	600
G$_4$	110	8x10^{16}	1100	300	600

Table 4-1 Si implant and annealing conditions for sample sets E, F and G

---

* Samples in this set were co-implanted with Er$^+$ at 400keV to an areal density of 3x10^{15}cm^{-2}, the relevant optical characterisation of which is discussed in the subsequent chapter

4.2.2 Photoluminescence spectroscopy

To obtain the PL spectra for the samples described in the previous chapter, i.e. samples A to D (see **Table 3-1**, Chapter 3) and for sample E for the excitation power dependent luminescence study, photo-excitation was provided by a 50mW CW 405nm solid state *Coherent cube* laser diode. The laser was focused onto the sample position using a 40x microscope objective lens to a spot size determined, using a *Graticules Ltd* calibrated micro-scale (0.1in/100 lines) and *Panasonic Super Dynamic* charge coupled device (CCD) camera to be ~120µm in diameter. The laser power was measured at the sample position with a *Sensor-und Lasertechnik* LP20 pyrometer calibrated at 4.93V/W and a digital storage oscilloscope (DSO). The PL was collected con-focally, dispersed by a single 150 lines/mm grating in a 0.5m spectrometer and detected using an N$_2$-cooled Indium Gallium Arsenide (InGaAs) array detector.

In order to measure the dependence of the excitation power on the ensemble PL transient from sample E the laser was triggered using a *TTi* TG4001 40MHz DDS arbitrary function generator producing 300µs pulses with a 50% duty cycle. The PL was detected by a *Thor-labs* PDA36A-EC Si amplified detector positioned in the collection path of the optical axis and the time signals displayed and recorded on a *Tektronix* TDS220 100MHz 1GS/s digital real-time oscilloscope.

In order to study the effect of FG annealing on the PL spectra, samples in set F were excited using a 514nm Ar$^+$ laser at a nominal power of 40mW. The laser was focused using a 40x microscope objective lens and the PL collected con-focally in a backscattering geometry and dispersed in the *Renishaw* micro-Raman spectrometer by a single 1800 lines/mm grating and detected using a CCD camera.

For low temperature PL, sample E was mounted on the cold finger of a recycling Helium (He) cryostat. Photo-excitation was provided by a 375nm laser diode at 10.3mW, with an unfocussed spot size of ~3mm. The PL was collected via focusing optics and dispersed in a 1m monochromator arrangement by a single 600 lines/mm grating and detected using an N$_2$-cooled *Edinburgh Instruments* EI-L single channel Germanium (Ge) detector. The PL signal was modulated using an optical chopper and amplified using referenced 'lock-in' detection to improve the signal to noise ratio. The sample temperature was monitored via thermocouple and controlled via integrated heater element using an *Oxford Instruments* ITC 503

temperature controller. All of the spectra were corrected for the system response, which was characterized using a broad band tungsten lamp.

4.2.3   Spectrally resolved photoluminescence transients

Measurement of the spectrally resolved PL transients from samples in set G, conducted in collaboration with the group of Dr. A Kenyon at University College London (UCL), were obtained after optical excitation using the 476nm line of an Ar$^+$ laser. The laser was switched using a *Pockels* cell arrangement with a sub-microsecond resolution and the PL transients detected using an IR sensitive *Hamamatsu* photomultiplier tube. The transient waveforms were recorded on a digital storage oscilloscope (DSO).

4.2.4   Raman Spectroscopy

Samples in set G were excited using the 514nm line of an Ar$^+$ laser at a nominal power of 40mW. Raman spectra were collected con-focally in a backscattering geometry and dispersed using a single 1800 lines/mm grating in the Renishaw μ-Raman system. The signals were detected using a charge coupled device (CCD) camera. The signal to noise ratio was improved in our experimental arrangement by a combination of optimized CCD pixel array usage, increased exposure time and by averaging accumulated spectra over a period of several minutes. The background scattering signal from the sapphire was subtracted using a virgin section of substrate and all measurements were conducted at room temperature.

4.3   Results and discussion

4.3.1   Photoluminescence Spectroscopy

4.3.1.1 Effect of Si-NC size distribution on the PL spectra

Figure 4-1 shows the PL peak energy and FWHM as a function of the Si-NC mean diameter for samples in sets A to D described in the previous chapter.
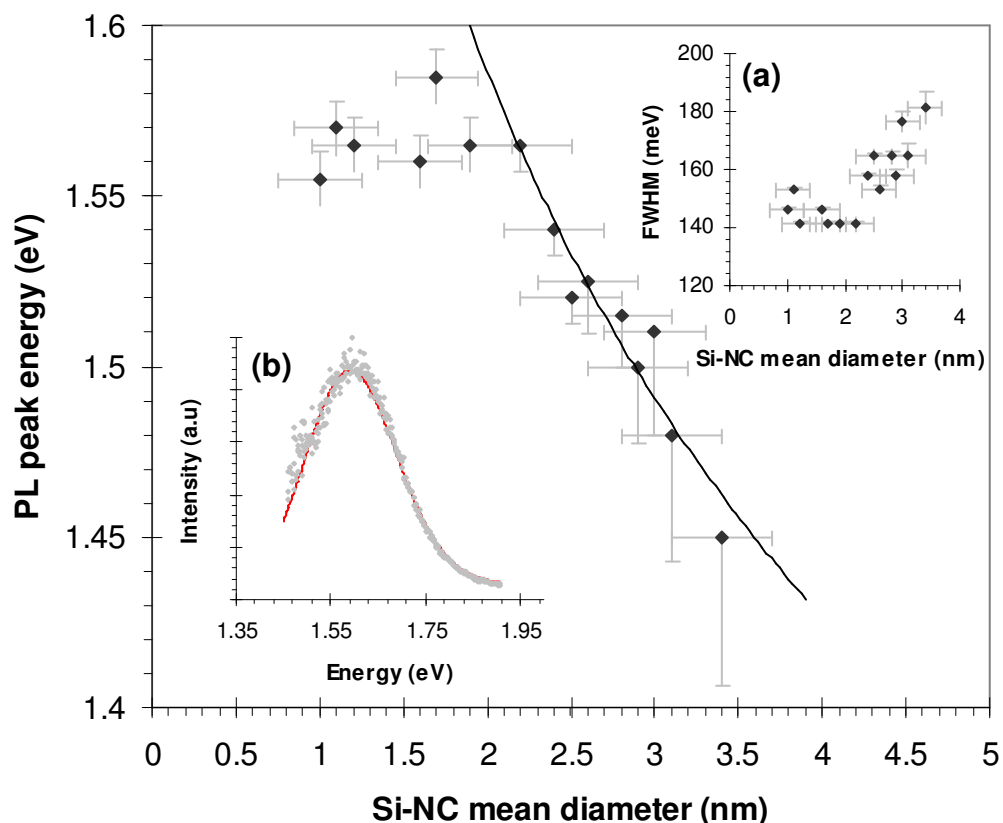
Figure 4-1 PL peak energy and inset (a) FWHM as a function of the Si-NC mean diameter (determined in the previous chapter from the TEM size histograms) for samples in sets A to D. The black line is a power law fit to the data points with $\overline{d} \geq 2$nm. Inset (b) shows a typical PL spectrum (sample A$_1$ – 1050°C, 3s) and the red line is a lognormal fit to the measured data.

All of the spectra in sample sets A to D were represented reasonably well by the lognormal function (red curves), the choice of which is justified by the phenomenological model developed by Islam and Kumar[154] (I-K). In that work, the PL line-shape was modelled by combining the effect of a lognormal Si-NC size distribution with a size dependent oscillator strength as well as emission resulting from recombination between localized surface states (LSS). The I-K model

assumes that, after excitation with a high energy photon, a portion of the photo-excited carriers relax non-radiatively to surface related 'defect-like' states within the forbidden gap before recombining radiatively. According to this model, for a constant $\bar{d}$, increasing σ results in a small red-shift in the PL peak and a large asymmetric broadening, specifically to higher energies. However, for a fixed σ the peak shift is a much stronger function of $\bar{d}$. The I-K model was also applied previously by Chen *et al*[155] to demonstrate the effect of structural order on the luminescence emission from nc-Si:H thin films.

We obtained peak emission energies, E_{peak} and standard deviations, σ_{PL} from the fits to our measured PL spectra for all samples in sets A to D using the standard lognormal function in Origin *V.6*, equation (42):

$$I_{PL} = I_{PL_0} + \frac{A}{\sqrt{2\pi}\sigma_{PL}E} \exp\left(-\frac{\ln\left(E/E_{peak}\right)}{2\sigma_{PL}^2}\right) \qquad (42)$$

The results indicate that as the isothermal anneal time is increased and particularly for the higher anneal temperatures, the peak shifts to lower energy. This is coupled with an increased asymmetric broadening to the high energy side. We know from our analysis of the TEM images in the previous chapter that both the mean crystallite size and distribution increase with annealing time and/or temperature, which confirms qualitatively the theoretical predictions of the I-K model. However, one cannot rule out a contribution to the higher energies from sub-nanometer particles because the imaging technique we described in the previous chapter relies specifically on the diffraction of the TEM electron beam from crystallites and is resolution limited to ~0.7nm. Indeed, evidence for high energy (1.65 – 1.95eV) light emission from amorphous silicon clusters in SiO$_2$ films was already reported[156, 157]. Additional contributions to emission broadening likely arise as a result of electron-phonon interactions as was previously reported by Sychugov *et al*[158] for single silicon quantum dots.

Figure 4-2 shows the standard deviation determined from the lognormal fits to the PL spectra as a function of that obtained from the lognormal fits to the TEM size histograms in the previous chapter.
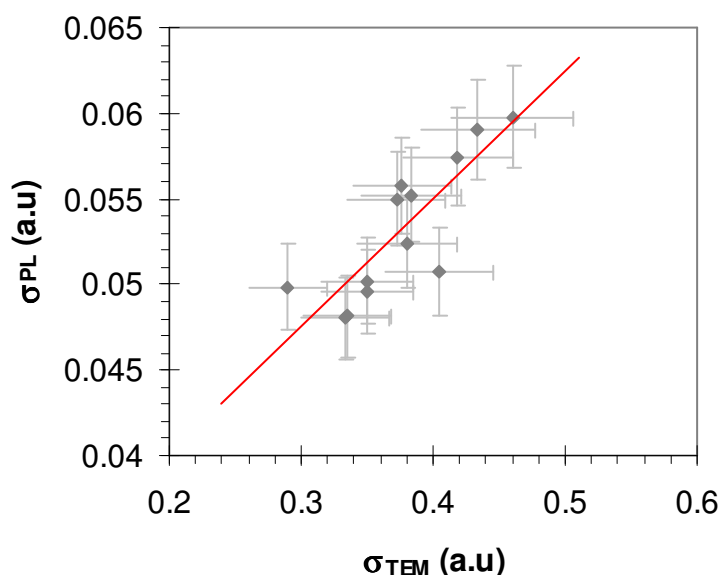
Figure 4-2 Standard deviation obtained from the lognormal fits to the PL spectra as a function of that obtained from the lognormal fits to the Si-NC TEM size histograms in the previous chapter. The red line is a best fit to the data illustrating the linear relationship between the spectral width and the Si-NC size distribution

It is clear from **Figure 4-1** that as the Si-NC size decreases, the band gap opens up and the PL emission energy increases, qualitatively in accordance with the quantum confinement of free electron and free hole states. **Figure 4-2** shows how the σ-value from the lognormal fit to the PL spectra varies with the σ-value obtained from the lognormal fit to the TEM stacked histograms in the previous chapter. Since the σ-value is related to the 'spread' or width of the distribution and the fact that the data in **Figure 4-2** can be described by a straight line, represents clear evidence that the line-width of the PL spectra is indeed a strong function of the Si-NC size distribution.

Despite these qualitative observations, the measured increase in emission energy for the range of Si-NC sizes we have examined is much smaller than expected from a pure quantum confinement perspective. For example, Ledoux *et al*[159] showed that their PL peak emission energy followed a $d^{-1.39}$ law in agreement with the theoretical predictions of Delerue *et al*[160] for a large range of Si-NC sizes. Whilst some deviation from the theoretical curve is notable for the PL from the

smallest Si-NCs they studied, the emission energy from similar size Si-NCs to those studied in this work are significantly higher (~400meV). This is likely explained by the differences in sample preparation, with Si-NCs obtained in [159] via pulsed laser pyrolysis of silane in a gas flow reactor, followed by a size selection via molecular beam discrimination using a chopper arrangement. They reported a narrow Si-NC size distribution of ~0.6nm using this technique but we note from our measurements that not only is the size distribution for the Si-NCs prepared by ion implantation and rapid thermal annealing always larger than this but it increases with annealing time and/or temperature from ~0.68nm at 1100°C, 1s to ~1.02nm at 1200°C, 50s. We note from the theoretical predictions of the I-K model[154] that a much stronger dependence of the PL emission on Si-NC mean diameter is obtained when the size distribution remains fixed. However, for a fixed mean Si-NC diameter, increasing the size distribution tends to lead to red-shifts in the PL peak.

We also note from our data that the emission energy is virtually unchanged for Si-NC sizes below ~2nm, suggesting that the observed luminescence is not purely due to free exciton annihilation, particularly for the smallest Si-NCs. Similar observations to ours were previously reported for porous silicon (p-Si)[144] and oxidized Si-NCs, either after ageing in air[145] or by post-preparation annealing in oxygen[146]. Wolkin *et al*[144] suggested that for hydrogen terminated Si-clusters the recombination should be via free excitons for all sizes of Si-NC and the increase in emission energy should tend towards that predicted by a rigid quantum confinement model, i.e. $E_{PL}(d_{nc}) \propto 1/d_{nc}^2$. However, for oxygen terminated nanocrystals, stabilized intra-gap states can form as a result of the presence of silicon oxygen bonds such as the silicon oxygen double covalent bond (Si=O) or the silicon-oxygen-silicon (Si-O-Si) bond at the nano-cluster surface. The authors in [144] proposed three different recombination mechanisms for oxygen terminated nano-clusters, the relative contribution of each being a strong function of the Si-NC size. These are designated zones I, II and III in **Figure 4-3**.
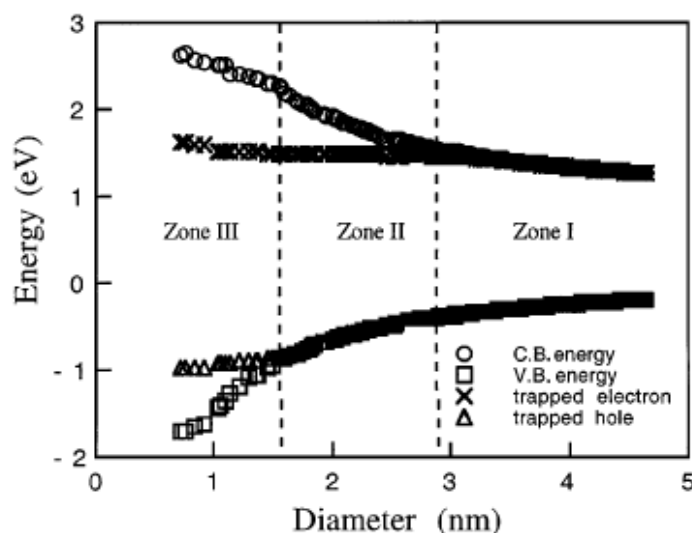
Figure 4-3 Electron and hole states in Si nanocrystals as a function of size and surface passivation. The trapped electron and hole states are p-states respectively localized on the Si and oxygen atoms of the Si=O bond, reproduced from [144]

In zone I, the energy of the stabilized Si=O surface state is larger than the exciton band gap and so emission always results from the annihilation of free excitons, regardless of the surface terminating species. In zone II the emission is dominated by the recombination between a trapped electron state and a free hole so that as the Si-NC size decreases, the emission energy still increases but at a much smaller rate compared with zone I. In zone III the emission results from the recombination of trapped electrons *and* trapped holes (trapped excitons) and so the emission energy is unchanged for Si-NC sizes below ~1.7nm. Such a model perhaps explains our observations, with the emission either resulting from recombination between trapped electron and free hole states for Si-NCs in the range 2 to 3nm and from the annihilation of trapped excitons for Si-NCs below 2nm. This suggests that despite the hydrogen passivation treatment (N$_2$:H$_2$ (5%), 500°C, 10 minutes) employed in our sample preparation procedure, a significant fraction of the Si-NCs in our samples may still be terminated by oxygen.

An additional explanation for the observed shallow increase in emission energy may also be due to stress effects at the SiO$_2$/Si-NC interface. Hofmeister *et al*[161] reported that the lattice plane fringes of Si-NCs can vary by as much as ~2% compared with bulk Si. This variation in the lattice parameter is due to the force exerted on the Si-NCs by the oxide and the direction of the force critically depends

on the nano-cluster size. The authors in [161] showed that for nano-clusters $\geq$ 3nm, the lattice parameter contracts relative to the bulk Si value but for smaller nano-crystals it expands. Indeed both tensile[162] and compressive[163] stresses resulting in red and blue shifted Raman TO phonon lines respectively were also reported in silica films containing Si-NCs. Such interfacial stresses can manifest in shifts as large as 250meV[164] in the observed PL emission energy and may result in larger Si-NCs exhibiting higher (and smaller Si-NCs lower) than expected emission energies, culminating in a suppression of the anticipated increase in emission with decreasing Si-NC size.

Figure 4-4 shows the evolution of the integrated PL intensity with anneal time for the experimental range of anneal temperatures.
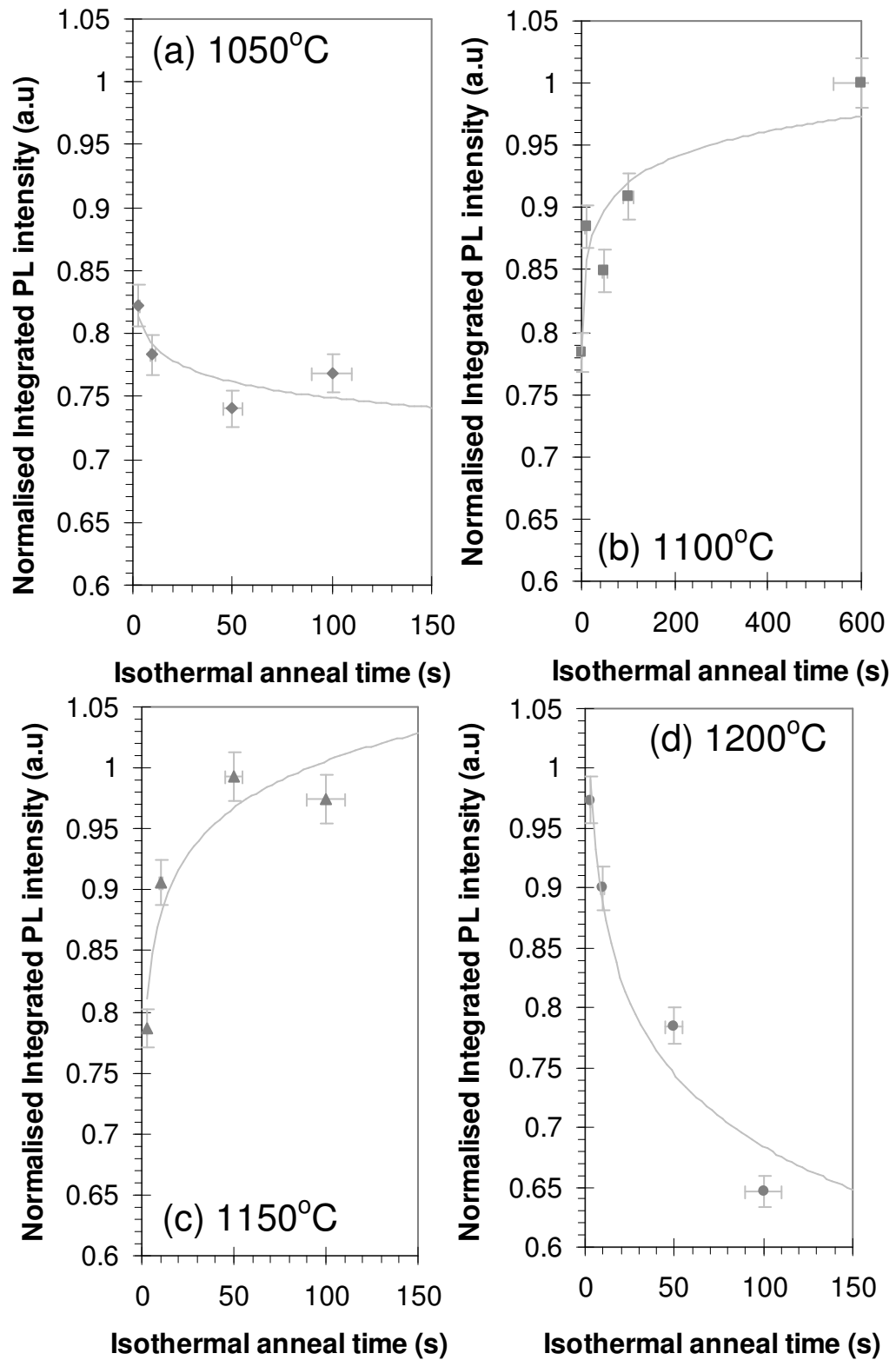
Figure 4-4 Evolution of the integrated PL intensity with isothermal anneal time, t$_A$ for T$_A$ = (a) 1050°C (b) 1100°C (c) 1150°C and (d) 1200°C. Data are normalised to the point corresponding to t$_A$ = 600s at 1100°C

At the lowest anneal temperature (1050°C) there is very little change in the PL intensity over the experimental anneal time frame. Samples annealed at 1100 and 1150°C exhibit a relatively sharp increase in the PL intensity in the first 20s before tending to an asymptotic level after ~50 to 100s. This is consistent with the rapid nucleation and Si-NC growth stage. Exactly the inverse behaviour is observed for the samples annealed at the highest temperature, 1200°C where the PL is monotonously quenched in this anneal time range. These results suggest that the PL yield is a complex function of the relative defect and Si-NC densities as well as the Si-NC size. Thus, for the lowest anneal temperature, the Si-NC formation and defect removal process proceeds relatively slowly presumably due to the lower diffusion coefficient[165]. The density of clusters remains relatively high however and so there are sufficient numbers of luminescent centres to compete with the non-radiative defect density. As the anneal temperature is increased to 1100°C, the formation of defect free Si-NCs evidently proceeds more quickly and the Si-NC luminescent fraction increases. This pattern continues up to 1150°C but for the highest anneal temperature (1200°C), the largest PL yield is observed for the shortest anneal time, presumably due to the much faster formation of defect free Si-NCs on account of the much larger diffusion coefficient. However, the Si-NC growth increases rapidly and their density is consequently diminished as a result of Ostwald ripening, both of which adversely affects the PL yield. According to these observations, the asymptotic level for the PL yield should then be a function of the Si excess concentration for fixed annealing conditions. To obtain the largest PL yield for a given Si excess concentration, this result suggests that there exists an optimum anneal time that is inversely proportional to the anneal temperature.

4.3.1.2 Effect of forming gas annealing on the Si-NC PL – molecular hydrogen passivation

A number of authors have studied the effect on the luminescence of hydrogen incorporation into silicon rich oxide films containing Si-nanocrystals, either by annealing in a forming gas (FG), usually an Ar:H$_2$ (5%)[147, 166] or N$_2$:H$_2$ (5%)[167] mixture or via plasma based hydrogen atom treatment (HAT)[168]. Increases in the PL intensity ranging from factors of 3 to 10 were typically reported after hydrogen incorporation and this is largely attributed to the passivation of electronically active P_b centres, the so called 'dangling bond' defects. We studied the effect of molecular hydrogen incorporation into our silicon rich (~7 at. % excess) oxide films containing small ($\overline{d}$ ~ 1nm) Si-nanocrystals formed after just 1s of *programmed* annealing at 1100°C in a rapid thermal processing unit. The dangling bond defect density in a-Si thin films[169] and oxide films containing Si-NCs[170] is known to be monotonically reduced with increased FG annealing temperatures up to ~500°C but increases again for higher temperatures, presumably due to the thermal dissociation of the Si-H bond[170]. Indeed the hydrogen passivation process is known to be completely reversible by annealing at relatively high temperatures, above ~600°C in a hydrogen free atmosphere[170]. We fixed the annealing temperature at 500°C and varied the annealing time in an N$_2$:H$_2$ (5%) FG in the time range: 0, 100, 1000 and 3600s. The effect on the luminescence spectral intensity and shape is shown in **Figure 4-5**.
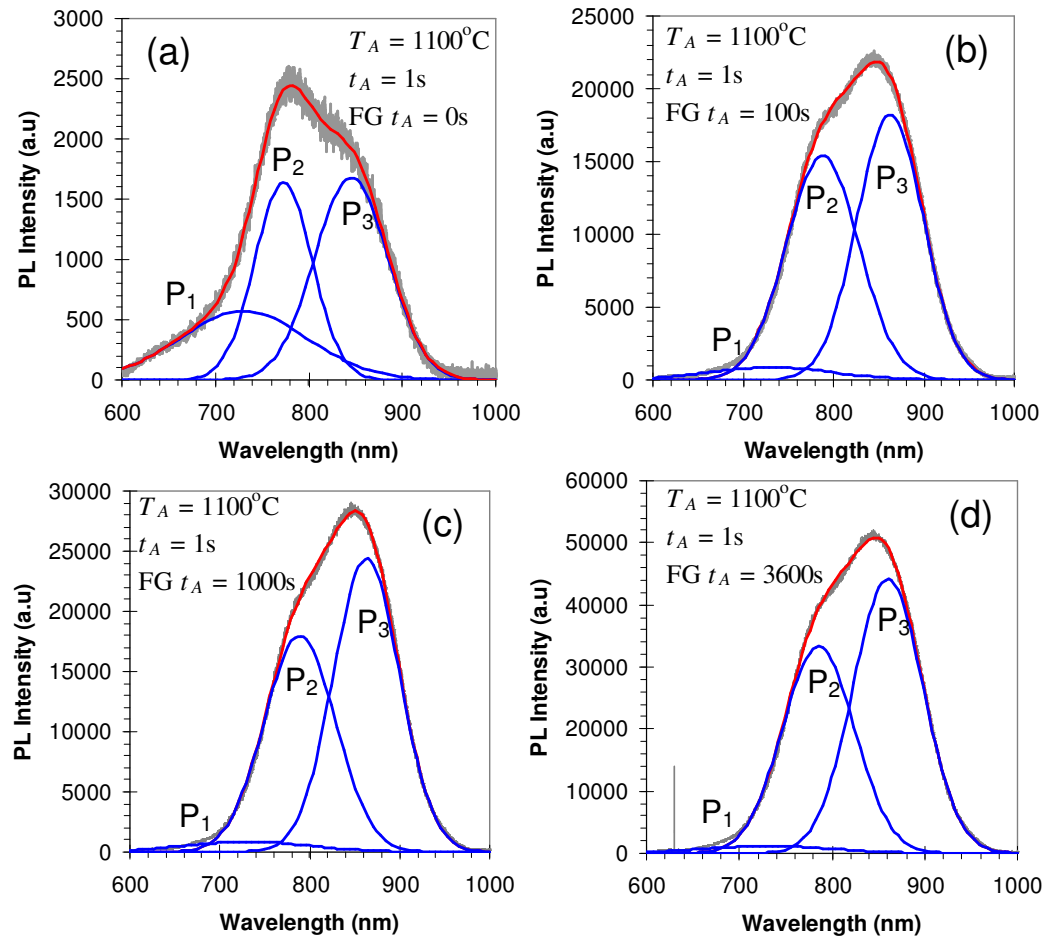
Figure 4-5 Si-NC RT PL spectra after pre-annealing for 1s at 1100°C followed by FG annealing at 500°C for (a) 0, (b) 100, (c) 1000 and (d) 3600s. The underlying blue curves, P$_1$ to P$_3$ are Gaussians extracted from a multiple Gaussian fit (red curve) to the measured data (grey lines)

Multiple Gaussian fits to the spectra are shown (red curve) with the underlying peaks denoted by the blue curves and labelled P$_1$ to P$_3$. The peak of the spectrum for the sample without FG annealing is ~750nm (P$_2$) with a large shoulder centred ~850nm (P$_3$) and a much smaller high energy shoulder centred ~730nm (P$_1$). After FG annealing for just 100s, the intensity of peaks P$_2$ and P$_3$ is increased by a factor of 10 whilst that of P$_1$ approximately doubles in intensity. We also note that the spectrum is now dominated by the long wavelength peak, P$_3$. Increasing the FG annealing time above 100s has a much less dramatic effect, with the intensity of peaks P$_2$ and P$_3$ increasing by a further factor of 2 as the annealing time is increased to 1 hour. P$_1$ increases by ~20% in the same annealing time range. The integrated PL intensity of peaks P$_1$ to P$_3$ as a function of isothermal (500°C) anneal time in the FG is shown in **Figure 4-6**.

121
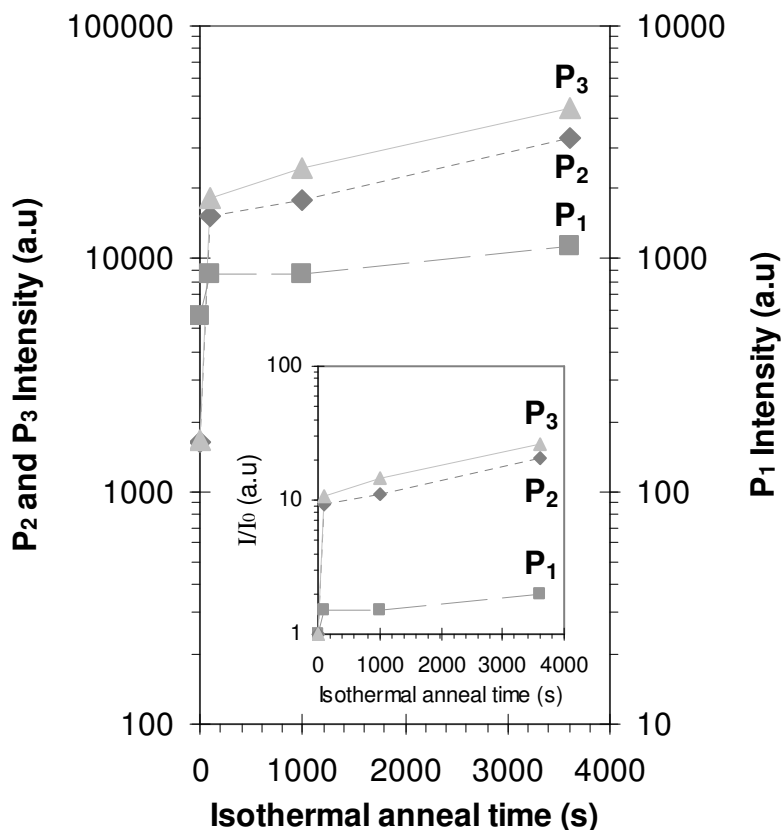
Figure 4-6 Integrated intensity of peaks P_1 (squares), P_2 (diamonds) and P_3 (triangles) as a function of isothermal (500^oC) FG anneal time. The inset shows the relative increase in the integrated intensity with FG anneal time for all of the peaks.

The dynamic behaviour of low temperature annealing in FG is very similar to that observed for the increase in PL intensity during high temperature annealing, i.e. a rapid increase followed by the tendency to an asymptotic level. This suggests that the two processes have a similar effect on the non-radiative, electronically active defects. At high temperatures (1000 to 1200^oC) this likely corresponds to reorganisation of the matrix during nanocrystal formation whilst the lower temperature annealing in hydrogen is indicative of the in-diffusion of hydrogen that occupies the remaining un-bonded atomic sites, likely those at the Si-NC/SiO_2 interface. Pellegrino *et al*[171] previously reported the correlation between the Si-NC PL intensity with electron spin resonance (ESR) signals associated with the interfacial dangling bond defect as a function of the annealing time at 1100^oC in N_2. They reported that the ESR signal initially increased in the first 30 minutes of high temperature annealing, reflecting an increase in the dangling bond defect density. The ESR intensity was then monotonically reduced with increased

annealing time up to ~500 minutes where it reached an asymptotic minimum. The PL intensity correspondingly reached an asymptotic maximum after the same anneal time. With regards the low temperature annealing in FG, Wilkinson *et al*[170] reported a rapid reduction in the ESR signal related to the density of P_b centres, the rate of which increased monotonically with annealing temperature in the range 305 to 510°C. Similar to our result, they reported an order of magnitude enhancement in the PL intensity after annealing in molecular hydrogen. The slightly larger enhancements observed in the current sample set could be due to the differences in the high temperature pre-FG annealing history. In [170] the high temperature treatment was for 1 hour at 1100°C, whereas in the present study for samples in set F we employed a rapid (1s) treatment at 1100°C. The latter likely leaves behind a larger density of electronically active dangling bonds at the Si-NC/SiO$_2$ interface, whilst the effectiveness of the FG annealing means that remaining dangling bonds are still terminated by molecular hydrogen on similar timescales. Whilst the longer treatment at high temperature reported in [170] means that there are fewer defect sites at which the molecular hydrogen can bond, if the final luminescence yield only depends on the dangling bond defect density, then in terms of thermal budget, it is much more efficient to employ short, high temperature treatments followed by longer, lower temperature FG treatments. The authors in [170] also compared the luminescence intensity after treatments in molecular hydrogen (H$_2$) with that after atomic hydrogen (H) treatment using an *alneal* process. They reported that the latter was able to provide a further factor 2 enhancement to the luminescence yield and suggested the existence of a subset of electronically active defects that may not be reactive with molecular hydrogen.

With regards the spectral shape reported in **Figure 4-5**, we note an apparent preferential enhancement of underlying luminescent centres emitting towards longer wavelengths. It was previously shown by Comedi *et al*[147] via x-ray diffraction (XRD) that the low temperature FG annealing does not lead to changes in the Si-NC size distribution. It is tempting to conclude then that larger Si-NCs, which would contribute to longer wavelengths of the PL spectrum due to a reduced exciton band gap are preferentially passivated by hydrogen, as was previously proposed[172]. However, an alternative explanation is that the long wavelength contributions to the luminescence spectrum are related to the recombination of trapped excitons at shallow defect states arising from strained or disordered Si

bonds at the Si-NC/SiO$_2$ interface[147]. Indeed the presence of an amorphous and therefore disordered transition region forming a shell around the crystalline core of the nanocrystals was already proposed[151, 173]. If the presence of such regions at the interface of Si-nanocrystals is independent of their size, then the preferential increase in long wavelength emissions is simply indicative of the passivation of dangling or strained bonds at the Si-NC/SiO$_2$ interface and does not necessarily pertain to any specific sub-set of nanocrystal sizes.

4.3.1.3 Spectrally resolved photoluminescence transients

The evolution of the luminescence intensity with isothermal anneal time is suggestive of the removal of non-radiative decay pathways. The observed luminescence intensity, I_{PL} is related to the observed luminescence lifetime, τ_{PL} according to the relation:

$$I_{PL} = \frac{N}{\tau_{PL}}$$

(43)

Where N is the concentration of emitters, in this case Si-NCs (or luminescent centres related to the Si-NCs, i.e. surface states). At room temperature, τ_{PL} is comprised of both radiative and non-radiative decay processes, characterised by lifetimes, τ_R and τ_{NR} respectively such that:

$$\frac{1}{\tau_{PL}} = \frac{1}{\tau_R} + \frac{1}{\tau_{NR}}$$

(44)

Assuming τ_R to be constant for a given size Si-NC with a band gap that corresponds to emissions at a specific wavelength, λ_{PL} and that typically $\tau_R \gg \tau_{NR}$[174], then reducing the number of non-radiative decay pathways ought to result in an increase in the observed PL lifetime, τ_{PL} measured at a specific wavelength, λ_{PL}. In order to corroborate this assertion, we measured the PL intensity and decay transients as a function of wavelength for four samples prepared on Al$_2$O$_3$ substrates (sample set G). Luminescence decay transients from Si-NCs are typically multi-exponential and have been analysed previously using the *Kohlrausch* or stretched exponential function of equation (45)[175]:

$$I_{PL}(t) = \exp\left(\frac{-t}{\tau}\right)^{\beta} \qquad\qquad (45)$$

Where $I_{PL}(t)$ is the PL intensity at time, t, τ is a characteristic (but not necessarily average) lifetime and β is usually referred to as the dispersion (or stretching) parameter having values between 0 and 1 (where $\beta = 1$ corresponds to a single exponential).

The observation of the stretched exponential describing luminescence transients associated with Si-NCs is interpreted as a superposition of single exponential decays with different lifetimes and may therefore be indicative of the presence of a distribution of lifetimes. This may arise specifically from large variations in non-radiative lifetimes associated with the 'trapping' (and release) of carriers at interfacial defect sites[176]. Alternatively, the stretched exponential may be indicative of the migration and trapping of excitons through a system of randomly distributed and possibly interconnected nano-crystals[177]. This latter assertion is tenuous however because Guillois *et al*[178] showed that the presence of the stretched exponential decay was independent of the Si-NC density in their study. Without loss of generality to the debate and assuming that the quantum confinement model is largely responsible for the observed PL emission energy, then measurement of the luminescence transient at a specific wavelength ought to sample Si-NCs of the same size. This being the case, one should not expect to find large variations in the radiative lifetime, τ_R. The fact that the stretched exponential persists even for single wavelength measurements then supports the existence of a wide distribution of non-radiative lifetimes even for similar size Si-NCs, which likely dominates the observed PL transients, particularly at room temperature.

We measured the rise and decay transients for samples in set G and fitted each curve with the stretched exponential function of equation (45) to obtain characteristic lifetimes and β-values for a range of wavelengths across the emission spectra. Example rise and decay transients along with their fitted curves for sample G$_4$ (1100°C, 300s) are shown in **Figure 4-7**.
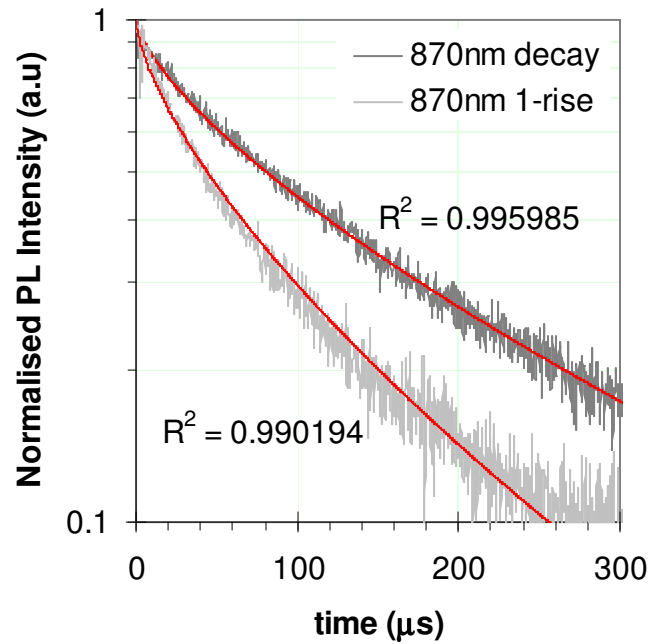
Figure 4-7 Measured PL rise (1-intensity) and decay transients measured at 870nm for sample G$_4$ (1100°C, 300s) along with their fitted curves (red lines) using the stretched exponential of equation (45). The accuracy of the fits is given by the R^2-values.

Figure 4-8 shows the characteristic rise and decay times and corresponding β-values obtained from the fits all as a function of the mean Si-NC diameter determined according to the annealing conditions (t_A, T_A) for each sample in set G.
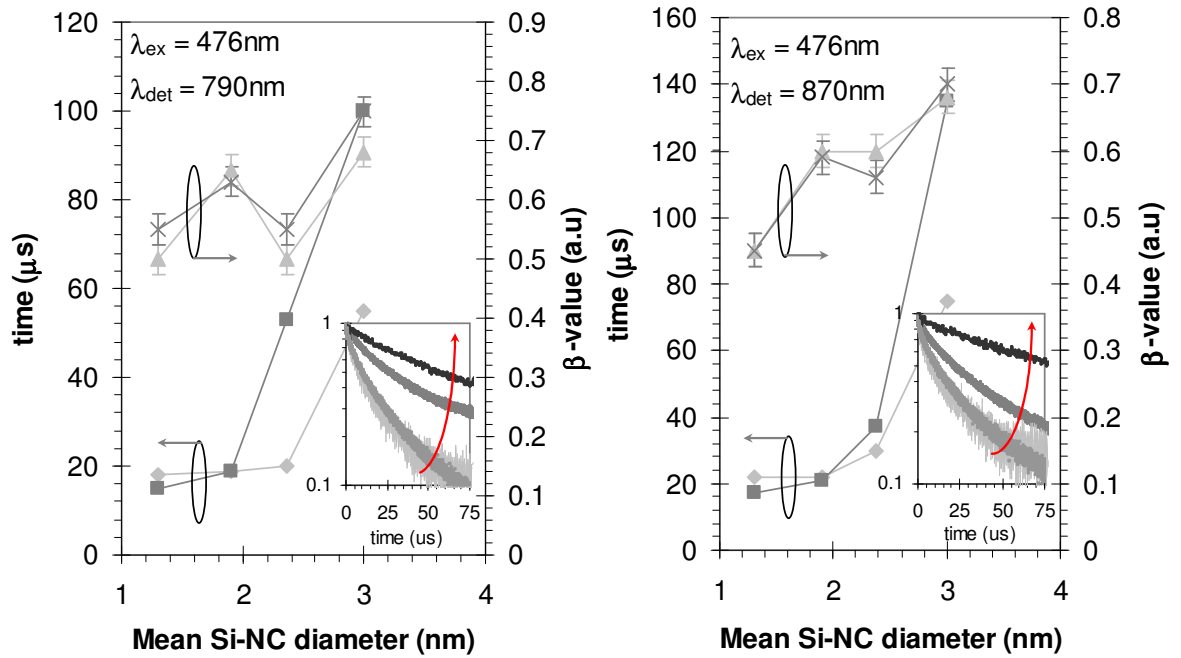
Figure 4-8 PL rise time (diamonds), decay time (squares), rise β (triangles) and decay β (crosses) as a function of the Si-NC mean diameter for sample set G at two different detection wavelengths, 790 and 870nm. The insets show the normalised decay transients, the characteristic lifetime of which increases with thermal budget as shown by the red arrows. Lines are guides to the eye.

The observed patterns in the PL transients are likely explained by a complex combination of the gradual removal of non-radiative decay channels and a gradual increase in the mean Si-NC diameter, both of which would result in an increase in the measured lifetime with annealing. Indeed the increase in PL intensity with increasing thermal budget is extremely well correlated with the increase in the measured lifetime for all detection wavelengths across the PL spectra as shown in **Figure 4-9**.
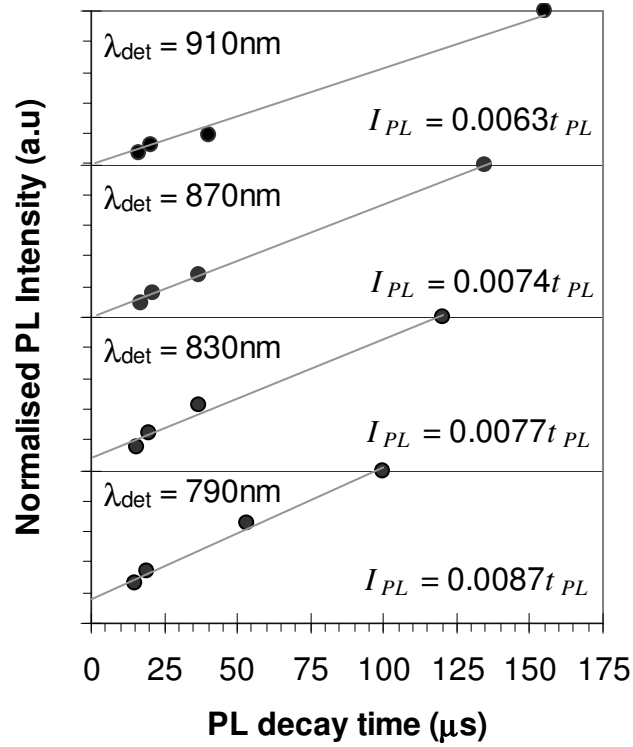
Figure 4-9 Normalized PL intensity (offset for clarity) as a function of the measured decay lifetime for a range of wavelengths across the PL emission spectra for sample set G

This result confirms that the contribution from τ_{NR} to the observed PL is diminishing with anneal time, as expected due to the removal of non-radiative defects. Note the gradients of the straight line fits to the data decrease with increasing wavelength suggesting that this process is more efficient at shorter wavelengths, i.e. for the smaller nanocrystals.

The rise and decay transients as a function of PL emission energy for the sample annealed for the longest time, sample G$_4$ (1100°C, 300s) is shown in **Figure 4-10**.
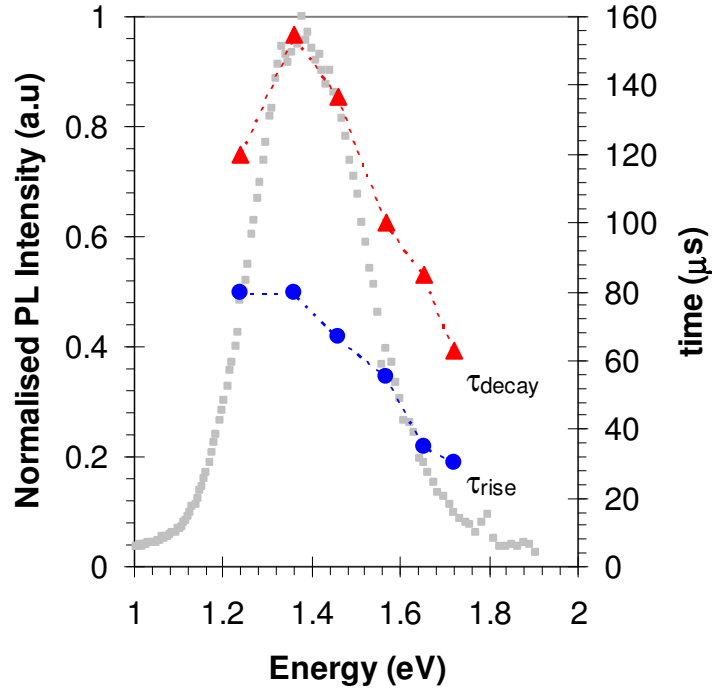
Figure 4-10 Characteristic rise (blue circles) and decay (red triangles) lifetimes and PL intensity (light grey squares) as a function of the emission energy for sample G$_4$

Assuming the excitation and decay dynamics of the Si-NCs can be described by a simple two level system, the rate equation for the excited state population can be written:

$$\frac{dN^*}{dt} = \sigma\phi\left(N - N^*\right) - \frac{N^*}{\tau_{decay}} \tag{46}$$

Where N is the total Si-NC population and N^* is the instantaneous number of Si-NCs in the excited state. τ_{decay} is the characteristic lifetime of the excited state, ϕ is the photon flux (exciting laser power) and σ is the excitation cross-section for Si-NCs with a specific band-gap according to their size, absorbing photons at the exciting laser energy. The product $\sigma\phi$ corresponds to the excitation rate, R_{exc} which may be obtained from the measured rise and decay transients according to equation (47):

$$R_{exc} = \sigma\phi = \frac{1}{\tau_{rise}} - \frac{1}{\tau_{decay}} \tag{47}$$

In addition, once the excited Si-NC population reaches a steady state, equation (46) readily reduces to:

$$N^* = \frac{\sigma\phi\tau_{decay}N}{1+\sigma\phi\tau_{decay}}$$

(48)

And N^* can be written in terms of the PL intensity, I_{PL} as follows:

$$N^* = I_{PL}\tau_{decay}$$

(49)

Substituting equation (49) into equation (48), we can write the relative number of Si-NCs emitting at each energy (or wavelength), N as:

$$N = \frac{I_{PL}\left(1+\sigma\phi\tau_{decay}\right)}{\sigma\phi}$$

(50)

We determined relative values for the number of emitting Si-NCs, N and the cross section, σ as a function of the emission energy, assuming a constant pump flux, ϕ of ~$1.8\times10^{20}cm^{-2}s^{-1}$ at 476nm and the result is shown in **Figure 4-11**.
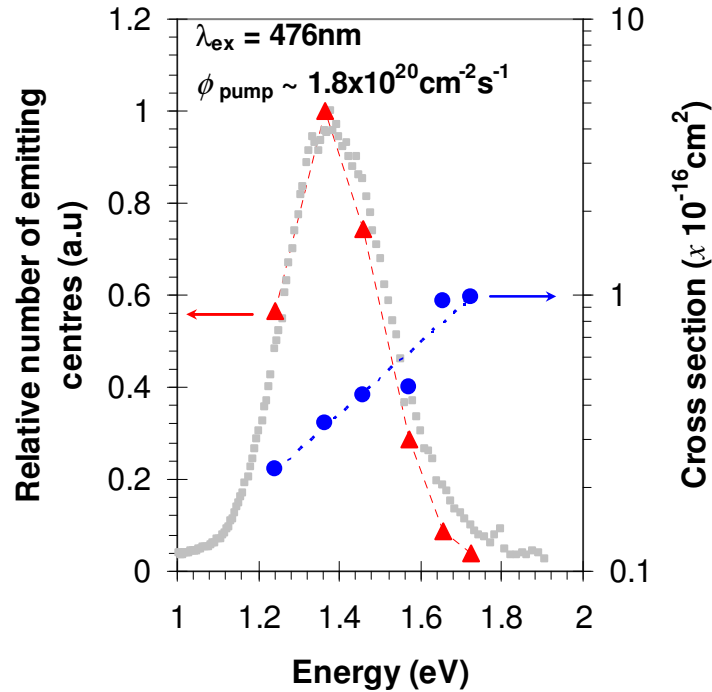
Figure 4-11 Calculated cross section (blue circles) and relative number of emitting Si-NCs (red triangles) as a function of the PL emission energy for sample G$_4$. The red line is a guide to the eye and the blue line is an exponential fit to the cross section data. The normalised PL intensity is plotted (grey squares) on the left hand y-axis for comparison

It is not surprising to find that the distribution of emitting Si-NCs follows the PL intensity exactly, however we note that the cross-section increases monotonically across the band from low to high energy and is highest (~$10^{-16}cm^2$) around 1.7eV. This is surprising because the nature of carrier localisation means that small Si-NCs should exhibit a smaller density of allowed conduction or valence band states than their larger counterparts, which is a direct consequence of quantum confinement. One might therefore expect to obtain a monotonically decreasing value for the cross section across the band from low to high energy because, for a given excitation energy, the density of available states increases with Si-NC size. Indeed, this result was already reported by Kovalev *et al*[179] for *p*-Si. The result we have obtained however is in better agreement with the findings of Garcia *et al*[180], also for Si-NCs in SiO_2 obtained via Si^+ implantation. They found a non-monotonic cross section across the PL emission band and attributed their observations to a complex combination of density of states and oscillator strength, the latter of which increases with the inverse of the Si-NC size[154]. Additionally, if the density of absorbing (small) nano-clusters is much higher than the population of emitting (large) clusters in the ensemble, then one might expect a larger density of available states at higher energy relative to the peak of the emission spectrum. This would support the hypothesis of preferential exciton migration from small to large clusters such that the relative number of emitting clusters does not necessarily correspond to the actual distribution of cluster sizes. The cross section across the emission band and the position of the peak value then depends on a complex combination of the density of states (as a function of Si-NC size and density), the oscillator strength (which increases with the inverse Si-NC diameter)[154] and the excitation wavelength. With respect to the latter, the authors in [180] showed that the peak of the absorption cross section shifted to shorter wavelength when the energy of the exciting laser was increased, which indicates an increase in the involvement of, in particular small nano-crystals in the luminescence process. They reported values for the cross section of between 2 and $8\times10^{-16}cm^2$, which is slightly higher than those obtained in this work. This could be due to the fact that the sample described in [180] contained ~20% excess Si, which is almost a factor of 3 higher than the excess Si in our sample. Increasing the amount of excess Si will yield a higher concentration of Si-NCs and a correspondingly higher density of states and larger cross section. As well as

variations in the cross section with excitation and emission energy, in the next section we present evidence that the measured cross section is also a strong function of the excitation flux.

4.3.1.4 Excitation power dependence of the Si-NC PL

The PL spectra as a function of excitation power at 405nm for sample E is presented in **Figure 4-12**.
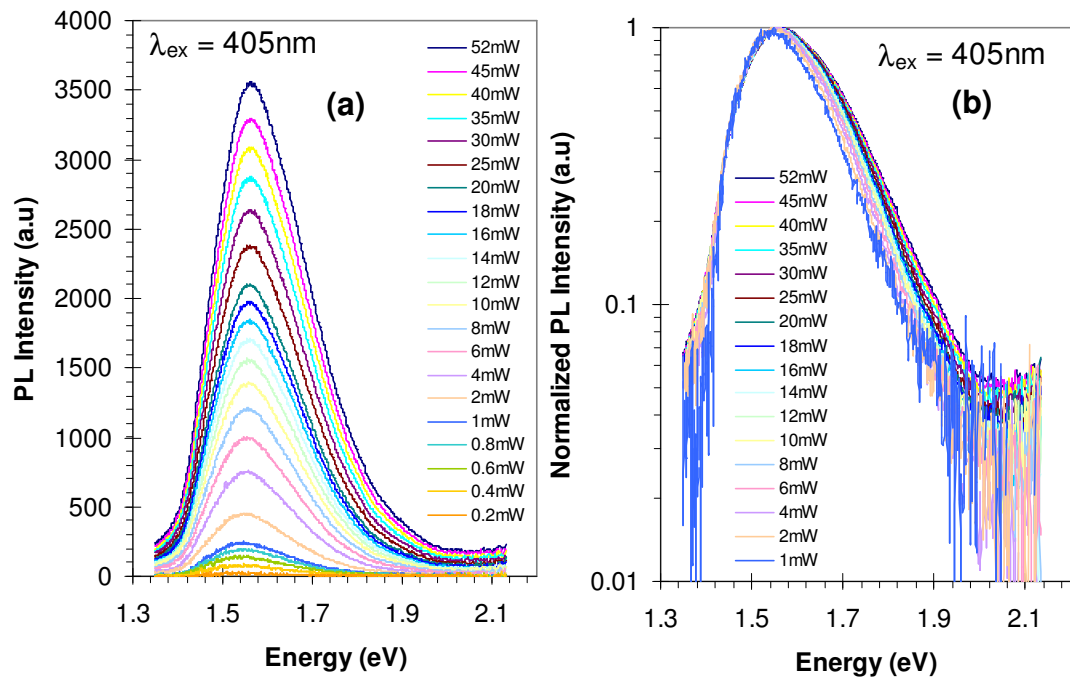
Figure 4-12 (a) Relative and (b) Normalised PL spectra (semi-log plot) as a function of the laser excitation power at 405nm for Sample E

The PL intensity increases monotonically with excitation power over the entire experimental range. It is also evident, particularly from **Figure 4-12 (b)** that the spectral shape changes with increasing excitation power, in particular we note a small blue-shift in the peak position and an inhomogeneous broadening to the high energy side with increasing excitation power. The peak shift and broadening are quantified in **Figure 4-13**.
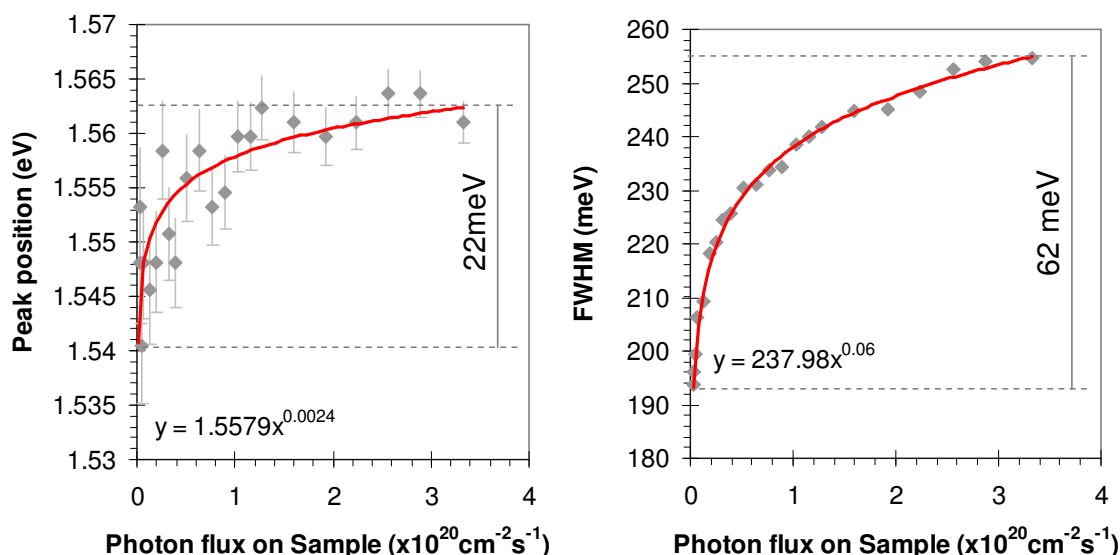
Figure 4-13 (a) Si-NC peak position and (b) FWHM as a function of the photon flux. Red lines are power fits to the data (indicated).

Both the peak position and broadening are reasonably well described by simple power laws, the value of which is indicated in the figure. The peak shifts by ~22meV and is broadened to the high energy side by ~62meV as the photon flux is increased from around 2.5×10^{18} to 3.3×10^{20} photons/cm^2/s. Similar observations were already reported for Si-NCs embedded in fused quartz wafers after Si$^+$ implantation[181] and in PECVD Si/SiO$_2$ super-lattice structures[182]. In general, this result suggests that luminescent centres emitting at longer wavelengths tend to become saturated at lower excitation flux relative to those centres emitting at higher energies. This imbalance arises due to the slower decay dynamics on the long wavelength side of the spectrum and is likely related to the size distribution of Si-NCs emitting at different wavelengths. If the largest Si-NCs remain excited for longer it is reasonable to assume that the population of largest Si-NCs will become saturated at lower excitation powers. Then, further increasing the excitation power should lead to a preferential excitation of smaller Si-NCs and a gradual shift in the observed PL peak to higher energies. We verified this by examining the dependence of the PL intensity on the excitation flux for a range of emission energies across the spectrum, as shown in **Figure 4-14**.
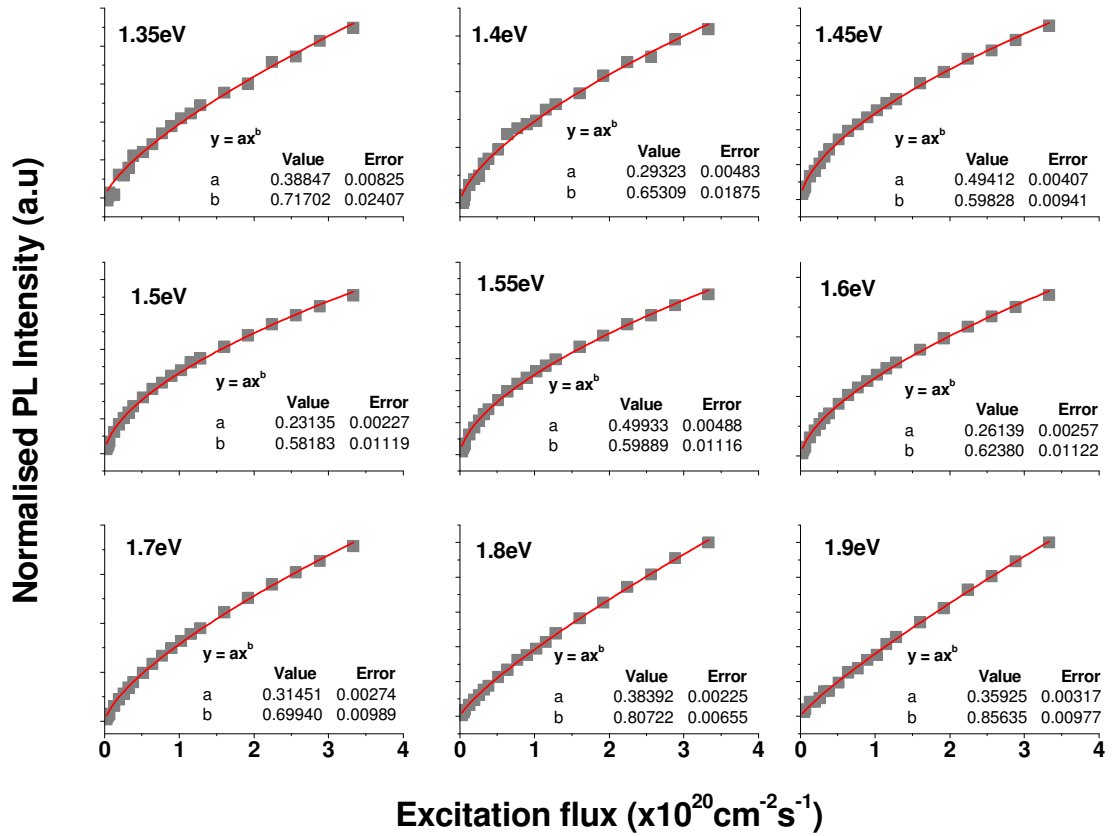
Figure 4-14 PL intensity as a function of the pump flux for a range of emission energies (indicated) across the PL spectrum of sample E. Red lines are power law fits to the data of the form $y = ax^b$ (values for a and b are indicated in each figure)

The data are adequately described using a power law function of the form $y = ax^b$ with the exponent b indicating the degree of saturation. For all emission energies b < 1 indicating a sub-linear behaviour over the experimental pump flux range. However, we note that b is much closer to 1 on the high energy side of the spectrum than on the low energy side as illustrated in **Figure 4-15**.
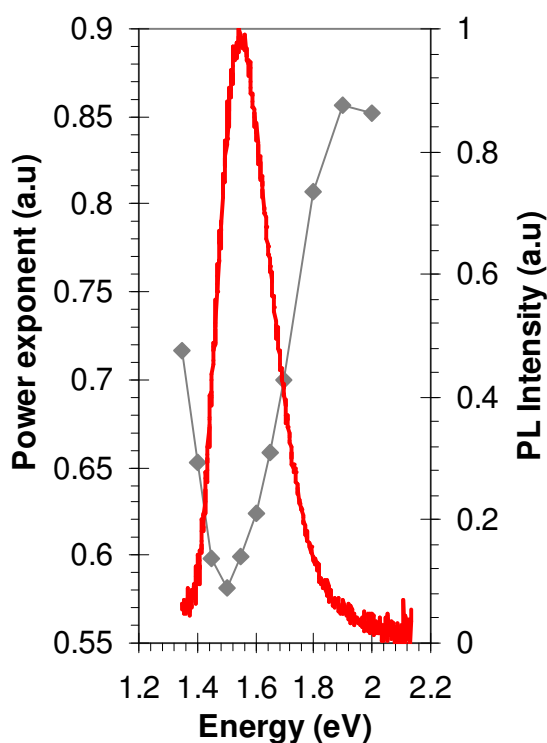
Figure 4-15 Power exponent, b (grey diamonds) and PL intensity (red curve) as a function of the PL emission energy for sample E

There is a clear anti-correlation between the power exponents and the PL decay times obtained earlier right across the spectrum, with the emitting centres around the peak exhibiting the longest decay times (~160µs) and the smallest exponent (~0.58), i.e. the PL intensity being closer to saturation. On the other hand, for the highest emission energies, we find the shortest decay times (~60µs) and the largest exponent values (~0.85). The latter population are therefore much farther from saturation over the experimental range of excitation powers employed here. This represents strong evidence that the luminescence yield and therefore spectral shape are dominated by the dynamics of the underlying luminescent centres and explains the observed blue-shift and broadening to high energies with increasing excitation power.

We also measured the ensemble luminescence rise and decay transients as a function of the excitation flux at 405nm, examples of which are shown in **Figure 4-16**.
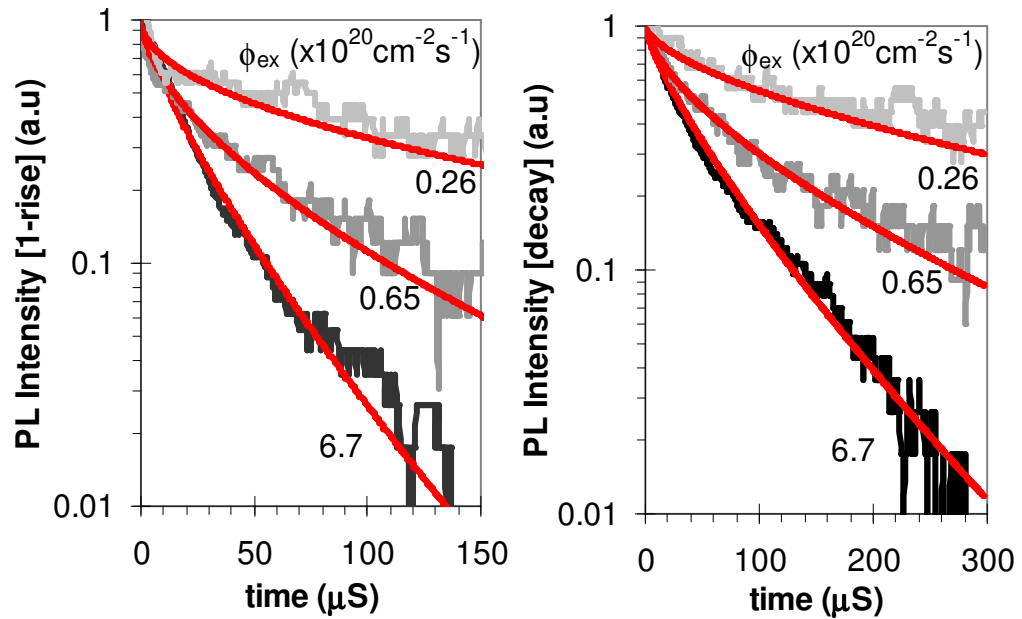
Figure 4-16 Si-NC sample E PL rise and decay transients as a function of the excitation flux (indicated) at 405nm. Red lines are stretched exponential fits to the data using equation (45)

As the excitation power is increased, the rate of both the decay and rise of the luminescence increase monotonically. By fitting the PL transients with the stretched exponential for a range of excitation powers, we quantified the rate of increase for both the rise and decay rates as a function of the excitation flux as shown in **Figure 4-17**.
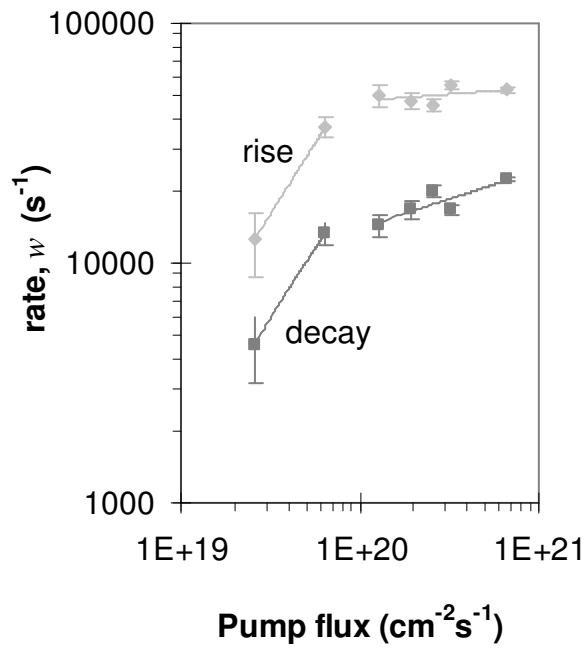
Figure 4-17 Si-NC PL rise and decay rates as a function of the pump flux at 405nm for sample E

At low power the rise and decay rates increase rapidly as the excitation flux is increased but increase much more slowly for excitation flux above 1×10^{20}cm^{-2}s^{-1} indicating that a saturation regime is being approached. Although the rise and decay rates both increase, we note that at higher excitation flux $\Delta w_{\text{rise}} \neq \Delta w_{\text{decay}}$, which results in a change in the overall excitation rate, R_{exc} with excitation flux. Then, the cross section, which is given by $\sigma = R_{exc}/\phi$ also varies with the pump flux as shown in **Figure 4-18**.
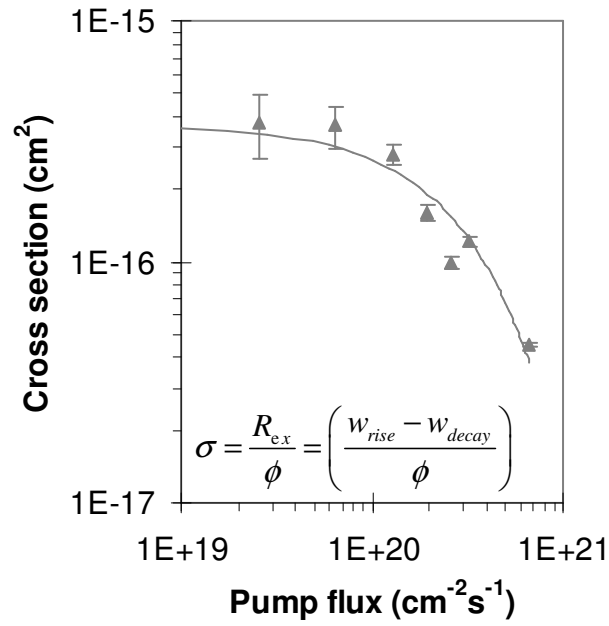
Figure 4-18 Si-NC cross section as a function of the pump flux at 405nm for sample E. The line is an exponential fit to the data.

The values we have obtained here for the cross section are much closer to those reported by Garcia *et al*[180] and higher than those we obtained earlier. This is likely because of the higher excitation energy employed in this experiment (3.1eV compared to 2.6eV). This strong dependence of the cross section on the pump flux perhaps explains some of the variations in the reported results and for a given range of pump fluxes, is likely a strong function of the size and density distribution of the nano-clusters in the film.

4.3.1.5 Temperature dependence of the Si-NC PL

In this section we examine the characteristic emission spectrum from the Si-NCs in sample E as a function of temperature. **Figure 4-19** shows how the spectrum varies with decreasing temperature in the range 300 to 9K.
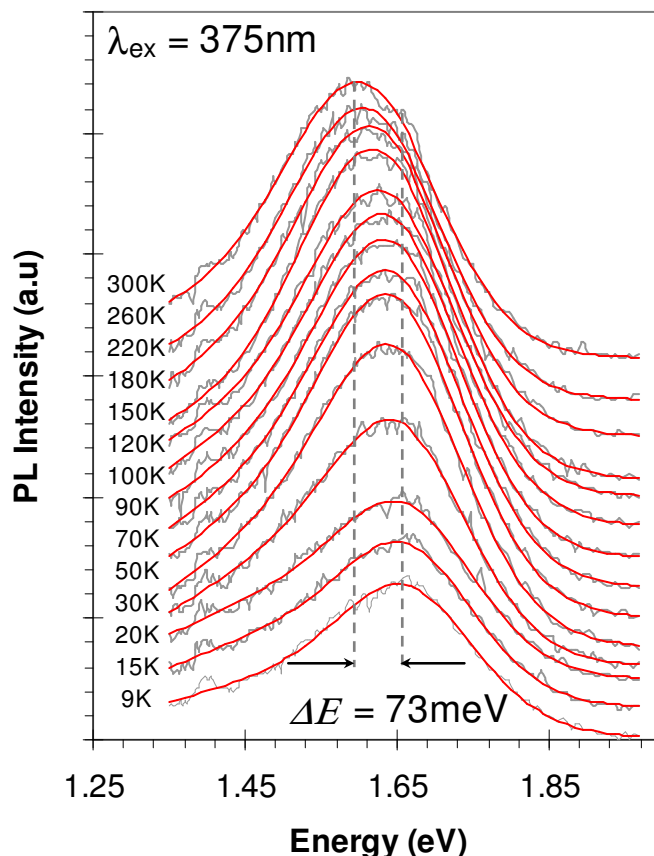
Figure 4-19 Si-NC PL spectra from sample E as a function of temperature between 9 and 300K. Red lines are fitted curves using the lognormal distribution function, equation (42) from which the peak energy, spectral width and integrated intensity were extracted. The dashed grey lines are guides to the eye showing the total spectral shift, ΔE with temperature

As can be seen from **Figure 4-19**, the spectra are monotonically blue shifted as the temperature is decreased. The peak shifts a total ~73meV as the temperature is decreased from 300 to 9K. The presence of the asymmetry can once again be attributed to a combination of Si-NC size distribution and inhomogeneity in the matrix stoichiometry, which gives rise to local electric field fluctuations and corresponding variations in the band-gap energy of the compound[183]. We extracted the peak emission energy from the fits to show how the band-gap

(corresponding to the PL peak) varies with temperature and this is shown in **Figure 4-20**.
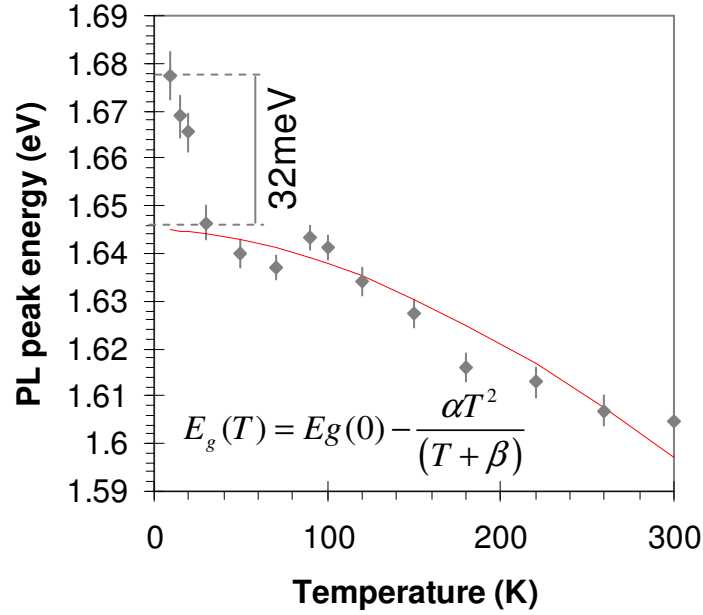
Figure 4-20 Si-NC PL peak energy as a function of temperature. The red line is a fit to the data using the semi-empirical Varshni model, equation (51)

In the temperature range from 300 to ~30K, the band-gap corresponding to the peak emission energy, $E_g(T)$ is reasonably well described by the semi-empirical Varshni model[184] of equation (51):

$$E_g(T) = Eg(0) - \frac{\alpha T^2}{(T + \beta)} \tag{51}$$

From the fit in **Figure 4-20**, we obtained characteristic values for $E_g(0)$ = 1.645eV, α = 4.5x10^{-4}eVK^{-1} and β = 550K.

Clearly the band-gap at $T = 0$ is larger than that of bulk silicon ($E_g(0)_{bulk}$ = 1.17eV), which is a consequence of the quantum confinement effect, the confinement energy being given by $E_{conf} = \Delta E_{Si-NC} - E_g(0)_{bulk}$ = 0.475eV, which is in excellent agreement with previously reported values[185, 186]. Here ΔE_{Si-NC} includes any shift in energy from the band edges due to binding energy and localized surface states after Islam and Kumar[154]. The change in band-gap with temperature ($\Delta E(T)$ ~73meV) over the experimental range is also larger than that of bulk Si (~50meV)[187]. $\Delta E(T)$ and α are functions of the Si-NC size[188, 189], both of which increase with decreasing Si-NC size indicating that the effect of temperature is more pronounced on the luminescence from smaller Si-NCs. Comparing the

values we have obtained for E_{conf}, $\Delta E(T)$ and α with those already reported suggests Si-NCs in our sample of 2 to 3nm, which is in good agreement with the TEM size histograms in the previous chapter. The β-value, which is supposed to be related to the Debye temperature is lower than that reported for bulk Si (630 to 645K)[190] but very close to values previously determined by Vogel *et al*[191] (515K) for nanocrystalline Si by an independent method, i.e. by measuring the temperature dependence of the X-ray diffracted Bragg peak and also by Baisheng *et al*[192] (531K) using a powder neutron diffraction method. This suggests that Si-NCs and Si powder exhibit similarly low values for the Debye temperature compared with bulk Si. This may be due to a softening of the thermal vibrations of the surface atoms[191], which for nanocrystallites would become increasingly significant due to their larger surface to volume ratio. The surface Debye temperature is much lower than the bulk value (310K)[190] and the low values obtained for nanocrystalline materials likely indicates the much stronger influence of the surface atoms in determining the thermal properties of these materials over the bulk.

Critically, we note that the Varshni model fails to describe the measured data below ~30K, where we observe an anomalous (additional) blue shift in the peak emission instead of the predicted asymptote. This high energy shift is coupled with a strong quenching of the luminescence intensity at low temperature as shown in **Figure 4-21**.
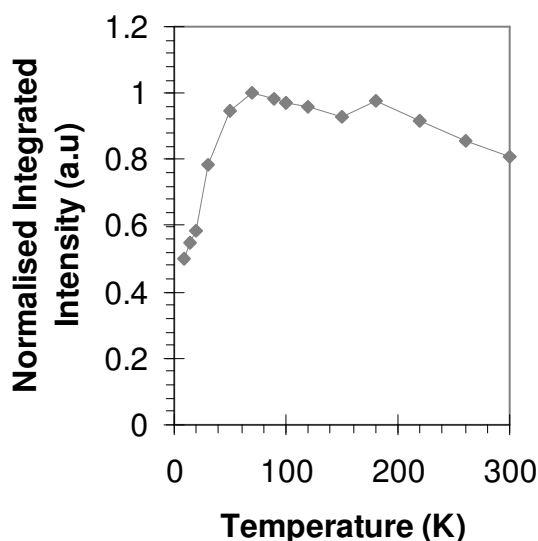
Figure 4-21 Temperature dependence of the integrated Si-NC PL intensity for sample E

Strikingly similar results were already reported for Si-NCs obtained via ion implantation of SiO_2[148, 187] and for Si-NCs obtained after deposition of SiO/SiO_2 layers to form superlattice structures[185, 186]. The quenching of the luminescence between 70 and 300K is attributed to the thermal activation of non-radiative processes and follows a similar trend to that of bulk silicon. However, rather than a continuous increase in the luminescence intensity as the temperature is decreased, we find that the luminescence intensity peaks around 70K and is quenched rapidly as the temperature is further decreased. This can be attributed specifically to an increase of around 2 orders of magnitude in the radiative lifetime[187], which results from the splitting of the localised excitonic levels into a spin-singlet and a spin-triplet state due to the strong electron-hole exchange interaction in Si-NCs. This is shown schematically in **Figure 4-22**.

$\Delta(d_{nc}) \sim 8 - 16\,\text{meV}$

$\dfrac{R_S}{R_T}(d_{nc}) \sim 300 - 800$
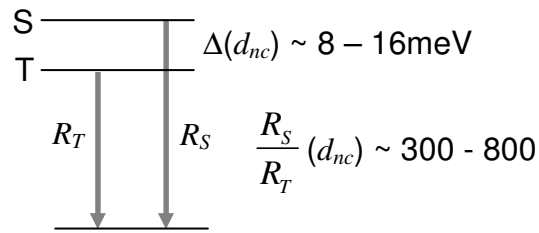
Figure 4-22 Schematic representation of the singlet (S) **and triplet** (T) **excitonic energy levels split by the electron-hole exchange energy (Δ).** R_T **and** R_S **represent the radiative rates of the triplet and singlet states respectively, adapted from [**[187]**]**

At room temperature, carriers can easily overcome the exchange energy to occupy the singlet state where they exhibit a characteristic lifetime of tens of microseconds. However, at very low temperatures, the thermal energy, $k_B T$ is lower than the exchange energy, Δ and the singlet state becomes depopulated and carriers can only occupy the triplet state, which is characterised by lifetimes on the order of a few milliseconds. Duong *et al*[148] recently developed the original model of Calcott *et al*[193] to describe the temperature dependence of the PL from silicon nanocrystals. According to the authors of [[148]], the total radiative and non-radiative recombination rates can be expressed in terms of the radiative rates of the singlet and triplet states and by the rate of non-radiative recombination

processes, R_N such as tunnelling out of the Si-NCs or by thermally activated processes.

The total radiative, R_R and non-radiative, R_{NR} rates are then given by equations (52) and (53) respectively:

$$R_R = \frac{3R_T + R_S \exp\left(\frac{-\Delta}{kT}\right)}{3 + \exp\left(\frac{-\Delta}{kT}\right) + d\exp\left(\frac{-E_A}{kT}\right)} \tag{52}$$

$$R_{NR} = \frac{pR_N + dR_N \exp\left(\frac{-E_A}{kT}\right)}{3 + \exp\left(\frac{-\Delta}{kT}\right) + d\exp\left(\frac{-E_A}{kT}\right)} \tag{53}$$

Where E_A is the height of the barrier from the triplet level, which exhibits a relative density of states, $d = N_{NR}/N_T$ through which non-radiative recombination can occur at a rate R_N and finally p describes the probability of tunnelling. Since the PL intensity should be proportional to the internal quantum efficiency, η which is defined as the ratio of the total *radiative* recombination rate to the total recombination rate, i.e:

$$I_{PL} \propto \eta = \frac{R_R}{R_R + R_{NR}} \tag{54}$$

We can therefore approximate the temperature dependence of the PL intensity $I_{PL}(T)$ by combining equations (52), (53) and (54) to obtain the following expression:

$$I_{PL}(T) \propto \eta = \frac{3R_T + R_S \exp\left(\frac{-\Delta}{kT}\right)}{3R_T + R_S \exp\left(\frac{-\Delta}{kT}\right) + pR_N + dR_N \exp\left(\frac{-E_A}{kT}\right)} \tag{55}$$

It was observed by Brongersma *et al*[187] that both the ratio of radiative rates, R_S/R_T and the exchange energy, Δ increase with decreasing Si-NC size. The quantum confinement model however predicts that the same size Si-NCs should emit light at the same energy, so by plotting $I_{PL}(T)$ for a specific emission energy, i.e. ~1.65eV, we can fix the values for $R_S/R_T = 310$ and $\Delta = 11$meV reported previously by the authors of [187]. Then there are just 3 fitting parameters to describe the measured data, the two non-radiative recombination rates; i) via tunnelling, pR_N

and ii) via thermal activation, dR_N and the activation energy, E_A. The results of our fitting and the model values are shown in **Figure 4-23**.
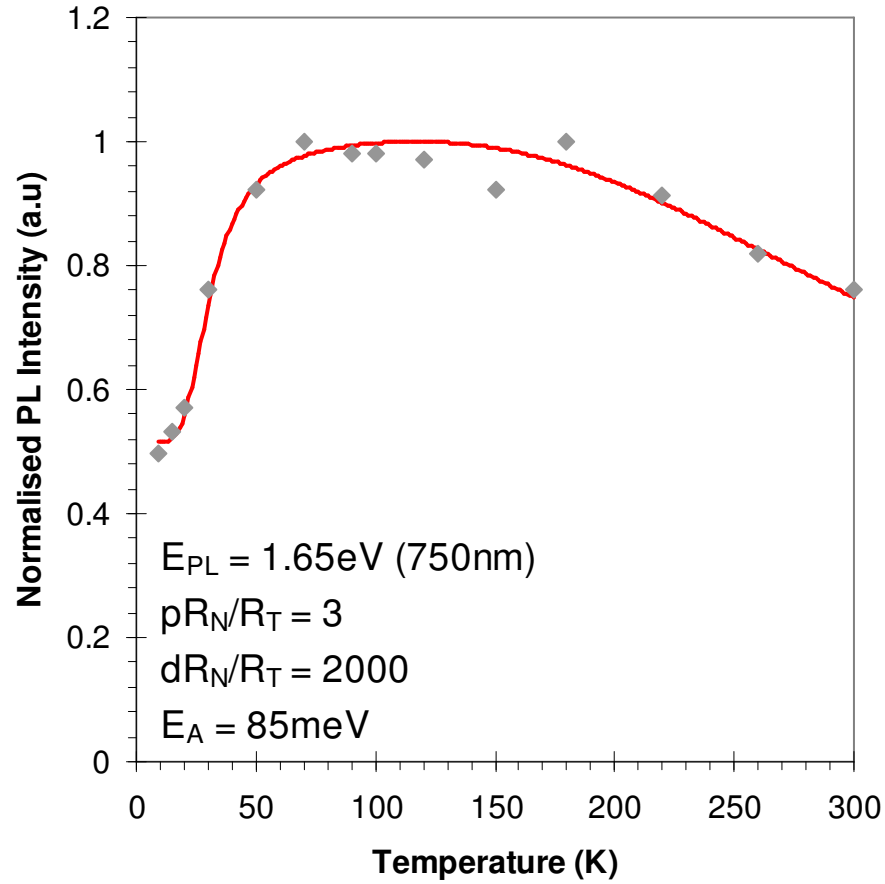
Figure 4-23 Normalised PL intensity as a function of temperature for sample E at 750nm (1.65eV) (grey squares) and fit according to equation (55). The fitting parameters are given in the figure. For pR$_N$ and dR$_N$, the values are given relative to R$_T$ for ease of comparison with those reported by Duong *et al*[148]

We obtained a very similar value to Duong *et al*[148] for the relative tunnelling probability, $pR_N/R_T = 3$ [2.5], which is expected to dominate at low temperature, and is also likely to be a strong function of the matrix properties, i.e. barrier thickness, matrix stoichiometry and Si-NC density. The values we obtained for $dR_N/R_T = 2000$ [3100] and the activation energy, $E_A = 85$meV [58meV] are respectively much lower and higher than those reported by the authors of [148]. This is apparent from the relative insensitivity of the PL intensity to temperature in our sample for T > 100K. For example, the PL intensity at 300K for our sample is ~80% of the peak intensity, compared with just 40% reported in [148].

Rinnert *et al*[185] argued that, for a given excitation power, the increase in the radiative lifetime at low temperature should result in the preferential saturation of the larger Si-NCs in a given distribution. Then the luminescence at low temperature is dominated by the smallest Si-NCs in the same distribution, which may explain the anomalous blue shift. The magnitude of the blue shift should then be a strong function of the Si-NC size distribution for a given sample, for example the authors in [185] reported a monotonic increase in the low temperature blue shift from 6 to 18meV for increasing Si-NC size distributions. The value we have obtained for our sample of ~32meV therefore suggests a much larger size distribution, which is likely due to the differences in sample preparation, i.e. Si-NCs formed via ion implantation in our case compared with Si-NCs formed in a SiO/SiO$_2$ super-lattice type structure, the latter of which is known to yield narrow size distributions[185, 194].

We also examined the PL intensity dependence on temperature for a range of emission energies across the PL spectrum of sample E as shown in **Figure 4-24**.
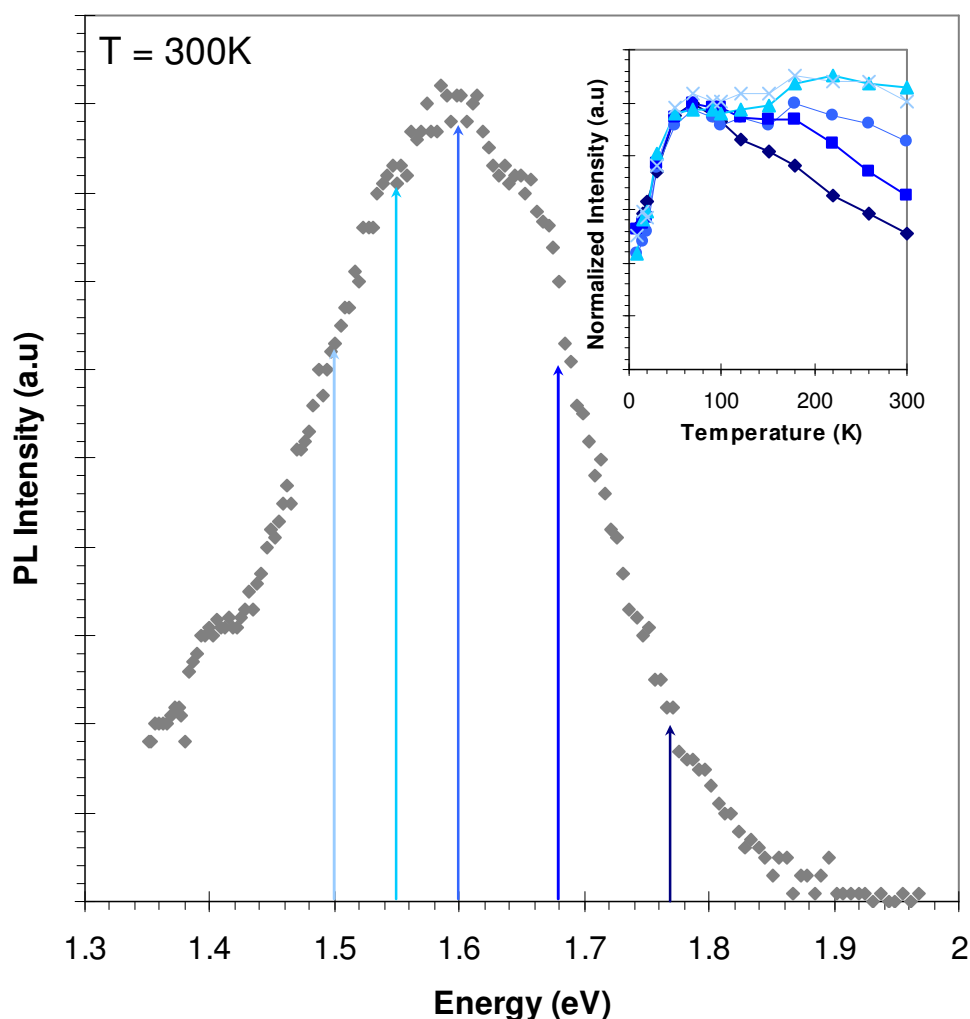
Figure 4-24 Si-NC sample E PL spectrum at T = 300K and inset the temperature dependence of the PL intensity for a range of emission energies across the spectrum from sample E.

Immediately obvious from the inset of **Figure 4-24** is the difference in the temperature dependence of the PL intensity across the spectrum in the high temperature regime (>70K). For the low energy (long wavelength) side of the spectrum, the PL intensity appears to be almost independent of temperature between 300 and 70K. On the other hand, for the high energy (short wavelength) side of the spectrum, the PL intensity is a strong function of the temperature over the same range. This supports the proposition that the larger Si-NCs in the ensemble are saturated and explains the broadening to the high energy side as the temperature is decreased in this range. This suggests that the thermally

activated non-radiative de-excitation processes are much more effective at higher energies, i.e. for emission corresponding to the smaller Si-NCs. This is illustrated in the Arrhenius plot of **Figure 4-25**.
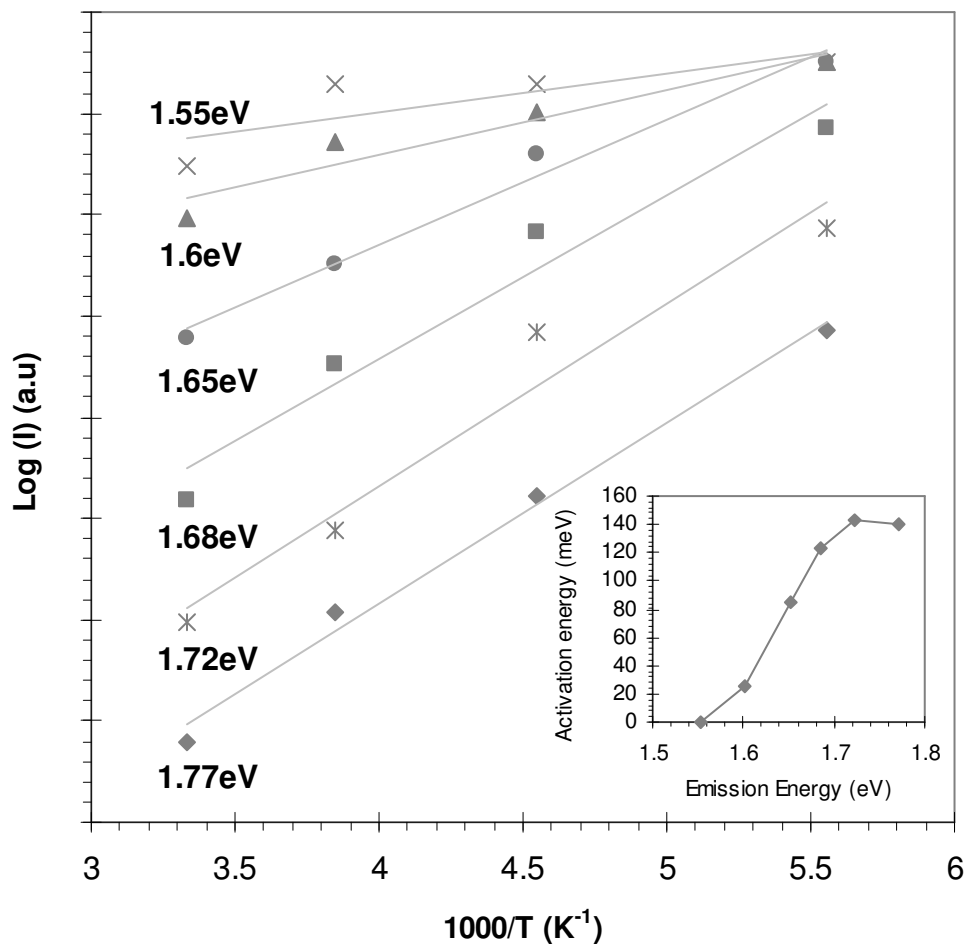
Figure 4-25 Arrhenius plot of the temperature dependence of the PL intensity (180 ≤ T ≤ 300K) for a range of emission energies across the spectrum of sample E. Inset: Thermal activation energy determined from the gradient of the straight line fits to the data as a function of the PL emission energy

4.3.2   Raman Spectroscopy

In order to further investigate the evolution of the SRSO with annealing time, we studied the Raman spectra from sample set G on Al$_2$O$_3$ (sapphire) substrates. The Raman signatures of amorphous and crystalline Si are uniquely distinguishable, which makes this technique particularly suitable to a study of the phase transformation of Si-NCs during annealing.

Obtaining Raman spectra from SRSO on silicon however is problematic due to the low volume fraction of randomly oriented Si-NCs, the weak signal from which can be swamped by the strong transverse-optical (TO) phonon mode at 520cm^{-1} from the substrate. Wellner *et al*[195] achieved this elegantly however for a single layer of Si-NCs in a thin oxide on Si using a combination of resonant excitation and exploitation of the Raman selection rules. In this case, the resonance condition was met by excitation at 3.4eV, corresponding to the direct *E$_0$'* gap in bulk silicon, at which the Raman scattering cross section is greatly enhanced. In addition, by cross polarizing the exciting and scattered light, the highly polarized substrate signal is suppressed, whereas the relative suppression of the signal from the Si-NCs is virtually unaffected by this due to their random orientation in the matrix.

Our choice of sapphire substrate, amongst other things, removed the stringent experimental requirements described above and enabled the collection of Raman signals via non-resonant excitation (514nm), without the use of a polarizer. Comparing the spectra with a pristine section of the substrate facilitated removal of the background scattering signal from sapphire, which is well documented[196, 197].

The Raman spectra for the four samples from set G are shown as a function of the annealing conditions in **Figure 4-26**.
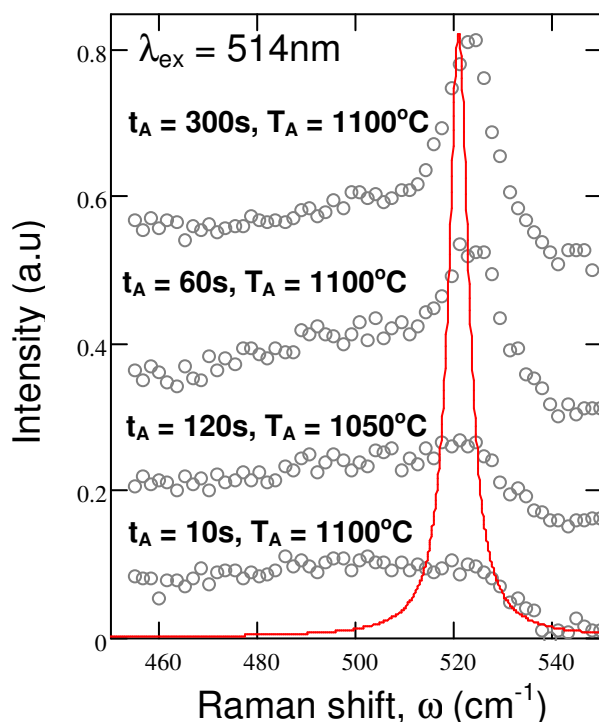
Figure 4-26 Room temperature Raman spectra (offset for clarity) for sample set G as a function of the annealing conditions (t_A, T_A) as indicated for each spectrum. The red line is the TO phonon mode from a reference single crystal bulk Si substrate.

Although the signals are weak, a complex spectral shape can be distinguished from the background between 450 and 540cm^{-1}. A broad featureless band centred around 500cm^{-1} is evident even after just 10s of annealing at 1100°C. This band falls away sharply above 525cm^{-1} and, as the annealing time is increased a sharper feature emerges around 520cm^{-1}.

It is noteworthy that the spectrum from the sample annealed for 120s at the lower temperature of 1050°C is only marginally more intense, yet significantly weaker, than those corresponding to 10 and 60s at 1100°C respectively. This indicates the much stronger dependence of Si-nanocrystal formation on T_A than on t_A in agreement with the TEM data presented in the previous chapter and previously reported observations[198].

In all of the measured spectra we note that the peak around 520cm^{-1} is asymmetrically broadened to lower frequencies, which has previously been attributed to the presence of a distribution of, in particular small Si-nanocrystals. This gives rise to a spread in the number of optically allowed modes, away from the *Brillouin* zone (BZ) centre, due to a phonon confinement effect in small nano-

crystallites. In single crystal semiconductors only the mode at the BZ centre (corresponding to a wave-vector, **q** = 0) is allowed due to the momentum conservation requirement. In Si this mode appears at ω_0 = 521cm^{-1} with a natural line-width at room temperature of Γ_0 ~ 3.5cm^{-1}. In amorphous Si the disrupted translational symmetry and absence of long range order leads to a relaxation of the selection rules and an extension in the number of allowed modes for **q** $\neq$ 0, leading to a broad band of optical phonon spectra centred around 480cm^{-1}. The localization of phonons to crystallites on the nanometer scale also leads to a relaxation of this selection rule and an uncertainty in the phonon momentum, which can give rise to additional Raman shifted spectra between 480 and 521cm^{-1}. A theoretical description (phonon confinement model - PCM) for the Raman line-shape in such nano-crystalline materials was provided in a seminal paper by Campbell and Fauchet[150] following on from an initial description of the Raman spectra from samples containing Si-microcrystallites by Richter *et al*[149]. Since these two works, the PCM has been applied generally to describe observations of peak shifts and asymmetric broadening in Raman spectra for a range of nanocrystalline and polymorphous materials[151-153]. The success of the PCM stems from its simplicity and the fact that it yields reasonably accurate values for the mean crystallite size and distribution of sizes in a given ensemble. Despite this, there appears to be some debate in the literature surrounding the choice of an appropriate phonon confinement function, often chosen arbitrarily to be Gaussian. Some workers reported reasonable agreement with measured data when the value of the Gaussian function is non-zero (e.g. 1/e) at the nanocrystal boundary, in a so-called 'soft confinement' model whereby the phonon wave-function effectively 'leaks' into the surrounding matrix. Others reported better agreement when the value of the Gaussian function was equal to zero at the nanocrystal boundary or by using a *sinc* function, analogous to the ground state electron in an infinite potential well, both of which represent 'rigid' confinement.

We tried several functions but found that our data was best described by an analytical function in which the allowed optical modes are represented by a lognormal distribution. This attaches some physical meaning to the confining function because the complex Raman spectrum is a superposition of optical modes from an ensemble nano-crystal population with a lognormal size

distribution, as determined from the TEM images in the previous chapter. We fitted our data with equation (56):

$$I\left(\omega,\overline{d},\sigma\right)=\int_0^1\left|C\left(q,\overline{d},\sigma\right)\right|^2\left[\left(\omega-\omega(q)\right)^2+\left(\Gamma_0/2\right)^2\right]^{-1}dq \qquad (56)$$

Where ω is the Raman shifted frequency and Γ_0 is the natural line-width of the first order Raman spectrum including instrumental broadening[152] taken to be equal to 5cm^{-1}. $\omega(q)$ is the phonon dispersion relation for optical phonons in bulk Si, which we have represented using the analytical form of equation (57) after Tripathi et al[152]:

$$\omega(q)=\omega_0\left(1-0.2q^2\right) \qquad (57)$$

With ω_0 (= 521cm^{-1}) the phonon frequency at q = 0. Here q has the units of $2\pi/a$, with a (= 0.543nm) being the lattice spacing in c-Si. Equation (57) accurately reproduces the dispersion relation for optical phonons along [001] for Si as shown in **Figure 4-27**.
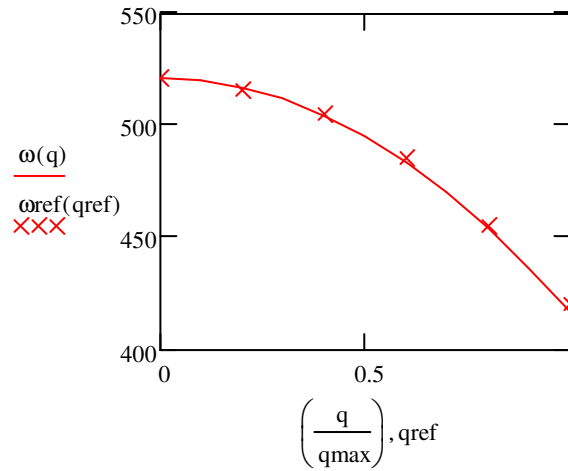
Figure 4-27 Optical phonon dispersion relation according to the analytical expression of equation (57) (solid line) and experimental data (crosses) from ref [199] for the $\Gamma \rightarrow$ X [001] direction in Si

Finally, $|C(q,\ \overline{d},\ \sigma)|$ is the phonon confinement function, which we have defined as:

$$\left|C\left(q,\overline{d},\sigma\right)\right|^2=\exp\left(\frac{-\log\left(q\overline{d}\right)^2}{2\sigma^2}\right) \qquad (58)$$

With $\bar{d}$ and σ the only fitting parameters required. Our model predicts both qualitatively and quantitatively the anticipated peak shift and broadening arising from phonon confinement in nano-crystallites, in excellent agreement with previously reported models[153]. To our knowledge this is the first such model to use the lognormal distribution function to represent the phonon confinement function. Gupta *et al*[153] described a model that included a lognormal distribution function in recognition of the fact that the Raman samples a distribution of particle sizes but this was used as a separately weighted sum over the range of particle sizes in addition to the Gaussian phonon confinement function. Since our model predicts both qualitatively and quantitatively a similar peak shift and broadening with nanocrystal size it should be computationally more efficient. **Figure 4-28** shows the results of our calculations for the Raman spectra, peak position and line-width assuming a near zero ($\sigma = 0.01$) size distribution for different size Si-NCs.
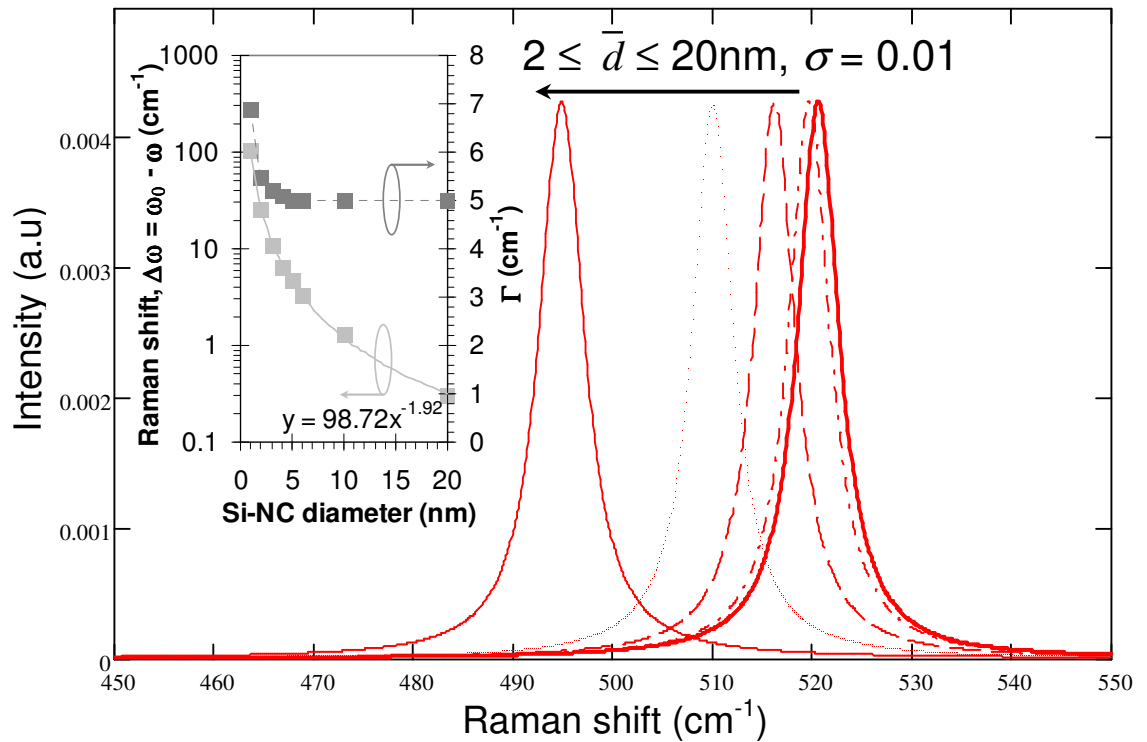
Figure 4-28 Calculated Raman spectra for the Si TO phonon mode as a function of Si-nanocluster mean diameter, $\bar{d}$ with a near zero ($\sigma = 0.01$) size distribution. The inset shows the calculated Raman peak shift relative to the bulk value, $\omega_0 = 521$cm^{-1} (left axis) with a power fit (indicated) to describe the data points as well as the line-width (right axis) as a function of the Si-NC diameter. The dashed grey line is a guide to the eye

If we take into account the size distribution we find that, in particular as the size distribution increases, the peak position may be blue shifted towards the bulk value, ω_0 = 521cm^{-1}. This observation, which is illustrated in **Figure 4-29** is peculiar to our definition of the phonon confinement function, i.e. being represented by a lognormal distribution of optical modes because we note the absence of this in the results of Tripathi *et al*[152] where a Gaussian function was used.
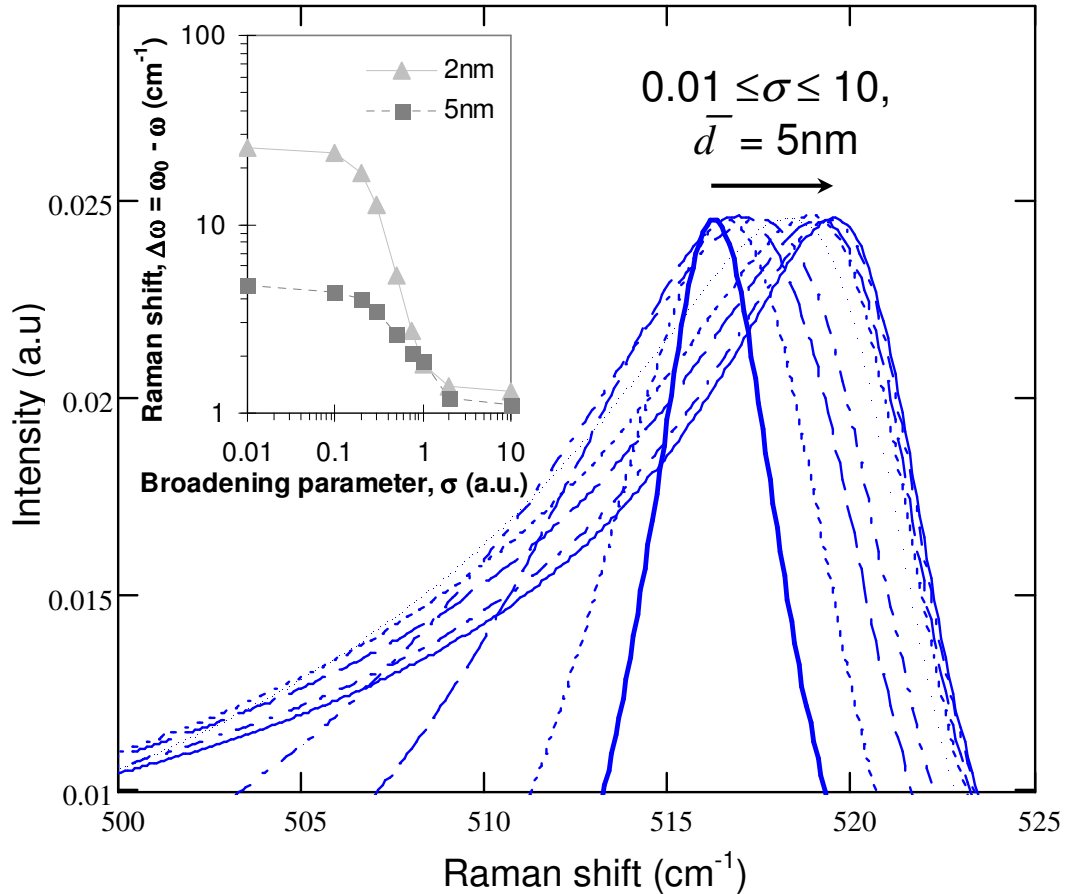
Figure 4-29 Calculated Raman spectra for $\overline{d}$ = 5nm as a function of increased broadening by varying 0.01 ≤ σ ≤ 10. Inset: Log-log plot showing the peak shift with respect to bulk *c*-Si ($\Delta\omega$ = ω_0 - ω) as a function of the broadening parameter, σ for $\overline{d}$ = 2 (triangles) and 5nm (squares). Lines are guides to the eye

This result indicates that, even where an ensemble nano-crystal population has a very small mean diameter, large red-shifts in the Raman peak may not be observed if the distribution of sizes is sufficiently large, which is frequently the case[200]. In particular, lognormal distributions will result in a larger diameter for the

most probable nano-crystal size due to the weighting of the asymmetry towards larger values compared with a standard Gaussian distribution[143]. The largest nano-crystals in any ensemble population will naturally exhibit an increased long range order, translational symmetry and a lower degree of phonon confinement compared to their smaller counterparts. As such the Raman peak position for the Si TO phonon for such distributions should tend towards that of the bulk value, ω_0 = 521cm^{-1}.

Figure 4-30 shows the fits to our measured data using equation (56) and **Table 4-2** details the fitting parameters, $\overline{d}$ and σ as well as the frequency shift, $\Delta\omega$ required to establish the most accurate fit.
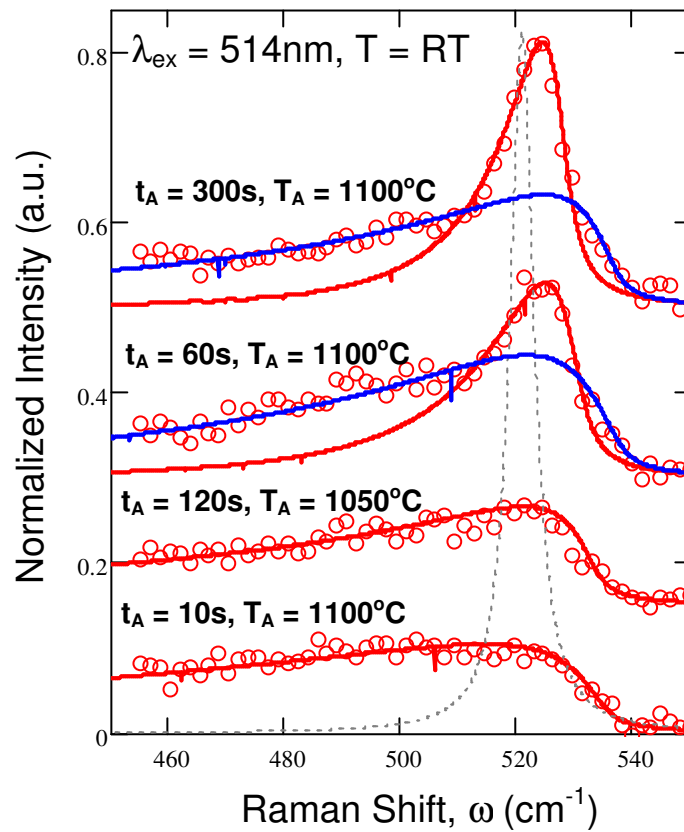
Figure 4-30 Measured (circles) Raman spectra (offset for clarity) for samples in set G after 514nm excitation. The red and blue bold lines are fits to the data using equation (56), which reveal an asymmetrically broadened Si TO phonon peak around 520cm^{-1}, attributed to the confinement and dispersion of phonon modes in small Si-nanocrystals having a specific size distribution. The grey dotted line is the calculated bulk c-Si reference spectra

Sample ID	Annealing conditions T_A (^{o}C), t_A (s)	$\bar{d}$ (nm)		σ (a.u)		$\Delta\omega$ (cm^{-1})	
		Red	Blue	Red	Blue	Red	Blue
G$_1$	1100, 10	1.34	-	0.331	-	15	-
G$_3$	1050, 120	1.83	-	0.333	-	13	-
G$_2$	1100, 60	3.5	1.9	0.210	0.250	11	18
G$_4$	1100, 300	4.6	2	0.22	0.300	8	16.5

Table 4-2 Fitting parameters used in the modelling of measured Raman spectra for Si-NC samples in set G

A number of interesting observations emerge from the fits; the first and most apparent being that only the Raman spectra for the samples subjected to the lowest thermal budget (and therefore having the smallest mean size and distribution – samples G$_1$ and G$_3$) can be described by a single fit (red line). For the samples annealed for the longer anneal times at the higher anneal temperature, G$_2$ (60s) and G$_4$ (300s), although the red curves adequately describe the sharp peak around 520cm^{-1}, an additional fit (blue line) was required to describe the broadening of the principal Raman peak to both slightly higher and much lower frequencies. We interpret this in the following way; for the shortest annealing times at 1100°C (or lower anneal temperature in the case of sample G$_3$) the matrix has not yet stabilized to that of stoichiometric silica but rather still contains a degree of solute and is therefore silicon rich. A population of small, possibly polymorphous/polycrystalline Si-NCs with a small mean diameter and relatively narrow size distribution is established but crystallization is likely incomplete after such a limited thermal budget[151]. As the annealing time is further increased, those established nano-clusters continue to grow and crystallize, whilst their size distribution also increases. A second population also then emerges from the remaining solute, which has very similar starting characteristics (size and crystalline fraction) to the 'original' population. Our calculations presented earlier suggest that the activation energy is a function of the isothermal annealing time and we showed that it is monotonously reduced from ~4.5 to ~2eV in the first 100s of annealing at 1100°C. This would favour the formation of additional clusters after longer annealing times provided there remains sufficient solute in the matrix and the annealing temperature is sufficiently high.

Parameters $\bar{d}$ and σ obtained from the Raman fitting were used to generate lognormal distribution functions for comparison with those obtained from the TEM stacked histograms for the samples in the previous chapter, which were prepared according to similar annealing conditions. These are shown in **Figure 4-31** and **Figure 4-32**.
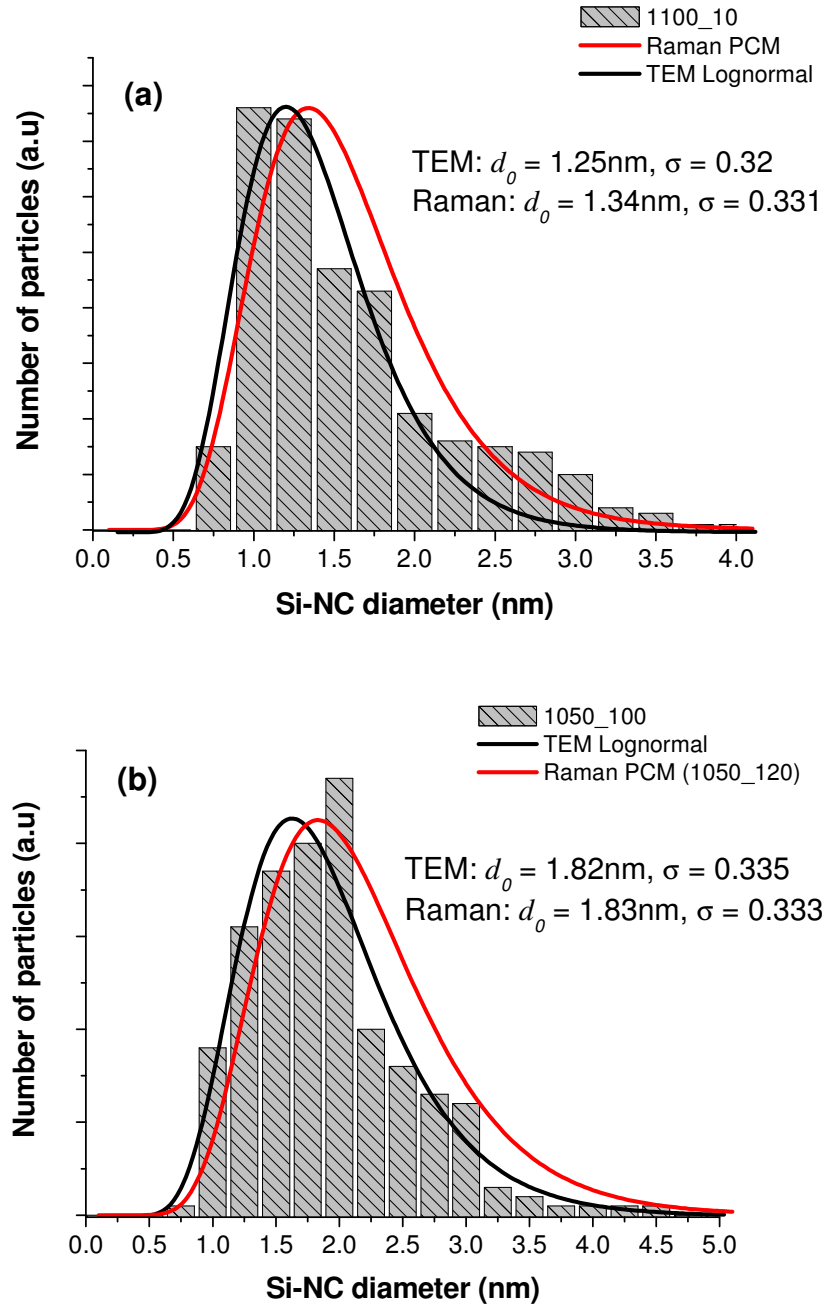
Figure 4-31 Si-NC size distributions obtained via TEM (grey columns) with the corresponding lognormal fit (black line) for (a) sample B$_4$ and (b) sample A$_4$ and lognormal fit (red line) using values for $\bar{d}$ and σ extracted from the Raman PCM for (a) sample G$_1$ and (b) sample G$_3$
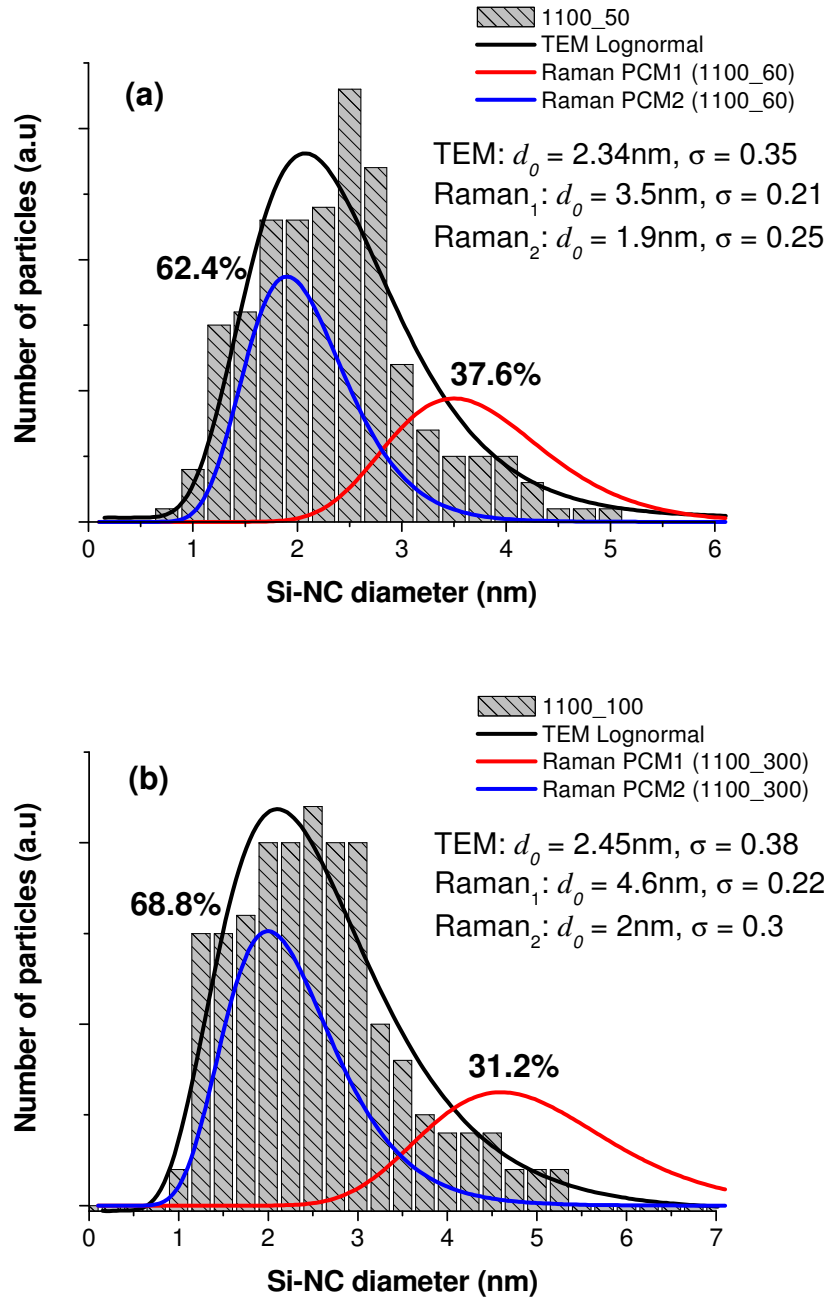
Figure 4-32 Si-NC size distributions obtained via TEM (grey columns) with the corresponding lognormal fit (black line) for (a) sample B$_5$ and (b) sample B$_6$ and lognormal fits (red and blue lines) using values for $\overline{d}$ and σ extracted from the Raman PCM for (a) sample G$_2$ and (b) sample G$_4$. The relative contribution of the two distributions to the total Raman spectra has been normalized to the size distribution obtained from the TEM size histograms.

Figure 4-31 reveals that the Raman fits using the PCM yield Si-NC size distributions that are well correlated with those determined via TEM in the short anneal time/lower anneal temperature regime, i.e. those containing the smallest mean cluster sizes and more narrow size distributions. Where the Raman fitting produced an apparent bimodal size distribution, **Figure 4-32** the relative contribution of each to the total Raman spectra was taken into account[†] and normalized to the size distribution obtained from the TEM size histograms. This result suggests that the observed size distribution obtained via TEM might be deconvoluted into two distinct Si-NC populations. Indeed, similar observations were previously reported for Raman analyses of amorphous nano-crystalline Si[201, 202] and porous Si[203] thin films.

It is worth mentioning that the PCM fits to the measured Raman spectra removes any requirement for a contribution from an amorphous phase. This does not indicate however that all of the excess Si from the matrix has formed into crystalline Si-nanoclusters, as evidenced by the continued removal of Si from the matrix to form additional cluster populations at the longer anneal times. There were a number of reports[151, 204, 205] in which the crystalline fraction was estimated by integrating the relative intensities of the higher frequency and lower frequency contributions to the Raman spectra from Si-NC samples. These observations assume that the lower frequency components, which typically diminish with annealing time (or temperature), are from a purely amorphous phase. Since the distributions we obtained from the Raman fitting do not require a contribution from an amorphous phase, such assumptions about the absolute phase of nano-clusters cannot be validated. Rather, our data leads us to conclude that the complex Raman spectra is a signature of a mixed phase model[206] in which some particles are crystalline, some are amorphous and some contain both crystalline and amorphous phases.

[†] The relative contribution of each of the distributions to the total Raman spectra was calculated from their respective integrated intensities using: $I = \int_{450 cm^{-1}}^{550 cm^{-1}} I(\sigma) d\sigma$

The second important observation from our Raman fitting is the significant frequency shifts required to align the calculated spectra with our measured data. As we have already mentioned, the PCM predicts a red-shift in the Raman peak relative to bulk c-Si for samples containing small Si-NC's. However, although we observed an asymmetric broadening to lower frequencies we did not observe such red-shifts in our Raman peaks. On the contrary, we did observe blue-shifted peaks with respect to bulk c-Si, the degree of which we found to be monotonously increased with annealing time. This may be explained in part by the increase in size distribution with isothermal annealing time, as observed from the TEM size histograms and as predicted by the calculations, shown in **Figure 4-29**. However, the size distributions we obtained from our fits to the Raman spectra are insufficient alone in explaining the magnitude of the blue-shift required to line up the calculated Raman peaks with our measured data. In fact, the corrected shifts turned out to be proportional to the inverse thermal budget (and therefore inverse Si-NC diameter). Such up-shifted Raman peaks were already reported and attributed to compressive stress[207, 208] or hydrostatic pressure[151], which acts in opposition to the effect of phonon confinement with the competition between the two effects determining the observed (measured) peak position. The magnitude of the stress, P can be estimated from the stress induced frequency shift relative to that predicted by the PCM, $\Delta\omega_s$ as[207]:

$$P(GPa) \approx 0.25\Delta\omega_s \left(cm^{-1} \right) \qquad (59)$$

Figure 4-33 shows the stress calculated using equation (59) from the observed frequency shifts, $\Delta\omega_s$ as a function of the Si-NC mean diameter, $\overline{d}$.
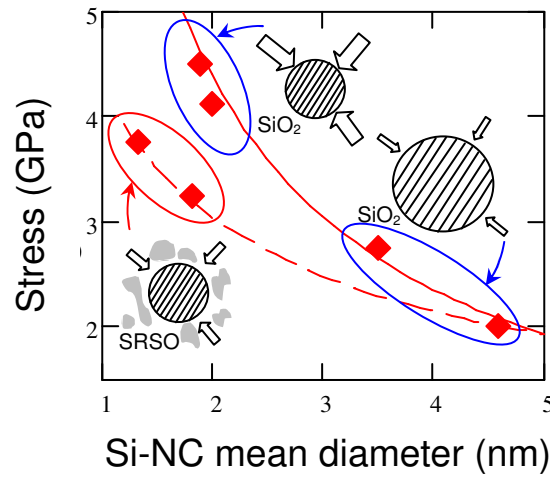
Figure 4-33 Compressive stress calculated from the up-shifted Raman peaks using equation (59) relative to that predicted by the PCM as a function of the Si-NC mean diameter. The lines are power law fits to the data of the form: $P = Ad^x$ **with** $A = 8.2$, $x = 0.9$ **(solid line) and** $A = 4.3$, $x = 0.5$ **(dashed line). In the inset we present a schematic picture of the relative stress experienced by different size Si-NCs embedded in matrices with different relative stoichiometry (e.g. SRSO - circled red and SiO$_2$ – circled blue) according to the annealing conditions. The size of the block arrows schematically represents the magnitude of the stress.**

In general, we find that the films containing the smallest Si-NCs exhibit the largest up-shift in the Raman peak relative to that predicted by the PCM. A similar result, both qualitatively and quantitatively was reported by Hernandez *et al*[151]. The stress is thought to arise due to the abrupt lattice mismatch between the matrix and the surface of the Si-NCs[151]. The larger surface to volume ratio of smaller Si-NCs then likely accounts for the much larger stress observed relative to samples containing larger Si-NCs. Hernandez *et al*[151] proposed that the smaller values determined for larger Si-NCs could be due to a combination of smaller surface to volume ratio and the presence of a pressure relieving amorphous shell that separates their crystalline core from the surrounding matrix. We note from our data that the stress determined for the smallest Si-NCs, i.e. those in samples G$_1$ (1100°C, 10s) and G$_3$ (1050°C, 120s) also differs from similar size Si-NCs (the second 'generation' Si-

NCs) in the samples annealed for much longer times. This may be attributed to the fact that the latter are formed later in the annealing cycle after the first population of (now larger) Si-NCs has already been established (as per the apparent bi-modal distribution determined from the Raman spectra). If the formation of the smaller Si-NC populations in these samples (G_2 and G_4) takes place by extraction of the remaining solute from the matrix (at longer anneal times) then the matrix should be closer to stoichiometric silica and the interface stresses relatively large. Similar size Si-NCs obtained after much shorter anneal times (or lower anneal temperature in the case of sample G_3) are likely to be embedded in a matrix that contains a larger fraction of solute and so the interface stresses, in this case, should be relatively smaller. The size dependent stress is analogous to small liquid droplets where the pressure difference across their interface is minimized by their growth with a corresponding change in their surface energy. If the pressure difference across the interface of a spherical Si-NC, $p_i - p_o = P$ results in an increase in particle size from r to $r + dr$, then the 'work done' $= PAdr$. The equivalent change in surface energy, $dE = \gamma dA$, where γ is the surface tension and dA is the corresponding change in surface area. Equating the 'work done' to the change in surface energy yields:

$$dE = \gamma dA = PAdr \qquad (60)$$

$$dE = \gamma 8\pi r dr = P4\pi r^2 dr \qquad (61)$$

$$P = \frac{2\gamma}{r} \qquad (62)$$

Equation (62) is the well known *Laplace-Young* equation. Using the values of P and r from **Figure 4-33**, we can estimate the value of γ for the Si-NCs as a function of their size. The values we calculated for γ increased monotonically from ~1.3 to ~2.4Nm^{-1} with mean particle size from ~1.25 to ~3nm above which it becomes asymptotic. This size dependence of the surface tension is qualitatively in very good agreement with other reports for a range of materials[209, 210] and is a general property of nano-particles. Quantitatively, the values obtained here are also in excellent agreement with literature values for the surface energy (tension) of Si, for example Jaccodine[211] reported values of 1.51Nm^{-1} for (110) and 2.13Nm^{-1} for (100) bulk Si by measuring the force required to induce a cleave along a particular crystal orientation.

4.4   Conclusions

By fitting the PL spectra obtained from samples prepared via ion implantation and rapid thermal annealing with lognormal functions, we have correlated the peak emission energy and width with the mean Si-NC diameter and size distributions obtained from TEM size histograms obtained in the previous chapter. We found that the PL peak is blue shifted and the spectrum is narrower for short anneal times and/or lower anneal temperatures, corresponding to samples with a smaller mean diameter and narrow size distribution. As the anneal time and/or temperature is increased the PL peak red-shifts and the width of the spectrum increases. These findings are qualitatively in agreement with the quantum confinement effect in which smaller Si-NCs exhibit a wider band gap than their larger counterparts. However, we found that the increase in the PL peak emission energy as the Si-NC size is reduced is much shallower than expected for emission corresponding to the annihilation of free excitons and for Si-NC sizes below ~2nm, the PL emission energy is virtually independent of the Si-NC size. These observations are remarkably similar to that reported by Wolkin *et al*[144] for porous silicon in which the shallow dependence of the emission energy with Si-NC size was attributed to either i) recombination between shallow electronic defect states within the forbidden gap and holes in the valence band for Si-NC sizes between 3 and 2nm or ii) recombination between shallow electronic defect states and shallow hole defect states, i.e. bound exciton states within the forbidden gap for Si-NC sizes less than 2nm. The presence of such defect states is thought to arise because of the formation of silicon-oxygen bonds, either Si-O-Si or Si=O, presumably at the Si-NC/SiO$_2$ interface, which act as carrier traps.

Measurement of the luminescence transients reveals a strong dependence on the emission energy, which likely reflects the underlying dynamics of different size Si-NCs in the ensemble. We showed that the relative number of emitting Si-NCs follows the spectral form as expected but that this does not overlap with the Si-NC cross section, which increases exponentially across the emission spectrum from low to high energies. This indicates that the PL results from a preferential exciton migration from small to large Si-NCs. The values we obtained for the cross section are slightly lower than those previously reported, which may be due to the lower concentration of excess Si in our sample.

The power dependence of the steady state and transient PL reveals a strong saturation behaviour, particularly for the larger Si-NCs, which results from their relatively slower decay dynamics. The cross section was also found to be a strong function of the excitation power confirming the saturation of available states for a flux, $\phi > 10^{20}$cm^{-2}s^{-1} at 405nm.

We found that the Si-NC PL intensity is also a strong function of the temperature. As the temperature is reduced from 300 to ~70K, the PL intensity increases due to a gradual decrease in the contribution of thermally activated non-radiative processes. Such processes are a strong function of the emission energy and therefore Si-NC size as revealed by the monotonic increase in the high temperature activation energy across the emission spectrum from low to high energy. For T < 70K, the PL intensity is quenched dramatically, which may be attributed to the splitting of the exciton levels into spin-singlet and triplet states, which arises due to the strong carrier exchange interaction in highly localized semiconductor material systems. At low temperature the thermal energy of the carriers is less than the exchange energy, which leads to a depopulation of the faster singlet state. The lifetime of the lower energy triplet state is orders of magnitude longer, which leaves the carriers susceptible to non-radiative relaxation via tunneling. The inherently slower decay dynamics means that this effect is more pronounced for larger Si-NCs, which is evidenced by an anomalous blue-shift in the emission energy at T < 30K. The size of this blue-shift supposedly increases with increasing Si-NC size distribution. The value we obtained of ~32meV for a Si$^+$ implanted oxide, which is much larger than that previously reported for Si/SiO super-lattice structures[185], which are known to yield narrower size distributions appears to support this hypothesis.

Finally we studied the Raman spectra corresponding to the Si TO phonon mode around 520cm^{-1} as a function of the annealing environment for Si$^+$ implanted oxide films on sapphire. The monotonic increase in the peak around 520cm^{-1} evidences the presence of Si-Si bonds and the formation of crystalline particles with increasing long range order. This is consistent with the formation and growth of the Si-NCs with annealing time. In order to explain the peak shift and asymmetric broadening we fitted the Raman spectra with a modified phonon confinement model based on that originally developed by Richter *et al*[149]. The degree of phonon confinement is expected to be a strong function of the Si-NC size and since the

total Raman spectrum represents a superposition of allowed optical modes, the line-shape should depend on the specific size distribution function. Based on our knowledge of the Si-NC size distribution from the previous chapter, we chose to represent the phonon confinement function also by a lognormal distribution with only two fitting parameters, the mean Si-NC diameter, $\overline{d}$ and the standard deviation, σ. This gives physical meaning to our model, with which we found excellent agreement with our measured data. The values obtained from the fits for $\overline{d}$ and σ using this approach were used to generate size distributions, which we then compared to those obtained from the TEM size histograms obtained in the previous chapter for similar annealing conditions. For the two independent techniques we found remarkable correlation for the size distributions for the samples containing the smallest Si-NCs and narrower size distribution. For the samples containing the largest Si-NCs and wider distribution the fits to our measured Raman spectra indicate that there may be a bi-modal size distribution, which was also reported previously for nc-Si formed in a-SiO matrices via laser annealing[212] and more recently in Si/SiO$_2$ multilayer structures prepared by magnetron sputtering[213]. Additionally, whilst the observed Raman peak position was qualitatively in agreement with that expected for phonon confinement in Si-NCs, i.e. a shift to lower frequencies with decreasing Si-NC size, the amount of shift was much smaller than expected. Our calculations revealed that for a given Si-NC mean diameter, the observed peak position is also a function of the size distribution with larger distributions leading to anomalous blue-shifted Raman peaks. However, this alone is insufficient to explain the small shifts we observed compared to those predicted by the phonon confinement model. Rather we propose the presence of stress in the films, which arises due to the abrupt lattice mismatch at the SiO$_2$/Si-NC interface and is therefore a strong function of the Si-NC size and matrix stoichiometry. Using the values we obtained for the pressure induced Raman shift in conjunction with the *Laplace-Young* equation we determined values for the Si-NC surface tension, which are in excellent agreement with the literature values. We are currently developing our PCM model further to include the combined effects of phonon confinement and stress on the observed Raman line-shape from Si-NC implanted thin oxide films.

4.5 References

143. V. A. Belyakov, V. A. Burdov, R. Lockwood and A. Meldrum, Advances in Optical Technologies **2008**, 279502 (2008).
144. M. V. Wolkin, J. Jorne, P. M. Fauchet, G. Allan and C. Delerue, Physical Review Letters **82** (1), 197 (1999).
145. J. S. Biteen, N. S. Lewis, H. A. Atwater and A. Polman, Applied Physics Letters **84** (26), 5389-5391 (2004).
146. M. Carrada, A. Wellner, V. Paillard, C. Bonafos, H. Coffin and A. Claverie, Applied Physics Letters **87** (25), 251911-251913 (2005).
147. D. Comedi, O. H. Y. Zalloum and P. Mascher, Applied Physics Letters **87** (21), 213110-213113 (2005).
148. P. H. Duong, P. Lavallard, A. Oliver and T. Itoh, physica status solidi (c) **0** (4), 1271-1274 (2003).
149. H. Richter, Z. P. Wang and L. Ley, Solid State Communications **39**, 625-629 (1981).
150. I. H. Campbell and P. M. Fauchet, Solid State Communications **58** (10), 739-741 (1986).
151. S. Hernandez, A. Martinez, P. Pellegrino, Y. Lebour, B. Garrido, E. Jordana and J. M. Fedeli, Journal of Applied Physics **104** (4), 044304-044305 (2008).
152. V. Tripathi, M. Nazrul Islam, Y. N. Mohapatra and P. Roca i Cabarrocas, The European Physical Journal of Applied Physics **39**, 203-209 (2007).
153. S. K. Gupta and P. K. Jha, Solid State Communications **149** (45-46), 1989-1992 (2009).
154. M. N. Islam and S. Kumar, Journal of Applied Physics **93** (3), 1753-1759 (2003).
155. H. Chen, W. Z. Shen and W. S. Wei, Applied Physics Letters **88** (12), 121921-121923 (2006).
156. H. Rinnert, M. Vergnat and A. Burneau, Journal of Applied Physics **89** (1), 237-243 (2001).
157. M. Molinari, H. Rinnert and M. Vergnat, EPL (Europhysics Letters) **66** (5), 674-679 (2004).
158. I. Sychugov, R. Juhasz, J. Valenta and J. Linnros, Physical Review Letters **94** (8), 087405 (2005).
159. G. Ledoux, J. Gong, F. Huisken, O. Guillois and C. Reynaud, Applied Physics Letters **80** (25), 4834-4836 (2002).
160. C. Delerue, G. Allan and M. Lannoo, Physical Review B **48** (15), 11024 (1993).
161. H. Hofmeister, F. Huisken and B. Kohn, The European Physical Journal D - Atomic, Molecular, Optical and Plasma Physics **9** (1), 137-140 (1999).
162. L. Khriachtchev, M. Rasanen, S. Novikov and L. Pavesi, Applied Physics Letters **85** (9), 1511-1513 (2004).
163. D. Nesheva, C. Raptis, A. Perakis, I. Bineva, Z. Aneva, Z. Levi, S. Alexandrova and H. Hofmeister, Journal of Applied Physics **92**, 4678 - 4683 (2002).
164. G. Ledoux, O. Guillois, D. Porterat, C. Reynaud, F. Huisken, B. Kohn and V. Paillard, Physical Review B **62** (23), 15942 (2000).
165. D. A. Porter, *Phase Transformations in Metals and Alloys*, 3 ed. (Taylor and Francis Group, 2009).

166. S. P. Withrow, C. W. White, A. Meldrum, J. D. Budai, D. M. Hembree and J. C. Barbour, Journal of Applied Physics **86** (1) (1999).
167. S. Savchyn, P. G. Kik, R. M. Todi and K. R. Coffey, Physical Review B **77** (205438) (2008).
168. K. Murakami, R. Shirakawa, M. Tsujimura, N. Uchida, N. Fukata and S.-i. Hishita, Journal of Applied Physics **105** (5), 054307-054305 (2009).
169. P. K. Lim, W. K. Tam, L. F. Yeung and F. M. Lam, Journal of Physics: Conference Series **61**, 708-712 (2007).
170. A. R. Wilkinson and R. G. Elliman, Nuclear Instruments and Methods in Physics Research Section B: Beam Interactions with Materials and Atoms **242** (1-2), 303-306 (2006).
171. P. Pellegrino, B. Garrido, C. García, R. Ferré, J. A. Moreno and J. R. Morante, Physica E: Low-dimensional Systems and Nanostructures **16** (3-4), 424-428 (2003).
172. S. Cheylan and R. G. Elliman, Applied Physics Letters **78** (13), 1912-1914 (2001).
173. N. Daldosso, M. Luppi, S. Ossicini, E. Degoli, R. Magri, G. Dalba, P. Fornasini, R. Grisenti, F. Rocca, L. Pavesi, S. Boninelli, F. Priolo, C. Spinella and F. Iacona, Physical Review B **68** (085327) (2003).
174. V. Jan, F. Anna, V. Frantiscaronek, A. Frantiscaronek, H. Jana, ccaron, ková, H. Martin, P. Ivan, Kate, rcaron, K. ina, uring, sová, D. ina and L. Jan, Advanced Functional Materials **18** (18), 2666-2672 (2008).
175. K. Zhuravlev and A. Kobitsky, Semiconductors **34** (10), 1203-1206 (2000).
176. X. Wen, L. V. Dao and P. Hannaford, J. Phys. D: Appl. Phys. **40**, 3573-3578 (2007).
177. J. Linnros, N. Lalic, A. Galeckas and V. Grivickas, Journal of Applied Physics **86** (11), 6128-6134 (1999).
178. O. Guillois, N. Herlin-Boime, C. Reynaud, G. Ledoux and F. Huisken, Journal of Applied Physics **95** (7), 3677-3682 (2004).
179. D. Kovalev, J. Diener, H. Heckler, G. Polisski, N. Künzner and F. Koch, Physical Review B **61** (7), 4485 (2000).
180. C. Garcia, B. Garrido, P. Pellegrino, R. Ferre, J. A. Moreno, L. Pavesi, M. Cazzanelli and J. R. Morante, Physica E: Low-dimensional Systems and Nanostructures **16** (3-4), 429-433 (2003).
181. A. Hryciw, A. Meldrum, K. S. Buchanan and C. W. White, Nuclear Instruments and Methods in Physics Research Section B: Beam Interactions with Materials and Atoms **222** (3-4), 469-476 (2004).
182. V. Vinciguerra, G. Franzo, F. Priolo, F. Iacona and C. Spinella, Journal of Applied Physics **87** (11), 8165-8173 (2000).
183. J. Krustok, H. Collan, M. Yakushev and K. Hjelt, Physica Scripta **T79**, 179-182 (1999).
184. Y. P. Varshni, Physica **34** (1), 149-154 (1967).
185. H. Rinnert, O. Jambois and M. Vergnat, Journal of Applied Physics **106** (2), 023501-023507 (2009).
186. J. Heitmann, F. Müller, L. Yi, M. Zacharias, D. Kovalev and F. Eichhorn, Physical Review B **69** (19), 195309 (2004).
187. M. L. Brongersma, P. G. Kik, A. Polman, K. S. Min and H. A. Atwater, Applied Physics Letters **76** (3), 351-353 (2000).
188. J. Derr, K. Dunn, D. Riabinina, F. Martin, M. Chaker and F. Rosei, Physica E: Low-dimensional Systems and Nanostructures **41** (4), 668-670 (2009).

189.   A. Franceschetti, Physical Review B (Condensed Matter and Materials Physics) **76** (16), 161301-161304 (2007).

190.   Y. Fukaya, A. Kawasuso, K. Hayashi and A. Ichimiya, Applied Surface Science **237** (1-4), 29-33 (2004).

191.   W. Vogel, S. Botti and S. Martelli, Journal of Materials Science Letters **17** (7), 527-529 (1998).

192.   Z. Baisheng, Y. Jilian, J. Lan and Y. Chuntang, Acta Cryst. **A46**, 435-437 (1990).

193.   P. D. J. Calcott, K. J. Nash, L. T. Canham, M. J. Kane and D. Brumhead, J. Phys.: Condens. Matter **5**, L91-L98 (1993).

194.   J. Heitmann, D. Kovalev, M. Schmidt, L. X. Yi, R. Scholz, F. Eichhorn and M. Zacharias, Materials Research Society **737** (2003).

195.   A. Wellner, V. Paillard, H. Coffin, N. Cherkashin and C. Bonafos, Journal of Applied Physics **96** (4), 2403-2405 (2004).

196.   M. Kadleíková, J. Breza and M. Veselý, Microelectronics Journal **32** (12), 955-958 (2001).

197.   R. N. Favors, Y. Jiang, Y. L. Loethen and D. Ben-Amotz, Review of Scientific Instruments **76** (3), 033108-033105 (2005).

198.   C. Bonafos, B. Colombeau, A. Altibelli, M. Carrada, G. Ben Assayag, B. Garrido, M. López, A. Pérez-Rodríguez, J. R. Morante and A. Claverie, Nuclear Instruments and Methods in Physics Research Section B: Beam Interactions with Materials and Atoms **178** (1-4), 17-24 (2001).

199.   R. Tubino, L. Piseri and G. Zerbi, The Journal of Chemical Physics **56** (3), 1022-1039 (1972).

200.   R. K. Soni, L. F. Fonseca, O. Resto, M. Buzaianu and S. Z. Weisz, Journal of Luminescence **83-84**, 187-191 (1999).

201.   D. Gracin, A. Gajovic, K. Juraic, M. Ceh, Z. Remes, A. Poruba and M. Vanecek, Journal of Non-Crystalline Solids **354** (19-25), 2286-2290 (2008).

202.   S. K. Ram, M. N. Islam, P. Roca i Cabarrocas and S. Kumar, Thin Solid Films **516** (20), 6863-6868 (2008).

203.   M. N. Islam and S. Kumar, Applied Physics Letters **78** (6), 715-717 (2001).

204.   R. Tsu, J. Gonzalez-Hernandez, S. S. Chao, S. C. Lee and K. Tanaka, Applied Physics Letters **40** (6), 534-535 (1982).

205.   S. B. Concari and R. H. Buitrago, Semiconductor Science and Technology **18** (9), 864-869 (2003).

206.   I. Stenger, B. Gallas, B. Jusserand, S. Chenot, S. Fisson and J. Rivory, Eur. Phys. J. Appl. Phys. **44** (1), 51-57 (2008).

207.   S. Yerci, U. Serincan and I. Dogan, Journal of Applied Physics **100**, 074301 (2006).

208.   G. Viera, S. Huet and L. Boufendi, Journal of Applied Physics **90** (8), 4175-4183 (2001).

209.   D. Mukherjee, A. Prakash and M. R. Zachariah, Aerosol Science **37**, 1388-1399 (2006).

210.   H. M. Lu and Q. Jiang, Langmuir **21** (2), 779-781 (2004).

211.   R. J. Jaccodine, Journal of The Electrochemical Society **110** (6), 524-527 (1963).

212.   M. C. Rossi, S. Salvatori, F. Galluzzi and G. Conte, Materials Science and Engineering B **69-70**, 299-302 (2000).

213.   V. Osinniy, S. Lysgaard, V. Kolkovsky, V. Pankratov and A. N. Larsen, Nanotechnology **20** (19), 195201 (2009).

5   Silicon and erbium co-implanted SiO$_2$

5.1   Introduction

Rare-earth doped glasses are routinely employed as gain media in optical amplifiers and lasers[214], the most common example being the erbium doped fiber amplifier (EDFA) for telecommunications applications. In the EDFA, stimulated emission arising from an electronic transition between the 1st excited state ($^4I_{13/2}$) and the ground state ($^4I_{15/2}$) of trivalent Er (Er^{3+}) produces gain for optical signals around 1.5μm. However, the very well defined, narrow electronic transitions of rare-earth ions places specific and demanding requirements on the optical pump source. The pumping efficiency is maximized in the EDFA for example using a combination of wavelength stabilized 980nm and 1480nm lasers, which correspond to the Er $^4I_{11/2}$ and $^4I_{13/2}$ intra-4f electronic transitions respectively. The relatively small absorption cross section ($\sim 10^{-21}$cm^2) for these transitions means that fiber lengths of 10's of meters are generally required to obtain a reasonable gain. This can be improved to some extent by increasing the Er concentration in the silica glass, although the relatively low solubility of Er in pure silica can result in the formation of Er ion clusters when the Er concentration exceeds $\sim 10^{20}$cm^{-3}. This reduces amplifier efficiency due to non-radiative decay processes such as pair induced quenching (PIQ), co-operative up-conversion (CUC) and excited state absorption (ESA) arising from parasitic Er ion-ion interactions. The solid solubility of Er in silica can be improved, for example by co-doping with Alumina (Al$_2$O$_3$) to produce an aluminosilicate glass[214, 215] and recent developments to mitigate Er clustering were also reported after co-doping Er with Ytterbium (Yb), which has led to the development of short length (cm scale), relatively high gain fiber amplifiers[216, 217].

An alternative route to improving amplifier efficiency is to enhance the Er cross section by introducing 'photo-sensitizers'. For example, intrinsic defect states in *chalcogenide* (Ge$_{33}$As$_{12}$Se$_{55}$) glasses were shown to exhibit a broad absorption edge that overlaps the Er 4*f*-shell electronic transitions leading to an enhanced absorption cross section[218]. The sensitization of Er ions in the presence of silicon nanocrystals (Si-NCs) in silica films has also been demonstrated[219, 220] and this in particular opens a potential route for CMOS compatible optical gain[221, 222] and Si-based lasing[223]. This material system has already been proposed as an active

gain medium for erbium doped waveguide amplifier (EDWA) devices[224], which could be monolithically integrated into a Si processor for inter-chip communications in future computing applications. To date this material system has yielded some impressive figures such as an enhancement of the Er cross section of 4 to 5 orders of magnitude and a room temperature (RT) photoluminescence (PL) enhancement of 2 to 3 orders of magnitude compared with standard Er doped silica. Such an efficient excitation of the Er proceeds due to the broad, continuous UV/visible Si-NC band-edge absorption, which is characterized by a much larger cross section (~10^{-15} to 10^{-16}cm^2)[225] than the Er^{3+}. The absorption of high energy photons generates electron-hole pairs in the Si-NCs, the recombination of which, rather than resulting in the emission of a photon, leads to the excitation of local Er^{3+} ions. Such an excitation scheme facilitates broadband pumping of the Er with low power laser diodes or even flash lamps at a fraction of the cost of laser pumped systems[226].

In spite of the obvious advantages, it is apparent that a deeper understanding of the exact mechanism of the 'sensitization' is required if these materials are to find application in future optoelectronic devices. Several notable works have offered insight into the most likely schema but this remains a persistent issue of debate. Certainly, there is strong evidence in support of a Förster type resonant energy transfer (FRET) model, in which quantum mechanical interactions of oscillating electromagnetic fields results in the exchange of virtual photons, (a dipole-dipole exchange interaction) between Si-NC excitons and the 4-f shell electrons in the Er^{3+} ions[227].

For example, Watanabe *et al*[228, 229] reported narrow periodic 'dips' in the low temperature Si-NC PL spectra around 800nm from samples containing a variety of rare-earth co-dopants such as neodymium (Nd^{3+}) and thulium (Tm^{3+})[229] as well as Er[228]. The position of these 'dips' were well correlated with the rare-earth electronic transitions and represent strong evidence of a combination of phonon assisted and quasi-direct Si-NC exciton recombination leading to a resonant energy transfer between Si-NCs and Er^{3+} ions. However, the observed Si-NC PL quenching across the entire spectrum as the rare-earth concentration is increased suggests the presence of an additional (and perhaps dominant) non-resonant energy transfer mechanism. Recently, Izeddin *et al*[230] proposed that the transfer mechanism was the result of a combination of 'hot' carrier phonon assisted relaxation and exciton recombination in the Si-NCs.

In any case and without loss of generality to the debate, what appears critical is the short range nature of the Si-NC-Er interaction, which depends on the Er dispersion in the matrix relative to the formation site of Si-NCs during thermal treatment. Co-locating Si-NCs and Er at specific depths in a host matrix using ion implantation is therefore expected to be of real benefit in optimizing the sensitizing effect. Using *Monte Carlo* based simulations such as the stopping and range of ions in matter (SRIM-2003 algorithm) one can obtain an accurate prediction of the depth and concentration profiles of both Si and rare-earth ions in silica.

The microscopic examination and *in-situ* chemical characterization of such materials is also imperative in understanding the luminescence process and provides physical substance to the debate surrounding the Er 'sensitization'. In particular, in this chapter we present a combined analysis of high resolution scanning transmission electron microscopy (STEM) images and electron energy loss spectra (EELS), which reveal a high spatial correlation between Si-NCs, Er and oxygen (O) in silica (SiO$_2$) after Si and Er co-implantation followed by a single high temperature (1100°C) annealing step in an N$_2$ ambient. Furthermore, by comparison with a *control* sample of Er doped SiO$_2$, prepared in exactly the same manner but without Si-NCs, we note that the formation of Si-NCs in the presence of Er appears to limit the diffusion, size and likely chemical nature of Er agglomerates, particularly important for high concentrations of Er where there is a susceptibility to cluster and/or complex formation[231].

We propose that these observations correspond to Er-O complexes within an amorphous silicon (*a*-Si) shell at the Si-NC/SiO$_2$ interface. The presence of a crystalline phase at the Si-NC centre, verified by High Resolution Electron Micrographs (HREM) and dark field (DF) diffraction contrast images and the low solubility of Er in crystalline Si (*c*-Si) would tend to suggest a preferential Er agglomeration toward the Si-NC/SiO$_2$ interface during formation, particularly when high concentrations of both Si and Er are obtained in a narrow region of the SiO$_2$ after co-implantation. The absence of narrow Stark related features in the Er emission spectrum at low temperature and an inhomogeneous broadening with increasing temperature, which are characteristic of Er confined within an amorphous, rather than a crystalline host further support these hypotheses. After comparing the luminescence to that from a SiO$_2$:Er *control* sample prepared in exactly the same manner but without Si-NCs, we find that, despite the observed spatial correlation, only a small fraction (~7%) of the Er are efficiently sensitized by

the Si-NCs. This is likely the result of a complexity of Auger-like non-radiative losses in both the Si-NCs at high pump flux, exacerbated by the low density of relatively large sensitizers (Si-NCs) and via Er ion-ion interactions on account of the observed clustering.

By varying the anneal conditions for an Er and Si co-implanted oxide on Al$_2$O$_3$ (sapphire) we have been able to isolate the effect of Si-NC size on the Er luminescence intensity. These results reveal that the sensitizing efficiency is proportional to the inverse Si-NC mean diameter and is increased by around an order of magnitude when Er is co-located with an ensemble Si-NC population with a mean diameter of 1.25nm compared to 2.45nm. This observation is in excellent agreement with other works[227, 232] and may be attributed to an increased overlap of Si-NC emitting and Er absorbing states and an increase in the oscillator strength of small Si-NCs. In addition, we find that the measured Er PL lifetime is also a function of the Si-NC size, in particular that it increases with the inverse Si-NC mean diameter. Similar reports recently attributed this to a variation in the local density of optical states (LDOS) due to the interaction between the Er^{3+} ions and the scattering field from the SiO$_2$/Si-NC interface, which increases the Er radiative recombination rate. Such a modification is expected to manifest in the observation of shorter PL lifetimes for Er close to larger Si-NCs in a similar way to the 'Purcell effect'.

5.2   Experimental details

5.2.1   Sample Preparation

The first sample set was prepared by collaborators at the Surrey ion beam centre according to the following procedure. A 500nm SiO$_2$ layer was grown by 'wet' thermal oxidation of (100) Si at 1000°C followed by the implantation of Er at 300keV for a range of concentrations according to **Table 5-1**.

All of the samples with the exception of sample H were then implanted with Si$^+$ ions at 80keV to an areal density of 8x10^{16}cm^{-2}. The samples were then subjected to a single anneal at 1100°C for 1 hour in an N$_2$ ambient to remove implantation damage, to obtain Si-NCs in samples J to N and to activate the Er in all of the samples.

Sample ID	Implanted Si concentration (x10^{16}at/cm^2)	Implanted Er concentration (x10^{15}at/cm^2)	Measured Er concentration[*] (x10^{15}at/cm^2)	
			RBS Detector 1	RBS Detector 2
H	0	3	No data	
J	8	3	3.37	3.27
K	8	1.5	1.54	1.52
L	8	0.8	0.79	0.79
M	8	0.3	0.32	0.3
N	8	0	-	

Table 5-1 Implanted concentrations of Si and Er in samples H - N

[*] For each sample, the Er concentration was determined from Rutherford backscattering spectroscopy (RBS) by collaborators at the University of Surrey in the group of Dr. Chris Jeynes[233].   M. Webb, Internal communication report on RBS results, G390:7, Job No. 1657, 2007.

In order to examine the Si-NC size effect on the sensitization of Er, a second sample set (G$_1$ to G$_4$ described in the previous chapter), prepared by collaborators at the Surrey Ion beam Centre in the group of Prof. Russ Gwilliam is described. For this set, a 500nm thermal oxide layer was grown from sputtered Si on Al$_2$O$_3$ (sapphire)†. All of the samples in this set were co-implanted with Er at 400keV and Si at 110keV to areal densities of 3×10^{15}cm^{-2} and 8×10^{16}cm^{-2} respectively.

The samples were annealed in an N$_2$ ambient using a *Jipelec* rapid thermal processing (RTP) unit at McMaster University, according to the conditions described in **Table 5-2**.

Sample ID	Anneal temperature, T_A (°C)	Anneal time, t_A (s)
G$_4$	1100	300
G$_3$	1050	120
G$_2$	1100	60
G$_1$	1100	10

Table 5-2 Anneal conditions for Si-NC:Er samples on Al$_2$O$_3$ (samples G$_1$ – G$_4$)

All of the samples were exposed to a short (10 minute) lower temperature (500°C) treatment in an N$_2$:H$_2$ (5%) forming gas to passivate the so-called 'dangling bond' (P_b) SiO$_2$/Si-NC interface type defects[234].

---

† Preparing these samples on Al$_2$O$_3$ facilitated pumping via the substrate as well as the Raman spectroscopy described in the previous chapter

5.2.2   Photoluminescence Spectroscopy

For room temperature (RT) PL, the samples were excited using a 10.3mW CW 375nm solid state *Coherent cube* laser diode. The laser was focused onto the sample using a 40x microscope objective lens to a spot size determined, using a *Graticules Ltd* calibrated micro-scale (0.1in/100 lines) and *Panasonic Super Dynamic* Colour CCTV camera to be ~120μm in diameter. The laser power was measured at the sample position with a *Sensor-und Lasertechnik LP20* pyrometer calibrated at 4.93V/W and a *Tektronix* digital storage oscilloscope (DSO).

In order to demonstrate 'broad-band' pumping of the Er via the Si-NCs a commercial *Fenix TK10* flash light was used as the excitation source.

The PL was collected con-focally, dispersed by a single 150 lines/mm grating in a 0.5m monochromator arrangement and detected using an N$_2$-cooled *Jobin Yvon* Indium Gallium Arsenide (InGaAs) array detector.

For the low temperature PL, samples were mounted on the cold finger of a recycling Helium (He) cryostat. Photo-excitation was provided by the 375nm laser diode at 10.3mW, with an unfocussed spot size of ~3mm. The PL was collected via focusing optics and dispersed in a 1m monochromator arrangement by a 600 lines/mm grating and detected using an N$_2$-cooled *Edinburgh Instruments EI-L* single channel Germanium (Ge) detector. The PL was modulated using an optical chopper and amplified using referenced 'lock-in' detection to improve the signal to noise ratio. The sample temperature was monitored via thermocouple and controlled with a built-in heater element using an *Oxford Instruments ITC 503* temperature controller. All of the spectra were corrected for the system response, which was pre-characterized using a Xenon lamp.

Measurements of the PL transients, conducted in collaboration with the group of Dr. Tony Kenyon at the University College London (UCL), were obtained after optical excitation using either the 476 or 488nm lines of an Ar$^+$ laser. The laser was switched using a *Pockell* cell arrangement and the PL transients detected using an IR sensitive *Hamamatsu* photomultiplier with a resolution, limited by the preamplifier of ~5μs. The transient waveforms were recorded on a digital storage oscilloscope (DSO).

5.2.3   Transmission and Scanning Transmission Electron Microscopy (TEM/STEM)

Transmission and Scanning Transmission Electron Microscopy (TEM and STEM) measurements were conducted in collaboration with colleagues in the group of Dr. Ursel Bangert at the University of Manchester, School of Materials Science. Energy Filtered Transmission Electron Microscopy (EFTEM) maps were obtained by filtering electrons at 29eV, which corresponds to the Er O$_{2,3}$ edge. High Resolution TEM (HRTEM) and Dark Field (DF) diffraction contrast images were acquired with a *Tecnai* Field Emission Gun TEM (FEGTEM) microscope operating at 300kV and the sample aligned with the Si <110> zone axes. Operation of and advice regarding the STEM was provided by Dr. Mahri Gass at the *Super-STEM*, Daresbury reseach facility. This facility houses an aberration corrected STEM, which is fitted with a *Nion* Mark II quadrupole-octupole corrector[235] operating at 100keV and this was employed to acquire HRTEM, Bright Field (BF) and High Angle Annular Dark Field (HAADF) images. An Ultra High Vacuum (UHV) *Gatan Enfina* system was used to obtain spectrum images.

5.3   Results and discussion

5.3.1   Si-NC-Er energy exchange in SiO$_2$:Er, Si-NC

In order to qualify the presence of a 'photo-sensitization' effect of Si-NCs on Er co-implanted species in these samples, two experiments were conducted. Firstly, by measuring the PL spectra for all of the samples in the first set as a function of Er concentration it is possible to examine the quenching of the Si-NC PL around 800nm (~1.6eV) relative to the enhancement of the Er PL around 1534nm (~0.81eV).

Secondly, by choosing pumping wavelengths that are not coincident with the absorption spectra of Er^{3+} in SiO$_2$ it is possible to separate the direct (resonant) from the indirect (non-resonant) excitation mechanisms. In this case we measured the Er luminescence spectrum at room temperature after excitation with a standard broad band flash light.

5.3.1.1 Effect of increasing Er concentration in samples J - N

The spectra and peak intensity for the Si-NC and Er luminescence from co-implanted samples, J – N are shown in **Figure 5-1 (a)** and **(b)** respectively.
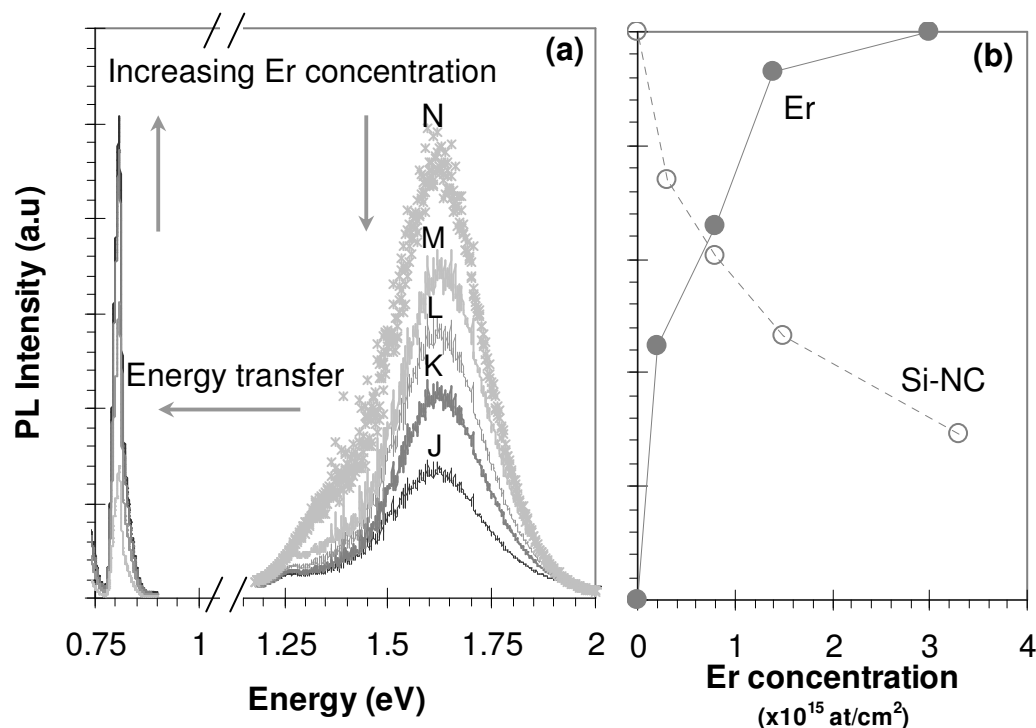
Figure 5-1 (a) Normalised RT spectra and (b) peak intensity of the Si-NC and Er luminescence from co-implanted oxide samples J – N

Two distinct emission bands are evident from the RT PL spectra in **Figure 5-1 (a)**; a broad (FWHM ~260meV), featureless band centered ~1.6eV (800nm), attributed to the annihilation of excitons inside the Si-NCs and a narrow (FWHM ~20meV) peak centered ~0.8eV (1534nm) due to intra-4*f* electronic transitions of the Er^{3+}. As shown in **Figure 5-1 (b)**, the intensity of the broad Si-NC band diminishes monotonically with increasing Er concentration whilst the narrow Er related spectra emerges and increases sharply with increasing Er concentration. This result indicates that the two processes are competitive and the ratio of Er PL increase to the Si-NC PL decrease of ~0.75 implies that this energy exchange process is extremely efficient.

5.3.1.2 Broad band pumping of the Er in sample J (SiO$_2$:Er,Si-NC)

A broadband pumping scheme is presented in which the Er^{3+} ions are excited indirectly via Si-NCs in co-implanted oxide (sample J) using a battery powered *Fenix TK10* (60 lumens) flash light. The flash light employs a commercial *Cree premium XR-E* lighting class blue-white LED[236] with a characteristic emission spectrum as shown in **Figure 5-2**.
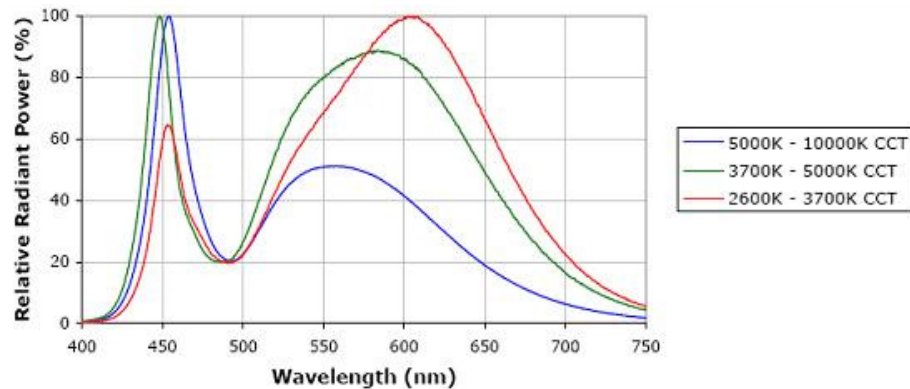
Figure 5-2 Emission spectrum for the commercial *Cree premium XR-E* **lighting class LED, courtesy of [236]**

To avoid coincidence of the flash light excitation with the principal absorption bands of SiO$_2$:Er[237] a 530nm long pass and a 632nm edge filter were included in the optical excitation path. The relative excitation power was varied using a combination of neutral density filters and the result is shown in **Figure 5-3**.
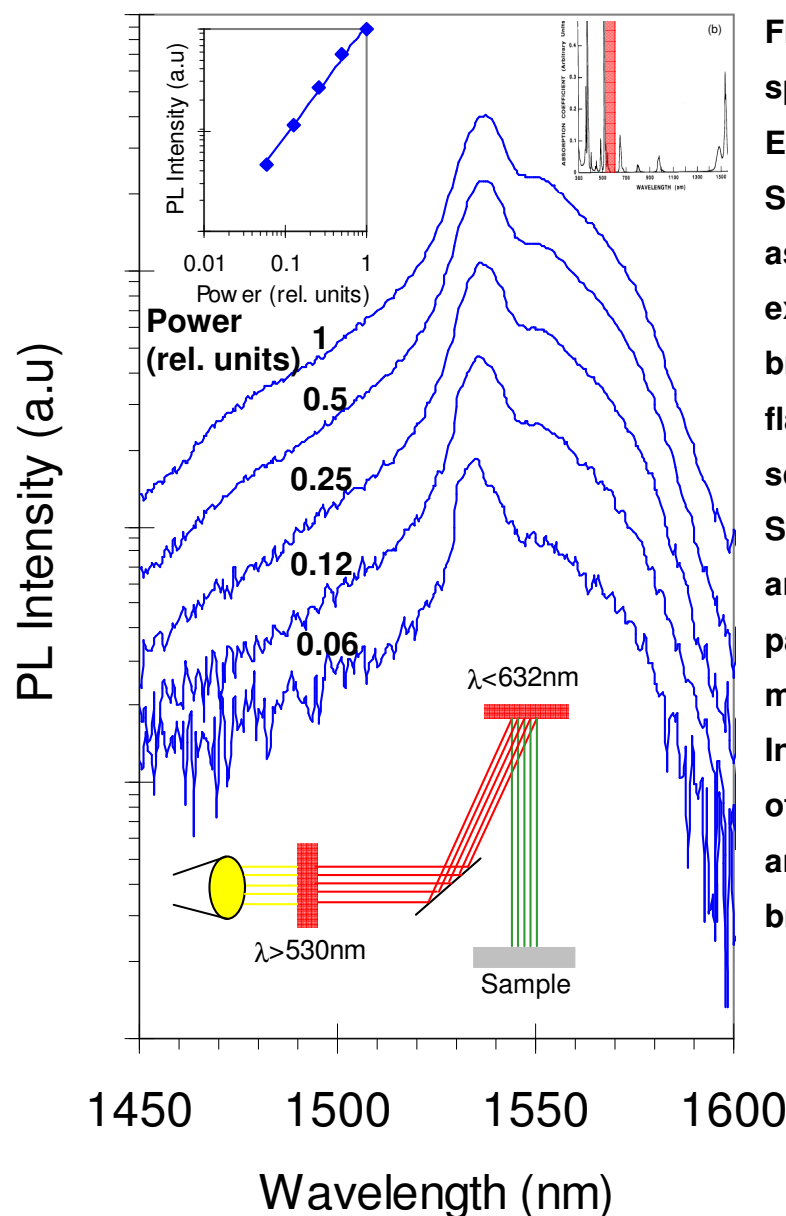
Figure 5-3 RT Er PL spectra and inset (top left) Er PL intensity from SiO$_2$:Er,Si-NC (sample J) as a function of relative excitation power using a broad band *Fenix TK10* flash light (note the log-scales). Inset (top right): SiO$_2$:Er absorption spectra and approximate excitation pass band (red bar), modified after Miniscalo[237]. Inset (bottom): Schematic of the experimental arrangement for selective broadband excitation

The shape of the Er PL spectrum is characteristic of that of Er doped SiO$_2$ and the PL intensity is linear with excitation power over the experimental range. We note from **Figure 5-3** inset (top right) that the excitation pass band partially overlaps the tail of the SiO$_2$:Er absorption band around 520nm, which corresponds to the Er $^2H_{11/2}$ optical transition. However, similar to that reported earlier[226], a factor 2 increase in the PL intensity was observed when the 530nm long pass filter was removed from the excitation path indicating that a significant fraction of the observed excitation with the 530nm filter included must be indirect, presumably via the Si-NCs. The increase in intensity after removing the 530nm long pass filter is likely the result of additional short wavelength resonant excitation from lamp emissions around 450nm where the spin-orbit and Stark splitting leads to a

complex overlap of the $^4F_{3/2}$ and $^4F_{5/2}$ Er^{3+} electronic levels. Obtaining RT luminescence after low power, non-resonant broadband pumping is clear evidence for the sensitization of Er via Si-NCs in sample J. From an engineering viewpoint, such a result has important implications for Si-based optoelectronic device applications operating in the telecommunications band around 1.5µm.

5.3.2 Structural, chemical and optical properties of samples H (SiO$_2$:Er) and J (SiO$_2$:Er, Si-NC)

5.3.2.1 Transmission and Scanning Transmission Electron Microscopy (TEM/STEM)

Figure 5-4 (a) is a HAADF image of sample H (SiO$_2$:Er) and **Figure 5-4 (b)** is an EFTEM map of the same image after filtering at 29eV, which corresponds to the Er O$_{2,3}$ absorption edge.
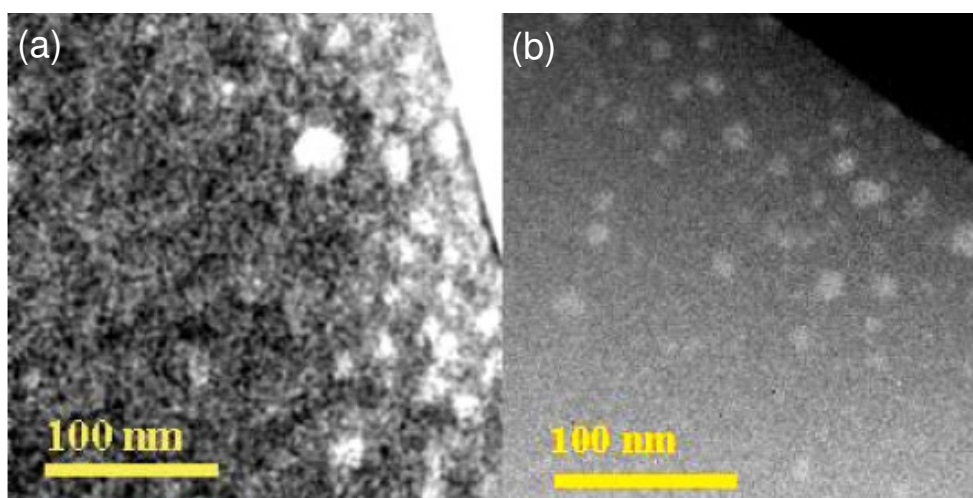
Figure 5-4 (a) HAADF image and (b) EFTEM map of the Er O$_{2,3}$ edge (29eV) for SiO$_2$:Er (sample H) which reveal a band of relatively large (10 to 40nm in diameter), amorphous, Er-rich clusters (bright) against the SiO$_2$ (dark) background

The implanted Er ions in sample H appear to have agglomerated into large amorphous structures, as determined by Fourier transforms (FT) of the HRTEM images, with diameters of 10 to 40nm in a band which extends from the surface of the SiO$_2$ to a depth of ~170nm. The migration and Er cluster formation in silica was previously reported by Kollewe *et al*[238]. They observed a similar re-distribution and agglomeration of the Er ions in pure silica, which they attributed to an introduction of stress or density gradients after ion irradiation and Ostwald ripening after high temperature annealing[238]. Point defects in the near surface layers, as a result of the ion irradiation, likely leads to a preferential diffusion in the direction of the surface and lower activation energy for nucleation of the Er atoms during high temperature annealing, similar to that reported for Si in the previous chapter.

In contrast, **Figure 5-5** shows a low magnification HAADF image of sample J, which reveals a ~110nm wide band containing the Si-NCs and Er centred at ~100nm depth below the surface of the SiO$_2$.
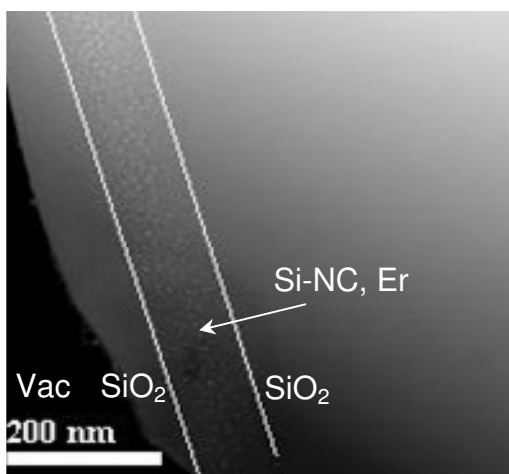
Figure 5-5 Low magnification HAADF TEM image of the SiO$_2$:Er,Si-NC (sample J) showing a ~110nm wide band, ~100nm below the SiO$_2$ surface containing the Si-NCs and Er atoms. The lines are guides to the eye.

The absence of large, amorphous structures and the different distribution of the Er in this sample suggests that the excess Si atoms play an important role as agglomeration centres for the Er ions. **Figure 5-6** shows higher magnification dark field (DF) diffraction contrast images from within the band, acquired under various reflections. These images reveal the presence of much smaller (< 10nm) randomly oriented, spherical crystallites buried in the amorphous SiO$_2$ layer.
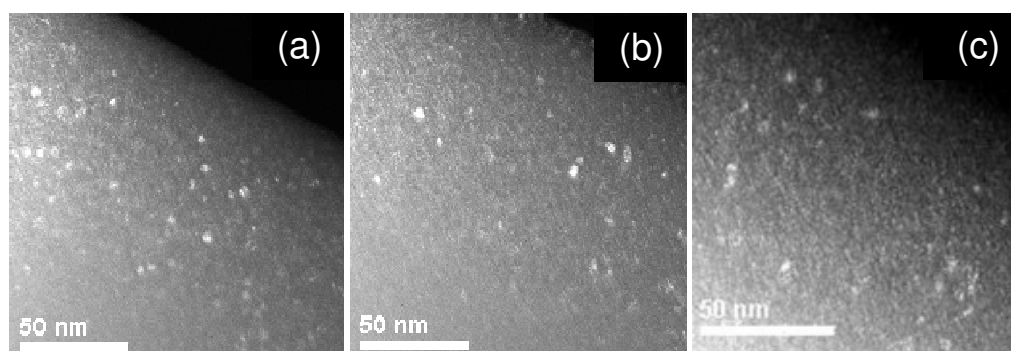
Figure 5-6 TEM DF diffraction contrast images of the Si-NC and Er doped region of sample J for (a) <022>, (b) <111> and (c) <200> reflections respectively

EELS spectrum imaging[239], **Figure 5-7 (a)** was performed in order to determine the chemical composition of the nano-crystals shown in the high magnification HAADF image, **Figure 5-7 (b)**, from within the band. The EELS spectra, from which power law backgrounds were subtracted, were taken from an area on a nano-crystal (red square, red curve) and away from any clusters (blue square, blue curve) in the SiO$_2$. The sample thickness, which was calculated using the *Kramers-Kronig* sum-rule[240] from low loss EEL spectra using standard *Gatan Digital Micrograph* algorithms[241] was determined to be ~20nm. A statistical evaluation revealed the density of the nano-crystals to be ~8x10^{17}cm^{-3} with ~70% of these in the range 3 to 4nm in diameter.
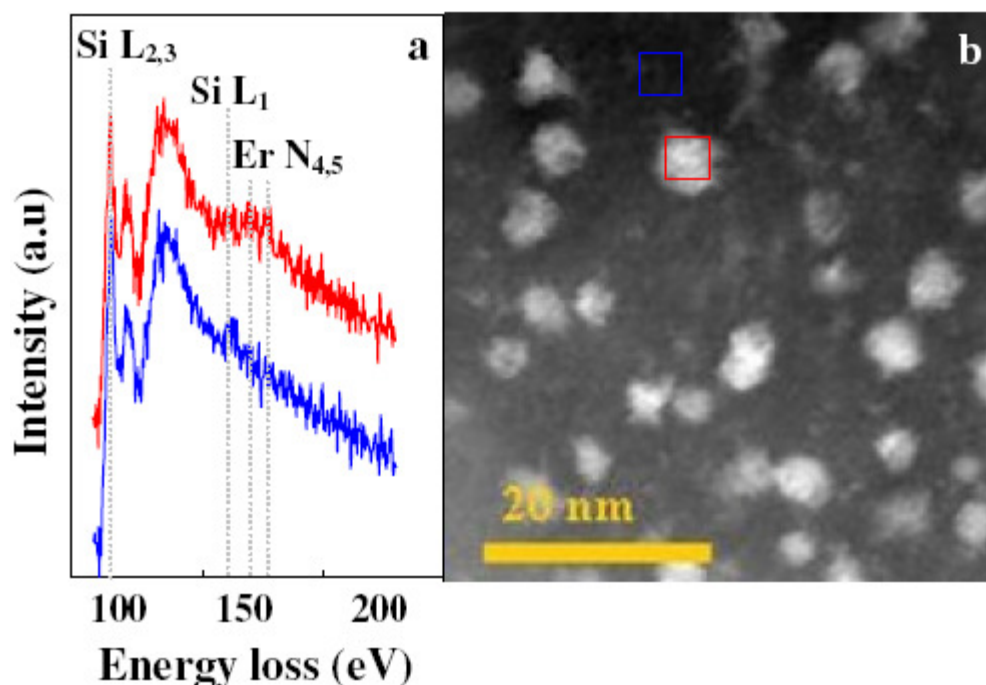
Figure 5-7 (a) EELS spectra (offset for clarity) obtained with the STEM beam ON (red square, red trace) and OFF (blue square, blue trace) a nanostructure shown in (b) high magnification HAADF image of sample J

Figure 5-7 (a) reveals a clear feature in the red spectrum in the energy range 168-175eV, which is characteristic of the Er N$_{4,5}$ edge, whereas there is no such feature in the blue spectrum. This is evidence of the presence of Er at the location of the nano-crystals.

Figure 5-8 (a) is a low magnification HAADF image showing a section of the Si-NC:Er band of sample J. This area was used to obtain intensity maps of the Si L$_{2,3}$, **Figure 5-8 (b)** and Er N$_{4,5}$, **Figure 5-8 (c)** absorption edges from an EEL spectrum image following power law background subtraction very close to the onset of the edges at ~99eV and ~168eV respectively.
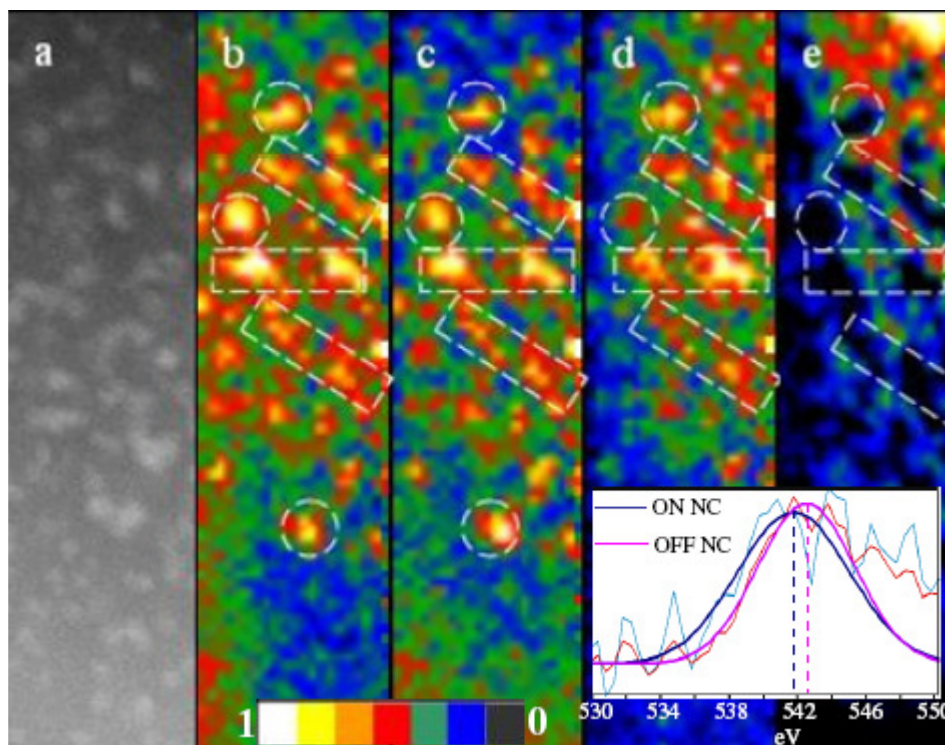
Figure 5-8 (a) HAADF image of the mapped area of sample J, (b) Si L$_{2,3}$ (98-101eV) and (c) Er N$_{4,5}$ (167-177eV) edge intensity maps. (d) FWHM and (e) peak energy of the Gaussian fits to the O -K edge (inset: Blue = nanocluster positions, Red = away from any nanoclusters). Dashed lines indicate correlations in the features of the images and the contrast of the maps corresponds to a colour-scale, which represents the linearly normalised image intensity in arbitrary units

The maps of **Figure 5-8 (b)** and **(c)** reveal an excellent correlation between the Si and Er distribution within the band indicating that Er likely accumulates around the Si-NCs during annealing. We note that there is no substantial Er aggregation outside of the Er:Si-NC band within the SiO$_2$ in sample J.

Figure 5-8 (d) and **(e)** represent the FWHM and energy loss peak of a Gaussian fit to the O K edge with white signifying a broader FWHM and higher energy and black signifying a narrower FWHM and lower energy Gaussian peak respectively.

Rare earth oxides exhibit lower onset energy as well as a split O K edge structure, for which a single Gaussian envelope will yield a lower peak energy and larger FWHM than a Gaussian fit to the single O K peak of pure SiO$_2$[242].

We find that the larger FWHM of the O K edge Gaussian fit is spatially correlated with the Si-NCs, **Figure 5-8 (d)** which in turn are strongly correlated with the Er. These observations are indicative of the presence of Er-O, presumably in a shell around the Si-NCs, in contrast to the narrower Gaussian, which appears elsewhere indicating the presence of pure SiO$_2$. **Figure 5-8 (e)** reveals that the peak energy of the Gaussian fit is also lower in the locations of Er agglomeration supporting the presence of an Er-O complex.

5.3.2.2 Excitation flux dependence of the Er PL (samples H and J)

Figure 5-9 depicts the PL spectra and **Figure 5-10** the relative PL intensities for samples H and J as a function of the excitation (pump) flux.
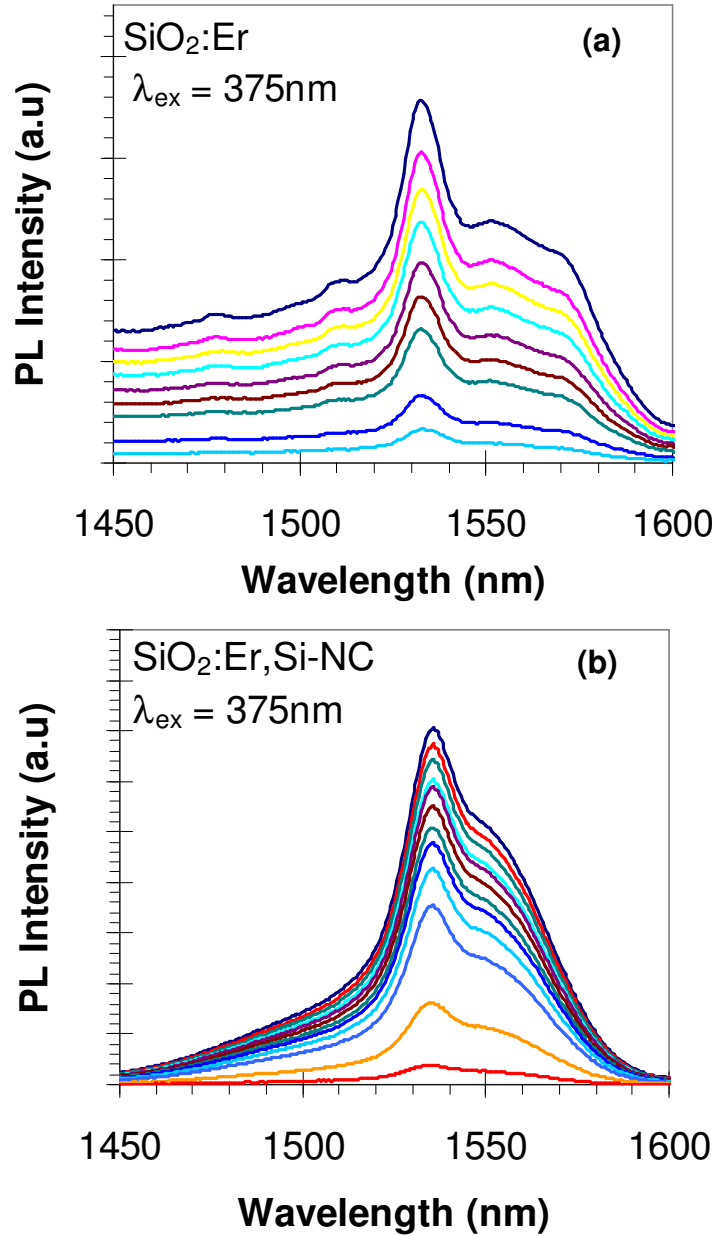
Figure 5-9 PL spectra for (a) SiO$_2$:Er (sample H) and (b) SiO$_2$:Er,Si-NC (sample J) as a function of the pump flux, ϕ in the range 1x10^{17} to 4.5x10^{19}cm^{-2}s^{-1} at 375nm
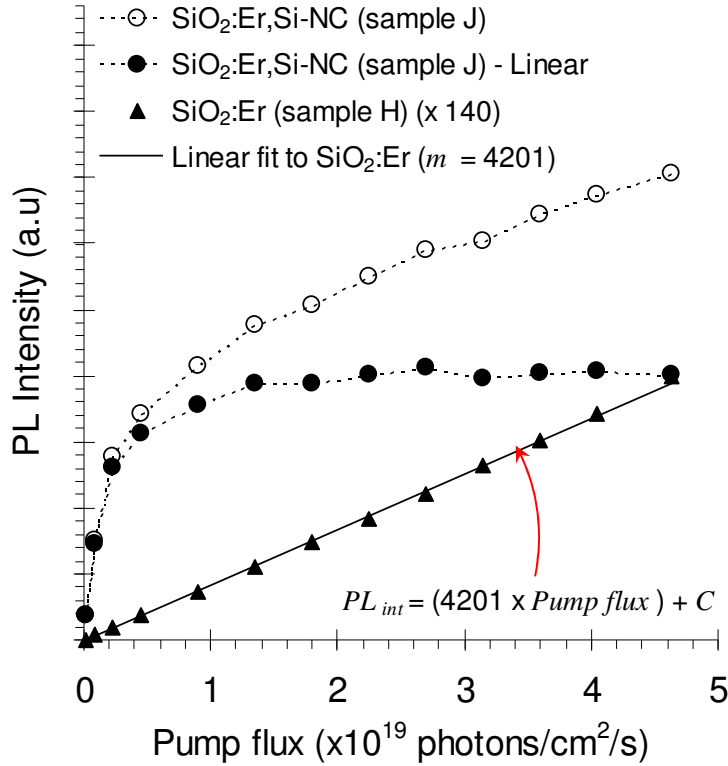
Figure 5-10 Relative PL intensities of SiO$_2$:Er (sample H) and SiO$_2$:Er,Si-NC (sample J) as a function of the pump flux at 375nm. The solid line through the data for sample H is a linear fit and the dashed lines through the data for sample J are guides to the eye

The Er in sample H exhibits a relatively weak RT luminescence intensity, which has a linear dependence on the pump flux across the entire experimental range. In the absence of sensitizers, Er doped SiO$_2$ is directly excited by a weak laser resonance, in this case ~3.3eV, which corresponds to the $^4I_{15/2} \rightarrow {}^2H_{9/2}$ Er transition, with an absorption cross-section[243], σ ~10^{-21}cm^2. The spin orbit and Stark splitting of the Er^{3+} energy levels and possible excitation schema are illustrated by **Figure 5-11**.
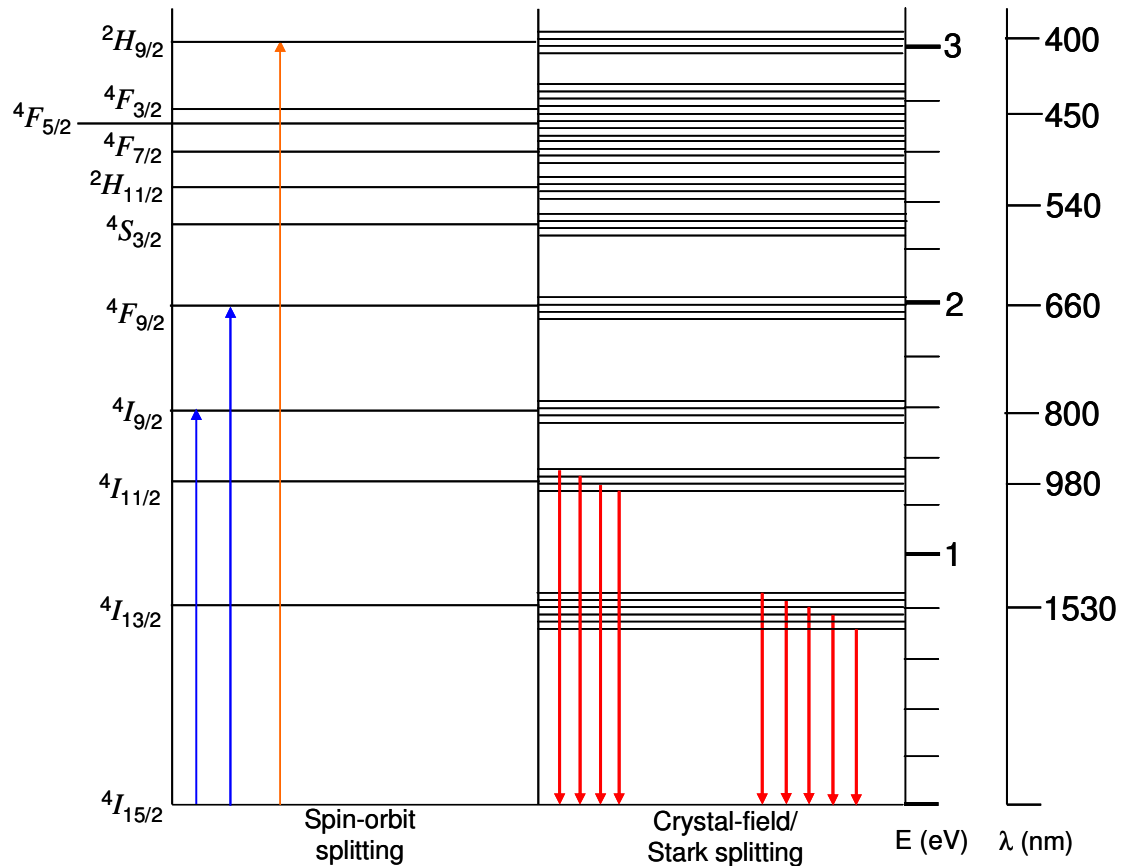
Figure 5-11 Spin-orbit and Stark splitting of the Er^{3+} energy levels. Possible resonant excitation (up-arrows) from the 375nm laser (orange) and Si-NC emission overlap (blue) are shown along with the most common Er emission lines (red down-arrows), adapted after [244]

The RT Er luminescence intensity around 1530nm is more than 3 orders of magnitude higher for the sample containing Si-NCs (sample J) at low pump flux (~10^{17} photons cm^{-2}s^{-1}). However, this enhancement diminishes throughout the range of pumping flux and the efficient Si-NC mediated excitation appears to saturate ~10^{19} photons cm^{-2}s^{-1}.

These observations are explained in terms of the excitation and decay dynamics of the Er excited state for the SiO$_2$:Er and SiO$_2$:Er,Si-NC material systems using a model of rate equations developed earlier by Kenyon *et al*[245]. In this way, the dynamics of the Si-NC and Er luminescent centres are modeled assuming each of them to be adequately represented by simple two-level systems.

187

Quantitative description for the Si-NC and Er luminescent centres - two level system model

For the SiO$_2$:Er material system (sample H), the transition of electrons in the isolated Er luminescent centres, between states N_1^H and N_2^H with a cross-section, σ can only proceed via the absorption of laser photons with flux, ϕ and energy, E. The spontaneous de-population of state N_2^H after time, τ_d may be accompanied by the emission of a photon of energy, $E_3 = E_2 - E_1$ according to **Figure 5-12**.
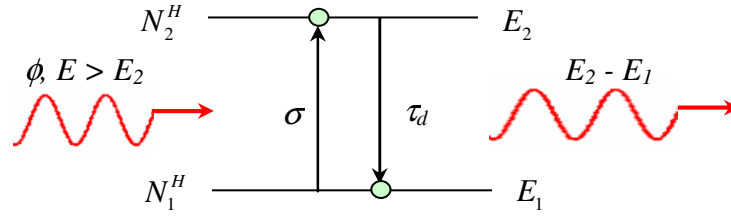
Figure 5-12 Schematic representation of the isolated Er ion as a two-level system in SiO$_2$:Er (sample H)

The rate of change of the population of state N_2^H is given by equation (63):

$$\frac{dN_2^H}{dt} = \sigma\phi N_1^H - \frac{N_2^H}{\tau_d} \tag{63}$$

And assuming all Er ions to be involved in the process, i.e. $N_{Er} = N_1^H + N_2^H$, then equation (63) may be written:

$$\frac{dN_2^H}{dt} = \sigma\phi\left(N_{Er} - N_2^H\right) - \frac{N_2^H}{\tau_d} \tag{64}$$

Under continuous (CW) pumping, the populations rapidly reach a steady state in which the rate of change $\frac{dN_2^H}{dt} = 0$ and equation (64) becomes:

$$\sigma\phi\left(N_{Er} - N_2^H\right) = \frac{N_2^H}{\tau_d} \tag{65}$$

Re-arranging for N_2^H then yields:

$$N_2^H = \frac{\sigma\tau_d\phi N_{Er}}{1 + \sigma\tau_d\phi} \tag{66}$$

For the SiO$_2$:Er,Si-NC system (sample J), the fraction of resonantly absorbed light depends on the exact excitation wavelength. However due to their much larger absorption cross-section ($\sigma_I \sim 10^6 \sigma$), almost all of the absorbed light may be assumed to be via the Si-NCs and the excitation of the Er in sample J should then proceed according to **Figure 5-13**.
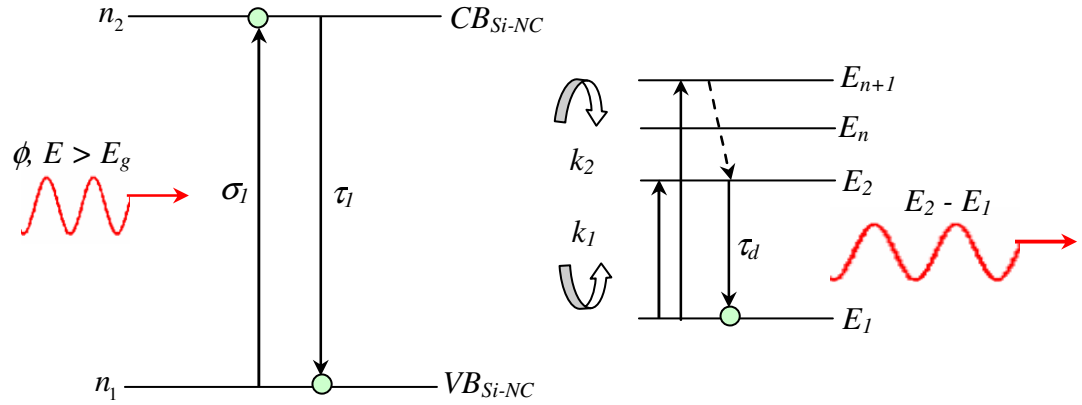
Figure 5-13 Schematic representation of the Si-NC and Er ion as coupled two-level systems in SiO$_2$:Er,Si-NC (sample J)

The process of excitation for the Si-NC can be considered similar to that described for the Er two level system in SiO$_2$:Er but an additional de-populating term is required, $n_2 \left(k_1 N_1^J + k_2 N_2^J \right)$ to account for the transfer of energy from Si-NC state n_2 to the Er ions, either through the ground state or the excited state, with respective transfer coefficients, k_1 and k_2. Then we have for the rate of change of the Si-NC excited state population:

$$\frac{dn_2}{dt} = \sigma_1 \phi n_1 - \frac{n_2}{\tau_1} - n_2 k_1 N_1^J - n_2 k_2 N_1^J \tag{67}$$

And again, assuming $N = n_1 + n_2$, we have:

$$\frac{dn_2}{dt} = \sigma_1 \phi \left(N - n_2 \right) - \frac{n_2}{\tau_1} - n_2 k_1 N_1^J - n_2 k_2 N_2^J \tag{68}$$

As before, CW pumping rapidly leads to a steady state population for the Si-NCs and a concomitant depletion of the Er ground state, such that $\frac{dn_2}{dt} = N_1^J = 0$ and $N_2^J \rightarrow N_{Er}$. Equation (68) then becomes:

$$\sigma_1 \phi \left(N - n_2 \right) = \frac{n_2}{\tau_1} + n_2 k_2 N_{Er} \tag{69}$$

And re-arranging for n_2 yields the Si-NC excited state population:

$$n_2 = \frac{\sigma_1 \tau_1 \phi N}{1 + \sigma_1 \tau_1 \phi + k_2 \tau_1 N_{Er}} \tag{70}$$

The corresponding rate of change of the excited Er population is given by equation (71):

$$\frac{dN_2^J}{dt} = k_1 n_2 N_1^J - \frac{N_2^J}{\tau_d} \tag{71}$$

And under steady state pumping, the excited Er population is then given by equation (72):

$$N_2^J = \frac{k_1 \tau_d n_2 N_{Er}}{1 + k_1 \tau_d n_2} \tag{72}$$

Empirically determined values for all of the defined quantities were either measured or have been obtained from the literature and are given in **Table 5-3**.

Quantity	Description	Value[ref]
τ_d	Er excited state lifetime in SiO$_2$	10ms[246]
N_{Er}	Er peak concentration (meas. RBS)	~3x10^{20}cm^{-3}
k_1	Si-NC - Er ground state transfer coeff.	3x10^{-15}cm^3/s[247]
σ_1	Si-NC excitation cross-section	(~10^{-15}cm^2)[248]
τ_1	Si-NC excited state lifetime (meas. PL transient)	~60µs
N	concentration of Si-NCs (meas. TEM)	~8x10^{17}cm^{-3}
k_2	Si-NC - Er excited state transfer coeff.	See text.

Table 5-3 Parameters describing the excitation mechanisms for the
SiO$_2$:Er,Si-NC material system

The magnitude of k_2 relative to k_1 was previously used to demonstrate that excited state absorption (ESA) could be effective in quenching the Er luminescence[245]. The authors in [245] reasoned that the transfer of energy from the Si-NC into an already occupied Er excited level such as E_2 would simply result in the excitation of carriers to higher states, e.g. from E_2 to E_n or E_{n+1} in **Figure 5-13**. Due to the rapid ($<< \tau_R$) and non-radiative nature of transitions between excited states, the

continuous cycling between such states thus represents an 'energy drain' on the system. They determined that the efficiency with which energy was transferred into the Er excited state was approximately equivalent to that for the ground state transfer, i.e. $k_1 \cong k_2$. From this, they concluded that ESA represented an effective non-radiative decay path for the excited Er population in this material system, which is likely exacerbated by the fact that the excited state lifetimes of the Si-NC n_2 and Er E_2 levels differ by ~2 orders of magnitude.

In this work, k_2 was determined by fitting equation (70) to the measured Si-NC PL peak intensity from samples J to N, which is proportional to n_2 as a function of Er concentration[‡], **Figure 5-14**.
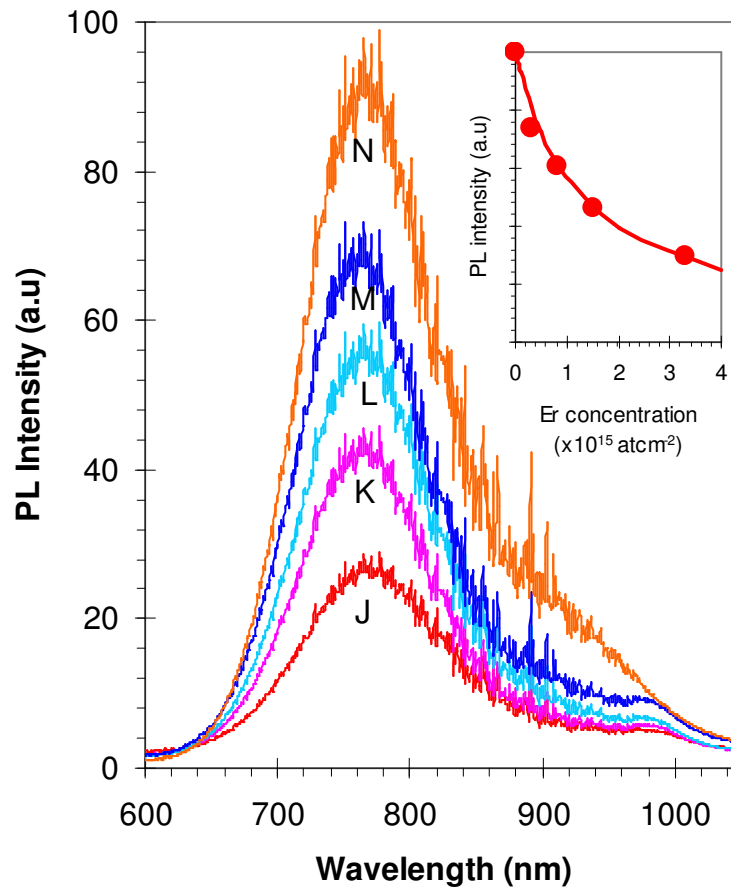
Figure 5-14 Si-NC PL spectra and inset peak intensity for samples J to N as a function of the Er concentration at $\phi \sim 10^{18} \text{cm}^{-2}\text{s}^{-1}$. The red-line is a fit to the data according to equation (70) with $k_2 = 1.35 \times 10^{-16} \text{cm}^3 \text{s}^{-1}$

An excellent fit to the measured data was obtained across the entire Er concentration range with $k_2 = 1.35 \times 10^{-16} \text{cm}^{-3}\text{s}^{-1}$. We note that this is an order of

---

[‡] In fact, $I_{PL} = n_2 / \tau_1$ and so changes in the Si-NC lifetime, τ_1 with Er concentration could affect this result. However, measurements of the Si-NC PL decay transients yielded no dependence on the Er concentration over the experimental range and so τ_1 was assumed to be constant.

magnitude smaller than that obtained previously[245] _and_ that of the ground state transfer coefficient, k_1. This result suggests that the process of energy transfer from the Si-NCs into the Er ground state is favored over that into higher excited states of the Er ions. Whilst the effectiveness of ESA in quenching the Er luminescence is significant, it may not be the principal quenching mechanism in our sample set.

It follows from equations (66) and (72) that the ratio of the Er luminescence intensity for sample J to sample H should depend on the pump flux according to equation (73).

$$R_{PL}(\phi) = \frac{N_2^J}{N_2^H} = \frac{k_1 n_2 (1 + \sigma \tau_d \phi)}{\sigma \phi (1 + k_1 \tau_d n_2)} \tag{73}$$

In fact, we find in agreement with the theoretical model described for Er doped Si[249], that an additional term is required for an adequate fit to describe our measured data, such that equation (73) becomes:

$$R_{PL}(\phi) = \frac{N_2^J}{N_2^H} = \frac{k_1 n_2 (1 + \sigma \tau_d \phi)}{\sigma \phi (1 + \beta \sqrt{k_1 \tau_d n_2} + k_1 \tau_d n_2)} \tag{74}$$

A detailed physical interpretation of the additional term in β, equation (74) was provided by the authors of [[249]], in which it was determined (for the Si:Er system) that non-zero values of β are characteristic of radiative limiting processes that arise, in particular due to Auger-assisted free carrier losses for example via Er-bound excitons or excited Erbium ions. β values previously determined for Er in crystalline Si were ~2 to 3 but we note that the β-parameter required for a good fit to our data is ~30, reflecting a much greater relative Auger quenching in our Si-NC:Er sample, an effect summarized in **Figure 5-15**.
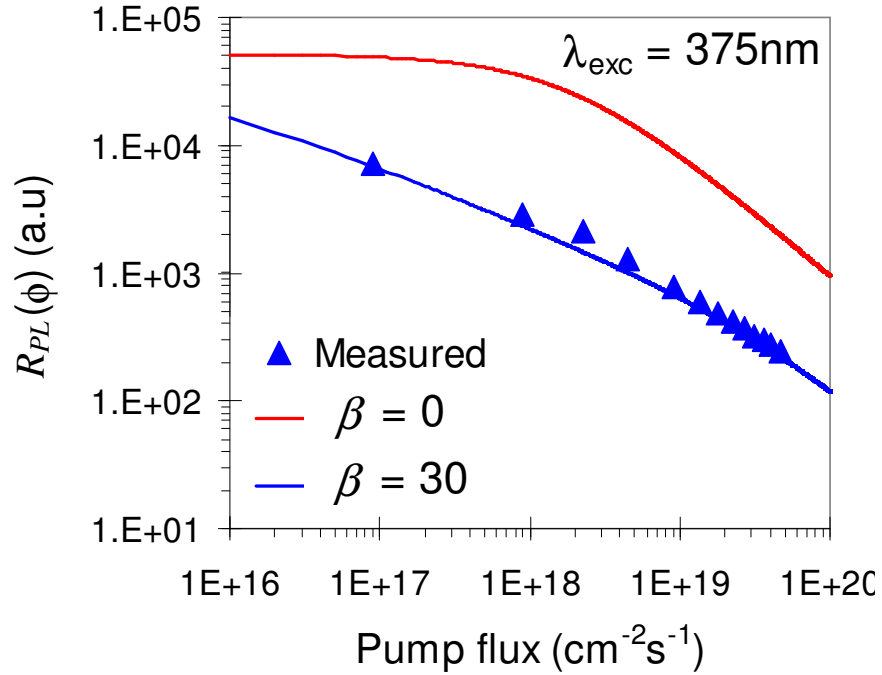
Figure 5-15 Measured (triangles) and calculated ratio of the Er PL peak intensities from equation (74) for SiO$_2$:Er,Si-NC (sample J) and SiO$_2$:Er (sample H) with β = 0 (red line) and β = 30 (blue line) as a function of the pump flux, ϕ at 375nm.

The order of magnitude increase in β obtained here likely reflects an increase in Auger-assisted processes. Presumably, this is in part due to Er ion-ion interactions such as co-operative up conversion (CUC) on account of the observed clustering. For Er concentrations ~10^{20}cm^{-3} a critical Er-Er separation, $R_{up} \leq$ 1nm was already reported for the onset of CUC in a standard SiO$_2$:Er EDFA material[250]. Given that the peak concentration in our sample is similar to this and the fact that we observe Er clustering from our TEM images, it is reasonable to assume even smaller Er-Er distances, which would give rise to an efficient energy migration. We note from the previous chapter that the Si-NC cross section is reduced considerably at high flux, also likely associated with Auger-type loss mechanisms, for which the simple model described here does not account. The large β-value we have obtained may therefore include a contribution from non-radiative losses in the Si-NCs.

An estimate of the contribution to the Er PL directly attributable to efficient excitation via the Si-NCs was determined by fitting equation (74) to our data and comparing this to the curve with β = 0 at ϕ ~ 10^{19}cm^{-2}s^{-1}. This yields a value of

~7%, which is in good agreement with those reported previously[251, 252] and yet this is despite the observed spatial correlation of Si-NCs and Er in sample J.

To put this into context, if we take into account all of the intermediate steps leading to Er excitation in sample J (i.e. photon absorption and exciton creation in the Si-NCs, followed by exciton annihilation resulting in the 'transfer' of energy into a nearby Er ion) then the flux dependent Er PL intensity can be characterized by an 'effective' cross section, σ_{eff} as defined by Franzo *et al*[253] and given by equation (75).

$$\frac{I_{Er}}{I_{Er}^{MAX}} = \frac{\sigma_{eff}\tau_d\phi}{1+\sigma_{eff}\tau_d\phi} \tag{75}$$

Where I_{Er}^{MAX} is the nano-cluster sensitized Er PL fraction and τ_d is the characteristic lifetime of the excited state, which we determined from PL transient measurements, **Figure 5-16** to be ~5ms.
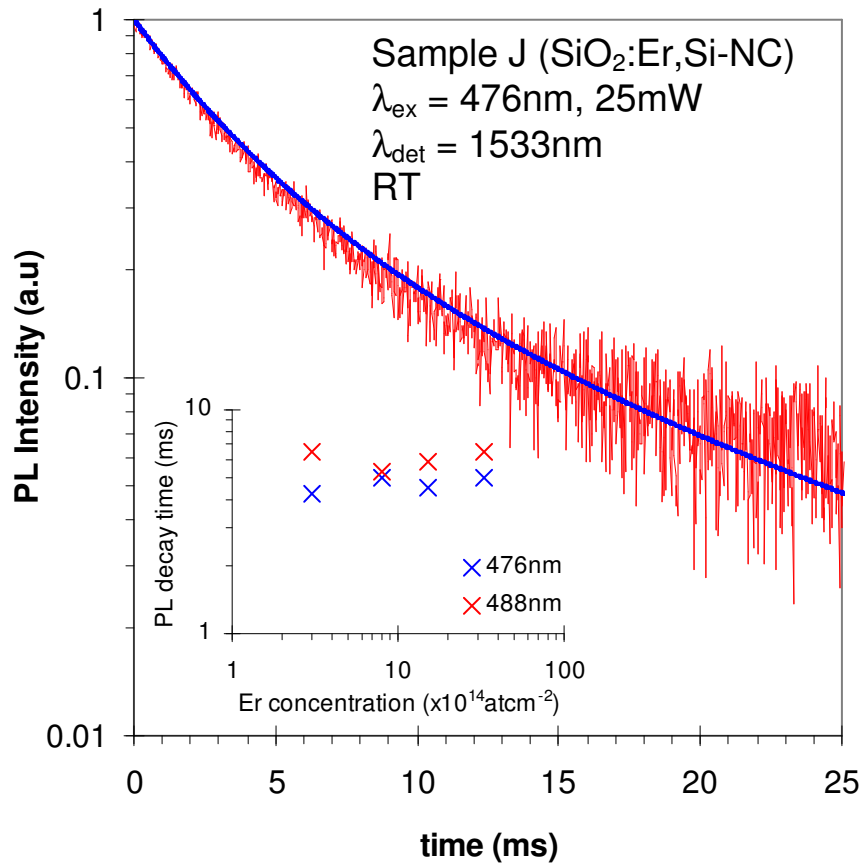
Figure 5-16 Measured Er PL decay transient (red curve) and stretched exponential fit (blue curve) for sample J. Inset: Er PL lifetime (1/e) as a function of Er concentration for samples J – M after excitation at 476nm (non-resonant) and 488nm (resonant)

The 'effective' cross section is then retrieved by fitting equation (75) to the pump flux dependent Er PL intensity from sample J after extracting a linear (direct excitation) contribution from the laser at high flux, **Figure 5-17**.

$$\frac{I_{Er}}{I_{Er}^{MAX}} = \frac{\sigma_{eff}\tau_d\phi}{1+\sigma_{eff}\tau_d\phi}$$
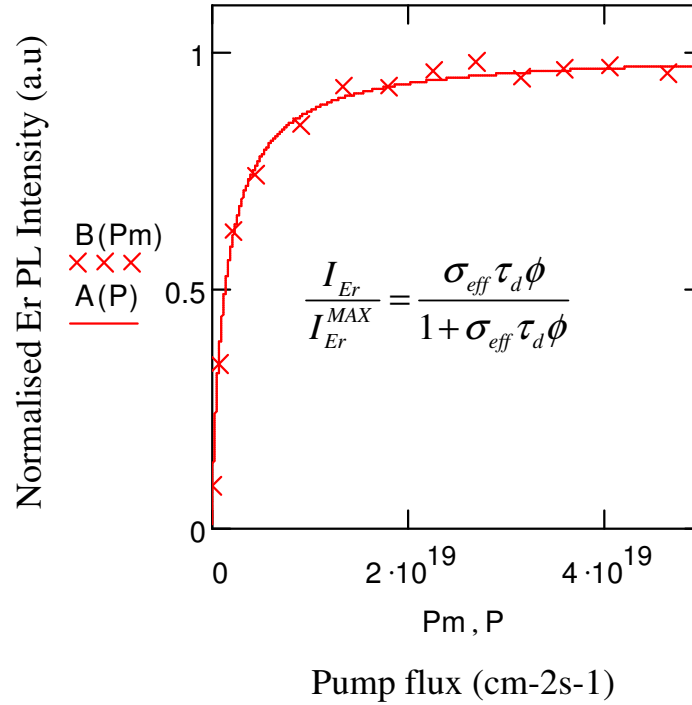
Figure 5-17 Measured (crosses) Er PL intensity as a result of excitation via Si-NCs in sample J as a function of the pump flux. The line is a fit to the data according to equation (75) with σ_{eff} ~ 1.5x10^{-16}cm^2

The fit yields a value for σ_{eff} ~ 1.5x10^{-16}cm^2 which is in excellent agreement with previously reported values[253, 254] and is more than 4 orders of magnitude greater than the direct excitation cross section for SiO$_2$:Er. Despite this efficient excitation, with only ~7% of the total Er excited this way and the remainder only excitable directly by a weak laser resonance, obtaining optical gain with a moderate pump flux would be impossible. If this 'effective' cross section could however be realized and maintained for all of the Er in such a sample then the transparency flux, which can be estimated from[251] $\phi_{1/2} = (\sigma_{eff}\tau_d)^{-1}$ should be on the order of ~1.4x10^{18}cm^{-2}s^{-1} (equivalent to just a few mw's in our experimental arrangement).

Therefore, in spite of the significantly larger Er cross section and the fact that we observe an excellent spatial correlation between the Si-NCs and Er in sample J, the small fraction of efficiently excited Er appears to be severely hampering the luminescence yield. Although the sensitization is expected to be improved with a

smaller Si-NC-Er interaction distance, de-excitation mechanisms associated with Er ion-ion interactions are clearly as effective over the same range.

It is noteworthy from the inset of **Figure 5-16** that the Er luminescence lifetime is almost un-changed over the entire range of Er concentration[§]. A previous study of the Si-NC-Er material system revealed that the Er luminescence lifetime is sensitive to the Si-NC size, specifically that it increases with the inverse nano-crystal diameter[255]. In the present sample set the Si-NC mean size and distribution should be almost identical for samples J to N due to the identical Si$^+$ implantation and annealing conditions. The fact that the Er PL lifetime is also un-changed might suggest that the sensitization of Er only occurs via a fraction of the nano-crystal population, perhaps those within a narrow size range. We note that the measured Er lifetime, ~5ms from sample J, which contains nano-crystals with a mode diameter ~3 to 4nm, is in excellent agreement with the previously reported values[255].

The fact that the Si-NC PL lifetime around 770nm does not change with increasing Er concentration, as shown in **Figure 5-18** indicates that the observed PL around is from Si-NCs <u>not</u> associated with Er ions, the density of which decreases with increasing Er concentration.

[§] The measured Er PL lifetime is ~6ms for 488nm (resonant) excitation and ~5ms for 476nm (non-resonant) excitation. The small increase in the measured lifetime for 488nm excitation can be expected due to the additional contribution from directly excited Er luminescent centres
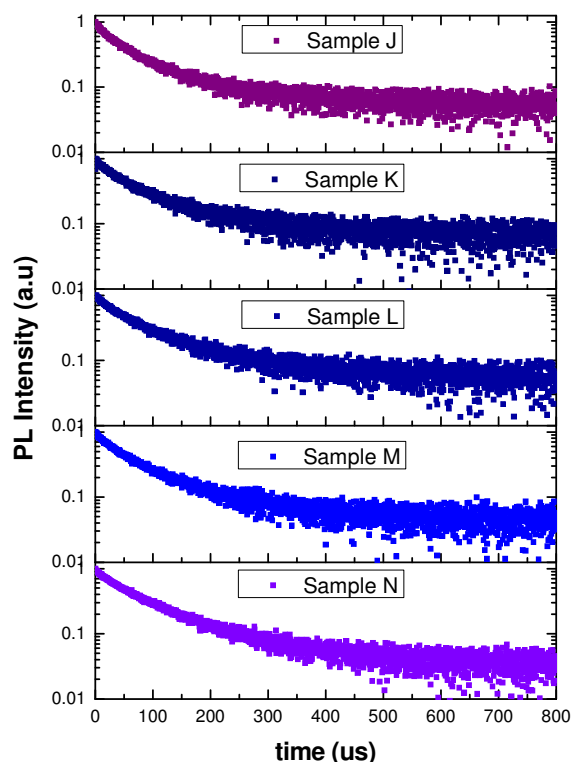
Figure 5-18 Si-NC PL decay transients at 770nm as a function of Er concentration for samples J – N

An alternative explanation could of course be that the observed Si-NC PL may not be a direct measure of exciton recombination but rather that the PL could be dominated by an intrinsic luminescent centre at the SiO$_2$/Si-NC interface such as the Si=O bond[253]. In this way, measurement of the PL decay transient would not necessarily reflect changes in the Si-NC excited state lifetime after Er doping.

5.3.2.3 Temperature dependence of the Er PL from Sample J (SiO$_2$:Er,Si-NC)

The temperature dependence of the Er PL intensity around 1.5µm was previously reported for c-Si:Er[249] and a-Si:H,Er[256]. At low temperatures, the intensity of the Er luminescence from Si:Er depends on the concentration of optically (or electrically) generated excitons and the concentration and capture cross-section of the Er iso-electronic 'trapping' centres. These Er 'traps' form defect like levels within the bulk Si band gap and the transfer of energy between excitons and Er 4f electrons then results in a radiative transition between the Er $^4I_{13/2}$ and $^4I_{15/2}$ states (~0.81eV). Er defect-related levels within the Si band gap are generally $\leq$ 200meV below the Si conduction band edge and depend on the exact chemical nature of the Er centre. In the case of c-Si, the 'back-transfer' of energy from excited Er ions to bound

excitons, characterised by an activation energy of 150meV, results in a quenching of the Er luminescence for temperatures above 77K.

This high temperature quenching is reduced significantly for Er in a-Si due to the increase in the band-gap (from ~1.1 to 1.5eV). The mismatch in energy between excited Er ions and the exciton band gap is sufficiently large so that the energy 'back-transfer' process is suppressed. This situation is further improved by incorporating hydrogen into the a-Si during the annealing process, which further increases the a-Si optical gap (from ~1.5 to 2eV)[256]. A similar size optical gap is observed for Si-nanocrystals in the range 2 to 5nm in SiO$_2$. In addition to the larger optical gap of the Si-NCs, the SiO$_2$ barrier between the Si-NCs and Er ions in this material system should provide further thermal isolation for the Er luminescence and is expected to completely suppress the 'back-transfer' process. We studied the thermal characteristics for the SiO$_2$:Er,Si-NC (sample J) for temperatures in the range 9 to 305K. **Figure 5-19** shows how the PL spectrum varies with temperature in this range.
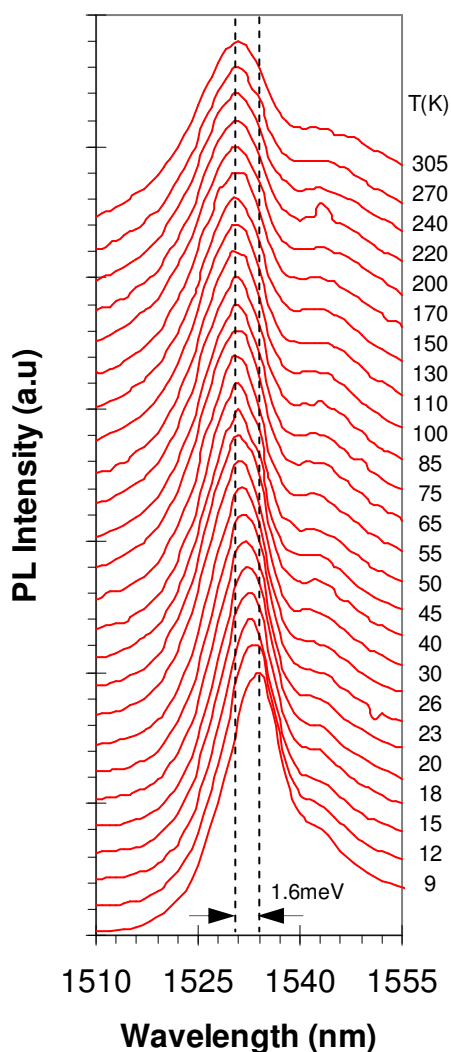
Figure 5-19 SiO$_2$:Er,Si-NC (sample J) Er luminescence spectra (resolution = 1nm) as a function of temperature in the range 9 to 305K

The first thing we note from **Figure 5-19** is the absence of well resolved Stark related spectral features in the Er luminescence at low temperature (9k). This, combined with an inhomogeneous broadening with increasing temperature is characteristic of Er embedded in an amorphous, rather than crystalline host matrix[257, 258].

Figure 5-19 also reveals a small (~1.6meV) but monotonic blue-shift in the peak position from 1534nm to 1531nm with increasing temperature in the range 9 to ~55k, above which the peak position is stable around 1531nm. This could be due to the fact that for the lowest temperature, 9K only the lowest Stark energy level of the Er^{3+} manifold is excited[259]. Increasing the temperature then leads to a broadening of these levels and the occupation of progressively higher levels until the uppermost level can be thermally excited. An alternative explanation is that there is a variation in the chemical arrangement of the Er ions in the matrix. For

199

example, the Er peak position was reportedly shifted to higher energies in oxygen rich (relative to oxygen poor) a-Si:H[260]. In the present sample, the observed shift might be indicative of a multiplicity of Er environments with variability in the local concentration of oxygen. The relative contribution of each Er luminescent centre to the observed PL spectrum would then be a function of temperature depending on its unique environment.

Figure 5-20 is an Arrhenius plot of the temperature dependence of the Er peak intensity at 1533nm.
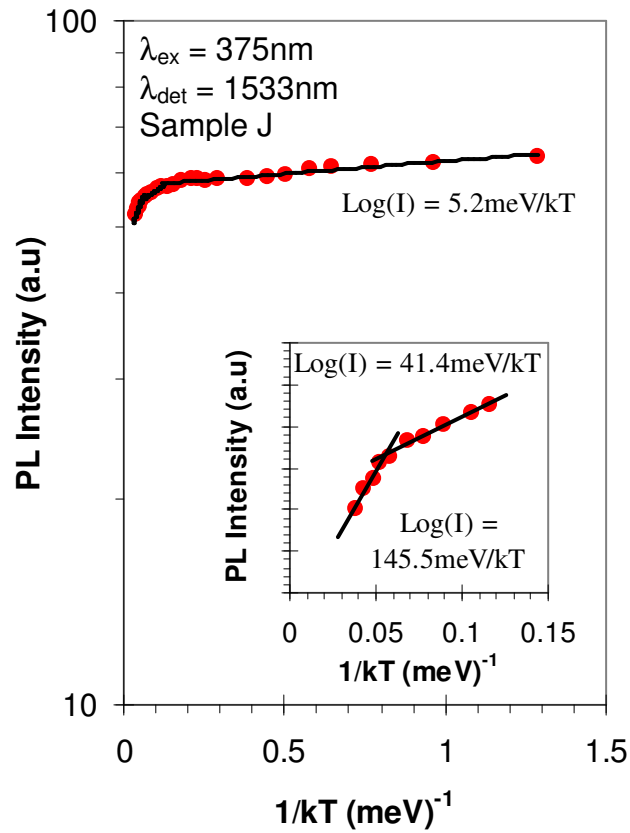
Figure 5-20 Measured (red circles) PL intensity at 1533nm as a function of the inverse temperature for SiO$_2$:Er,Si-NC (Sample J). Inset: Region showing the high temperature thermal activation of carriers, characterised by activation energies, E_1 = 145.5meV and E_2 = 41.4meV. Black lines are fits to the data according to equation (76)

The Arrhenius plot of **Figure 5-20** reveals only a small dependence on temperature, with a ratio of RT to 9K PL intensity, $R^* = I_{PL}(RT)/I_{PL}(9K) = 0.433$ for the peak at 1533nm. Two thermal activation energies are apparent from the peak intensity at high temperature and a third activation is observed in the low temperature regime. These were determined from the gradient of the Arrhenius curve using equation (76):

$$I(T) = \frac{I(0)}{1 + \exp\left(\frac{-E_1}{kT}\right) + \exp\left(\frac{-E_2}{kT}\right) + \exp\left(\frac{-E_3}{kT}\right)} \qquad (76)$$

In this case the activation energy E_1 corresponds to the highest temperature regime, 220 to 305K and was found to be ~145meV. An intermediate energy, E_2 ~41meV was observed for temperatures in the range 100 to 200K and a low temperature activation energy, E_3 ~5meV was determined for temperatures between 9 and 100K. For the latter, similar values (between 5 and 8meV) were reported in Er-doped Si-nanocrystals prepared via RF sputtering[261] and CVD[262] indicating that the low temperature activation of Er in the Si-NC material system has general characteristics. We find that the values for the high temperature thermal activations obtained in this work tend to be closer in agreement with those reported for Er-O donor complexes in Er and O co-implanted Si[263]. One of these, 'Er-1' with E ~150meV was identified, specifically after high temperature annealing. A shallow level ~40meV was also specifically attributed to O aggregates with the involvement of intrinsic defects in a separate work describing Er implanted Si[264].

Closer examination of the thermal characteristics of the PL band around 1.5μm in sample J reveals a significant variation in the thermal characteristics depending on the exact emission wavelength. **Figure 5-21** shows the variation in temperature dependence of specific emission lines extracted from the spectra in **Figure 5-19**.
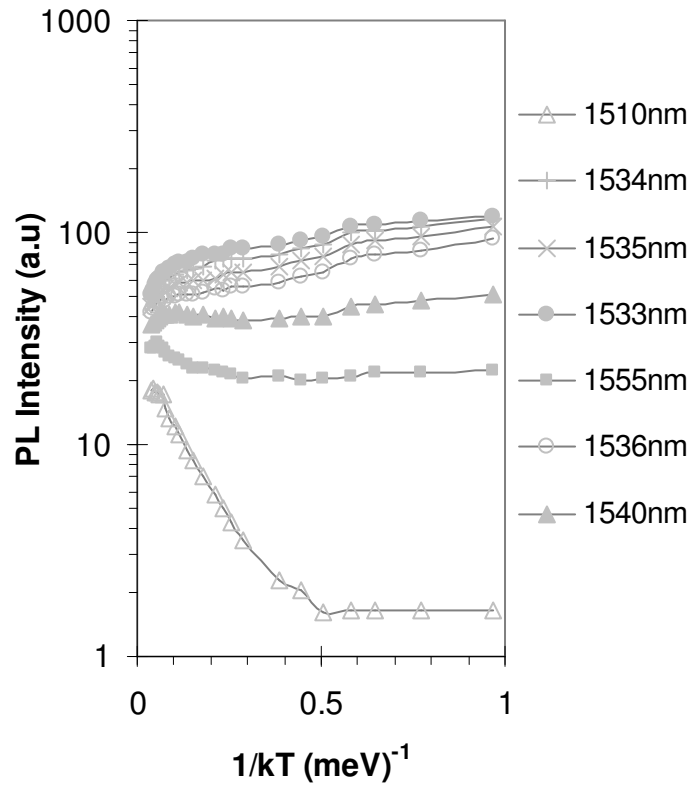
Figure 5-21 Spectrally resolved PL intensity as a function of inverse temperature for SiO$_2$:Er,Si-NC (sample J)

For the emission lines around the centre of the band (~1525 to 1545nm), we observe a monotonic quenching of the PL as the temperature is increased, i.e. a positive thermal activation energy. However, emission lines at the extremity of the spectrum around 1510nm (0.82eV) and 1555nm (0.79eV) exhibit a negative thermal activation energy up to ~170K above which they appear to saturate. The latter is characteristic of the defect related luminescence (DRL) normally observed in Er implanted Si[265]. This indicates that the Er^{3+} optical transitions from sample B are seated on top of DRL peaks, which may be related to interfacial misfit or loop dislocations at the SiO$_2$/Si interface or in the Si substrate. By extending the spectral scanning range, we found that the low temperature PL revealed a number of emission lines in the visible to near infra-red (NIR) region of the spectrum from sample B as shown in **Figure 5-22**.
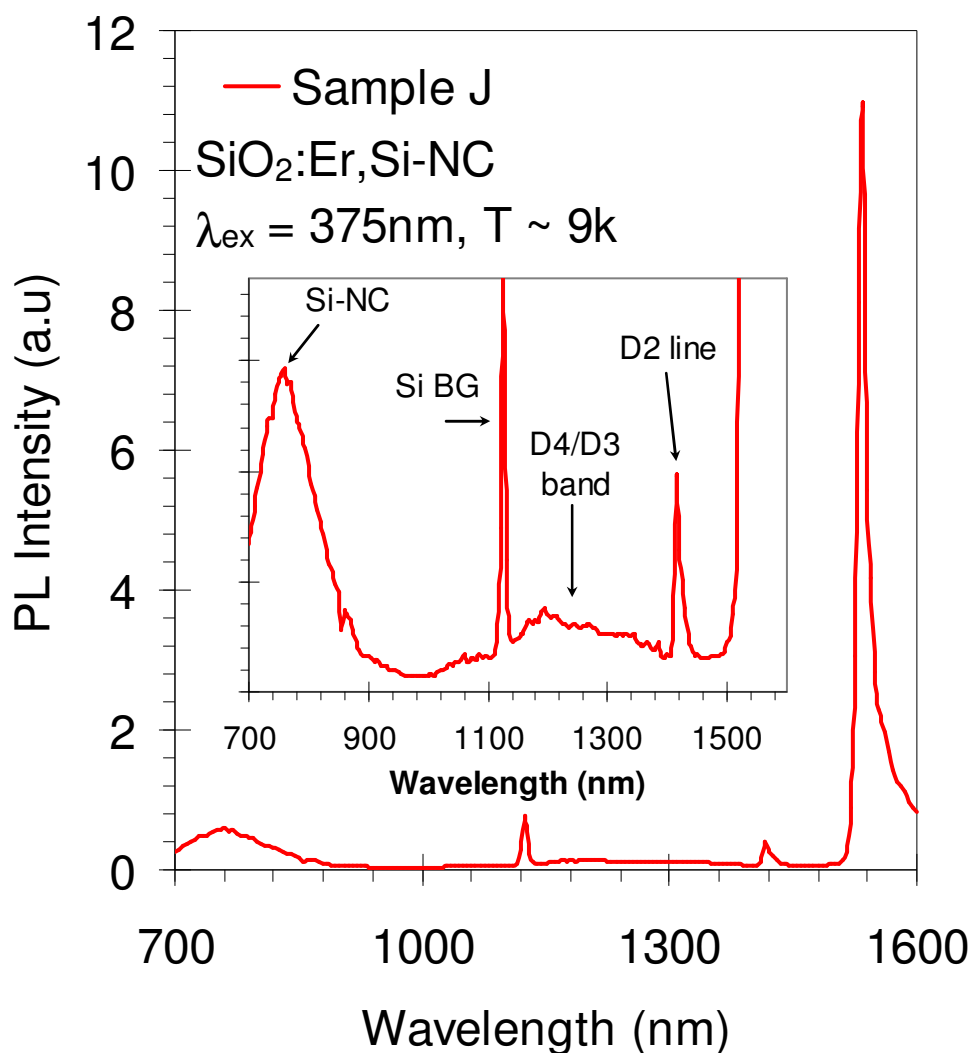
Figure 5-22 Low temperature (9K) visible/NIR PL spectrum for SiO$_2$:Er,Si-NC (sample J). Inset: Enlarged region showing detailed spectral features

The sample exhibits a complex visible/NIR emission spectrum between the Si-NC (~760nm) and the Stark-split Er^{3+} excited state transitions (1534nm). The narrow emission line around 1100nm, which is completely quenched for temperatures in excess of ~80K, is attributed to exciton recombination from the Si conduction band edge in the bulk Si substrate.

The broad emission band centred ~1200nm is tentatively attributed to the D4 defect band, which was previously reported for implanted Si[266]. In fact, dislocation loops in Si give rise to a characteristic set of NIR emissions in the range 1200 to 1550nm. The higher energy DRL tends to be assigned to recombination at shallow states in the bulk Si band gap that arise due to strain fields around dislocations. Broadening of this band towards lower energies (~1300nm) may be indicative of

the presence of phonon replicas, which were also reported in dislocated Si[266]. Broad emissions around 1200nm were also previously reported by Izeddin *et al*[230, 267] from which the luminescence dynamics were determined to be very fast with the observation of a decay time constant on the sub-microsecond timescale. This is somewhat surprising since rapid decay kinetics are not normally associated with the recombination of carriers at defect-like states, nor do they tend to exhibit such broad emission spectra, especially at low temperature. The narrow emission around 1420nm, assigned D2 is also commonly observed after ion implantation and thermal annealing of Si.

A complex picture of the excitation and de-excitation processes emerges after having studied the low temperature photoluminescence from sample J. The spectral shape and temperature dependence of the Er luminescence intensity strongly suggest that the Er luminescent centers are associated with the formation of complex *a*-Si:H,Er-O agglomerates after ion implantation and high temperature annealing. The observation of additional peaks in the NIR spectrum at low temperature reveals a strong DRL, which is probably associated with dislocations in the Si substrate.

5.3.3   Effect of Si-NC size on the sensitization of Er

Numerous studies have so far attempted to isolate the origin of fractional Er sensitization however it is likely that the low fraction of Si-NC mediated Er excitation is attributable to a complex combination of factors. As we have said, this is likely due, in part to the excitation and decay dynamics of the Si-NC and Er luminescent centres[230], which exacerbate the issue of non-radiative Auger-type losses via mechanisms such as excited state absorption (ESA)[245, 252] and co-operative up-conversion. In addition, there remains the possibility in the Si-NC-Er system that energy is efficiently 'back-transferred' to the Si-NCs themselves[230, 268]. Recent theoretical predictions by Garcia *et al*[251] revealed that the relatively low fraction of Si-NC mediated Er excitation may also be due to a low sensitizer (Si-NC) density. We note that the samples described in the previous section (J to N) have a relatively low density ($\sim 8 \times 10^{17}$cm^{-3}) of large (~ 3 to 4nm) Si-NCs, as determined from the HRTEM images. Using equation (70) and the parameters given in **Table 5-3**, we can calculate the fraction of Si-NCs in the excited state as a function of the pump flux, **Figure 5-23**.

$$\frac{n_2(1x10^{19})}{N} x100 = 17.6\%$$

Pump flux (photons/cm2/s)
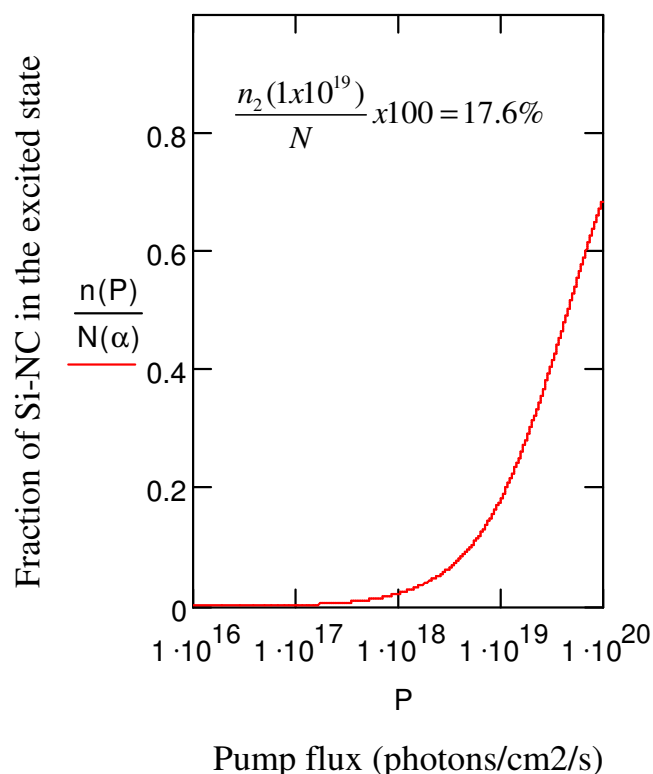
Figure 5-23 Fraction of Si-NC in the excited state, _n$_2$(P)/N_ as a function of pump flux at 375nm calculated from equation (70). The value corresponding to the efficient Si-NC mediated Er PL saturation (~1x10^{19}cm^{-2}s^{-1}) is indicated

We note from **Figure 5-23** that, at the pump flux corresponding to the efficient Si-NC mediated Er PL saturation in sample J, (~1x10^{19}cm^{-2}s^{-1}) the fraction of Si-NCs in the excited state may be as low as ~17%[**] and this only increases to ~50% at the highest experimental pump flux of 4.54x10^{19}cm^{-2}s^{-1}. This implies that the 'effective' sensitizer density i.e. the number of excited Si-NCs may actually be much lower than the actual number of Si-NCs, i.e. that estimated from the TEM images. These figures indicate that the fraction of excited Er could also be severely hampered by the low density and excitation and decay dynamics of the sensitizer (Si-NC) population. Increasing the density of, in particular small Si-NCs may offset the effect of Auger losses to some degree simply by reducing the number of Er ions per Si-NC and limiting the deleterious effects of Er ion-ion interactions[245]. Small Si-NCs have already been shown to exhibit superior sensitization of Er luminescent centers[269] probably on account of the larger

---

[**] These figures provide an incidental estimate of the maximum number of Er ions pumped by each Si-NC in sample J; assuming ~17% of the Si-NC concentration (0.17x8x10^{17}cm^{-3}) only efficiently pumps ~7% of the Er concentration (0.07x3.3x10^{20}cm^{-3}), then each Si-NC pumps ~170Er ions

oscillator strength, which improves the efficiency of energy transfer into higher excited Er states[270]. Increasing the sensitizer density is particularly important if, as the TEM images presented earlier suggest, the Si-NC formation sites act as nucleation centers for Er ions during high temperature annealing. Obtaining a large density of small Si-NCs however requires careful control over the sample fabrication conditions. It was previously shown for example, that increasing the amount of excess Si reduces the Er sensitization due to a concomitant increase in the mean Si-NC diameter for fixed annealing conditions[269, 270].

In this section we present the results of combining learned outcomes from our work on rapid thermal processing (RTP) of Si implanted oxides (Chapter 3) with Er co-doping to show the effect of Si-NC size on the Er luminescence. **Figure 5-24** shows the PL spectra for Si and Er co-implanted SiO$_2$ grown from sputtered Si on Al$_2$O$_3$ (samples G$_1$ to G$_4$) after varying the annealing conditions.
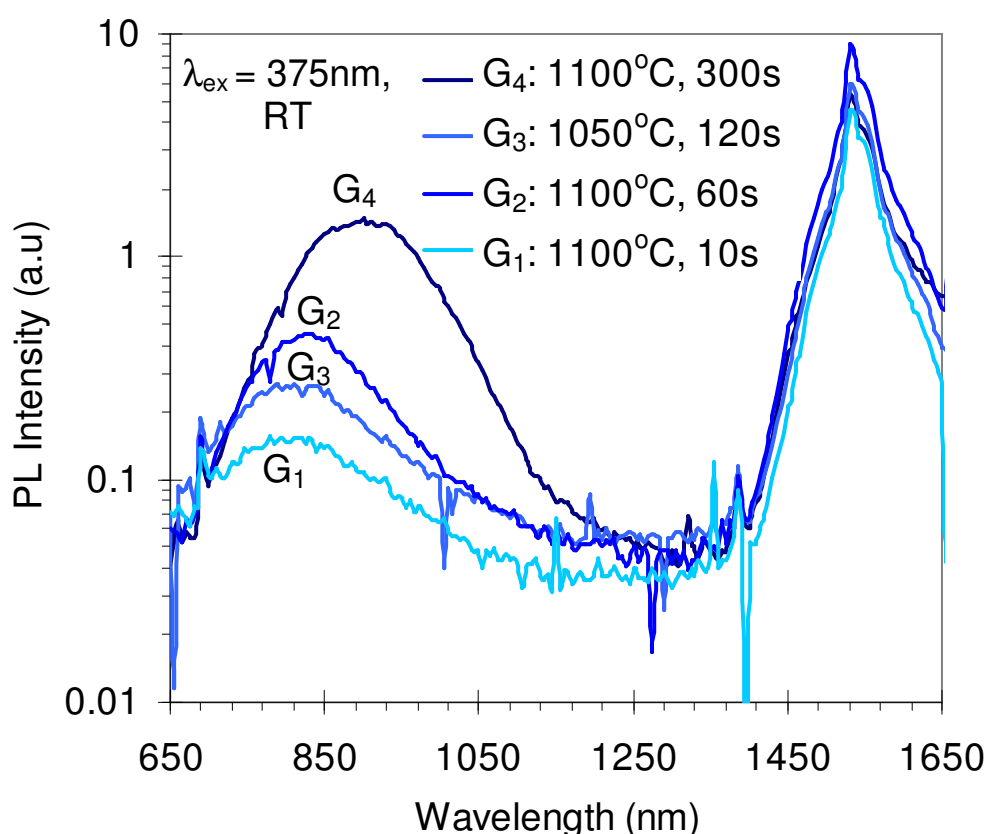
Figure 5-24 RT PL spectra for SiO$_2$:Er,Si-NC (samples G$_1$ to G$_4$) on Al$_2$O$_3$. Note the log-scale on the ordinate axis

Figure 5-24 reveals two distinct emission bands, a visible to NIR emission band between 650 and 1100nm and an IR emission band between 1400 and 1650nm.

The former is attributed to the band edge recombination of excited carriers in the Si-NCs and the latter is attributed to the $^4I_{13/2}$ intra-4f electronic transition in the Er^{3+} ions. Immediately evident is the monotonic red-shift in the Si-NC peak emission energy with increasing thermal budget. This is in accordance with a quantum confinement model in which smaller Si-NCs exhibit a larger band gap and correspondingly shorter wavelength emissions. The increase in Si-NC size with anneal time corresponds to the continued growth of the Si-NCs according to an Ostwald ripening model and subsequent narrowing of the band gap. Given that all of the samples studied here contain the same Si and Er concentration, the effects of anneal time and therefore Si-NC size can yield information about the relative Er sensitizing efficiency. In the absence of any TEM images for this particular sample set, the Si-NC mean diameter, $<d>$ was estimated from the dependence on anneal temperature, T_A and time, t_A as determined from TEM images for similar samples in Chapter 3. These values are given in **Table 5-4**.

Sample ID	Estimated Si-NC mean diameter, $<d>$ (nm)	PL Peak energy (eV)
G$_4$	2.45	1.38
G$_2$	2.34	1.50
G$_3$	1.82	1.57
G$_1$	1.25	1.59

Table 5-4 Estimated Si-NC mean diameter and corresponding peak PL emission energy for samples G$_1$ – G$_4$

We find that the longer anneal times[††] generally yield a larger total integrated PL intensity[‡‡] presumably due to the gradual removal of non-radiative defects. The removal of such defects specifically affects the Si-NC exciton luminescence suggesting that the most effective non-radiative channel is probably the dangling bond type defects at the SiO$_2$/Si-NC interface as previously reported by Pellegrino *et al*[234]. This is justified by the fact that the observed increase in the measured Si-

---

[††] In the case of sample Q, the longer anneal time is less effective in reducing the number of non-radiative defects neither does it have as large an effect on the Si-NC size due to the slightly lower anneal temperature of 1050°C

[‡‡] The integrated intensity referred to here was obtained from $I = \int\limits_{650nm}^{1650nm} I(\lambda)d\lambda$

NC PL lifetime is exactly correlated with the increase in intensity as shown in **Figure 5-25**.
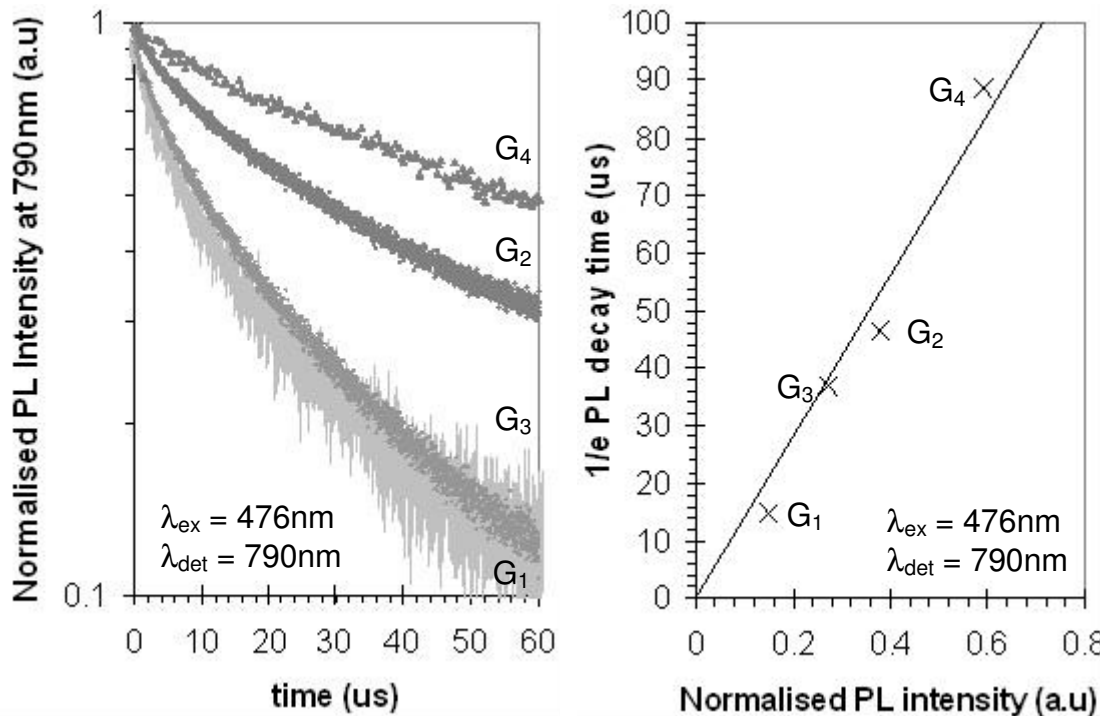
Figure 5-25 (a) Measured Si-NC PL decay transients and (b) 1/e decay time as a function of the Si-NC PL intensity at 790nm for samples G$_1$ to G$_4$

As well as variations in the fraction of radiative to non-radiative lifetimes, τ_R/τ_{NR}, observed differences in the Si-NC PL decay transients can result from differences in the Si-NC size. However, according to the quantum confinement model, the same size Si-NCs in any given sample should emit light at the same emission energy. Variations in the measured lifetime associated with Si-NC size are therefore eliminated by measuring the PL decay transients for each sample at a specific wavelength, in this case arbitrarily chosen to be 790nm. The observed differences in the measured lifetime therefore only reflect changes in τ_R/τ_{NR}, which is a function of the defect density.

The integrated intensities for the Si-NC and Er bands[§§] as well as the total are shown, as a function of the Si-NC mean diameter in **Figure 5-26**.
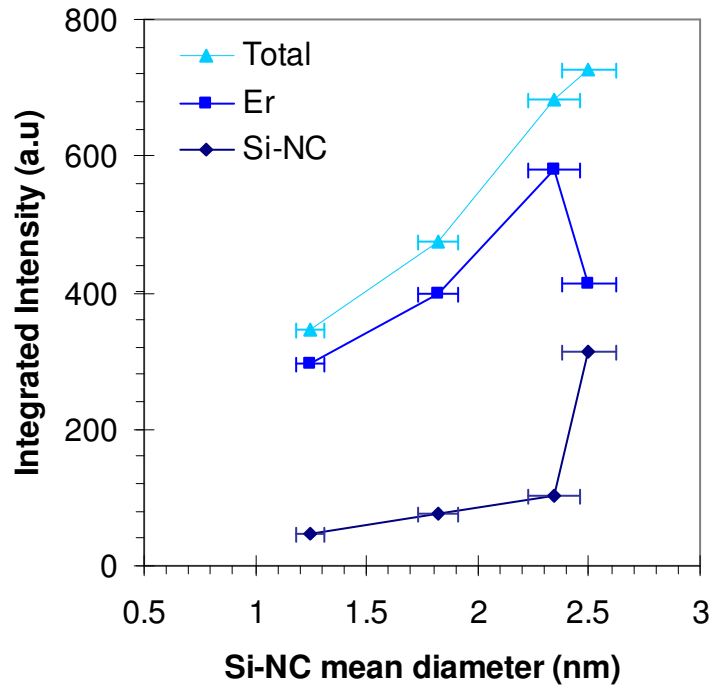
Figure 5-26 Integrated intensities of the Si-NC and Er luminescence bands and the total all as a function of the Si-NC mean diameter for sample set G. Lines are guides to the eye

Figure 5-26 reveals that the Er PL intensity passes through a maximum for the sample annealed for 60s at 1100°C (sample G$_2$, $<d>_{Si-NC}$ = 2.34nm) but then decreases again for the sample annealed for the longest time. If the Er PL yield is only a function of the non-radiative defect concentration then one would expect the intensity to increase monotonically with anneal time. The fact that the Er PL passes through a maximum and then decreases for the longest anneal time suggests that the sensitization of Er is adversely affected by the increase in size of the Si-NCs. The I_{Er}/I_{Si-NC} ratio is a convenient measure of the Er^{3+} excitation efficiency because it eliminates variations in the Si-NC absorption cross section and sample specific quantities such as reflection coefficient and thickness. This is plotted in **Figure 5-27** as a function of both the Si-NC mean diameter and peak emission energy.

[§§] The integrated intensities referred to here were obtained from $I = \int\limits_{650nm}^{1200nm} I(\lambda)d\lambda$ and $I = \int\limits_{1200nm}^{1650nm} I(\lambda)d\lambda$
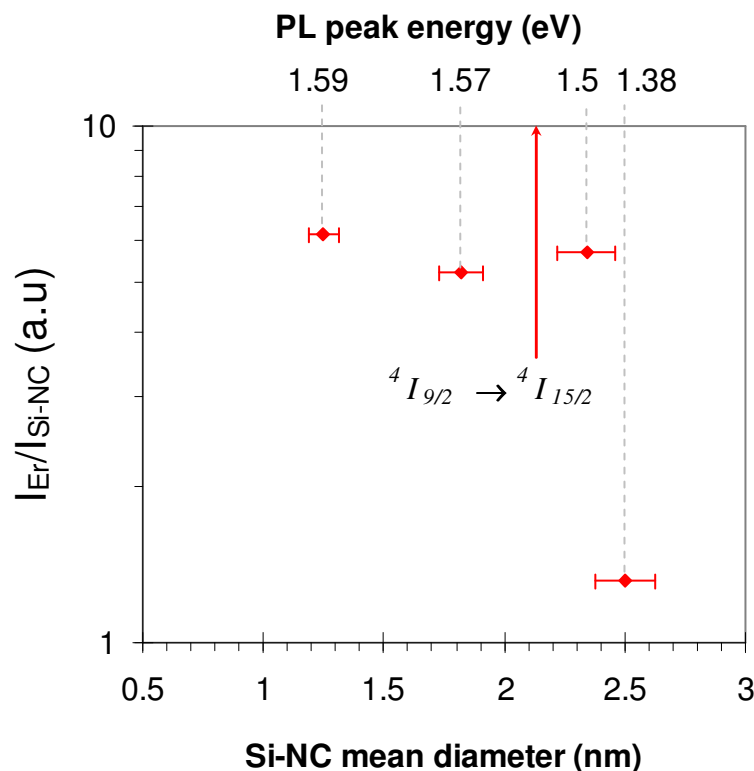
Figure 5-27 Relative Er^{3+} excitation efficiency as a function of the Si-NC mean diameter for sample set G. The Si-NC PL peak emission energy is also shown for each data point on the upper x-axis with dashed lines to guide the eye. The red line indicates the $^4I_{9/2} \rightarrow {}^4I_{15/2}$ Er^{3+} transition energy at 1.53eV

This result indicates that the Er^{3+} excitation efficiency is dependent on the Si-NC size in agreement with several published works[227, 232, 269]. This may be in part due to the improved overlap between Si-NC emitting and Er absorbing states in samples emitting around 1.53eV, which corresponds to the $^4I_{9/2} \rightarrow {}^4I_{15/2}$ Er^{3+} electronic transition (red line in **Figure 5-27**).

In fact, if we take into account the observed variations in Si-NC PL lifetime with annealing time, then this effect is further enhanced, particularly for the samples containing the smallest Si-NCs. Since the Si-NC-Er energy transfer process is likely in competition with other non-radiative, defect mediated processes, then the reduction of the latter, for example by increasing the anneal time should improve the Si-NC mediated Er excitation efficiency. The relative excitation efficiency for samples annealed for the shortest times (having the smallest Si-NCs) is therefore artificially low in **Figure 5-27** compared with the sample annealed for the longest times because the latter contains a lower density of non-radiative defects. If we correct the PL intensity for differences in the measured Si-NC PL lifetime, i.e. by

normalizing the spectra to the Si-NC peak, then the Er excitation efficiency is enhanced for the smaller Si-NCs as shown in **Figure 5-28**.

The plot shows I_{Er}/I_{Si-NC} (a.u) versus Si-NC $\langle d \rangle$ (nm), with the fit equation:

$$I_{Er}/I_{Si-NC} = 569.1e^{-2.1\langle d \rangle}$$

Legend: ▲ Un-corrected, ▢ Si-NC lifetime corrected
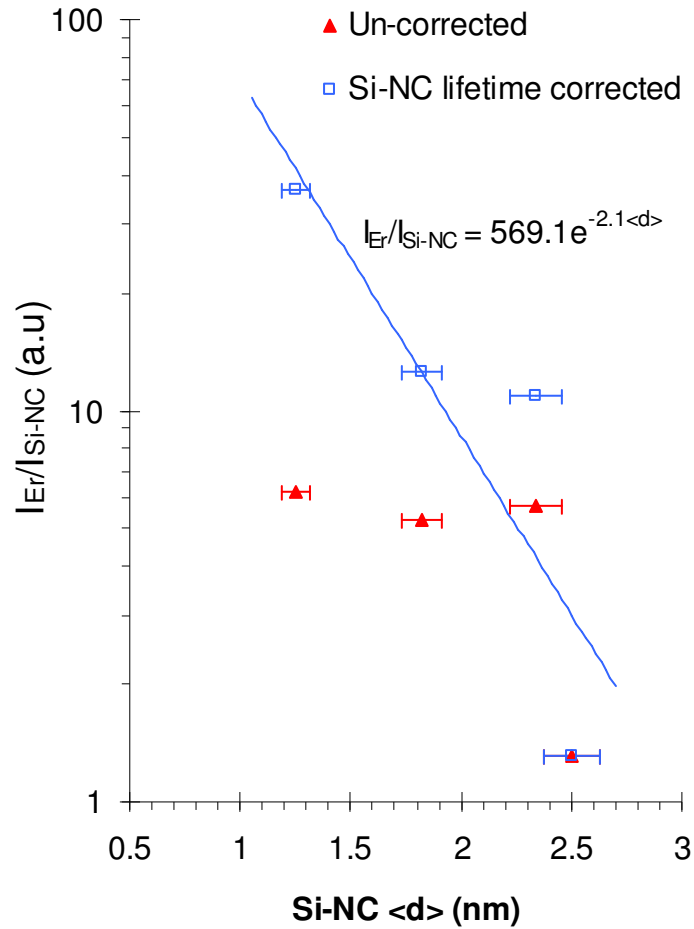
Figure 5-28 Un-corrected and Si-NC PL lifetime corrected ratio of Er to Si-NC PL intensity as a function of Si-NC mean diameter for sample set G. The line is an exponential fit to the Si-NC lifetime corrected data

So far, we have neglected variations in both Si-NC density and Er PL lifetime as a function of anneal time and it is important to quantify such variations particularly as they likely affect the observed PL yield and therefore accuracy of our excitation efficiency estimate. We know from the Ostwald ripening phenomenon and the TEM study in Chapter 3 that the Si-NC density decreases with isothermal anneal time, following approximately $N \propto 1/t$ in the first 100s of annealing. Our measurements indicated a decrease in the relative Si-NC density of around a factor of 4 for an annealing time increase from 10 to 100s above which it tended to an asymptotic minimum.

Also, measurement of the Er PL transients at 1534nm for the same sample set revealed that both the decay and rise times are a function of the anneal time (and therefore Si-NC size). In this case, we found that the observed Er PL rise and decay times were inversely proportional to the Si-NC mean diameter as shown in **Figure 5-29**.
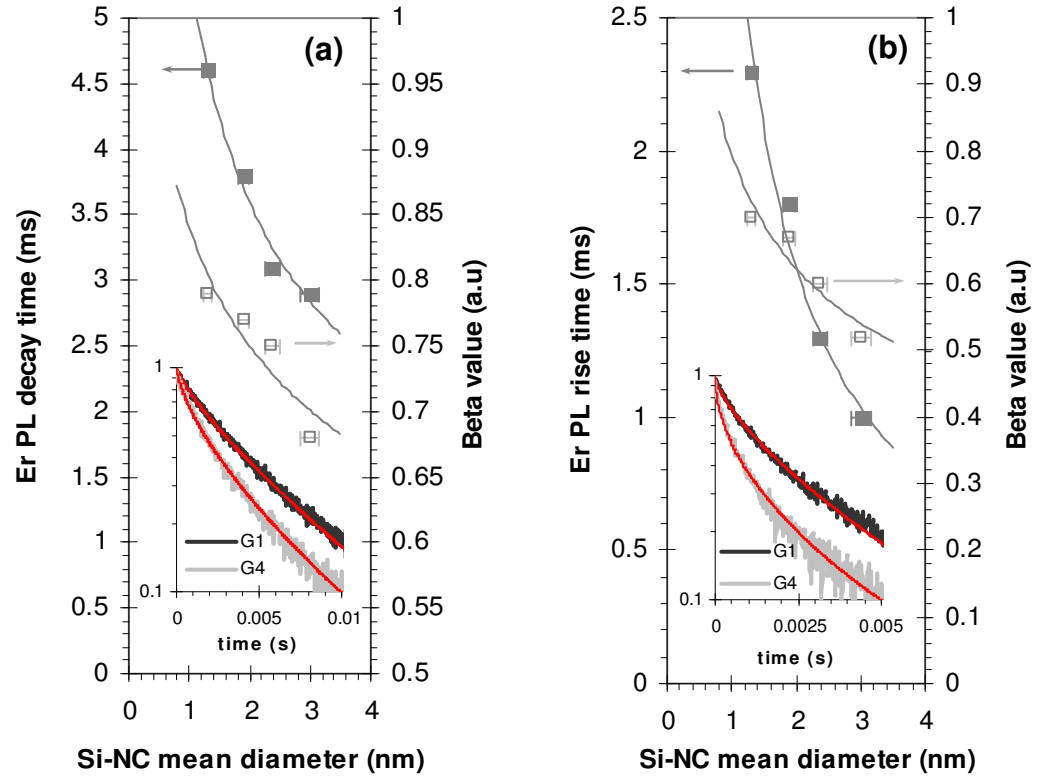
Figure 5-29 Er PL a) decay and (b) rise times and corresponding β-values determined from stretched exponential fits to the transients for samples G$_1$ – G$_4$. Lines are guides to the eye. Example transients are shown, along with their fitted curves in the insets

A recent investigation of the Er PL decay transients as a function of the Si-NC size was also reported by Horak *et al*[271] in which modifications to the observed Er PL lifetime were attributed to fluctuations in the local density of optical states (LDOS). This effect is particularly evident for Er ions positioned very close to larger Si-NCs. In regions where the local permittivity changes abruptly such as at the SiO$_2$/Si-NC interface, a strong interaction can result between an emitter (in this case Er) and the scattering field from the interface. This change in the LDOS manifests in a modification of the radiative recombination rate of the emitter, the degree of which is dependent on the material either side of the interface and the emitter-interface distance. By assuming the Si-NC to be a dielectric nano-sphere with sub-

wavelength dimensions (~few nanometers), Horak *et al*[271] showed that the enhancement to the Er spontaneous emission lifetime can be written:

$$\frac{\tau_{SRSO}}{\tau_{SiO_2}} \cong \left|1+\frac{2(\varepsilon-1)}{\varepsilon+2}\left(\frac{a}{r}\right)^3\right|^{-2} \tag{77}$$

Where τ_{SRSO} and τ_{SiO_2} are the Er spontaneous emission lifetimes in SRSO and SiO$_2$ respectively, ε is the ratio of the permittivity of the Si-NC to that of the surrounding matrix, a is the Si-NC radius and r is the distance of the Er ion from the centre of the Si-NC (i.e. $r = a + R$ where R is the Si-NC-Er separation). If we take τ_{SiO_2} to be the measured Er lifetime in pure stoichiometric silica, i.e. ~10ms, then the calculated spontaneous emission lifetime of Er coupled to Si-NCs can be plotted either as a function of the Si-NC diameter for various Si-NC-Er separations or as a function of Si-NC-Er separation for a variety of Si-NC sizes as shown in **Figure 5-30**.
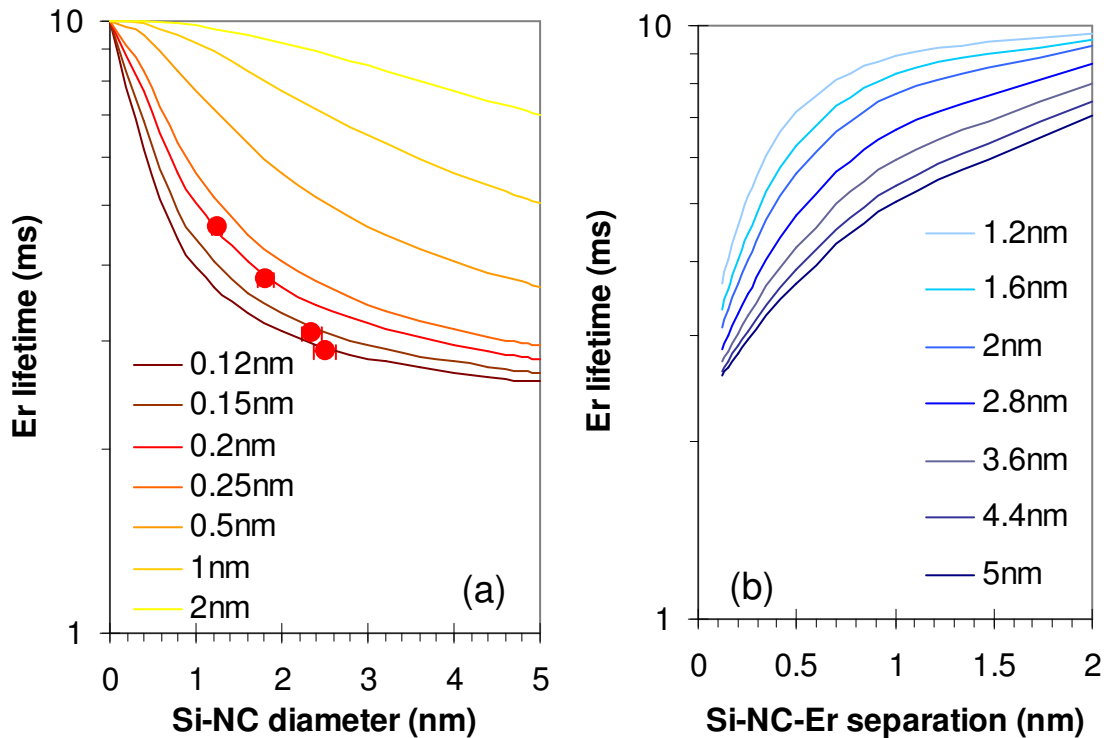
Figure 5-30 Calculated (equation (77)) Er lifetime as a function of (a) Si-NC diameter for a range of Si-NC-Er separations and (b) Si-NC-Er separation for a range of Si-NC sizes. The red circles in (a) are the data corresponding to the present sample set (samples G$_1$ – G$_4$)

The calculation predicts that the Er PL lifetime is reduced when the Si-NC-Er separation is small and/or the Si-NC is large. Given our estimate of the mean Si-NC sizes, this suggests a Si-NC-Er separation increasing from 0.12 to 0.2nm with increasing Si-NC diameter. This can be interpreted in two ways depending upon whether the observed PL lifetime is made up of mainly non-radiative or mainly radiative processes. In the first case, i.e. if $\tau_{PL} \sim \tau_{NR}$, then the reduction in the observed lifetime for Er ions with increasing Si-NC diameter would correspond to an increase in non-radiative recombination, for example via an efficient 'back-transfer' process whereby the excited Er ion efficiently transfers energy back into the Si-NC. Whilst this process is not likely, due to the large energy mismatch between the 1st excited state of the Er ion and the Si-NC band edge (the process would require the assistance of multiple phonons) it cannot be entirely ruled out. Indeed, such a process would be more likely for larger Si-NCs on account of their smaller band-gap compared with small Si-NCs. An increase in non-radiative effects could also be due to pair induced quenching or other energy migration processes related to Er clustering, which would shorten the observed lifetime. On the other hand, if the processes are mainly radiative, i.e. if $\tau_{PL} \sim \tau_R$, then the result we have obtained would suggest an increase in the radiative rate, $w_R = 1/\tau_R$ for Er ions positioned close to, in particular large Si-NCs. The fact that the data points do not lie along a single curve but appear to cut across the curves may be explained in one of two ways; firstly, the Er could be randomly distributed with respect to the Si-NCs, which is a reasonable assumption considering the samples were prepared via ion implantation followed by extremely short anneal treatments. This would also explain the relatively short lifetime and presence of the stretched exponential in the PL transients, similar to that reported previously by Franzo *et al*[253]. Alternatively, this could indicate that the permittivity of the matrix is a function of the anneal time. In the calculations we assumed a matrix permittivity of 1.46 as for stoichiometric SiO$_2$ but if we consider that after such short thermal treatments there remains a fraction of solute in the matrix, then it is reasonable to assume that the matrix may be sub-stoichiometric (SiO$_x$, x < 2), which would yield a higher permittivity and thereby affect the observed lifetime.

In either case, a further correction should be made to our estimate of the sensitizing efficiency, $I_{Er}/I_{Si\text{-}NC}$ which would be increased further [or decreased] for samples containing the smallest Si-NCs if the effect is mainly radiative [or non-radiative]. This could be tested by measuring the Er PL lifetime as a function of the

Si-NC size at low temperature to minimize the contribution of non-radiative processes. Then, if the variation in PL lifetime with Si-NC size persists, we could more confidently attribute the effect to an increase in the radiative rate as a result of the Purcell effect. Assuming the effect is due to an increase in the radiative rate for Er ions close to large Si-NCs, then a further correction for the change in radiative rate along with a correction for the Si-NC density yields the sensitizing efficiency, $I_{Er}/I_{Si\text{-}NC}$ as a function of the Si-NC mean diameter as shown in **Figure 5-31**.

The plot shows the curve with the equation:

$$I_{Er}/I_{Si\text{-}NC} = 370.0e^{-1.4<d>}$$

with axes labeled $I_{Er}/I_{Si\text{-}NC}$ (a.u) versus Si-NC $<d>$ (nm).
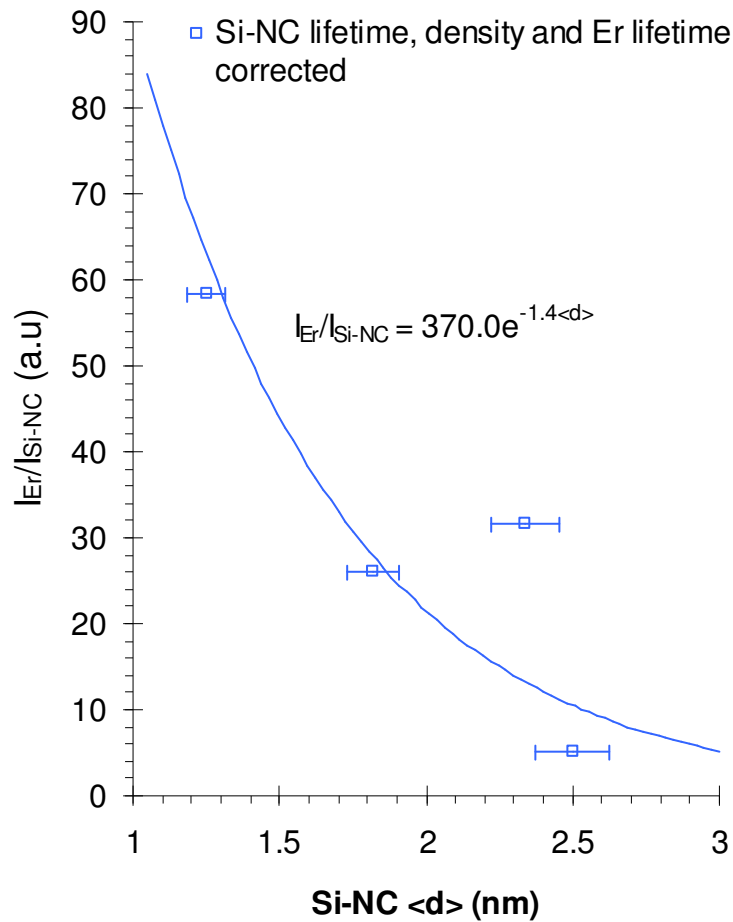
Figure 5-31 Si-NC PL lifetime, density and Er lifetime corrected ratio of Er to Si-NC PL intensity as a function of Si-NC mean diameter for sample set G. The line is an exponential fit to the corrected data

The corrected data generally suggests an improvement in the sensitizing efficiency with decreasing Si-NC size by as much as a factor of ~12 for the sample containing the smallest Si-NCs over that containing the largest Si-NCs. The data are reasonably well described by an exponential function with the outlying data point, for $<d>$ = 2.34nm corresponding to the sample with the best overlap of Si-NC emitting and Er absorbing states ($^4I_{9/2} \rightarrow {}^4I_{15/2}$) in the emission energy range.

The exponential increase in the sensitizing efficiency for samples containing small Si-NCs may be attributed to a much stronger absorption coefficient, which increases exponentially with increasing energy > 1.5eV[272]. Despite the fact that the proximity effect described here appears to provide a small improvement in the internal quantum efficiency ($\eta_{Er} = \tau_R/\tau_R+\tau_{NR}$) for the Er in the proximity of larger Si-NCs, increasing the density of small Si-NCs is still likely to be beneficial overall with respect to the Er luminescence yield. This is because of the fact that the efficiency of non-resonant coupling of energy between small Si-NCs and co-located Er^{3+} ions is improved by around an order of magnitude compared with the larger Si-NCs. In addition, increasing the Si-NC density should reduce the number of Er ions per Si-NC (with the ideal case being one Er ion per Si-NC[245]) and thereby reduce non-radiative relaxation via Er ion-ion interactions. This may be achieved by increasing the Si excess concentration and annealing at 1100°C for short timescales (< 100s). Longer anneal times can be tolerated if the samples are exposed to slightly lower anneal temperatures, for example 1050°C because of the temperature dependence of the diffusion coefficient of Si in SiO$_2$[273]. Improving the absolute integrated PL intensity without further affecting the Si-NC size can then be effected through longer timescale (~1 hour), lower temperature (~500°C) thermal treatments in mixed N$_2$:H$_2$ (5%) forming gas atmospheres, which has already been shown to reduce the concentration of dangling bond type defects[274], as we confirmed in Chapter 4.

5.4   Conclusions

We have shown that by combining relatively high concentrations of Er and Si in SiO$_2$ by co-implantation and employing a single, high temperature anneal, that it is possible to obtain a high spatial correlation between Si-NCs, Er and O. This was verified by combining high resolution electron microscopy and EELS spectroscopy for a SiO$_2$:Er,Si-NC *test* (sample H) and a SiO$_2$:Er *control* (sample J). These observations are attributed to a preferential agglomeration of Er at the Si-NC/SiO$_2$ interface during Si-NC formation, particularly as the Si-NC core makes the *a*-Si to *c*-Si phase transition, which would be concomitant with a reduced Er solubility limit. A direct comparison of the luminescence intensities of the Er PL for samples H and J reveals an enhancement, in the presence of the Si-NCs of more than 3 orders of magnitude at low excitation flux. However, this enhancement diminishes rapidly with increasing pump flux as a result of the saturation of the low fraction of Er apparently sensitized by Si-NCs. We estimate this fraction to be ~7% and attribute the diminishing enhancement primarily to Auger-type losses in the Si-NCs at high pump flux and via Er ion-ion interactions on account of the observed clustering.

One of the major technical challenges that persist with this material system is overcoming this low fraction of Er apparently 'coupled' to Si-NCs, which appears to be independent of sample preparation.

In fact much larger fractions of the Er population may be sensitized by the Si-NCs than is determined purely by measuring the steady state PL. For example, by investigating the Er excitation dynamics over many orders of temporal magnitude, the authors in [230] alluded to the fact that, after an extremely rapid and efficient Si-NC mediated sensitization, the majority of the Er ion population, dependent on their relative physical or chemical arrangement in the matrix, remain susceptible to radiative limiting Auger processes that occur on the nanosecond timescale before the energy can be extracted radiatively from the Er population on the millisecond timescale. Therefore the issue of how to increase the fraction of Er sensitized by Si-NCs may be a moot point if the suppression of non-radiative mechanisms cannot be achieved. We note from prior theoretical predictions[275, 276] that increasing the fraction of Si-NC sensitized Er may be obtained in part by the preferential increase in the density of small Si-NCs. This is also likely to offset the

Auger losses in part simply by reducing the number of Er excited by each Si-NC. Since the Si-NC mean size and relative density were shown to be a function of both the anneal time and temperature, one possible route to increasing the Si-NC density whilst independently controlling their size could be to use rapid thermal processing (RTP). We executed a brief assessment of the viability of this approach by applying some of the learned outcomes from our earlier work on rapid thermal annealing of Si-rich oxides and combined this with Er implantation to quantify the effect of Si-NC size on the Er luminescence. We compared four samples with identical Si excess and Er concentrations for annealing around 1100°C for times in the range 10 to 300s. We found that the absolute integrated intensity is improved for longer isothermal anneal times due to the gradual removal of non-radiative defects, likely the 'dangling bond' type defects (P_b centres) at the SiO$_2$/Si-NC interface. This is apparent from the PL decay transients, which were measured at 790nm with a characteristic lifetime that increases by a factor of ~6 when increasing the annealing time from 10 to 300s at 1100°C. This increase in lifetime was well correlated with the observed increase in the Si-NC PL intensity over the experimental range of annealing time. After correcting the total integrated PL intensity for differences in the measured PL decay time and relative Si-NC density, the sensitization of the Er luminescence was obtained by plotting the Er to Si-NC peak intensity ratio as a function of the Si-NC mean diameter (and peak emission energy). We found that the 'sensitization' efficiency increased by a factor of 12 with the inverse Si-NC mean diameter from 2.45 to 1.25nm. This is in excellent agreement with several other works and is attributed to the improved absorption cross section and oscillator strength associated with small Si-NCs.

5.5   References

214. M. J. F. Digonnet, *Rare-Earth-Doped Fiber Lasers and Amplifiers*, 2nd ed. (Marcel Dekker AG, Basel, 2001).

215. J. A. Buck, *Fundamentals of Optical Fibers*, 2nd ed. (Wiley, Hoboken, N. J., 2004).

216. Q. Wang, R. Ahrens and N. K. Dutta, Optical Society of America (2004).

217. S. W. Harun, H. A. Abdul-Rashid, S. Z. Muhd-Yassin, M. K. Abd-Rahman, K. K. Jayapalan and H. Ahmad, Optics & Laser Technology **40** (1), 88-91 (2008).

218. S. G. Bishop, D. A. Turnbull and B. G. Aitken, Journal of Non-Crystalline Solids **266-269** (Part 2), 876-883 (2000).

219. K. Imakita, M. Fujii and S. Hayashi, Physical Review B **71** (19), 193301 (2005).

220. M. Wojdak, M. Klik, M. Forcales, O. B. Gusev, T. Gregorkiewicz, D. Pacifici, G. Franzò, F. Priolo and F. Iacona, Physical Review B **69** (23), 233315 (2004).

221. L. Pavesi, L. Dal Negro, C. Mazzoleni, G. Franzo and F. Priolo, Nature **408** (6811), 440-444 (2000).

222. P. M. Fauchet, J. Ruan, H. Chen, L. Pavesi, L. Dal Negro, M. Cazzaneli, R. G. Elliman, N. Smith, M. Samoc and B. Luther-Davies, Optical Materials **27** (5), 745-749 (2005).

223. J. Lee, Journal of lightwave technology **23** (1), 19 (2005).

224. H.-S. Han, S.-Y. Seo, J. H. Shin and N. Park, Applied Physics Letters **81** (20), 3720-3722 (2002).

225. C. Garcia, B. Garrido, P. Pellegrino, R. Ferre, J. A. Moreno, L. Pavesi, M. Cazzanelli and J. R. Morante, Physica E: Low-dimensional Systems and Nanostructures **16** (3-4), 429-433 (2003).

226. A. J. Kenyon, C. E. Chryssou, C. W. Pitt, T. Shimizu-Iwayama, D. E. Hole, N. Sharma and C. J. Humphreys, Materials Science and Engineering B **81** (1-3), 19-22 (2001).

227. V. Y. Timoshenko, M. G. Lisachenko, B. V. Kamenev, O. A. Shalygina, P. K. Kashkarov, J. Heitmann, M. Schmidt and M. Zacharias, Applied Physics Letters **84**, 2512-2514 (2004).

228. K. Watanabe, M. Fujii and S. Hayashi, Journal of Applied Physics **90** (9), 4761-4767 (2001).

229. K. Watanabe, H. Tamaoka, M. Fujii, K. Moriwaki and S. Hayashi, Physica E: Low-dimensional Systems and Nanostructures **13** (2-4), 1038-1042 (2002).

230. I. Izeddin, D. Timmerman, T. Gregorkiewicz, A. S. Moskalenko, A. A. Prokofiev, I. N. Yassievich and M. Fujii, Physical Review B (Condensed Matter and Materials Physics) **78** (3), 035327 (2008).

231. C. Maurizio, F. D'Acapito, F. Priolo, G. Franzò, F. Iacona, E. Borsella, S. Padovani and P. Mazzoldi, Optical Materials **27** (5), 900-903 (2005).

232. J. Heitmann, M. Schmidt, M. Zacharias, V. Y. Timoshenko, M. G. Lisachenko and P. K. Kashkarov, Materials Science and Engineering B **B105**, 214-220 (2003).

233. M. Webb, Internal communication report on RBS results, G390:7, Job No. 1657, 2007.

234. P. Pellegrino, B. Garrido, C. García, R. Ferré, J. A. Moreno and J. R. Morante, Physica E: Low-dimensional Systems and Nanostructures **16** (3-4), 424-428 (2003).
235. O. L. Krivanek, Ultramicroscopy **78** (1), 1-11 (1999).
236. http://www.cree.com/Products/xlamp7090_xre.asp.
237. W. J. Miniscalco, Lightwave Technology, Journal of **9** (2), 234-250 (1991).
238. D. Kollewe, T. Bachmann and W. Sigle, Physics Letters A **253** (5-6), 305-308 (1999).
239. J. A. Hunt and D. B. Williams, Ultramicroscopy **38** (1), 47-73 (1991).
240. R. F. Egerton, *Electron Energy-Loss Spectroscopy in the Electron Microscope*, 2nd ed. (Plenum, New York, 1996).
241. Gatan., *EELS Analysis User's Guide Rev. 1.2.1.* (2003).
242. S. Schamm, G. Scarel and M. Fanciulli, *Rare earth oxide thin films: growth, characterization and applications.* (Springer-Verlag, 2006).
243. P. G. Kik and A. Polman, Materials Science and Engineering: B **81**, 3-8 (2001).
244. D. E. Blakie, MSc Thesis, McMaster University, 2006.
245. A. J. Kenyon, W. H. Loh, C. J. Oton and I. Ahmad, Journal of Luminescence **121** (2), 193-198 (2006).
246. A. Lidgard, Electronics letters **27** (11), 993 (1991).
247. D. Pacifici, G. Franzò, F. Priolo, F. Iacona and L. Dal Negro, Physical Review B **67** (24), 245301 (2003).
248. B. Garrido, M. López, A. Pérez-Rodríguez, C. García, P. Pellegrino, R. Ferré, J. A. Moreno, J. R. Morante, C. Bonafos, M. Carrada, A. Claverie, J. de la Torre and A. Souifi, Nuclear Instruments and Methods in Physics Research Section B: Beam Interactions with Materials and Atoms **216**, 213-221 (2004).
249. D. T. X. Thao, C. A. J. Ammerlaan and T. Gregorkiewicz, Journal of Applied Physics **88** (3), 1443-1455 (2000).
250. S. Sergeyev, S. Popov, D. Khoptyar, A. T. Friberg and D. Flavin, J. Opt. Soc. Am. B **23** (8), 1540-1543 (2006).
251. C. García, P. Pellegrino, Y. Lebour, B. Garrido, F. Gourbilleau and R. Rizk, Journal of Luminescence **121** (2), 204-208 (2006).
252. C. J. Oton, W. H. Loh and A. J. Kenyon, Applied Physics Letters **89** (3), 031116 (2006).
253. G. Franzò, V. Vinciguerra and F. Priolo, Applied Physics A: Materials Science & Processing **69** (1), 3-12 (1999).
254. P. Noe, H. Okuno, J. B. Jager, E. Delamadeleine, O. Demichel, J. L. Rouviere, V. Calvo, C. Maurizio and F. D'Acapito, Nanotechnology **20** (35), 355704 (2009).
255. V. Y. Timoshenko, D. M. Zhigunov, P. K. Kashkarov, O. A. Shalygina, S. A. Teterukov, R. J. Zhang, M. Zacharias, M. Fujii and S. Hayashi, Journal of Non-Crystalline Solids **352** (9-20), 1192-1195 (2006).
256. M. Kechouane, D. Biggemen and L. R. Tessler, physica status solidi (c) **1** (2), 285-289 (2004).
257. A. V. Kholodkov, K. M. Golant and L. D. Iskhakova, Journal of Non-Crystalline Solids **352**, 3808-3814 (2006).
258. D. Biggemann, D. Mustafa and L. R. Tessler, Optical Materials **28** (6-7), 842-845 (2006).
259. A. A. Choueiry, A.-M. Jurdyc, B. Jacquier, F. Gourbilleau and R. Rizk, Optical Materials **30** (12), 1889-1894 (2008).

260. J. H. Shin, R. Serna, G. N. van den Hoven, A. Polman, W. G. J. H. M. van Sark and A. M. Vredenberg, Applied Physics Letters **68** (7), 997-999 (1996).

261. M. F. Cerqueira, M. Losurdo, T. Monteiro, M. Stepikova, M. J. Soares, M. Peres and P. Alpuim, physica status solidi (a) **204** (6), 1769-1774 (2007).

262. M. F. Cerqueira, M. Losurdo, M. Stepikhova, P. Alpuim, G. Andres, A. Kozanecki, M. J. Soares and M. Peres, Thin Solid Films **517** (20), 5808-5812 (2009).

263. A. J. Kenyon, Semiconductor Science and Technology **20** (12), R65-R84 (2005).

264. V. V. Emtsev, D. S. Poloskin, E. I. Shek, N. A. Sobolev and L. C. Kimerling, Materials Science and Engineering B **81** (1-3), 74-76 (2001).

265. N. A. Sobolev, A. M. Emel'yanov, E. I. Shek, V. I. Sakharov, I. T. Serenkov, Y. A. Nikolaev, V. I. Vdovin, T. G. Yugova, M. I. Makovijchuk, E. O. Parshin and S. Pizzini, Materials Science and Engineering B **91-92**, 167-169 (2002).

266. M. Kittler, T. Arguirov, W. Seifert, X. Yu, G. Jia, O. F. Vyvenko, T. McHedlidze, M. Reiche, J. Sha and D. Yang, Materials Science and Engineering: C **27** (5-8), 1252-1259 (2007).

267. I. Izeddin, T. Gregorkiewicz and M. Fujii, Physica E: Low-dimensional Systems and Nanostructures **38** (1-2), 144-147 (2007).

268. A. J. Kenyon, S. S. Bhamber and C. W. Pitt, Materials Science and Engineering: B **105** (1-3), 230-235 (2003).

269. M. Fujii, M. Yoshida, S. Hayashi and K. Yamamoto, Journal of Applied Physics **84** (8), 4525-4531 (1998).

270. F. Gourbilleau, C. Dufour, R. Madelon and R. Rizk, Optical Materials **28** (6-7), 846-849 (2006).

271. P. Horak, W. H. Loh and A. J. Kenyon, Optics Express **17** (2), 906 (2009).

272. Z. Ma, X. Liao, G. Kong and J. Chu, Applied Physics Letters **75** (13), 1857-1859 (1999).

273. M. Uematsu, H. Kageshima, Y. Takahashi, S. Fukatsu, K. M. Itoh, K. Shiraishi and U. Gosele, Applied Physics Letters **84** (6), 876-878 (2004).

274. M. Lopez, B. Garrido, C. Garcia, P. Pellegrino, A. Perez-Rodriguez, J. R. Morante, C. Bonafos, M. Carrada and A. Claverie, Applied Physics Letters **80** (9), 1637-1639 (2002).

275. B. Garrido, C. Garcia, P. Pellegrino, D. Navarro-Urrios, N. Daldosso, L. Pavesi, F. Gourbilleau and R. Rizk, Applied Physics Letters **89** (16), 163103 (2006).

276. F. Gourbilleau, C. Dufour, R. Madelon and R. Rizk, Journal of Luminescence **126** (2), 581-589 (2007).

6   Silicon and phosphorus co-implanted SiO_2

6.1   Introduction

The specific interaction of silicon nano-clusters (Si-NCs) with shallow impurity dopant species such as phosphorus (P) and boron (B) has generated considerable interest in optoelectronics[277-281] and more recently for potential application in photo-voltaic technologies for 'all silicon tandem solar cells'[282-284]. However, if such materials are to find commercial device application it is evident that a more complete understanding of the optical and electronic properties of p- or n-type Si-NCs is required.

Generally, the selective doping of individual nanostructures represents a significant technical challenge. In particular, obtaining equivalent carrier concentrations to those routinely achieved in bulk Si (~10^{20}cm^{-3})[285] is much more difficult in Si-NCs, principally because of their small volume fraction and randomly disperse nature in thin films prepared by conventional deposition or sputter techniques. The probability of co-locating a Si-NC with an impurity atom can be improved to some extent, whilst maintaining CMOS compatibility using ion implantation. Accurate prediction of the Si$^+$ and impurity ion depth and concentration profiles can be obtained by *Monte Carlo* methods, for example using the *stopping and range of ions in matter* (SRIM) freeware simulation[286].

Doping individual nanostructures may be further complicated by the recent proposal that there exists a nano-crystal size limit, below which impurity levels formed by P$^+$ dopants may not be sufficiently shallow to generate additional carriers at room temperature[287]. Using a combination of *ab initio* pseudo-potential and effective mass approximations, the authors of [287] showed that the binding energy, $E_B{}^*$ of the defect electron to the impurity ion inside Si-NCs is proportional to the inverse nano-cluster radius, ($E_B \propto 1/r$), which the authors attributed to a quantum confinement effect of the defect electron.

Even where there is ionization of the donor impurity, for example in larger Si-NCs, other effects could limit the carrier concentration. For example, the presence of

---

* The binding energy in this case was defined as the energy required to ionize a P doped Si-nanocrystal by removing an electron (I_d) minus the energy gained by adding the electron to a pure Si-nanocrystal (A_p), $E_B = I_d - A_P$

point defects, surface states, dangling bonds or even localized stresses[288] all represent deep level traps[279] for the additional electron.

However, the motivation of current researchers remains the potential of future devices based on controlling the electronic and optical properties of individual Si-NCs and, despite the technical challenges described there is much to be excited about. For example, the optical absorption characteristics of phosphosilicate glass (PSG) containing relatively large (4.7nm diameter) Si-NCs was previously reported by Mimura *et al*[279]. Si-NCs in glass matrices are known to exhibit an exponentially rising, broad absorption in the UV/blue region of the spectrum, which arises due to band-edge transitions in the nano-clusters[289]. In addition, an infra-red (IR) absorption band was observed in the PSG, which increased monotonically with phosphorus concentration. This was attributed to an increase in Auger assisted intra-valley transitions of free carriers after ionization of P$^+$ atoms inside the larger Si-NCs. This observation was concomitant with a monotonic quenching of the photoluminescence from the Si-NCs, presumably as a result of the annihilation of optically generated excitons via Auger excitation. This result suggests that, at least for Si-NCs with $d \geq 5$nm, the defect level arising from P$^+$ doping is sufficiently shallow to generate additional free carriers at room temperature via impurity ionization.

Although some workers have reported photoluminescence quenching for P$^+$ doped Si-NCs[279, 290] others have reported enhanced luminescence compared to un-doped samples[278, 279, 291]. Such observations appear particularly sensitive to the annealing environment during material preparation. At present, the exact mechanism for the observed PL enhancement with phosphorus concentration is a matter of active debate in the literature, although there is strong experimental evidence to suggest that the presence of phosphorus results in a Si-NC surface passivation effect[279, 291, 292]. This could be similar to that obtained after hydrogen atom treatment (HAT)[293] or annealing in mixed gas atmospheres such as Ar:H or N$_2$:H$_2$ where the density of electronically active defects is reduced by terminating dangling bonds (P_b centres) at the SiO$_2$/Si-NC interface with hydrogen donors. Previous work on electron spin resonance (ESR) signals associated with the P_b centre were correlated with photoluminescence from Si-NCs in a PSG matrix[281]. The intensity of the ESR signal, which is proportional to the density of dangling bond defects, was reduced dramatically by co-doping the Si-NCs in SiO$_2$ with phosphorus, i.e. by incorporating the Si-NCs in a PSG matrix. This result was

correlated with a quenching of the luminescence around 0.9eV and an increase in the luminescence around 1.4eV, attributed to the recombination of photo-excited carriers at the Si-NC band edge. The lower diffusivity of phosphorus in Si/SiO$_2$ makes it more attractive than hydrogen as a surface terminating species, particularly during high temperature thermal treatments where H$_2$ diffusion can lead to a passivation reversal.

Recently, an alternative explanation of the PL enhancement obtained after P$^+$ doping was offered based on an envelope function approximation[294, 295]. This model ascribes the observed PL enhancement to an inter-valley (Γ-X) mixing of electronic states, resulting from the presence of phosphorus ions inside the Si-NCs. The perturbing potential within the Si-NC, arising from the short range Coulomb interaction between a single donor impurity and the additional electron was predicted to increase the **k**-space overlap of electron and hole wave-functions and subsequently increase the radiative to non-radiative phonon assisted transition probability.

Fujii *et al*[296] also reported an enhanced room temperature luminescence after co-doping Si-NCs with phosphorus and boron (BPSG). This observation, which was coupled with a large red-shift in the emission spectrum from ~1.3 to 0.9eV, i.e. 400meV for C_B ~0.76 and C_P ~1.26 mol. %, was also characterised by an increase in the recombination rate and strong thermal quenching of the luminescence. These low energy emissions were attributed to an electron transition between donor and acceptor impurity levels (D-A pairs) within the Si-NC band gap. These results suggest that individual (and in some cases multiple) impurity atoms such as phosphorus _can_ reside within Si-NCs without ionization necessarily resulting in non-radiative recombination through Auger excitation and implies that multi-atom doping of individual nanostructures could be a distinct possibility.

An extensive study of the near-IR luminescence spectra from silicon and phosphorus co-implanted SiO$_2$ with a phosphorus concentration, which was varied over 4 orders of magnitude, is presented in this work. The effect of the annealing environment on the luminescence from phosphorus doped Si-NC ensembles is examined and similar observations of PL enhancements to those already reported are explained in terms of a nano-cluster surface passivation effect by the phosphorus, particularly for small Si-NCs. We note that for samples annealed at higher temperatures, the luminescence is always monotonically quenched with increasing phosphorus concentration, regardless of the exact preparation. A

simple statistical model is presented to describe this observation, which provides an incidental estimate of the Si-NC size distribution. The model is based on the assumption that the ionization of a single phosphorus atom inside a large (> 5nm) Si-NC results in a three-body interaction, which provides an efficient non-radiative recombination channel for photo-excited electrons via Auger relaxation.

6.2   Experimental details

Three sample sets (P, Q and R) of thermally grown (1000°C) SiO_2 (500nm) on (100) Si are described, which were co-implanted with Si^+ and P^+ according to the following procedures: samples in set P were implanted with Si^+ at 80keV to a dose of 8×10^{16}cm^{-2} and annealed in a quartz tube furnace for 5 minutes at 1050°C in an N_2 ambient to form Si-NCs. These samples were then implanted with P^+ at 80keV to a range of doses according to **Table 6-1**. A second lower temperature anneal at 800°C for 15 minutes in N_2 was applied to activate the P^+ after implantation.

Sample ID	P^+ concentration (x10^{14}cm^{-2})	Si:P Ratio
P_1	0.1	8000
P_2	0.5	1600
P_3	1	800
P_4	3	267
P_5	8	100
P_6	50	16

Table 6-1 Implanted phosphorus concentration for SiO_2:Si-NC, P sample set P

The samples in set Q were implanted with both Si^+ and P^+ prior to any annealing. The Si^+ was implanted at 80keV to a dose of 8×10^{16}cm^{-2} and the P^+ was implanted at 80keV to a range of doses according to **Table 6-2**. These samples were then subjected to a single high temperature anneal at 1050°C for 5 minutes in an N_2 ambient to form Si-NCs, remove implantation damage and activate the P^+.

Sample ID	P$^+$ concentration (x10^{14}cm^{-2})	Si:P ratio
Q$_1$	0.1	8000
Q$_2$	0.5	1600
Q$_3$	1	800
Q$_4$	3	267
Q$_7$	5	160
Q$_5$	8	100
Q$_8$	10	80
Q$_6$	50	16
Q$_9$	300	2.67
Q$_{13}$	0	N/A

Table 6-2 Implanted phosphorus concentration for SiO$_2$:Si-NC, P sample set Q

The samples in set R were also implanted with both Si$^+$ and P$^+$ prior to any annealing. The Si$^+$ was implanted at 80keV to a dose of 8×10^{16}cm^{-2} and the P$^+$ was implanted at 80keV to a range of doses according to **Table 6-3**. These samples were then subjected to a single high temperature anneal at 1100°C for 1 hour in an N$_2$ ambient to form Si-NCs and activate the P$^+$.

Sample ID	P$^+$ dose (x 10^{14}cm^{-2})	Si:P ratio
R$_1$	0.8	1000
R$_2$	3	267
R$_3$	10	80
R$_4$	50	16
R$_5$	0	N/A

Table 6-3 Implanted phosphorus concentration for SiO$_2$:Si-NC, P sample set R

For optical characterisation, the samples were excited using the 514nm line of an Argon ion (Ar$^+$) laser at a nominal power of 10mW. The photoluminescence was

collected con-focally and dispersed in the *Renishaw* μ-Raman system and measured using a charge coupled device (CCD) camera. All measurements were conducted at room temperature. Measurements of the PL transients, conducted in collaboration with the group of Dr. A Kenyon at the University College London (UCL), were obtained after optical excitation using the 476nm line of an Ar$^+$ laser. The laser was switched using a Pockel's cell arrangement and the PL transients detected using an IR sensitive *Hamamatsu* photomultiplier with a resolution, limited by the preamplifier of ~5μs. The transient waveforms were recorded on a digital storage oscilloscope (DSO).

After initial PL measurements, all of the samples in sets P and Q (except sample Q$_{13}$, which was used as a reference) were subjected to an extended, high temperature anneal at 1100°C for 30 minutes in an N$_2$ ambient. Further CW PL measurements were carried out to determine the effect of this extended high temperature anneal on the luminescence integrated intensity as a function of the P$^+$ concentration.

6.3   Results and discussion

6.3.1   Effect of implant and annealing scheme on the Si-NC PL

The room temperature PL spectra for the phosphorus doped samples from sets P and Q are shown as a function of wavelength in **Figure 6-1**.
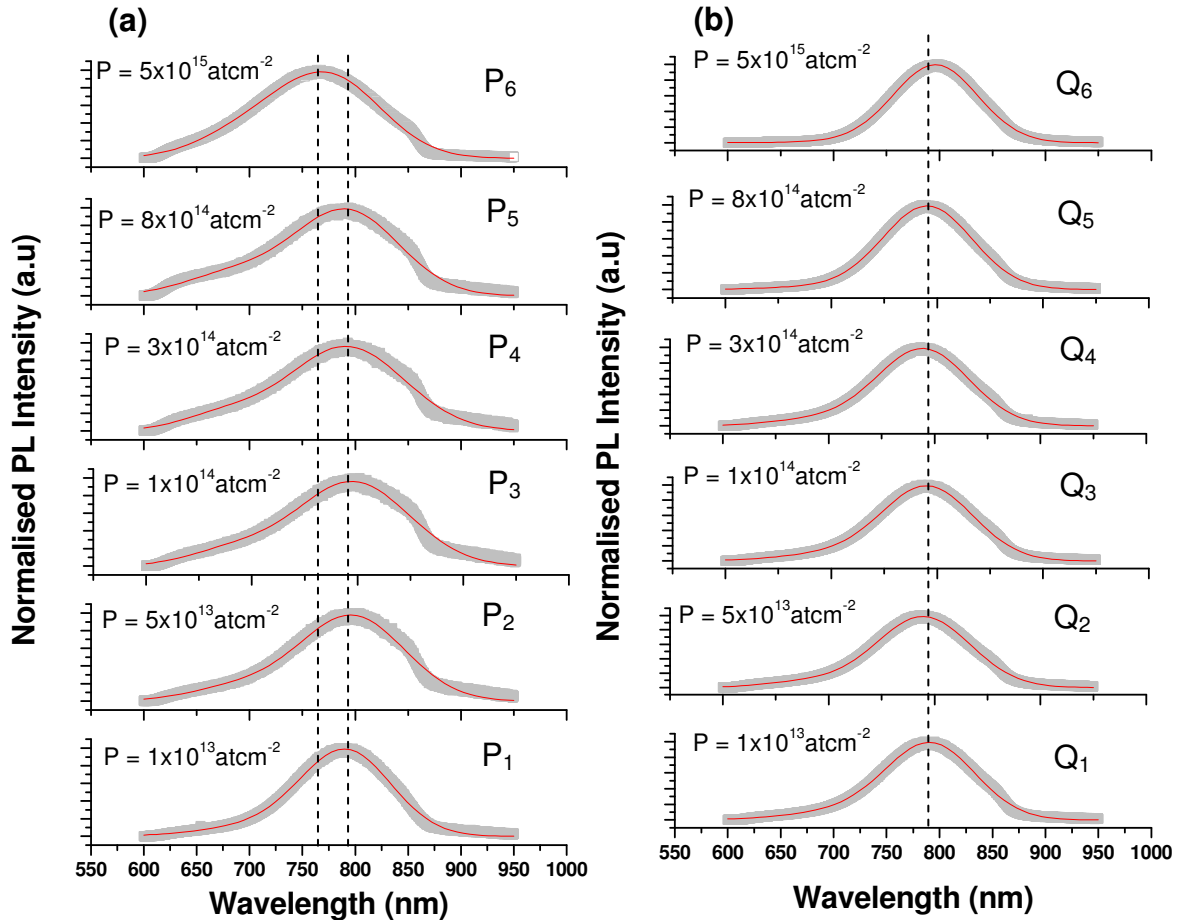
Figure 6-1 Measured PL spectra (grey points) and double Gaussian fit (red line) for phosphorus doped samples in (a) set P and (b) set Q with phosphorus concentrations indicated. Dashed lines are guides to the eye highlighting the blue-shift in sample set P with increasing P$^+$ dose

The spectra are typical of Si-NCs in SiO$_2$[297, 298], with a broad peak centred around 800nm. The fit was obtained using *OriginPro8* standard analysis functionality assuming Gaussian functions. *OriginPro8* provides a non-linear least squares routine to describe such data using the *Levenberg-Marquardt* algorithm (LMA). A numerical solution is obtained by minimizing the sum of the squares of the differences between the empirical dataset and a model fit. This is an iterative solver that initiates with a user definition for the number of peaks and initial

estimates of their position and full-width at half maximum (FWHM). Such a fitting process carries with it a degree of ambiguity as it is possible to obtain a converging solution even if the initial estimates are far from the actual values of the dataset. On the other hand it is possible to obtain a reasonable fit without having identified all of the spectral components. Caution on the part of the user is therefore required since the routine will return an increasingly accurate fit as the number of peaks at first iteration (or replicas) is increased. In the case of the present dataset, accurate fits with typical χ^2 values in the range 0.98918 to 0.99916 were obtained with a double Gaussian model, which is most evident for sample set P, probably on account of the lower absolute intensity relative to samples in set Q.

High energy contributions to the PL spectrum around 650nm (~1.9eV) have previously been attributed to oxide defect related luminescent centres, most notably the non-bridging oxygen hole centre (NBOHC), which arises after the cleaving of strained Si-O bonds during ion irradiation[299]. Quenching of the relative intensity of this peak is typically observed with increasing annealing temperature above 600°C, indicative of the removal of such defects due to matrix reordering[300]. On the contrary, the intensity of the longer wavelength, principal emission peak generally increases with annealing time, particularly for annealing temperatures above 900°C. This peak also exhibits a red-shift with annealing time and temperature, which is a fingerprint of increasing Si-NC size that coincides with a band-gap narrowing in accordance with the quantum confinement model for band edge recombination[301]. The relative luminescence intensity of the two contributions suggests that the process of carrier trapping at oxide related defects is competitive with band-edge radiative recombination in Si-NCs. The presence of defect related luminescence centres in ion implanted samples is not surprising, particularly for the case of sample set P. Recall that the P$^+$ implantation in this set came after the high temperature (1050°C) anneal during which the Si-NCs were formed. The amorphization of the Si-NCs by the phosphorus irradiation, combined with the subsequent lower temperature anneal (800°C), which would have been much less effective at removing irradiation damage in the oxide matrix, might explain the relatively strong contribution at higher energies because of an increased density of NBOHC centres. Alternatively, an increase in the contribution to the luminescence from shorter wavelengths could be due to an increase in the density of smaller luminescent Si-NCs, for example due to the amorphization of the larger clusters by

the phosphorus irradiation. Longer wavelength emissions were previously attributed to shallow defect-like states within the Si-NC band-gap that are known to be sensitive to hydrogen passivation[302]. Alternatively, these emissions could be due to larger Si-NCs.

Heavily phosphorus doped glasses 'soften' at much lower temperatures than un-doped SiO$_2$ matrices because Si-O-Si bonds are substituted by hydroxyl radicals, e.g. Si-O-POH which increases the open volume density[303]. This lowers the melting temperature[304] and increases the thermal expansion coefficient relative to pure silica glass and can result in an increased ion diffusion length. For the silicon rich oxide (SRO) system, particularly sample sets Q and R in which the Si-NCs were formed in the presence of phosphorus doped glass, this could lead to an accelerated segregation of the Si and SiO$_2$ phases[305] as well as a more effective matrix re-ordering i.e. defect removal. The re-crystallization of bulk Si is also known to be accelerated following amorphization via high dose phosphorus ion irradiation[306]. These factors could influence the nano-cluster formation dynamics providing crystalline Si-NCs with a superior quality interface with the SiO$_2$, relative to un-doped samples.

This might explain the general observation of increased luminescence intensity at lower energies and the much smaller contribution from high energy emissions for samples in set Q compared to those in sample set P. Even for an equivalent fraction of ionized donors in sample sets P and Q, the un-doped Si-NCs in set Q might exhibit a lower concentration of electronically active non-radiative defects. This would explain the reported increase in luminescence lifetime for phosphorus doped Si-NC samples reported by Belyakov *et al*[295].

A comparison of the integrated intensity and position of the principal peak obtained from the fits for each of the spectra for samples sets P and Q is presented in **Figure 6-2**.
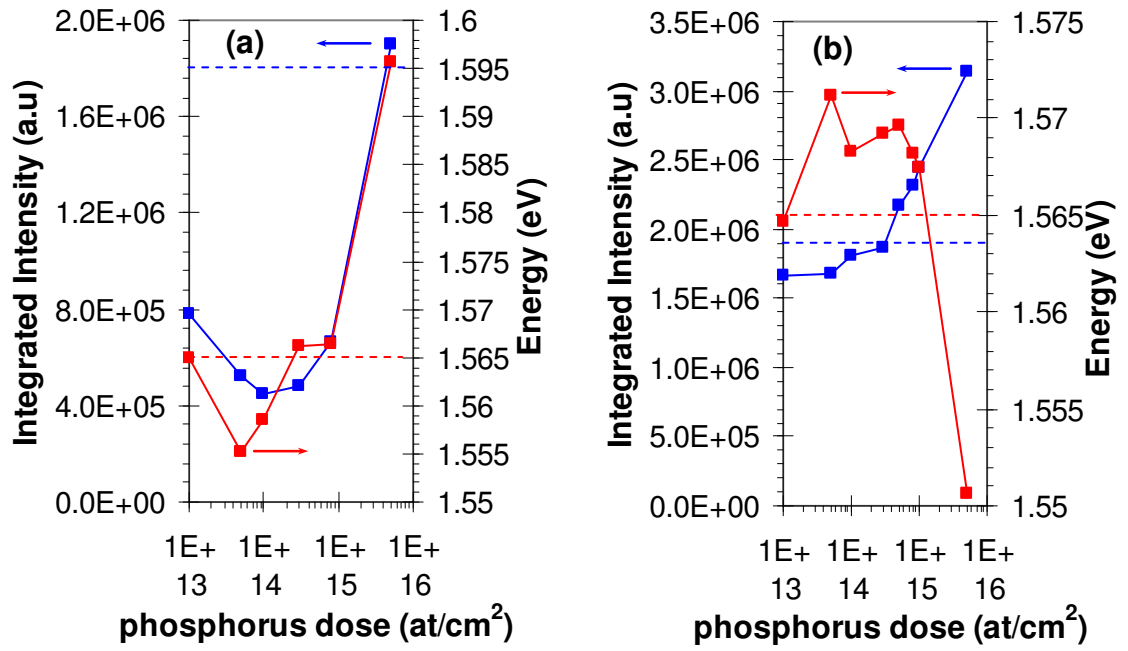
Figure 6-2 Integrated intensity (blue) and peak emission energy (red) for phosphorus doped samples in (a) set P and (b) set Q. The blue and red dashed lines indicate the integrated intensity and peak emission energy respectively for the un-doped reference sample, Q$_{13}$

A monotonic increase in the PL intensity with phosphorus concentration is observed for P$^+$ > 8x10^{14}cm^{-2}, which is independent of preparation. In sample set P this increase follows an initial quenching of up to 75% for low phosphorus concentrations until, at the highest phosphorus concentration (5x10^{15}cm^{-2}) the PL intensity is completely recovered to that of the un-doped reference sample. A small red shift accompanies the drop in intensity for the lowest phosphorus concentration but the peak is monotonically blue shifted as the intensity increases with increasing phosphorus concentration. In sample set Q the integrated PL intensity is fractionally reduced for low phosphorus concentration but increases with phosphorus concentration up to 5x10^{15}cm^{-2}, where it is enhanced by around a factor of 2 relative to the un-doped reference. The peak position for this sample set is initially blue shifted for the lowest phosphorus concentrations, whilst a monotonic red shift follows the gradual increase in intensity up to the largest phosphorus concentration. The luminescence was completely quenched at the highest phosphorus concentration of 3x10^{16}cm^{-2}, which could be due to the formation of phosphorus metal precipitates[283].

These results are collectively interpreted in terms of the interaction of the P$^+$ ions with Si-NCs of different sizes in the ensemble. The increased likelihood of doping

larger nano-clusters means that they are most likely to become optically inactive due to impurity ionization, which should lead to an efficient and rapid non-radiative recombination via Auger excitation. This might explain the initial quenching of the luminescence intensity and blue shift in sample set Q for low phosphorus concentrations. That this is only observed for sample set Q may be because of the different preparations, which would lead to a much higher concentration of electronically active defects induced after the phosphorus irradiation in sample set P. The lower temperature (800°C) thermal treatment would have been much less effective at removing these defects and re-crystallizing nano-clusters. In sample set Q the optical inactivity of the largest nano-clusters, as a result of dopant ionization at low phosphorus concentrations, may be compensated for by the remaining un-doped nano-clusters, which are expected to be well formed with a larger 'defect free' fraction due to both the higher anneal temperature (1050°C) and presence of phosphorus in the glass matrix during formation. This might explain why the luminescence intensity is only fractionally reduced for samples in set Q relative to the un-doped reference. The fact that the luminescence intensity increases monotonically over the same phosphorus concentration range for both sample sets may be indicative of the preferential optical activation of a specific fraction of the Si-NC population.

If we assume a relatively uniform concentration of both Si-NCs and P^{+} in the oxide, the probability of doping a nano-cluster increases with the P^{+} concentration and Si-NC size. The largest Si-NCs in any given distribution are therefore more likely to contain and ionize a P^{+} ion than their smaller counterparts. On account of the significantly larger surface to volume ratio of smaller Si-NCs, the interaction of phosphorus ions with these is much more likely to be surface related. As it turns out, this is not just because of the statistical probability of the relative position in the SiO$_2$ matrix, but also because substitutional sites towards the centre of Si-NCs are not energetically favourable for phosphorus atoms[287]. The role of the P^{+} ion in this case could involve the termination of interfacial P_b centres, the so-called 'dangling bond' type defects, in a similar way to hydrogen, thereby optically activating small Si-NCs (assuming little or no contribution to the PL from the same smaller defective Si-NCs in the absence of P^{+}). Based on the range of P^{+} employed in these experiments, over which the PL is monotonically increased, a 'critical diameter', d_{nc} for the ionization cut-off is proposed, below which P^{+} preferentially interacts with the nano-clusters in a passivating function. Assuming

all excess Si atoms are involved in the formation of spherical Si-NCs and that only one P$^+$ ion is required to passivate and therefore optically activate a small Si-NC, then this 'critical diameter' is given by equation (78):

$$d_{critical} = \sqrt[3]{\frac{6V_{critical}}{\pi}} = \sqrt[3]{\frac{6nV_{Si}}{\pi}} \tag{78}$$

Where $V_{critical}$ is the volume associated with small P$^+$ passivated Si-NCs, V_{Si} is the volume occupied by a single Si atom (calculated from the Si atomic radius plus half the bond length, ~272pm[307]) and n is the number of Si atoms comprising such a Si-NC. Using this expression and the Si:P ratio above which the PL is monotonically increased (~100 in the case of both sample sets) for n, then $d_{critical}$ ~2.5nm. Despite the obvious simplicity of this calculation, the supposition that Si-NCs with $d <$ 2.5nm cannot support P$^+$ atoms, except via surface termination is in good agreement with the theoretical predictions of Chan et $al.$[287] The authors in [[287]] used a density functional theory (DFT) approach to show that, for Si-NCs with $d <$ 2nm it is energetically favourable for phosphorus atoms to occupy sites towards the surface, rather than the centre of the Si-NCs.

The passivation of dangling bond defects by P$^+$ at the Si-NC surface might be more effective when formation occurs in the presence of the impurity ions because of grain boundary 'gettering' of the impurities, which was already reported for phosphorus doped bulk Si[308]. Indeed we have observed similar behaviour in the case of Si-NCs forming in the presence of Erbium ions[309]. In the present study this might explain the observation of the larger PL enhancement for sample set Q over the same P$^+$ concentration range.

Whereas the fraction of ionized donors increases with the mean nano-cluster diameter, the fraction of donors that contribute to nano-cluster surface passivation in this way should be proportional to the inverse mean diameter. This is evidenced by the fact that, for extended annealing, particularly at elevated temperatures $\geq$ 1100°C, which increases the mean nano-cluster diameter, we found that the integrated luminescence was always monotonically quenched with increasing P$^+$ concentration, regardless of the sample preparation. The evolutionary growth of Si-NCs continues, even in the absence of further excess Si, according to the Ostwald ripening process, which results in a further increase in the number of ionized donors.

In Chapter 3 we showed how the size and density distribution of nano-clusters in a given ensemble evolves with the isochronal and isothermal annealing conditions. Annealing at 1050°C for 100s produces a log-normal size distributed nano-cluster population with a mean diameter ~1.82nm and standard deviation ~0.335. In this population, the largest fraction of nano-clusters has $d_{nc} < 2.5$nm (i.e. $d < d_{critical}$). Annealing at the elevated temperature of 1100°C for 100s yields a nano-cluster population with a mean diameter ~2.45nm and standard deviation ~ 0.38. The largest fraction of nano-clusters in this distribution has $d_{nc} > 2.5$nm (i.e. $d > d_{critical}$). In the present sample sets, the continued growth beyond the 'critical diameter' should therefore result in a significant increase in the fraction of ionized donors, particularly for heavily doped samples. The fraction of Si-NCs with d just below the 'critical diameter' prior to the extended high temperature anneal, can be expected to have grown in size sufficiently such that passivating P$^+$ ions at their surface become enveloped by their host during growth. This explains the dramatic reduction in nano-cluster luminescence intensity, which was observed for both sample sets P and Q after the extended high temperature annealing where the role of the P$^+$ ions not only cease to perform a passivating function but also become ionized inside the Si-NCs and therefore contribute to Auger recombination.

Drawing a direct parallel with the work of Belyakov *et al*[301], we note that differences in their observations, i.e. a monotonic quenching with increasing P$^+$ concentration after Si$^+$ $\Rightarrow$ 1100°C $\Rightarrow$ P$^+$ $\Rightarrow$ 1000°C can be explained by the higher anneal temperature (1000°C) after the P$^+$ implantation compared to the lower temperature (800°C) latter anneal in this work. This latter higher temperature treatment would have effected Si-NC growth leading to an ensemble population with a larger mean diameter and hence larger fraction of ionized donor impurities with phosphorus concentration.

6.3.2   Effect of phosphorus concentration on the Si-NC PL after high temperature annealing

The PL spectra for sample set R are shown in **Figure 6-3**. The broad PL peak centred between 750 and 770nm is similar to that obtained for the previous sample sets and is typical of that obtained from a SiO$_2$ sample containing an ensemble of Si-NCs.
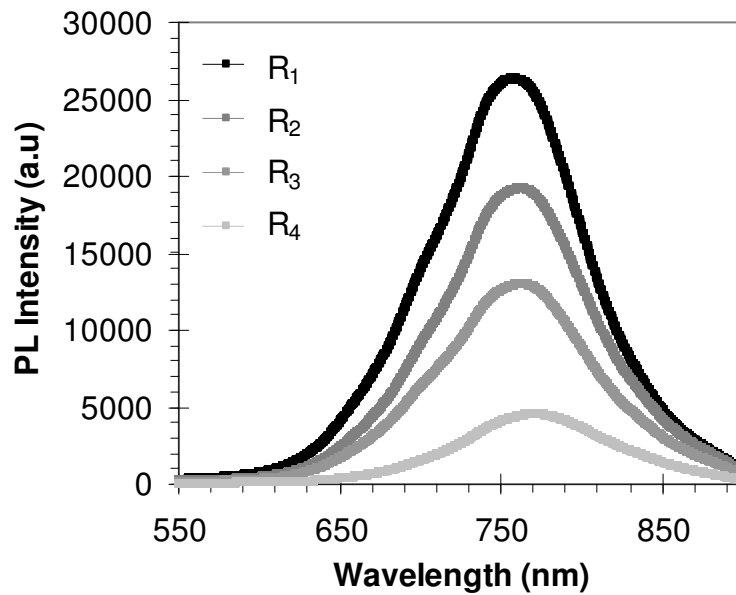
Figure 6-3 Photoluminescence spectra for sample set R as a function of P$^+$ concentration

Not shown in **Figure 6-3** is the spectrum for the sample which contained no phosphorus, R$_5$ which was identical to that obtained for the sample doped with a phosphorus concentration of 8×10^{13}cm^{-2}, sample R$_1$. Notable for this sample set is the monotonic decrease in intensity with increasing phosphorus dose. This is identical to the previous sample sets, where the PL was monotonically reduced with phosphorus concentration only after annealing above 1100°C. Given that the intensity for the samples with the lowest phosphorus dose and the un-doped sample in this set are identical, and that a significant relative decrease in intensity occurs for the sample doped using a phosphorus ion dose of 3×10^{14}cm^{-2}, we conclude that we do not observe surface passivation of Si-NCs via phosphorus doping for this sample set. Since the formation of Si-NCs and the phosphorus doping took place simultaneously in the present sample set, as in sample set Q, thereby removing the possibility that nano-clusters would be susceptible to

236

phosphorus induced irradiation damage, as for sample set P, the difference observed between these results and those of sample set Q (prior to the extended anneal) can only be due to the longer annealing (1 hour) at the elevated temperature of 1100°C.

Similar to sample set Q, the presence of phosphorus in the SRO for the present sample set could lead to an accelerated phase segregation and enhanced crystallization. Although the larger mean diameter of the Si-NCs after annealing at 1100°C is likely to give rise to an increased number of ionized donors and subsequently, an increase in the Auger de-excitation of excited carriers in the Si-NCs with P$^+$ concentration, the relatively low defect concentration might explain a more efficient luminescence yield from the un-doped population.

We measured the PL decay transients around the peak for all of the samples in set R and these are shown in **Figure 6-4**.
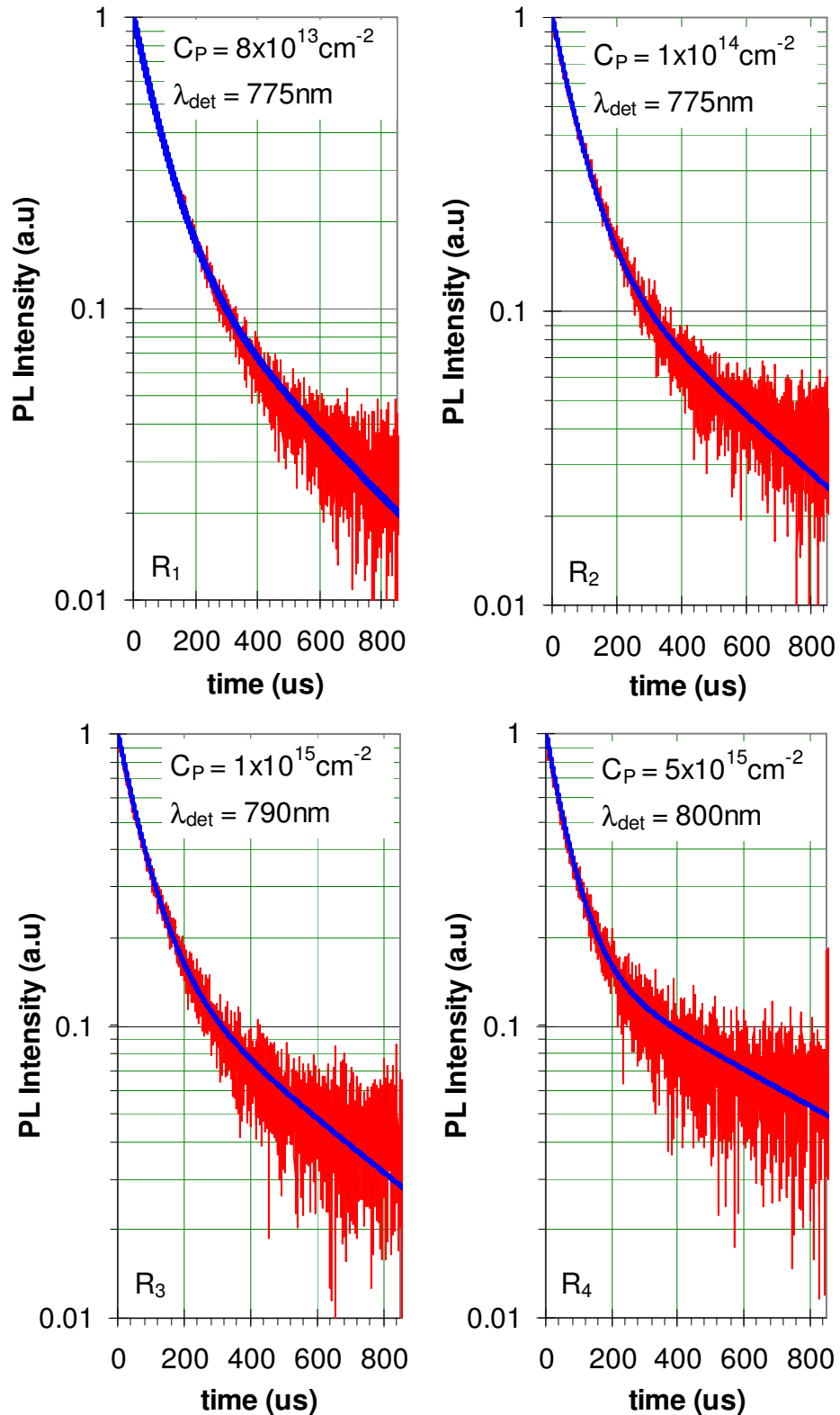

Figure 6-4 PL decay transients measured at the PL peak position for the phosphorus doped samples in set R. Phosphorus concentrations, C_P and the detection wavelength, λ_{det} are indicated on each spectrum

The decay transients were adequately described using the 'stretched exponential' function, which has the form, $I = I_0\,exp(-t/\tau)^{\beta}$, where β is a 'stretching parameter' with values between 0 and 1 where 1 indicates a single exponential. The stretched exponential is usually interpreted physically as a measure of system disorder, which increases inversely with the magnitude of β.

It is noteworthy that the characteristic 1/e lifetime, $\tau \sim 100\mu s$ obtained from the fits is virtually unaffected with increasing phosphorus concentration. Observations of increases in the characteristic lifetime were previously reported for samples annealed at higher temperature, particularly when the PL was detected at longer wavelengths[310]. This was attributed to higher quality nano-clusters forming at higher anneal temperatures. The absence of a significant lifetime dependence on P$^+$ concentration in the present sample set indicates that the observed luminescence is from un-doped nano-clusters and the lower integrated PL intensity is simply due to the larger fraction of ionized impurities. The monotonically decreasing intensity with increasing phosphorus concentration in this sample set indicates that the un-doped, luminescent nano-crystal fraction is inversely proportional to the phosphorus concentration. This behaviour can be adequately modelled using a simple statistical approach, which also provides an incidental estimate of the Si-NC size distribution within the sample ensemble.

As before, we maintain the assumption that the probability of a spherical Si-NC containing a phosphorus ion in a SiO$_2$ matrix, having a uniform concentration of both, depends on both the phosphorus ion concentration and the nano-cluster size. Then, the probability that a nano-cluster does <u>not</u> contain a phosphorus ion, $p(P,n)$ and therefore remains optically active may be written:

$$p(P,n) = \left(1 - \left[\frac{P}{Si}\right]\right)^{n} \tag{79}$$

Where P is the phosphorus ion dose, Si is the silicon ion dose (in this case fixed at $8\times10^{16}cm^{-2}$) and n is the number of silicon atoms forming a nano-cluster. **Figure 6-5** reveals the calculated fraction of un-doped Si-NCs as a function of nano-cluster diameter, d_{nc} for a range of phosphorus doses and as a function of phosphorus dose, P for a range of nano-cluster sizes.
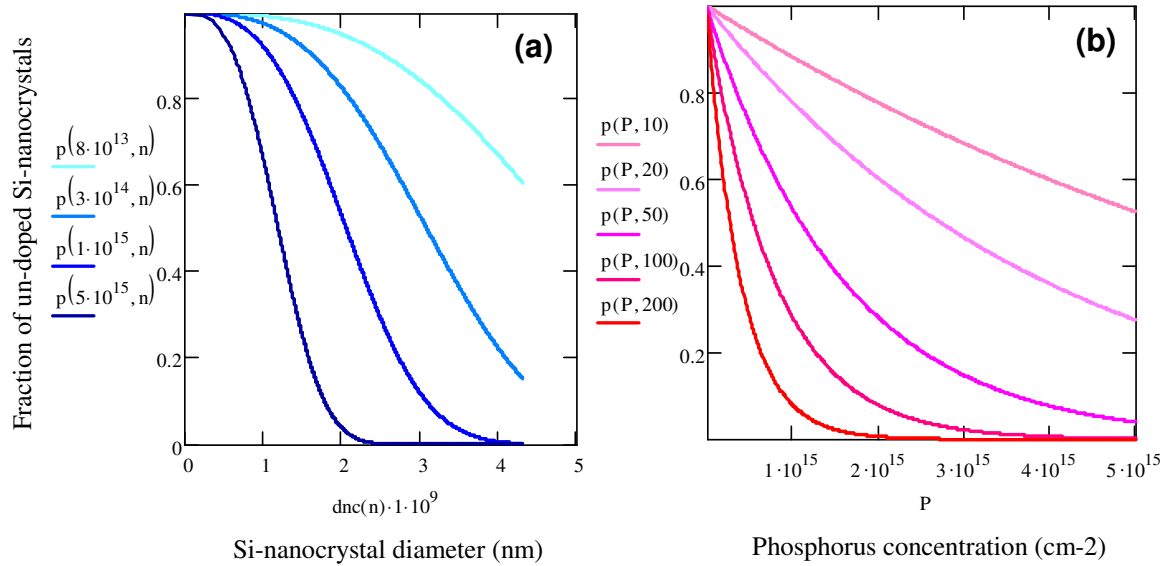
Figure 6-5 Calculated (equation 79) fraction of un-doped Si-NCs as a function of (a) nano-cluster diameter for increasing phosphorus concentration in the range 8x10^{13} – 5x10^{15}cm^{-2} and (b) phosphorus concentration for increasing number of Si atoms, *n*: 10, 20, 50, 100 and 200 corresponding to nano-cluster diameters: 1.17, 1.48, 2, 2.53 and 3.2nm

This model assumes that a single dopant ion, present inside a Si-NC, results in the introduction of an efficient Auger de-excitation process for any exciton and thus the nano-cluster becomes 'dark'. It is evident from **Figure 6-5** that, for the highest phosphorus concentration in sample set R (5x10^{15}cm^{-2}), all nano-clusters with $d >$ 2.5nm are likely to be doped and therefore ought to be optically inactive. The model therefore makes a prediction on the evolution of the peak emission wavelength with increasing phosphorus dose, specifically that the emission should shift to the blue, consistent with the increased likelihood of 'darkening' of larger Si-NCs for the lower phosphorus doses.

Figure 6-6 describes the relative, integrated PL intensity of the spectra shown in **Figure 6-3** as a function of phosphorus dose.
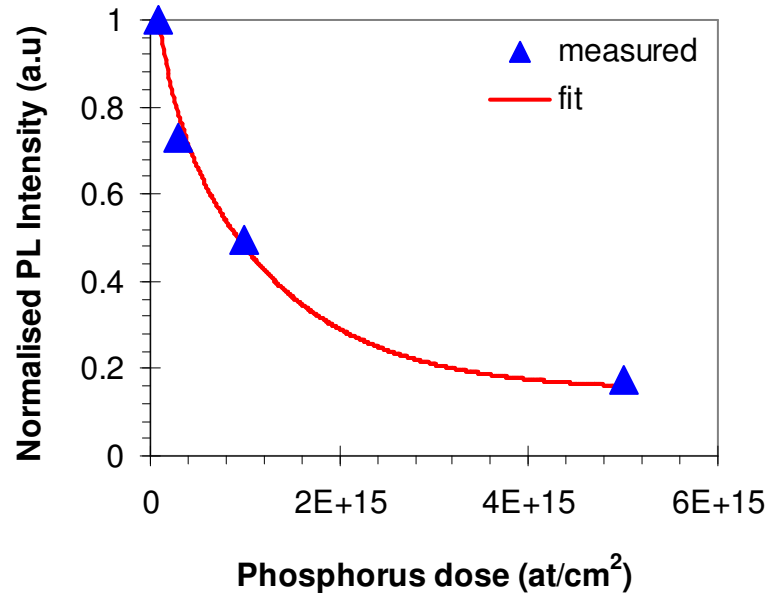

Figure 6-6 Measured (diamonds) and calculated (line) (from equation (80)) integrated PL intensity, normalised to the lowest P$^+$ dose (Sample R$_1$) as a function of phosphorus dose

The solid line is a fit to the experimental data, which is derived directly from equation (79) and represented by equation (80):

$$I = \sum_{i=1}^{\infty} I(0,n)_i\, p(P,n)_i + C \qquad (80)$$

Where I is the normalised PL intensity, $p(P,n)_i$ is the probability that a nano-cluster consisting of n_i atoms <u>does not</u> contain a phosphorus ion from equation (79), $I(0,n)_i$ is the PL intensity due to all nano-clusters containing i atoms if no phosphorus were present in the sample and C is a constant PL intensity, which is not affected by the phosphorus doping.

Excellent agreement between the experimental data and the fitted line is obtained for $n = 100$, which corresponds to a nano-cluster diameter of 2.53nm. We note that if a weighted distribution is used, e.g. $0.8n_1 + 0.2n_2$, where $n_1 = 95$ and $n_2 = 170$ then the fit may be marginally improved for the lower phosphorus concentrations. These values correspond to nano-cluster diameters of 2.48 and 3.01nm respectively, i.e. only two sizes are required to represent the entire Si-NC size distribution in the ensemble. Taking into account the weighting of the distribution

returns a value for the mean Si-NC diameter of 2.61nm. Necessary also was an estimated contribution from the constant PL component C of ~15% of $I(0,n)_i$, the likely origin of which is the incomplete overlap of the phosphorus implantation profile with that of the Si-NCs. For example, imperfect coincidence of the silicon and phosphorus implant profiles would leave a fraction of Si-NCs too far from any dopant to provide an Auger de-excitation channel, regardless of the phosphorus concentration. This situation may be avoided through the use of multiple-energy phosphorus ion implants. Although the data fitting leaves open the possibility for multiple solutions to equation (80), the prediction of Si-NCs with a mean diameter of ~2.5 to 2.6nm is not unreasonable and is in good agreement with the PL peak emission wavelength. In [290] the authors utilized a Poisson statistical model to obtain a nano-cluster diameter of 3nm from samples emitting light at a longer wavelength than the samples described here, consistent with a larger mean Si-NC diameter. In addition, the size of Si-NCs determined here are in excellent agreement with the 'critical diameter' representing the ionization 'cut-off' we determined earlier from sample sets P and Q.

The observation of a small red-shift with increasing phosphorus dose, which is approximately half of that measured for sample sets P and Q after the extended high temperature anneal is consistent with emission from nano-clusters in the advanced stages of ripening after nucleation. Increases in Si-NC size are much smaller in the advanced stages of growth (Ostwald ripening stage) compared with the early nucleation stage, which can be expected after annealing for much longer times at 1100°C. We note that the red-shift in the case of the present sample set is accompanied by a small spectral narrowing, particularly on the high energy side of the spectra, with increasing phosphorus dose. This observation is likely related to the further removal of irradiation damage such as the NBOHC oxide related defect centres, with extended high temperature annealing. The monotonic reduction in the density of optically active, defect related luminescent centres with increasing phosphorus dose is anticipated if the phosphorus indeed enhances phase segregation, Si crystallization and repair of the SiO$_2$ matrix. In addition, the contribution from well formed optically active nano-clusters, despite the overall reduction in density can be expected to be more efficient on account of the reduced density of electronically active non-radiative dangling bond type defects.

6.4   Conclusions

By careful control of the annealing environment after co-implantation of Si$^+$ and P$^+$, it is possible to obtain an enhancement in the Si-NC related PL intensity of around a factor of 2 for a P$^+$ concentration of 5×10^{15}cm^{-2}, compared with an un-doped reference sample.

For samples already containing an ensemble population of Si-NCs, the implantation of P$^+$, followed by a relatively low temperature (800°C) dopant activation, initially leads to a quenching of the integrated luminescence by as much as ~75% relative to an un-doped reference for phosphorus concentrations below 1×10^{14}cm^{-2}. Increasing the P$^+$ concentration however leads to a complete recovery of the integrated luminescence to the same level as the un-doped reference at a P$^+$ concentration of 5×10^{15}cm^{-2}. For samples prepared in this manner, we observe a monotonic blue shift in the spectral peak and an inhomogeneous broadening to the high energy side of the spectra that monotonically increases with P$^+$ concentration.

We note from prior studies of phosphorus doped glasses that the presence of P$^+$ can result in a 'softening' of the SiO$_2$ (glass) matrix by substituting Si-O-Si bonds with, for example Si-O-POH surface groups[303]. This lowers the melting temperature and increases the thermal expansion coefficient[304] of the matrix, which can lead to an increased Si$^+$ diffusion length[311]. Consequently, the Si and SiO$_2$ phase segregation process in silicon rich oxide (SRO) could be accelerated by the presence of P$^+$ in comparison to an un-doped SRO, for the same annealing conditions. This may lead to an enhanced nano-cluster formation along with the suppression of non-radiative defects as a result of matrix reordering and may explain the red-shift and enhanced integrated intensity in samples where the Si-NC formation proceeds in the presence of phosphorus.

The observations described in this work are attributed to a combination of factors, each of which plays a role in determining the optical activity of a Si-NC, which depends critically on its size. The increased likelihood of doping larger nano-clusters means that they are most likely to become optically inactive due to impurity ionization, which leads to an efficient and rapid non-radiative recombination via Auger excitation. The observed luminescence increase over the same phosphorus concentration range in both sample sets P and Q is interpreted in terms of a preferential optical activation of smaller Si-NCs. Based on the Si$^+$ to

P$^+$ ratio employed in these experiments, we propose a 'critical diameter' of ~2.5nm in good agreement with prior theoretical predictions, below which individual P$^+$ ions are not ionized inside the Si-NC but rather they suppress electronically active defects by passivating surface dangling bonds at the SiO$_2$/Si-NC interface. The relative contribution of these processes to the total luminescence yield therefore depends on the mean Si-NC diameter of a given ensemble, which explains the variety of results reported for this material system. Based on our observations, we propose that the fraction of donors that contribute to nano-cluster surface passivation is proportional to the inverse Si-NC mean diameter, whereas the fraction of ionized donors increases with the mean Si-NC diameter. This is evidenced by the fact that, for extended annealing at elevated temperatures $\geq$ 1100°C, which increases the mean Si-NC diameter, the integrated luminescence is always monotonically quenched with increasing P$^+$ concentration, regardless of the sample preparation. In fact, the relative quenching of the luminescence with increasing P$^+$ concentration for samples annealed at elevated temperatures ($\geq$ 1100°C) can be modelled adequately using a simple statistical approach, from which an incidental estimate of the nano-cluster mean diameter ~2.5 to 2.6nm was obtained. We find that this estimate is in excellent agreement, both with the observed peak emission wavelength and that predicted by extrapolation of values based on prior observations of the Si-NC growth dynamics. This is in accord with a diffusion limited nucleation and growth process, followed by Ostwald ripening. A blue shift in the emission with increasing phosphorus concentration, also predicted by the statistical model, was only observed for samples subjected to phosphorus irradiation of pre-formed Si-NCs followed by a lower temperature (800°C) anneal. This is explained in terms of the combined doping of larger and the passivation of smaller defective nano-clusters in the ensemble.

We note that, according to the explanation offered here, the PL enhancement obtained by P$^+$ doping should increase with the inverse mean nano-cluster diameter. This hypothesis could be tested by varying the isothermal (1050°C) anneal time of a Si$^+$ and P$^+$ co-implanted SiO$_2$ in the ratio ~100:1 over the range 1 to 3600s in a rapid thermal processing (RTP) unit. The samples annealed for the shortest times will contain a larger fraction of small Si-NCs and the PL enhancement, provided by the P$^+$ should therefore be larger than for samples annealed for the longer times.

6.5   References

277.   V. Svrcek, A. Slaoui, J. C. Muller, J. L. Rehspringer, B. Hönerlage, R. Tomasiunas and I. Pelant, Physica E: Low-dimensional Systems and Nanostructures **16** (3-4), 420-423 (2003).

278.   D. I. Tetelbaum, S. A. Trushin, A. N. Mikhaylov, V. K. Vasil'ev, G. A. Kachurin, S. G. Yanovskaya and D. M. Gaponova, Physica E: Low-dimensional Systems and Nanostructures **16** (3-4), 410-413 (2003).

279.   A. Mimura, M. Fujii, S. Hayashi, D. Kovalev and F. Koch, Physical Review B **62** (19), 12625 (2000).

280.   M. Fujii, A. Mimura, S. Hayashi and K. Yamamoto, Applied Physics Letters **75** (2), 184-186 (1999).

281.   M. Fujii, A. Mimura, S. Hayashi, K. Yamamoto, C. Urakawa and H. Ohta, Journal of Applied Physics **87** (4), 1855-1857 (2000).

282.   E. C. Cho, M. A. Green, G. Conibeer, A. Song, Y. H. Cho, G. Scardera, S. Huang, S. Park, X. J. Hao, Y. Huang and L. V. Dao, Advances In Optoelectronics 2007 (2007).

283.   X. J. Hao, E. C. Cho, G. Scardera, E. Bellet-Amalric, D. Bellet, Y. S. Shen, S. Huang, Y. D. Huang, G. Conibeer and M. A. Green, Thin Solid Films **517** (19), 5646-5652 (2009).

284.   G. Conibeer, M. Green, R. Corkish, Y. Cho, E.-C. Cho, C.-W. Jiang, T. Fangsuwannarak, E. Pink, Y. Huang, T. Puzzer, T. Trupke, B. Richards, A. Shalav and K.-l. Lin, Thin Solid Films **511-512**, 654-662 (2006).

285.   M. Asheghi, K. Kurabayashi, R. Kasnavi and K. E. Goodson, Journal of Applied Physics **91** (8), 5079-5088 (2002).

286.   J. F. Ziegler, *The Stopping and Range of Ions in Solids (Stopping and Range of Ions in Matter)*. (Pergamon Pr, 1985).

287.   T. L. Chan, M. L. Tiago, E. Kaxiras and J. R. Chelikowsky, Nano Letters **8** (2), 596-600 (2008).

288.   M. L. Ciurea, in *Nanoelectronics and Photonics From Atoms to Materials, Devices and Architechtures*, edited by A. Korkin and F. Rosei (Springer, New York, 2008).

289.   D. Kovalev, H. Heckler, G. Polisski and F. Koch, physica status solidi (b) **215** (2), 871-932 (1999).

290.   A. L. Tchebotareva, M. J. A. de Dood, J. S. Biteen, H. A. Atwater and A. Polman, Journal of Luminescence **114** (2), 137-144 (2005).

291.   D. I. Tetelbaum, O. N. Gorshkov, S. A. Trushun, D. G. Revin, D. M. Gaponova and W. Eckstein, Nanotechnology **11**, 295-297 (2000).

292.   D. Tetelbaum, O. Gorshkov, V. Burdov, S. Trushin, A. Mikhaylov, D. Gaponova, S. Morozov and A. Kovalev, Physics of the Solid State **46** (1), 17-21 (2004).

293.   A. Uedono, T. Mori, K. Morisawa, K. Murakami, T. Ohdaira, R. Suzuki, T. Mikado, K. Ishioka, M. Kitajima, S. Hishita, H. Haneda and I. Sakaguchi, Journal of Applied Physics **93** (6), 3228-3233 (2003).

294.   V. A. Belyakov and V. A. Burdov, Physical Review B (Condensed Matter and Materials Physics) **79** (3), 035302-035309 (2009).

295.   V. A. Belyakov, A. I. Belov, A. N. Mikhaylov, D. I. Tetelbaum and V. A. Burdov, Journal of Physics: Condensed Matter **21**, 045803 (2009).

296.   M. Fujii, K. Toshikiyo, Y. Takase, Y. Yamaguchi and S. Hayashi, Journal of Applied Physics **94** (3), 1990-1995 (2003).

297. A. P. Knights, J. N. Milgram, J. Wojcik, P. Mascher, I. F. Crowe, B. Sherliker, M. P. Halsall and R. M. Gwilliam, physica status solidi (a) **206** (5), 969-972 (2009).

298. J. H. Shim and N. H. Cho, Glass Physics and Chemistry **31** (4), 525-529 (2005).

299. A. J. Kenyon, P. F. Trwoga, C. W. Pitt and G. Rehm, Journal of Applied Physics **79** (12), 9291-9300 (1996).

300. K. A. Jeon, J. H. Kim, J. B. Choi, K. B. Han and S. Y. Lee, Materials Science and Engineering: C **23** (6-8), 1017-1019 (2003).

301. V. A. Belyakov, V. A. Burdov, R. Lockwood and A. Meldrum, Advances in Optical Technologies **2008**, 279502 (2008).

302. D. Comedi, O. H. Y. Zalloum and P. Mascher, Applied Physics Letters **87** (21), 213110-213113 (2005).

303. S. Prakash, W. E. Mustain, S. Park and P. A. Kohl, Journal of Power Sources **175** (1), 91-97 (2008).

304. N. I. Belyusenko and Y. P. Kareev, Glass and Ceramics **36** (4), 206-208 (1979).

305. M. Fujii, Y. Yamaguchi, Y. Takase, K. Ninomiya and S. Hayashi, Applied Physics Letters **85** (7), 1158-1160 (2004).

306. D. Tetelbaum and A. Gerasimov, Semiconductors **38** (11), 1260-1262 (2004).

307. W. C. O'Mara, R. B. Herring and L. P. Hunt, *Handbook of Semiconductor Silicon Technology*. (William Andrew Publishing/Noyes, 1990).

308. A. Bentzen and A. Holt, Materials Science and Engineering: B **159-160**, 228-234 (2009).

309. I. F. Crowe, R. Jalili-Kashtiban, B. Sherliker, U. Bangert, M. P. Halsall, A. P. Knights and R. M. Gwilliam, Journal of Applied Physics **107** (044316) (2010).

310. M. Fujii, K. Imakita, K. Watanabe and S. Hayashi, Journal of Applied Physics **95** (1), 272-280 (2004).

311. K. Sumida, K. Ninomiya, M. Fujii, K. Fujio, S. Hayashi, M. Kodama and H. Ohta, Journal of Applied Physics **101** (3), 033504-033505 (2007).